Università
degli Studi
della Campania
Luigi Vanvitelli

Dottorato di Ricerca in AMBIENTE DESIGN E INNOVAZIONE
Ph.D ENVIRONMENT DESIGN AND INNOVATION

Curriculum SCIENZE E TECNOLOGIE SOSTENIBILI PER L’AMBIENTE E IL TERRITORIO
Curriculum SCIENCES AND SUSTAINABLE TECHNOLOGIES FOR THE ENVIRONMENT
SSD – ICAR/07
Ciclo | Cycle 32°

DOCTOR EUROPAEUS

Comportamento di pali sotto carichi statici e termici
Behaviour of piles under static and thermal loading

Chiara Iodice
Alessandro Mandolini
GViggiani
Raffaele Di Laora
Biagio Morrone

Dottoranda | Ph.D Candidate Chiara IODICE
Tutor | Supervisor Prof. Alessandro MANDOLINI
Tutor internazionale | International Supervisor Prof. Giulia VIGGIANI
University of Cambridge
Co-tutor | Co-Supervisor Dr. Raffaele DI LAORA
Co-tutor | Co-Supervisor Prof. Biagio MORRONE
Coordinatore | Coordinator Prof. Mario BUONO

Maggio 2020
May 2020

Dipartimento di Ingegneria

Dipartimento di Scienze e Tecnologie
Ambientali Biologiche e
Farmaceutiche

Scuola di Medicina e Chirurgia
Dipartimento di Medicina
Sperimentale

Contents

List of symbols

Latin symbols

a	coefficient regulating soil stiffness profile
A	pile cross-sectional area
$\mathcal{A}$	fourth-order tensor
a_f	constant of the Hypoplastic model
A_g	constant of the Hypoplastic model controlling the magnitude of G_0
a_i	dimensionless parameter for two-layer soil
$AiryA_i$	Airy function
$AiryB_i$	Airy function
a_y	size of the yield surface for the Modified Cam-Clay model
a_{y0}	initial size of the yield surface for the Modified Cam-Clay model
a_{y1}	constant of the Hypoplastic model controlling the shape of the asymptotic state boundary surface
b	coefficient regulating soil stiffness profile
$\mathbf{b}$	body force vector per unit mass
c	cohesion
$c\|_0$	initial cohesion yield stress for the Mohr-Coulomb model
C_i	integration constants
c_i	scalar multiplayer for the thermo-Hypoplastic model
c_p	soil specific heat
$c_{p,c}$	concrete specific heat
$c_{p,s}$	solid skelton specific heat
$c_{p,w}$	water specific heat
c_T	constant of the thermo-Hypoplastic model controlling the accumulation of volumetric contraction after the first thermal cycle
d	pile diameter
$\mathbf{d}$	asymptotic direction of the strain rate
$\mathbf{D}$	Euler’s stretching tensor
$\mathbf{D}_e$	elastic tangent stiffness fourth-order tensor
$\mathbf{D}_{ep}$	tangent stiffness fourth-order tensor
D_r	relative density
$\mathbf{D}^{TE}$	strain rate tensor for thermal volumetric change of soil particles
e	void ratio
$\dot{e}$	void ratio rate

$\bar{e}$	deviatoric eccentricity for the Mohr-Coulomb model
E	pile Young’s modulus
e_0	initial void ratio
$e_{0'}$	initial void ratio on the Thermal Stabilization line
e_T	current void ratio on the Normal Consolidation Line
e^*_T	current void ratio on the Thermal Stabilization Line
f	yield surface
F	yield surface for the Mohr-Coulomb model
f_d	picnotropy factor
f_d^A	value of the picnotropy factor at the asymptotic state boundary surface
F_m	Matsuoa-Nakai factor
f_s	barotropy factor
f_u	collapse potential factor
g	plastic potential
G	soil shear modulus
$\bar{G}$	gradient of the soil shear modulus with depth
G_{eff}	soil effective shear modulus
G_{in}	soil initial shear modulus
G_L	soil shear modulus at pile tip
$G_{L/2}$	soil shear modulus at pile mid length
G_m	plastic potential for the Mohr-Coulomb model
G_{mech}	soil mobilized shear modulus
G_0	small strain soil shear modulus
G_1	soil shear modulus of the shallower layer for two-layer soil
G_2	soil shear modulus of the deeper layer for two-layer soil
G_{90}	initial shear stiffness after a 90° change in the strain path direction
$\boldsymbol{h}$	function for the hardening law
h	Heaviside function
h_1	thickness of the shallower layer for two-layer soil
h_2	thickness of the deeper layer for two-layer soil
H_p	hardening modulus
$\hat{H}_p$	hardening modulus
$\boldsymbol{H}_T$	second-order constitutive tensor
$\boldsymbol{I}$	fourth-order identity tensor
$I_i(x)$	first kind modified Bessel function
I_1	stress invariant
I_2	stress invariant
I_3	stress invariant

J^{el}	elastic part of the volume ratio between current and reference configurations for the Modified Cam-Clay model
J^{pl}	inelastic volume change for the Modified Cam-Clay model
k	spring stiffness along pile shaft
$\boldsymbol{k}$	hydraulic conductivity tensor
$\bar{k}$	earth pressure coefficient
$\hat{\boldsymbol{k}}$	intrinsic permeability tensor
K	ratio of the flow stress in triaxial tension and compression for the Modified Cam-Clay model
K	pile axial stiffness from the load-settlement curve
k_b	spring stiffness at pile base
$\bar{k}_{\mathrm{G}}$	gradient of the spring stiffness with depth
k_i	spring stiffness along pile shaft of layer i
K_{in}	pile axial initial stiffness from the load-settlement curve
k_m	spring stiffness along pile shaft of layer m
k_p	plastic hardening modulus
$\hat{k}_p$	plastic hardening modulus
K_s	soil bulk modulus
k_t	spring stiffness at pile top
k_T	slope of the Thermal Stabilization Line
K_w	water bulk modulus
k_w	hydraulic conductivity
k_0	earth pressure coefficient at rest
L	pile length
$\mathscr{L}$	fourth-order tensor
l_T	constant of the thermo-Hypoplastic model controlling the slope of the Normal Consolidation Line
M	slope of the Critical State Line in the q- p' plane
$\mathscr{M}$	forth-order tangent stiffness tensor for the Hypoplastic model
m_R	constant of the Hypoplastic model
m_{rat}	ratio between G_{90} and G_0
m_T	constant of the Hypoplastic model
m_v	solid skeleton compressibility
m_w	water compressibility
n	soil porosity
$\boldsymbol{n}$	unit normal to the yield surface
N	pile axial load
$\boldsymbol{N}$	second-order tensor

$n_{active\ piles}$	number of active piles
$N_{analytical}$	thermal axial load derived from the energy solution
n_{cycles}	number of thermal cycles
N_c	pile bearing capacity factor for cohesion
N_{FEM}	thermal axial load derived from the finite element analyses
N_{fixed}	thermal axial load at head of a fixed-head pile
n_g	constant of the Hypoplastic model controlling the magnitude of G_0
$\boldsymbol{n}_g$	unit normal to the plastic flow
N_{head}	thermal axial load at pile head
N_i	pile thermal axial load in layer i
$n_{inactive\ piles}$	number of inactive piles
N_{max}	pile maximum thermal axial load
N_q	pile bearing capacity factor for the overload
n_T	constant of the thermo-Hypoplastic model controlling the shift of the Normal Consolidation Line
N_1	pile thermal axial load in the shallower layer for two-layer soil
N_2	pile thermal axial load in the deeper layer for two-layer soil
O_c	constant of the Hypoplastic model controlling the position of the Critical State Line
p'	mean effective stress
p'_c	preconsolidation mean stress
p'_e	Hvorslev’s equivalent pressure
p'_r	reference mean effective stress
p'_{ref}	reference mean effective stress
p'^{el}_t	elastic tensile strength of the material for the Modified Cam-Clay model
p'_0	initial mean effective stress
q	deviatoric stress
$\boldsymbol{q}$	vector of the internal state variables
$\dot{\boldsymbol{q}}$	rate of the internal state variables
Q	applied mechanical axial load at pile head
Q_b	base load
Q_s	shaft load
$\boldsymbol{q}_{\boldsymbol{cond}}$	heat flux vector by conduction
$\boldsymbol{q}_{\boldsymbol{conv}}$	heat flux vector by convection
q_b	unit base resistance
q_s	unit shaft resistance
r	third invariant of the deviatoric stress tensor
R	size of the elastic range for the Hypoplastic model

$\bar{R}$	correction factor for the soil shear modulus
R_b	base bearing capacity
R_c	pile bearing capacity
R_{FEM}	pile bearing capacity for finite element analyses
R_G	correction factor of the soil shear modulus
r_m	magical radius
R_{mc}	function of the Lode angle for the Mohr-Coulomb model
R_{mw}	function of the Lode angle for the Mohr-Coulomb model
R_s	shaft bearing capacity
R_t	total bearing capacity
r_0	pile radius
s	pile spacing
$\boldsymbol{s}$	deviatoric stress tensor
s_u	soil undrained shear strength
t	constant of the Modified Cam-Clay model controlling the shape of the yield surface in the deviatoric plane
T	temperature
$\dot{T}$	temperature rate
$\boldsymbol{T}$	stress tensor
$\dot{\boldsymbol{T}}$	stress cate tensor
T_0	initial temperature
u	pore water pressure
$\dot{u}$	pore water pressure rate
u_p	pile displacement
u_{p1}	pile displacement of the shallower layer for two-layer soil
u_{p2}	pile displacement of the deeper layer for two-layer soil
$\bar{u}_l$	dimensionless displacement at pile tip
$\bar{u}_0$	dimensionless displacement at pile head
$\boldsymbol{v}$	Darcy velocity vector
v_κ	specific volume at the reference pressure on the unloading-reloading line
w	pile head settlement
W	pile self-weight
x_i	coefficient regulating the spring stiffness calibration
z	depth
z_1	depth of the shallower layer for two-layer soil
z_2	depth of the deeper layer for two-layer soil
z_{i-1}	depth of top interface of layer i
z_m	depth of bottom interface of layer m

$z_{m\text{-}1}$	depth of top interface of layer m
$\bar{z}_N$	depth corresponding to zero pile displacement
$z_{N=Nmax}$	depth corresponding to zero shear stress and pile displacement
$z_{\tau=0}$	depth corresponding to zero shear stress and pile displacement
$\mathbf{1}$	second-order identity tensor
$\mathbf{0}$	null vector

Greek symbols

α	linear thermal expansion coefficient of pile material
$\bar{\alpha}$	coefficient for the shaft bearing capacity (total stress approach)
α_c	linear thermal expansion coefficient of concrete
α_f	constant of the Hypoplastic model controlling the soil non-linearity
α_s	linear thermal expansion coefficient of solid particles
α_{st}	physic-chemical coefficient
α_w	linear thermal expansion coefficient of water
β	constant of the Modified Cam-Clay model controlling the shape of the yield surface in the q-p' plane
β_r	constant of the Hypoplastic model controlling the rate of evolution of the intergranular strain tensor
β_s	volumetric thermal expansion coefficient of solid particles
β_w	volumetric thermal expansion coefficient of water
γ	shear strain
Γ	specific volume at the reference pressure on the Critical State Line
$\dot{\gamma}$	plastic multiplayer
γ_e	elastic component of the shear strain
Γ_p	plastic component of the shear strain
γ_{sat}	saturated soil unit weight
γ_T	constant of the thermo-Hypoplastic model controlling the rate of irreversible volumetric contraction
γ_t	total shear strain
$\Gamma(x)$	Gamma function
δ	coefficient for spring stiffness calibration
$\bar{\delta}$	optimum value of the coefficient for spring stiffness calibration
$\boldsymbol{\delta}$	intergranular strain second-order tensor
$\dot{\boldsymbol{\delta}}$	intergranular strain tensor rate
$\vec{\boldsymbol{\delta}}$	direction of the intergranular strain tensor
δ_f	friction angle between pile and soil

ε	meridional eccentricity
$\dot{\varepsilon}$	strain rate tensor
ε_a	axial component of the strain
$\dot{\varepsilon}_a$	axial component of the strain rate
$\varepsilon_{\Delta T}$	free thermal axial strain
$\boldsymbol{\varepsilon}_e$	total elastic strain tensor
$\dot{\boldsymbol{\varepsilon}}_e$	elastic strain rate tensor
$\dot{\boldsymbol{\varepsilon}}_p$	plastic strain rate tensor
ε_p	thermal axial strain
$\dot{\varepsilon}_r$	radial component of the strain rate
$\varepsilon_{T\text{-}Rstr}$	restrained thermal axial strain
ε_v	volumetric strain
$\varepsilon_{v,e}$	elastic component of the volumetric strain
$\varepsilon_{v,p}$	plastic component of the volumetric strain
$\varepsilon_{v,t}$	total volumetric strain
$\varepsilon_{v,th}$	thermal component of the volumetric strain
ζ	dimensionless interface depth
θ	Lode angle
ϑ	constant of the Hypoplastic model controlling the accumulation of strains or stresses in cyclic loading paths
Θ	ratio between top and shaft stiffness
Θ_L	ratio between top and shaft stiffness (energy solution)
κ	compression index in the $(1+e)$-ln p' plane
κ^*	compression index in the ln$(1+e)$-ln p' plane
λ	swelling index in the $(1+e)$-ln p' plane
λ^*	swelling index in the ln$(1+e)$-ln p' plane
$\dot{\lambda}$	plastic multiplayer
λ_1	pile-soil wavenumber referred to the first layer for two-layer soil
λ_L	pile-soil wavenumber (energy solution)
λ_p	pile-soil wavenumber for constant stiffness
λ_{th}	soil thermal conductivity
$\lambda_{th,c}$	concrete thermal conductivity
$\lambda_{th,s}$	thermal conductivity of solid skeleton
$\lambda_{th,w}$	thermal conductivity of water
μ	pile-soil wave number for Gibson soil
μ_w	dynamic viscosity of the pore water
ν	Poisson’s ratio

N	specific volume at the reference pressure on the Normal Consolidation Line for the Modified cam-Clay model
N^*	specific volume at the reference pressure on the Normal Consolidation Line for the Hypoplastic model
ξ	ratio between the thickness of deeper and shallower layers
ρ	ratio between the shear modulus of deeper and shallower layers
$\bar{\rho}$	normalized magnitude of the intergranular strain tensor
ρ_g	bulk density of the soil
ρ_s	grains density
ρ_w	water density
ρ_{w0}	density of the water at the reference temperature
$\boldsymbol{\sigma}$	total stress tensor
$\dot{\boldsymbol{\sigma}}$	total stress tensor rate
$\boldsymbol{\sigma'}$	effective stress tensor
σ_a	principal axial component of the stress
$\dot{\sigma}_a$	principal axial component of the stress rate
σ_r	principal radial component of the stress
$\dot{\sigma}_r$	principal radial component of the stress rate
σ'_{v0}	effective vertical stress
$\sigma_{z,L}$	total vertical stress at $z = L$
σ'_z	effective vertical stress
$\sigma'_{z,L}$	effective vertical stress at $z = L$
τ	shear stress at pile-soil interface
τ_i	shear stress at pile-soil interface of layer i
τ_1	shear stress at pile-soil interface in the shallower layer for two-layer soil
τ_2	shear stress at pile-soil interface in the deeper layer for two-layer soil
φ	friction angle
φ_c	friction angle at critical state
φ_m	mobilized friction angle
Φ	shape function
Φ'	derivative of the shape function with respect to z
χ	constant of the Hypoplastic model controlling the interpolation between the reversible elastic and non-linear hypoplastic responses
ψ	dilation angle
ω	constant of the Hypoplastic model

Ω	ratio between shaft and base stiffness
$\overline{\Omega}$	ratio between shaft and base stiffness for Gibson soil
Ω_L	ratio between shaft and base stiffness (energy solution)

Operators

d	increment
$\det$	determinant
∂	derivative
Δ	variation
Σ	sum
tr	trace of a tensor
∇	gradient
$\nabla\cdot$	divergence
$\langle\ \rangle$	Macaulay brackets
$\cdot$	inner product with single contraction
$:$	inner product with double contraction
$\otimes$	dyadic product

List of figures

List of tables

Abstract

Energy piles are capable to store heat from the surrounding soil and to carry it to the superstructure for heating during winter, whereas during summer the transmission is simply reversed. This allows to supply or save heat seasonally and cyclically. The exchange of energy is possible because piles interact with the ground at depths suitable for the exploitation of the geothermal energy with low enthalpy. For this scope, they are equipped with small pipes in which a heat carrier fluid can circulate thanks to a pump.

This foundation has therefore the double role of transferring both structural loads (from the structure to the ground) and heat (from ground to structure and vice versa). In recent years, such a foundation system has been employed in a lot of public and private applications, the key of its success lying in the undeniable advantages in terms of energy sustainability.

The main geotechnical issues concerning energy piles address the additional stresses and the settlements caused by the cyclic temperature variation inside the pile and the surrounding soil.

With regard to the stress state, because of the restraint imposed by the surrounding soil and the building, a change in pile temperature turns out to be a change in pile stress along its shaft and at its ends. At the current stage, the analysis of energy piles must be necessarily carried out through the use of numerical techniques. Therefore, the first scope of this work is to provide simple tools to assist practitioners in the Ultimate Limit State (ULS) design of thermal piles. To this end, in analogy with the single pile subjected to mechanical load, exact analytical solutions are herein developed for the problem at hand employing a Winkler-type model, with reference to homogeneous and two-layered soils as well as for subsoil whose stiffness varies linearly with depth. For more general subsoil conditions, approximate energy solutions are derived assuming a simplified displacement profile and then exploiting the principle of virtual works. The spring stiffness has been calibrated for the last type of solutions by comparison with finite element analyses and novel expressions for evaluating the springs properties have been proposed for the specific problem of thermally-loaded piles. These solutions provide accurate results if compared against numerical and experimental data, and thus can help the practitioners in designing thermal piles by means of simple hand calculations.

A further objective of the thesis is to investigate the effect of both mechanical load and thermal cycles on the behavior of a single energy pile in terms of settlement and axial load. Fully coupled thermo-hydro-mechanical analyses have been carried out using the Finite Element code ABAQUS. The single pile is installed in a normally consolidated clay behaving according to different constitutive models involving the Mohr-Coulomb, the Modified Cam-Clay and the Hypoplastic model. The latter is employed with and without the thermal formulation, capable to account for the thermal collapse of NC clays during heating. Both fixed- and free-head piles are considered. Results are presented in terms of pile axial load and settlement at the end of several thermal cycles. To highlight the effect of the different constitutive assumptions, the local performance at the element scale is also discussed. In this way, with reference to the cyclic behaviour observed in the real applications, the performance of the classical elasto-plastic models is discussed by comparing with the predictions of the advanced models.

In the last section, to prove the predictive capabilities of the simple analytical approach with reference to the monotonic loading condition, comparisons have been made with the thermally-induced axial load and settlements experienced by the pile modelled in the FE analysis. This allows identifying some aspects related to the calibration of the stiffness in the closed-form expressions as function of the load level. To this end, a simple procedure has been proposed through an analogy with the pile axial stiffness calculated from the load-settlement curve. The main advantage of this procedure is that its application requires solely the availability of the load-settlement curve of the pile and no constitutive choices are necessary. This way, the estimation of the monotonic thermally-induced axial force can be carried out by the designer without making use of complex numerical analyses.

The thesis is divided into seven Chapters and two Appendixes.

In *Chapter 1* an overview of the main features of the energy geostructures is reported. Then, attention is devoted to the energy piles. The state of knowledge is presented with reference to the main findings obtained via field and laboratory tests, numerical techniques and analytical approach, considering both the single energy pile and the group of energy piles.

In *Chapter 2* closed-forms solutions for the ULS design of piles are presented. First of all, the proposed model is described and the mathematical formulation for the thermally-induced displacement is derived in the form of a second-order differential equation, with respect to the case of homogeneous, two-layer and Gibson soil. Then, the exact solutions in terms of thermally-induced axial load are presented. The approximate solutions are derived with the aim of developing simpler close-form expressions suitable for a more general subsoil condition. Finally, the calibration of the spring stiffness and the comparisons with experimental data are reported.

The *Chapter 3* is used to introduce the constitutive models employed in the numerical analyses presented in the subsequent Chapters. In particular, the mathematical formulation of the Linear Elastic, the Mohr-Coulomb, the Modified Cam-Clay and the Hypoplastic model with and without the thermal term is reported. As concerns the thermal term, since this part has been implemented by the writer extending the available routine written for the isothermal version of the hypoplastic model, the validation by comparisons with drained and undrained triaxial tests is also reported. The last section addresses the thermo-hydro-mechanical coupling reporting the mathematical formulation and the meaning of the parameters involved in the various processes.

In *Chapter 4* the ABAQUS code and the 2D finite element model used for the fully coupled thermo-hydro-mechanical analyses are presented. The 2D model is described in terms of boundary conditions, type and dimensions of the elements employed for both pile and soil. The geometrical, mechanical and thermal features of the pile are also described along with the mechanical and thermal characteristics of the soil. Regarding the latter, the calibration of the constitutive models is presented. In particular, the Hypoplastic model has been chosen as a reference model on which the parameters of the other simpler models are calibrated.

In *Chapter 5* the results of the fully coupled thermo-hydro-mechanical analyses are presented dividing the loading steps into mechanical and thermal phases. As concerns the mechanical phase, the bearing capacity of the pile is derived both with reference to the load-settlement curves obtained employing the different models and via the static formulae. Moreover, the choice of the load level at which the following thermal variation are applied is discussed. Indeed, the thermal loading phase refers to the simultaneous application of the given mechanical load level and of the thermal cycles. The restraining condition imposed at pile head is discussed and the thermal field is presented. The results are discussed for each constitutive model with reference to the global performance of the free-head pile in terms of axial force, settlements, average axial strain and position of the null point along with the behaviour at the local scale at different depths. As concerns the latter, the response is presented in terms of shear and volumetric strains, excess pore pressure, local settlements, stress state in the deviatoric plane and loading paths in the q-p' plane. For the fixed-head pile, the axial load and the average axial strain are reported. A final discussion which summarises the main results is also provided.

The *Chapter 6* is devoted to the comparisons between the analytical approach and the numerical analyses for monotonic loading conditions. Then, the procedure for the estimation of the effective shear modulus to employ for the definition of the spring stiffness is presented.

In *Chapter 7* the thesis is concluded by summarising the main results achieved. Moreover, possible fields of interest for further research are described.

The *Appendix I* reports the mathematical derivation of both the exact and the approximate solutions obtained employed the analytical approach. Moreover, the expressions of the settlements, the depth of zero displacements, the shear stress and the axial load are reported for some soil stiffness distributions.

The *Appendix II* provides a description of the implementation of the thermal term for the thermo-hypoplastic model.

Sommario

I pali energetici sono pali di fondazione che, interagendo con il terreno a profondità utili per lo sfruttamento della risorsa geotermica a bassa entalpia, sono in grado di provvedere anche al fabbisogno energetico dell'edificio. Lo scambio termico è possibile in quanto il palo è equipaggiato medianti tubicini, collegati direttamente alla gabbia di armatura, all'interno dei quali, tramite l'impiego di una pompa di calore, scorre un fluido termovettore. Tale fluido, essendo in grado di scambiare calore con il terreno circostante, consente di riscaldare l'edificio durante l'inverno e di raffreddarlo durante l'estate, in modo da ridurre, ed in alcuni casi eliminare, l'impiego di combustibile fossile.

I pali energetici assolvono, pertanto, al duplice compito di trasferire i carichi strutturali (dalla struttura al terreno) ed il calore (dal terreno alla struttura e viceversa). Negli ultimi anni, grazie ai vantaggi ottenibili in termini di sostenibilità energetica, l'impiego di tali sistemi ha subito un forte impulso sia nel settore pubblico che in quello privato.

I principali problemi geotecnici connessi all'impego dei pali energetici riguardano essenzialmente gli sforzi assiali ed i cedimenti aggiuntivi causati dalla variazione ciclica della temperatura di palo e terreno.

Riguardo lo stato di sforzo, a causa dei vincoli imposti dal terreno e dalla presenza di una struttura di collegamento tra le teste dei pali, la variazione di temperatura si traduce in una variazione di sforzo assiale lungo il fusto del palo nonché alla testa ed alla punta. Allo stato delle conoscenze attuali, l'analisi dei pali energetici deve essere necessariamente eseguita impiegando analisi numeriche. Pertanto, il primo scopo del presente lavoro di tesi è quello di fornire uno strumento semplice che possa assistere i progettisti nella progettazione allo Stato Limite Ultimo (SLU) dei pali energetici. A tale scopo, in analogia con quanto è stato fatto in riferimento ai pali di fondazione soggetti a carico meccanico, sono state sviluppate delle soluzioni analitiche esatte per terreno omogeneo, bistrato e per terreno con modulo di taglio variabile linearmente con la profondità (tipo Gibson), utilizzando un modello a molle elastiche tipo Winkler. Con riferimento a condizioni di sottosuolo generiche, assumendo un profilo di spostamenti del palo semplificato e, successivamente, sfruttando il principio dei lavori virtuali, sono state ricavate anche soluzioni analitiche approssimate. La rigidezza delle molle è stata calibrata per tali soluzioni approssimate tramite confronti con analisi agli elementi finiti; a tal proposito, sono state ricavate nuove espressioni per le proprietà delle molle, che sono specifiche per il caso dei pali caricati termicamente. Dal confronto con analisi numeriche e con dati

sperimentali, è stato possibile confermare che le soluzioni proposte danno risultati accurati e che, pertanto, possono fungere da semplice strumento di calcolo in fase di progettazione.

Un ulteriore obiettivo della tesi è stato quello di studiare gli effetti, sia in termini di sforzo assiale che di cedimento, della contemporanea applicazione del carico meccanico e di cicli termici ad un palo energetico isolato. Pertanto, tramite l'impiego di ABAQUS, codice agli elementi finiti, sono state condotte analisi numeriche termo-idro-meccaniche accoppiate. Il palo singolo è installato in argille normalmente consolidate il cui comportamento costitutivo è stato descritto utilizzando diversi modelli, tra cui il Mohr-Coulomb, il Cam-Clay Modificato ed il modello Ipoplastico. Riguardo quest'ultimo, la formulazione termica consente anche di tener conto del collasso volumetrico delle argille normalmente consolidate quando soggette ad incrementi di temperatura. Il palo è stato studiato sia in condizioni di testa libera di spostarsi che in condizioni di testa perfettamente vincolata. I risultati sono presentati in termini di sforzo assiale e spostamento alla fine di diversi cicli termici. Allo scopo di evidenziare gli effetti delle diverse scelte costitutive effettuate, l'analisi dei risultati ha riguardato anche la scala locale. Infine, con riferimento a quanto osservato sperimentalmente, la risposta dei classici modelli elasto-plastici è stata confrontata con quella ottenuta impiegando i modelli avanzati.

Nell'ultima parte della tesi, l'approccio analitico è stato confrontato con i risultati delle analisi numeriche in condizioni di carico termico monotono, sia in termini di sforzo assiale che di cedimento. In questo modo è stato possibile identificare alcuni aspetti collegati alla calibrazione della rigidezza da utilizzare nelle espressioni analitiche approssimate, in funzione del livello di carico. A tale scopo, è stata proposta una semplice procedura iterativa basata sull'analogia con la rigidezza assiale del palo ricavata dalla curva carico-cedimento. Il principale vantaggio nell'applicare tale procedura consiste nel fatto che è richiesta la solo disponibilità della curva carico-cedimento e non è necessario effettuare alcuna scelta costitutiva. In questo modo il calcolo dello sforzo assiale in fase di progettazione non richiede l'impiego di analisi numeriche complesse.

La tesi è suddivisa in sette Capitoli e due Appendici.

Nel *Capitolo 1* è riportata una panoramica relativa alle principali caratteristiche delle strutture geo-energetiche. Successivamente, l'attenzione è focalizzata sui pali energetici. Il capitolo riporta lo stato dell'arte con riferimento alle principali caratteristiche del comportamento dei pali, isolati ed in gruppo, dedotte mediante prove in sito ed in laboratorio, analisi numeriche ed approccio analitico.

Nel *Capitolo 2* sono ricavate le soluzioni analitiche per la progettazione allo SLU dei pali energetici. Dopo aver descritto il modello proposto, è presentata la formulazione matematica del profilo di spostamenti, in forma di equazione differenziale del secondo ordine, per i casi di terreno omogeneo, bistrato e Gibson. Sono ricavate, poi, le soluzioni esatte relative allo sforzo assiale indotto dalla variazione di temperatura e quelle approssimate per condizione di sottosuolo generalizzata. Infine sono presentati la calibrazione delle molle ed i confronti con i dati sperimentali e le analisi numeriche.

Nel *Capitolo 3* è descritta la struttura matematica dei modelli costitutivi utilizzati nelle analisi numeriche. In particolare, è riportata la formulazione dei modelli Lineare-Elastico, Mohr-Coulomb, Cam-Clay Modificato e Ipoplastico, con e senza la parte termica. Quest'ultima è stata implementata dalla scrivente e, pertanto, nel capitolo è riportata anche la validazione di tale implementazione attraverso confronti con prove triassiali in condizioni drenate e non drenate. Nell'ultima sezione del capitolo è illustrata la formulazione termo-idro-meccanica accoppiata utilizzata nelle successive analisi numeriche.

Nel *Capitolo 4* è descritto il modello 2D assialsimmetrico adoperato nelle analisi agli elementi finiti. In particolare, sono illustrate le condizioni al contorno, la tipologia e le dimensioni degli elementi utilizzati per palo e terreno. Inoltre, sono riportate le caratteristiche geometriche, meccaniche e termiche del palo oltre che quelle meccaniche e termiche del terreno. Infine è presentata la calibrazione dei modelli costitutivi impiegati, tenendo presente che il modello Ipoplastico è scelto come modello di riferimento sul quale calibrare i parametri degli altri modelli.

I risultati delle analisi numeriche termo-idro-meccaniche accoppiate sono presentati nel *Capitolo 5*. Riguardo la fase meccanica, è riportata la curva carico-cedimento ottenuta con i diversi modelli costitutivi oltre che il calcolo relativo alla capacità portante del palo tramite le formule statiche; sono, inoltre, riportati i livelli di carico meccanico scelti da applicare alla testa del palo contemporaneamente alla variazione di temperatura. Successivamente, oltre a chiarire la scelta delle condizioni di vincolo alla testa, sono presentati anche i profili di temperatura nel palo e nel terreno. Per la condizione di palo libero, i risultati sono discussi, per ciascun modello costitutivo, con riferimento a sforzo assiale, cedimenti, deformazioni medie e posizione del punto di nullo. Inoltre, per 4 elementi all'interfaccia palo-terreno posizionati a diverse profondità, la risposta è riportata anche in termini di deformazioni volumetriche e di taglio, pressione interstiziale, cedimenti locali, stato di sforzo nel piano deviatorico e percorsi di carico nel piano q-p'. Riguardo il palo vincolato, il comportamento globale è descritto in termini di sforzo assiale e deformazione media. La fine del capitolo è dedicata ad una sintesi dei principali risultati.

Nel *Capitolo 6* sono presentati i confronti tra l'approccio analitico e quello numerico in condizioni di carico termico monotono. Infine è riportata una procedura iterativa per la stima del modulo di taglio efficace da utilizzare nella definizione della rigidezza delle molle.

La tesi è conclusa con il *Capitolo 7* che è dedicato alla sintesi dei principali risultati ottenuti. Infine, sono discussi possibili scenari di ricerca nel campo dei pali energetici.

In *Appendice I* sono riportati i passaggi utilizzati per derivare sia le soluzioni analitiche esatte che quelle approssimate. Inoltre, per alcune tipologie di terreno sono presentate le espressioni del profilo di spostamento lungo il fusto del palo, della profondità a cui tale profilo si annulla, dello sforzo di taglio e dello sforzo assiale lungo il fusto.

Nell'Appendice II è descritta l'implementazione della parte termica del modello Ipoplastico.

1.Energy geostructures

1.1.Introduction

The increase in the global energy demand is led by the economic growth especially of the emerging countries. The traditional supply comes from fossil fuel, i.e. coal, petroleum, oil and natural gas. Fossil fuels are non-renewable sources that have a detrimental impact on the global climate change since their use and combustion contributes to the increase in the emission of the CO_2 in the atmosphere, to the greenhouse effect and to the global warming. The largest demand of energy comes from industries followed by buildings and transports.

Nevertheless, a smart use of the available sources along with new environment-friendly energies can allow for a more sustainable energy management. Indeed, the increase of the global energy needs can be offset by the growth of the energy efficiency. The International Energy Agency (IEA), that tracks every year the future patterns of the global energy system via the World Energy Outlook, has demonstrated that, despite the increase in the size of the global economy, the enhancement of the energy efficiency can allow the reduction of the emission by the 2040. These results are obtained applying the Efficient World Scenario that is a sustainable approach to the use of the energy based on the announced internationally agreed objectives in the field of climate change, access to modern energy and air quality. In fact, to achieve a reduction in the fossil fuels exploitation in the near future, many legislations have been already approved in different countries all over the word. One of the objectives is to promote the use of alternative renewable energies such as the hydro, the solar and the geothermal or the use of sources coming from biomass, biofuels and wind. Among these, promising expectations lie in the exploitation of the geothermal energy.

The word geothermal has a Greek etymology (geo, -thermos) meaning “earth heat” and refers to the energy coming from the earth that can be readily extracted almost everywhere. On average, the geothermal gradient is such that the Earth temperature increases of 3°C every 100m of depth; thus, the 99% of the Earth has a temperature higher than 1000°C. The geothermal sources are classified based on the enthalpy, expressing the quantity of energy that a system can exchange, as (i) high-enthalpy (characterized by the maximum workable temperature, T, >150°C), or (ii) low-enthalpy (T<150°C) resources (Haenel et al., 1988). Following the geothermal gradient, the exploitation of the high-enthalpy energy requires the use of very deep systems, 4÷6 km, while low temperature reservoirs necessitate up to about 2 km lengths. The high-enthalpy energy is typically used in geothermal power plants for the production of the electricity (the first one was built in Larderello, Italy, in 1827); the low-enthalpy sources are related to the extraction of hot water from deep aquifers (hydrothermal system) and to the use of heat pump (HP) systems (Fig. 1.1).

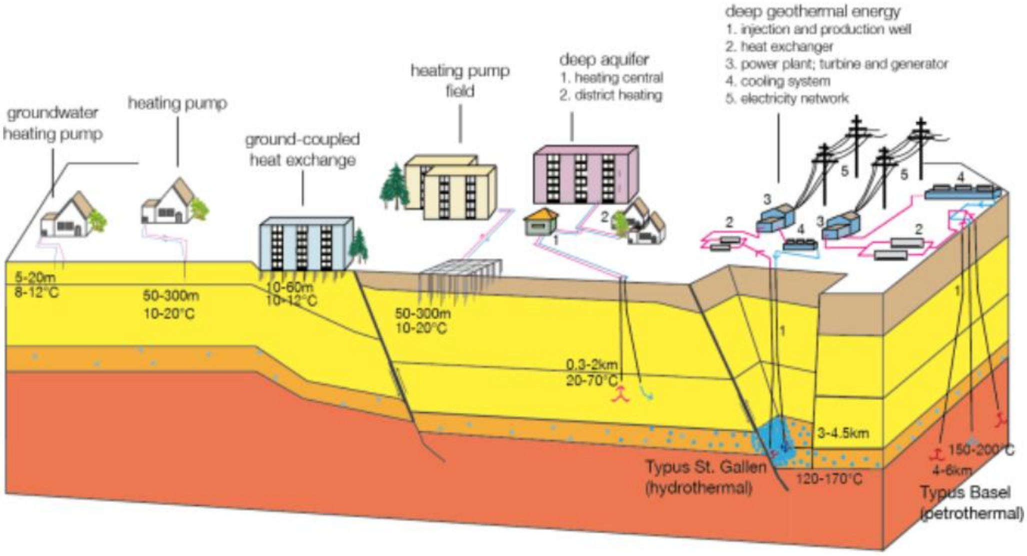

Figure 1.1. Geothermal systems (from Hirschberg et al., 2014)

In principle, the HPs extract and transfer heat via a refrigeration cycle and can be coupled with open loop or with closed loop pipework forming the Ground Source Heat Pump systems (GSHP). An open loop system involves the direct extraction of water from shallow aquifers. A closed loop line is composed of small heat absorber pipes in which a heat carrier fluid circulates tanks to a pump; it can be installed into boreholes in direct contact with the ground (length of about 300m) or can be buried into energy geostructures.

Thanks to the integration with these pipes, the energy geostructures are geotechnical systems that, along with the structural function, are used as heat exchangers with the ground. These systems include all the ground embedded structures such as shallow foundations, piles, diaphragm walls, anchors and tunnels (Fig. 1.2), and are usually referred as shallow geothermal systems, since they are characterized by operational depths up to 60m. Due to the working lengths, the energy geostructures interact with the ground at a relatively constant temperature. Indeed, the temperature of the ground is influenced by seasonal fluctuations up to a depth of about 10m, after which it can be considered constant ranging between 8°C and 16°C depending on the site.

As heat exchangers, the geostructures can contribute to the thermal welfare of a building. During winter the air is colder than the ground and the heat can be extracted with the aim of warming up (cooling of the energy geostructure); during summer the external air is warmer than the ground and heat can be injected with the purpose of cooling down (heating of the energy geostructure).

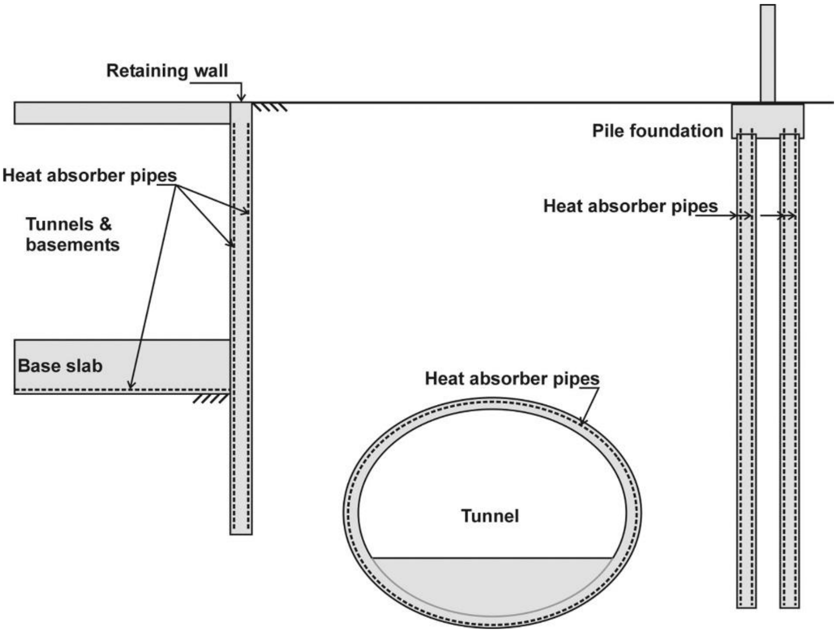

Figure 1.2. Energy geostructures (from Bourne-Webb et al., 2016)

In principle, the GSHPs are composed of three parts: the ground, the heat pump and the building. These elements are linked by two circuits: (i) the primary circuit contains the pipework buried inside the energy geostructures, having the function of connecting the ground to the heat pump (Ground Heat Exchanger, GHE); (ii) the secondary circuit is a network of closed fluid-base pipes installed in the floors and in the walls of the building with the purposed of linking the heat pump to the building itself. The fluid that circulates in the primary circuit is usually a mixture of water and glycol acting as antifreeze. The HP has a central role in the system since it adsorbs heat from a low temperature source and increases its temperature requiring the consumption of electricity. It is composed by the evaporator, the compressor, the condenser, the expansion valve, the control system and, eventually, by the reversing valve; the working fluid is the refrigerant having the property of evaporating at low temperatures. The performance of the heat pump is evaluated via the following indicators ranging between 2 and 7:

- instantaneous energy performance indicators defined as the ratio between the energy output for heating or cooling the building and the energy input:
  - ➢ Coefficient of Performance, COP, refers to the operation during winter;
  - ➢ Efficiency Energy Ratio, EER, refers to the operation during summer;

- seasonal energy performance indicators defined as the ratio between the annual heating or cooling demand of the building and the annual electricity consumption:
  - Seasonal Coefficient of Performance SCOP, refers to the operation during winter;
  - Seasonal Energy Efficiency Ratio, SEER, refers to the operation during summer.

Considering that the main role of heat pumps is to increase the temperature extracted from the ground, the efficiency of the heat pump is strongly affected by the difference between this extracted temperature and the demanded temperature. For example, to achieve a cost-effective system, the value of the COP should be at least equal to 4. To this aim, in the primary circuit, the temperature shouldn’t be lower than 0-5°C, while, in the secondary circuit, it shouldn’t exceed 35-45°C (Brandl, 2006). As concern the second requirement, the use of pipes buried in the floors or in the walls of the building allow to satisfy the building needs at lower temperature with respect to the classical radiators.

The majority of heat pumps are equipped with the reversing valve and, thus, are able to reverse their working cycle allowing the use of the same device for heating and cooling purposes. In this way the seasonal operation mode assures an energy balance throughout the year since the heat is extracted from the ground during winter and it is injected in the ground during summer. This mode is really suited for low permeability soils and groundwater regime with low hydraulic gradients. Anyway the operation can involve only heating or cooling; in this case soils with high permeability and groundwater regime with high hydraulic gradients are required since they allow a recharge of the ground as reservoir.

The most widespread GHEs are the energy foundations composed by energy piles. In figure 1.3 the layout of a GSHP coupled with energy piles is reported. Piles foundation are structural elements whose function is to transfer the mechanical loads from the building to the ground. When the piles are equipped with closed-loop pipes they gain the role of heat exchangers with the surrounding soil. Even though the energy pile technology involves different construction methods, the most popular is the cast in-situ pile. In a bored energy pile, the absorber pipes, made of high density polyethylene, are bond to the reinforcing cage before the concrete casting (Fig. 1.4). These heat exchange loops can be installed in single U-shape, double U-shape, W-shape and in spiral or helix configurations. The last one is not common in practice. The diameter of the pipes is in the range of 20÷25 mm, with a thickness of the wall ranging between 2 mm and 2.3 mm depending on the diameter.

The pile structural section is made of concrete whose good thermal properties make the energy piles more effective in transferring the heat with respect to the boreholes;

indeed, the good thermal conductivity ($\lambda_{th,c}$) and heat storage capacity ($c_{p,c}$) allow to enhance the heat exchange.

The heat transport from the soil to the heat carrier fluid within the absorber pipes involves (i) the heat transfer in the soil, (ii) the exchange between the soil and the concrete, (iii) the conduction inside the concrete, (iv) the heat exchange between the concrete and the pipes, (v) the conduction inside the walls of the pipes and (vi) the heat transfer between the pipes and the fluid (Brandl, 2006).

As deep foundations, energy piles are designed (i) to have an adequate safety margin against the structural and the geotechnical failure conditions (Ultimate Limit State, ULS) and (ii) to guarantee acceptable absolute and differential settlements under working load conditions (Serviceability Limit State, SLS). The thermal interaction with the surrounding soil determines a different thermo-mechanical response in terms of stresses and strains if compared to the application of mechanical loads only. Indeed, the thermal expansion or contraction of the pile is constrained by the presence of the soil, of the building and, possibly, of stiffer layers at pile base; the restrained axial strains turn into thermally-induced axial stress.

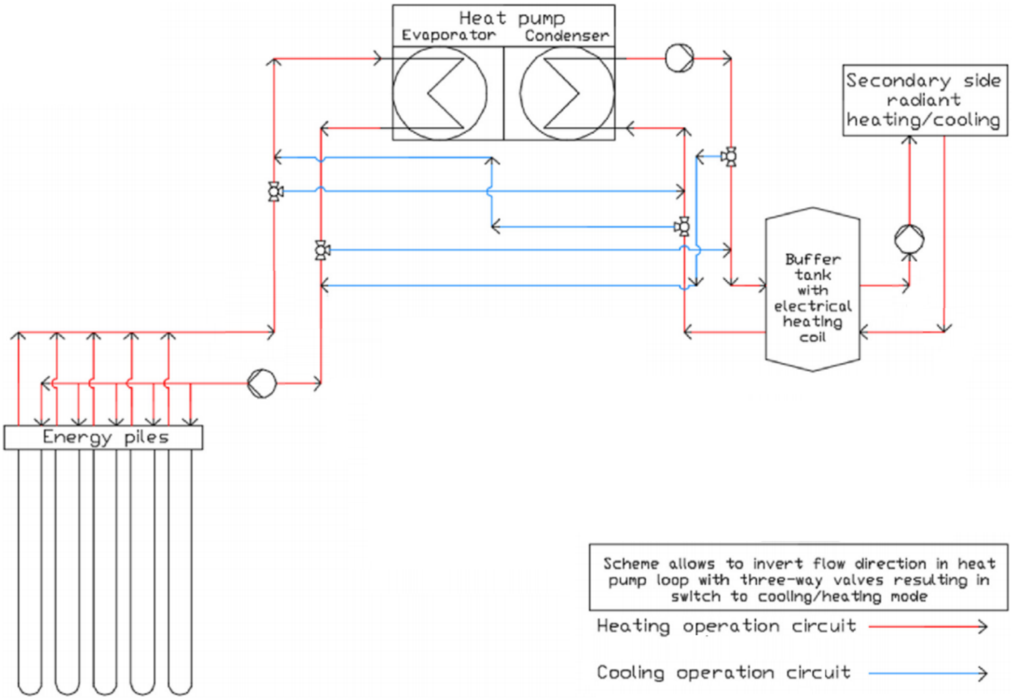

Figure 1.3. Layout of the GSHP coupled with energy piles (adapted after Fadejev et al., 2017)

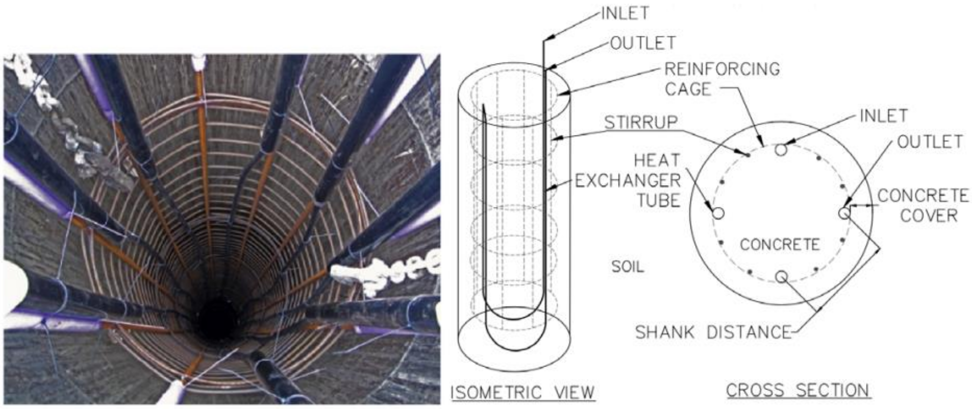

Figure 1.4. Heat exchanger pipes in energy piles (from Caulk et al., 2016).

In figure 1.5 simplified schemes by Bourne-Webb et al. (2013) are reported in terms of restrained axial strain ($\varepsilon_{T\text{-}Rstr}$), thermally-induce axial load ($N = EA\varepsilon_{T\text{-}Rstr}$, E and A being the Young’s modulus and the pile cross section, respectively) and shear stress (τ). The variation of the temperature is considered in combination with the application of the mechanical load. In the case of heating, a compressive load develops in addition to that due to the mechanical load (Fig. 1.5a); if the pile ends are restrained the restrained axial strains and, consequently, the axal load increase (Fig. 1.5c). The interface of the upper part of the pile is interested by thermally-induced negative friction, i.e. the transmetted friction forces are in opposite direction with respect to that transmetted by the mechanical load. In the case of cooling, the thermally-induced axial force is a tensile load and negative friction develops in the lower part of the pile (Fig. 1.5b and d); at the base, the overall load can be tensile. In geneal, at increasing both the restraint provided by the structure and by the stiff soil layer at the base, the condition of a perfectly restrained body is approaced with axial strain totally restrained and no development of the shear stress at the interface.

It is important to consider that the thermal loading induces cyclic solecitation to the energy pile. In fact, the seasonal variation of the temperature determines the alternation of heating and cooling in respons to the building needs. The cyclic loading condition may affect not only the axial force distribution but even the settlements; the pile could be interested by accumulation of cyclic settlements that is more or less significant depending on the soil type.

All this aspects characterising the energy pile behaviour must be taken into account especially with reference to the design stage.

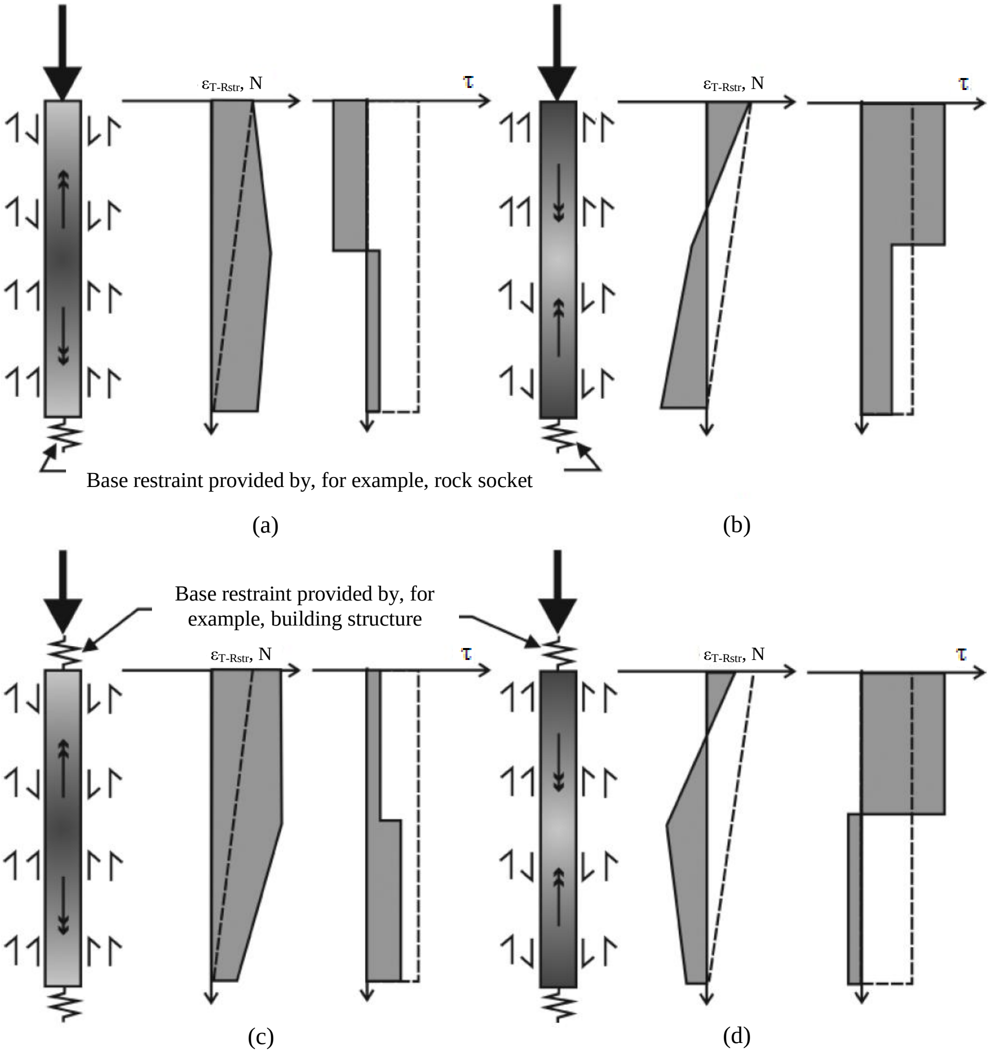

Figure 1.5. Thermally-induced axial force and shear stress (from Bourne-Webb et al., 2013).

1.2.Literature review

The use of energy geostructures is quite recent. The first energy building dates back to the 1985 and was realized in Austria; it is a detached house founded on energy piles (Ennigkeit and Katzenbach, 2001). In the following years, the geothermal systems spread especially throughout Austria, Germany and Switzerland involving the construction of huge buildings along with towers and public facilities. Among this, in 1996, the high-rise "Main Tower" building was built in Frankfurt resting on a piled-raft foundation composed of 112 energy piles; its structure included a thermo-active retaining system (Ennigkeit and Katzenbach, 2001; Katzenbach et al. 2008).

In 1997 the piles and retaining walls of a rehabilitation centre in Austria were equipped with absorber pipes to supply energy in seasonal operation mode for a total of 143 energy piles (Brandl, 2006). In 1999 the construction of the new terminal of the Zürich airport, the Dock Midfield, started; the foundation was designed with more than 300 energy piles out of the 440 required piles (Pahud and Hubbuch, 2007).

Later on, the use of the geothermal energy was enlarged to other systems such as the tunnels. The first energy tunnel, the Lainzer tunnel, was built in Vienna in 2003 (Brandl, 2006; Adam and Markiewicz, 2009). The cut and cover method and the New Austrian Tunnelling Method were used for the construction of its sections, among which two employed energy systems equipped for research purposes, i.e. energy piles and energy geotextile. In particular, the lot LT24 was executed with the cut and cover and was composed of bored piles of which each third pile was an energy pile for a total number of 59; the NATM was used for the lot LT22 with the installation of the first energy geotextile. Moreover, to locally reduce the groundwater level, energy wells were also built. The energy extracted was used for the heating of a school building adjacent to the tunnel.

In recent years, the energy plants using energy piles are increasing in Europe, United States, China, Australia and Japan. In figures 1.6 and 1.7 the number of energy piles installed in Austria and in UK is reported updated to 2004 and 2016, respectively.

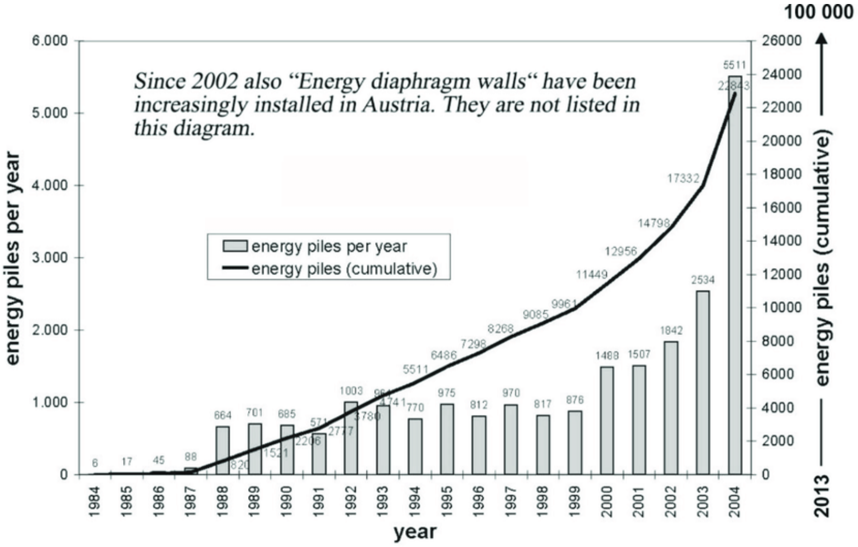

Figure 1.6. Energy piles installed in Austria (from Brandl, 2008)

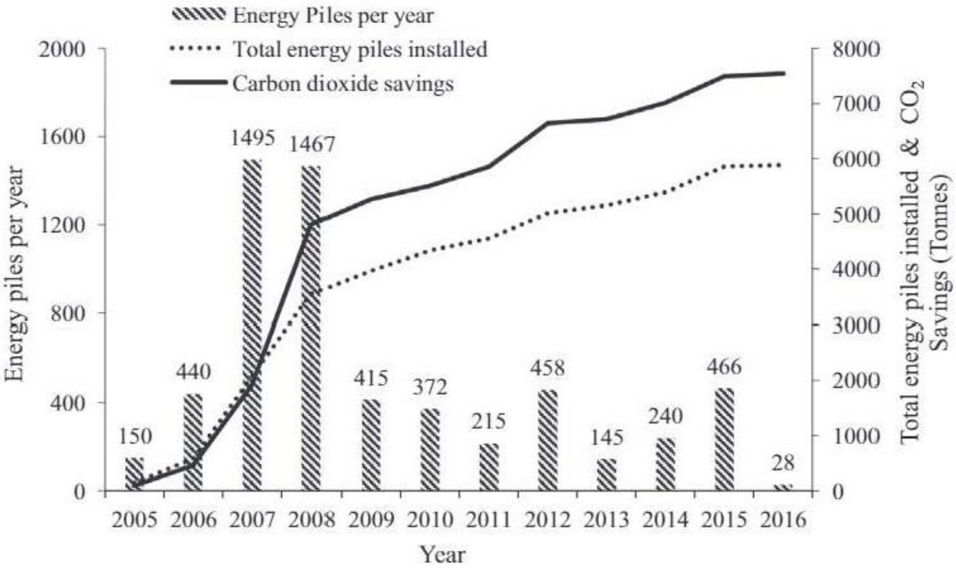

Figure 1.7. Energy piles installed in UK (from Sani et al., 2019)

To better understand the behaviour of both pile and soil when subjected to temperature variations, many researches have been carried out. Nevertheless, the study of the performance of these systems is still challenging. In the following sections, a review of the main results concerning the performance of the energy piles is presented.

1.2.1. Soil response to thermal loading

The thermal activation of the energy piles causes the temperature variation of the structure itself and of the surrounding soil. Clearly, the overall performance of the system is affected by the behaviour of a volume of soil in the vicinity of the foundation and by the interaction between pile and soil at the interface. For this reason, it is important to investigate the soil response at the element scale when subjected to the change of its initial temperature along with the interaction at the interface.

In the following, the thermo-mechanical response of clay and sand is reported, while the interface performance will be discussed in a separate section.

When energy piles are installed in fine-grained soils, the overconsolidation ratio (OCR), i.e. the ratio between the preconsolidation stress and the current vertical effective stress, plays a major role in determining the behaviour of these soils when subjected to a variation of their temperature. Results of laboratory tests on soil specimens (i.e. Campanella and Mitchell, 1968; Baldi et al., 1988 and 1991; Hueckel et al. 1998; Burghignoli et al., 2000; Sultan et al., 2002; Cekerevac and Laloui, 2004;

Abuel-Naga et al., 2006a, 2006b and 2007; Vega and McCartney, 2014; Di Donna and Laloui, 2015a) have proven that the volumetric change of clay soils caused by temperature variation depend on the stress history. In particular, normally consolidated and slightly overconsolidated clays experience volumetric contraction when heated in drained conditions (Fig. 1.8a). In fact, the increase in temperature determines a decrease in the shear strength of the individual interparticle contacts which it is likely to result from the increase in the thermal energy. When the thermal energy increases, there is a higher probability of bond slippage or failure. This turns out in a partial collapse of the soil structure with a decrease in the void ratio (Campanella and Mitchell, 1968). In the cooling phase not the entirely strain is recoverable and, thus, accumulation of irreversible strain takes place. The thermally-induced contraction stabilizes within few cycles when additional contacts between the particles are established (Fig. 1.8b).

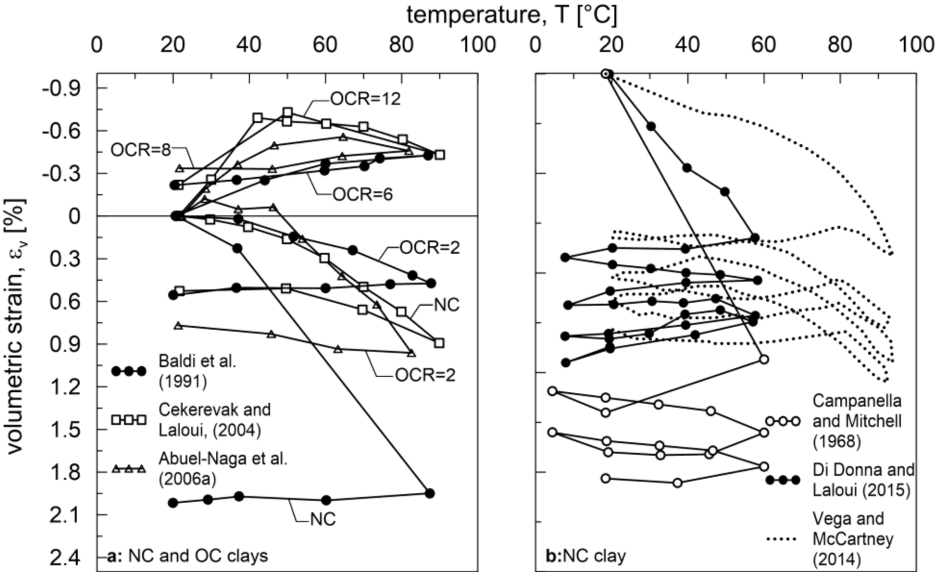

Figure 1.8. Volumetric strains of NC and OC clays subjected to temperature variations.

On the other hand, highly overconsolidated clays expand during heating whereas contract during cooling showing a thermo-elastic behaviour when subjected to multiple thermal cycles.

For saturated soils in undrained condition, the difference between the thermal expansion coefficient of water, α_w, and soil skeleton, α_s, causes the variation of the pore water pressure. The thermal expansion coefficient of the water is a function of the temperature, T; if the temperature is higher than about 5°C, its value is bigger than that of the grains. When the soil temperature is increased, the volume of the soil and its void ratio would increase too; the higher dilation of water counterpoises this effect producing an overall increase in pore water pressure. The opposite occurs when the temperature decreases. For a normally consolidated clay the thermal collapse would induce a reduction in the void ratio; in undrained conditions, this behaviour causes an additional rate of excess pore pressure. Moreover, Campanella and Mitchell (1968) show that the pore water pressure - temperature relation has a tendency to be hysteretic from the early temperature cycles. A similar behaviour is found by Plum and Esrig (1969). They performed a cyclic heating and cooling test in a triaxial apparatus in undrained conditions on a low plasticity clay; the hysteretic behaviour was found after 4 cycles.

Other effects of the temperature variation are related to the preconsolidation pressure and the normal compression line (NCL). Di Donna and Laloui (2015a) performed oedometric tests to analyse the volumetric behaviour of NC clay when subjected to a monotonic increase of the temperature. It was found that the elastic domain decreased in size with increasing the temperature showing a downward shift of the NCL. This is in accordance with the results of other experiments (i.e. Campanella and Mitchell, 1968; Hueckel and Baldi, 1990; Sultan et al., 2002; Cekerevac and Laloui, 2004) showing NCLs parallel to each other at different temperatures. Abuel-Naga et al. (2006a) report the result of oedometric test on a NC clay subjected to one thermal cycle. The soil sample was heated and cooled back to its initial temperature and, after that, it was subjected to the increase of the vertical effective stress. It was found that, during the thermal cycle the volume decreased and that, during the following consolidation phase, a higher stress was needed to reach again the yielding. This behaviour is known as apparent thermally-induced overconsolidation state. The same result is found in earlier experiments by Hueckel and Baldi (1990).

Another effect of the temperature variation is that when the samples is subjected to thermal cycles, the initial void ratio and the plasticity index affect the number of cycles required for the stabilization of the irreversible volumetric contraction. Larger thermo-plastic volumetric strains are caused by higher plasticity index or void ratio (Abuel-Naga et al., 2007; Di Donna and Laloui, 2015a). Moreover, the higher the temperature, the faster the consolidation, i.e. the consolidation coefficient and the hydraulic conductivity increase likely due to the reduction of water viscosity caused by the temperature increase (Towhata et al., 1993; Burghignoli et al., 2000; Abuel-Naga et al., 2006b; Di Donna and Laloui, 2015a).

Although the experimental evidence about the influence of temperature on the soil peak strength is contradictory, many studies show that the critical state friction angle is independent of the temperature (i.e. Burghignoli et al, 2000 Cekerevac and Laloui, 2004; Hueckel and Baldi, 1990; Hueckel et al. 1998). Nevertheless, in the cases in which the friction angle is affected by the temperature variation (i.e. Hueckel and Pellegrini, 1989; Cekerevac and Laloui, 2004) the effects are limited and, thus, can be neglected.

The thermal behaviour of clay can strongly affect the performance of the energy foundations. Figure 1.9 reports the results obtained by Ng et al. (2014a) further analysed in the section related to the laboratory tests where a discussion about the small scale experiments is provided. It can be noted that a pile installed in lightly overconsolidated clay experience greater accumulation of irreversible settlements if compared to a pile in overconsolidated clay.

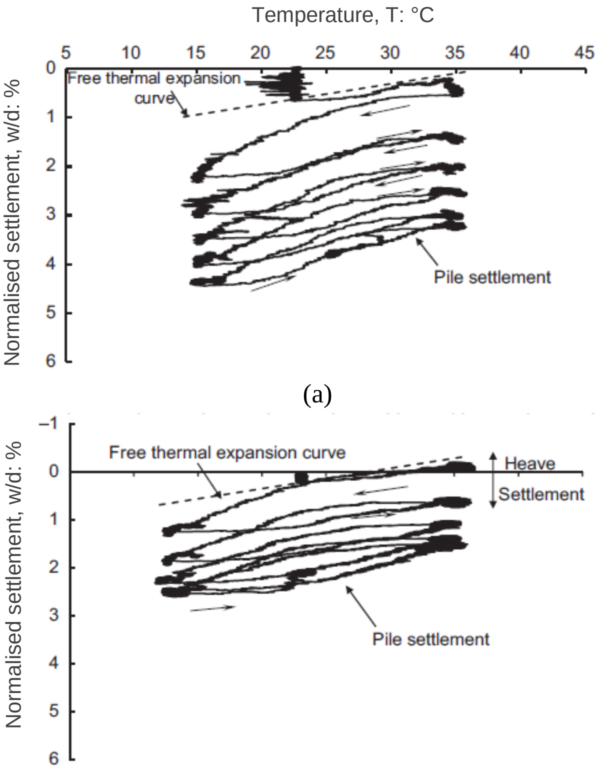

(a)

(b)

Figure 1.9. Settlement of a pile installed in clay: (a) OCR=1.7, (b) OCR=4.7 (after Ng et al. 2014a).

As concerns the sandy soils, since the temperature variation has a limited effect on the soil behaviour a lower number of studies is available. Ng et al. (2016a) report the results of triaxial tests executed on saturated the Toyoura sand samples. The soil specimens were prepared at different relative densities, D_r. Three series of tests were performed (i) to study the volumetric behaviour caused by the temperature variation of the samples under the same stress level and different densities, (ii) under different stress levels but same relative density, and (iii) to investigate the response after heating and cooling of samples having different relative densities. In monotonic loading, the temperature was increased of 27°C, while in cyclic loading, it was increased and then decreased to the initial conditions for a total of 2 cycles. It was found (Fig.1.10) that loose and medium dense sand (i.e. D_r = 20% and 70%, respectively) contract in the early heating phase (from 23°C to 35°C) and then expand (from 35°C to 50°C). This behaviour is likely to be caused by plastic contraction and soil hardening and anyhow has a minor impact since in the second cycle the response got reversible and was characterized by expansion during heating and contraction during cooling regardless of the density. Larger volumetric contraction was found at higher applied stress level The dense sand showed expansion during the whole test.

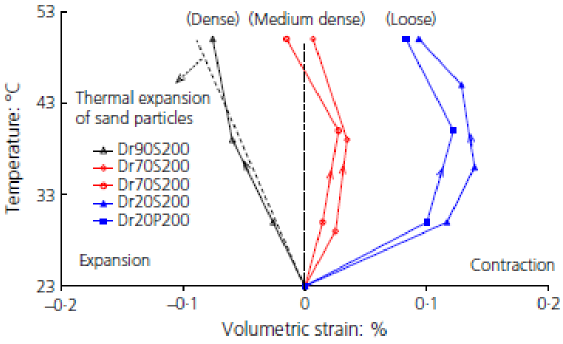

Figure 1.10. Volumetric behaviour of sand at 200kPa (after Ng et al. 2016a).

1.2.2. Soil-structure response to thermal loading

The performance of the pile-soil interface subjected to cyclic thermal loading has been studied using laboratory tests and finite element analyses. In particular, the behaviour of the interface is controlled by two main mechanisms (i) the cyclic expansion and contraction of the pile and (ii) the soil response to temperature variations.

Di Donna et al. (2015b) show the results of a series of tests carried out in a direct shear apparatus equipped for non-isothermal soil-concreate interface tests. Clay-concrete and sand-concrete interfaces along with soil-soil samples were analysed at different temperatures; monotonic and cyclic loading paths were applied. The shear tests were executed under constant normal stiffness (CNS) and constant normal load (CNL) conditions. Moreover, the interface behaviour was tested considering medium and high roughness for the clay-concrete samples and smooth, medium and high roughness conditions for the sand-concrete specimens. In the case of clay-concrete contact, the response of the interface depends from the temperature variation, while, in accordance to the thermo-elastic behaviour of the sandy soils, no thermal impacts were visible for the sand-concrete interfaces. In particular, the strength and the adhesion between clay and concrete increased with increasing the temperature. The latter effect, more evident for the high roughness case, can be justified considering the thermally-induced consolidation of the clay. As a consequence, the increase of the temperature improved the interface performance. Nevertheless, the thermally-induced cyclic stress at the sand-concrete interface had an effect similar to the cyclic degradation phenomenon detected for cyclic axial loading of piles in saturated sandy soils that should be taken into account in practise.

Similar results were obtained by Ng et al. (2016b). They performed a series of finite element analyses investigating the behaviour of a semi-floating energy pile embedded in sandy soil in terms of cyclic shearing at the interface imposed by the cyclic temperature variation. As a result, the decrease of the horizontal stress along with the volumetric contractions caused the reduction of the shaft resistance. Stabilization was found only after a considerable number of cycles. After 50 cycles, the resistance decreased up to 90% for increasing the pile diameter and the range of temperature variation.

Considering the above, the major role played by the interaction at the pile-soil interface in the case of sandy soils, should be carefully taken into account in the design of the thermal piles.

1.2.3. Laboratory tests

Taking the advantage of more controlled condition with respect to the field investigation, numerous tests on energy piles have been executed in laboratory on small scale models. In the following, a discussion of the main findings is reported.

Ng et al. (2014a) show the result of two single energy pile tests performed in the centrifuge of the Hong Kong University of Science and Technology at 40g. The piles, 420mm long with a diameter (*d*) of 22mm (model scale), were installed in a saturated kaolin clay with a layer of Toyoura sand at the bottom of the model to allow drainage. The clay was prepared with two different overconsolidation ratios equal to 1.7 and 4.7 for each test, respectively. The energy pile was subjected to mechanical load and to 5 thermal cycles. The temperature was increased of about 13°C during heating and then decreased of about 10°C during cooling. Each thermal cycle lasted 8 months in the prototype scale. Two reference tests were carried out to assess the pile bearing capacity; for the mechanical load during coupled tests, a factor of safety of 2.5 was used. The results of the thermo-mechanical loading showed accumulation of cyclic settlements at decreasing rate (Fig. 1.9). In particular, the displacements after the application of the mechanical load were equal to 0.67% *d* and to 0.1% *d* while the final displacement was 3.8% *d* and 2.1% *d* for the lightly and the heavily overconsolidated clay respectively. The observed ratcheting was much more evident in the case of OCR=1.7 with lesser reduction in the accumulation of settlements cycle after cycle.

The same centrifuge device was used by Ng et al. (2014b and 2016c) to investigate the behaviour of piles installed in the saturated Toyoura sand at 40g. The pile diameter was 22mm, while the embedded length of the pile was equal to 490mm and to 420mm in the first (Ng et al., 2014b) and the second (Ng et al., 2016c) test, respectively. The applied mechanical load was taken as the 40% of the pile bearing capacity evaluated via a test on a reference pile. The aim of the first test was to investigate the performance of a wished-in-place pile with applied mechanical load and different temperature increments without thermal cycles. It was found that at increasing the variation of the temperature, the neutral plane, located at the depth of zero thermally-induced displacement, shifted toward the pile toe causing a redistribution of the axial force (Fig. 1.11a) and that the capacity of the pile increased. After 4 months of continuous heating, the initial pile heave was followed by settlements. In the second test, the performance of a displacement and a replacement pile subjected to working load and to 5 thermal cycles was compared. Each cycle lasted 8 months in the prototype scale. During heating the temperature was increased of 7°C while during cooling it was decreased of 7°C. The results in terms of settlement are reported in figure 1.12. At the end of the thermal cycles the displacement pile showed a final heave likely caused by the densification of the soil during the pile installation, while the replacement pile exhibited accumulation of settlements with decreasing rate.

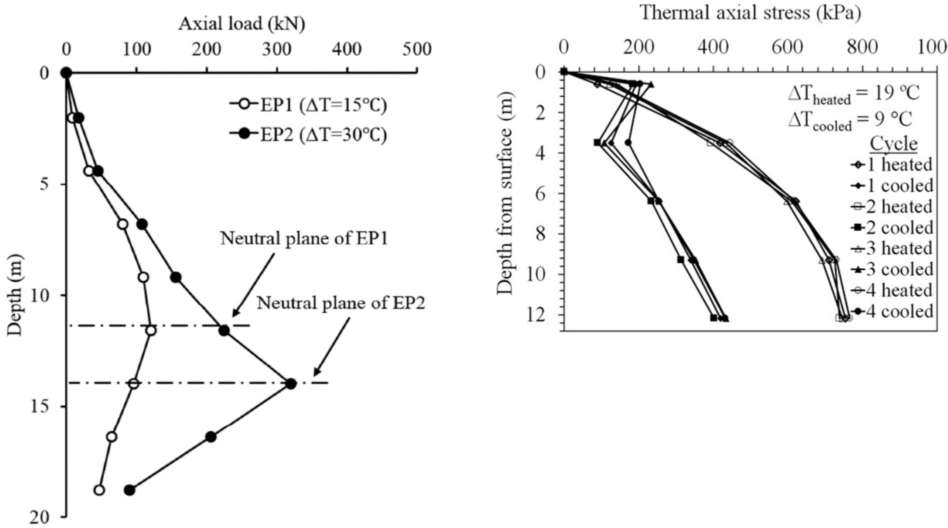

(a) (b)

Figure 1.11. Thermally-induced axial force distributions: (a) effect of temperature variation on a floating pile (after Ng et al. 2014b), (b) effect of base restraint (after Stewart and McCartney, 2013).

Stewart and McCartney (2013) report the results of a centrifuge test at 24g carried out on a single pile whose length was of 533mm with a diameter of 50.8mm in the model scale. The pile was installed in unsaturated silt and its tip was embedded in a rigid layer to simulate end-bearing boundary condition. The pile head was free to move under the applied mechanical load in combination with 4 thermal cycles. The temperature variation was of 19°C and 10°C in heating and cooling, respectively. It was found that the maximum value of the axial load was at pile tip and that no significant variation occurred cycle after cycle (Fig. 1.11b). Therefore, for end-bearing piles the null point is located at pile base. A slight accumulation of settlement was also observed.

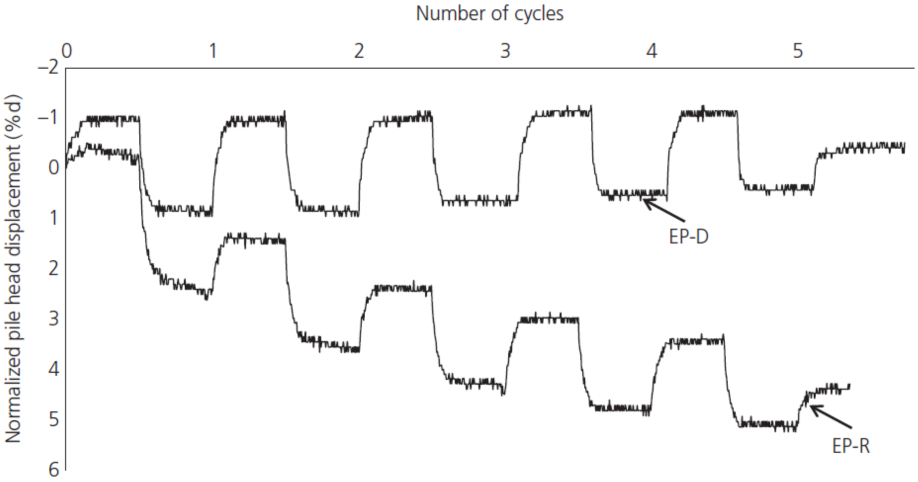

Figure 1.12. Pile head displacements for displacement pile, RP-D, and replacement, EP-R, pile (after Ng et al. 2016c).

Goode and McCartney (2015) performed a series of centrifuge tests at 24g on single energy piles in dry sand and in unsaturated compacted silt. The piles, 63.5mm in diameter, had a length of 342.9mm (short pile) or 533.4mm (long pile) in the model scale. The short piles were semi-floating, while the long piles were end-bearing piles resting on the bottom of the centrifuge container. At head, free and fixed boundary conditions were considered for the test in the dry sand with long pile. For all the other test, the pile head was free to move. After the application of the mechanical load, the foundations were heated at different temperature, the scope of the tests being the study of the effect of the different restraint conditions at the base. The results of the tests performed in unsaturated silt showed greater value of the thermally-induced axial force compared with the results obtained for the tests in sand; this difference is likely due to a greater initial radial stress in the silt. For the same reason, the semi-floating piles in silt exhibited an increase in their bearing capacity when heated, while, in contrast to Ng et al. (2014b), negligible effects were found in the case of sandy soil. The axial force was larger for long piles compared with short piles.

Moreover, the fixed-head condition lead to an increase of the axial force of about 100% for the end-bearing pile in dry sand compared with the free-head condition.

Nguyen et al. (2017 and 2019) performed small-scale tests to investigate the behaviour of single energy piles after the application of mechanical load and of 30 heating and cooling cycles. In the first series of tests (Nguyen et al. 2017), the pile was installed in dry sand, while in the second ones (Nguyen et al. 2019) it was embedded in saturated overconsolidated clay. The diameter and the length of the piles were 20mm and 600mm respectively. Mechanical reference tests were performed to assess the pile ultimate resistance. 4 thermo-mechanical tests were carried out at different load levels (0%, 20%, 40% 60% of pile bearing capacity) applying 30 cycles of temperature variation in the range of ± 1°C. After performing all the tests, accumulated irreversible cyclic settlements were found to be larger when a higher mechanical load is applied; the largest settlements were observed during the early cycles. In contrast with the results reported by Stewart and McCartney (2013), for the tests in sand, the thermally-induced axial load increased cycle after cycle with increasing the applied load, while remains constant when no load is considered at pile head (Fig. 1.13). In terms of axial force, a similar result was numerically obtained from the back analysis of the test in clay.

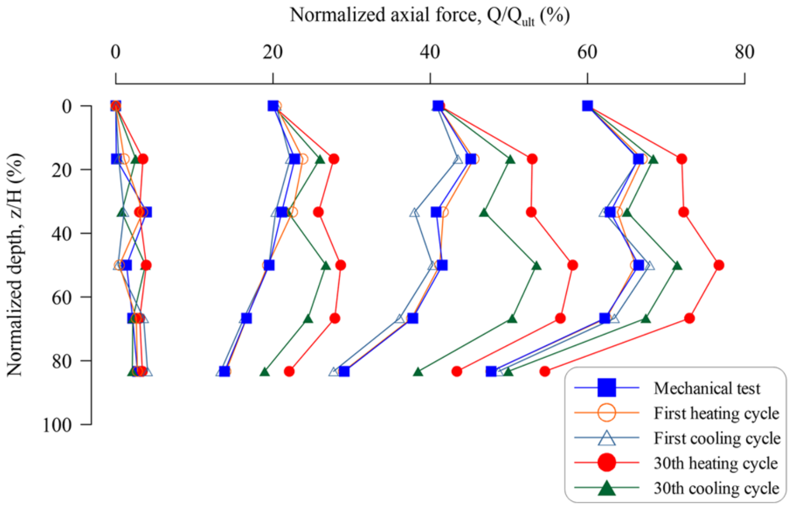

Figure 1.13. Cyclic axial force distribution, effect of different magnitude of mechanical load applied at pile head (after Nguyen et al. 2017).

Wu et al. (2018) report the results of a series of small scale tests. The energy piles, 450mm in length with a diameter (*d*) of 23mm, were installed in saturated normally consolidated clays. The scope of the tests was to investigate the influence of an adjacent non-energy pile (spacing of 3*d*) on the behaviour of the single energy pile in terms of displacement. To this aim, the energy pile was tested without the adjacent pile and with and without a cap connection with the adjacent pile. The pile bearing capacity was determined via a load test. During the thermo-mechanical tests, a mechanical load equal to the 40% of the pile capacity was applied at its head while the temperature was changed of 14°C and -13°C in heating and cooling respectively; a total of 5 cycles was simulated. As observed by Ng et al. (2014a), the data showed accumulation of irreversible displacements with a constant rate cycle after cycle. The smallest settlements were recorded when the energy pile was capped with the non-energy pile; the adjacent pile was subjected to the thermally-induced displacement field, with smaller differential in the case of capped configuration. The soil affected by the temperature variation was subjected to the increase and decrease of pore water pressure during heating and cooling, respectively, with a small accumulation cycle after cycle.

Ng and Ma (2019) show the result of a group test on 3 traditional piles and 1 energy pile carried out in a centrifuge at 60g. The piles had a hallow square cross-section of dimension 20x20mm and a length of 550mm in the model scale; they were installed in a saturated layer of Toyoura sand. The pile heads were connected through a raft not in contact with the ground. A single pile test was carried out to assess the pile bearing capacity. The ultimate capacity of the group was taken as 4 times the single pile capacity; the mechanical load was applied adopting a factor of safety of 2. A total of 10 heating and cooling cycles was performed; each cycle lasted 8 months in the prototype scale. The applied temperature variation was of ±7°C. The thermal activation of just 1 pile caused a non-symmetrical loading condition. Gradual accumulation of irreversible group settlements and tilting with decreasing rate followed by the redistribution of the axial force among the piles was observed; indeed, for the traditional piles, the axial force increased of the 30%.

To summarise, the main findings obtained with the laboratory investigation are listed below:

- the accumulation of the thermally-induced irreversible displacements increase cycle after cycle, especially in clays;
- the presence of traditional piles allows the reduction of the induced settlements;
- the mechanical load at pile head has two main effects on the pile performance: the accumulated displacements and thermally-induced axial force increase cycle after cycle with increasing the applied load, while no variation of the cyclic axial force is observed if the pile is subjected only to the temperature variation;
- the installation technology is also important since the use of replacement pile may induce accumulation of settlements during the first cycles;
- different magnitude of the applied temperature variation, different constraints at pile head and soil layers with different stiffness cause the redistribution of the axial force along the shaft and at the ends;

- the activation of only 1 pile in a group generates non-symmetrical loading condition and, consequently, may induce non negligible differential settlements; moreover, the redistribution of the axial force between the piles is also observed.

1.2.4. Field investigation

The best way to investigate the thermo-mechanical behaviour of the energy piles is to perform full-scale in situ tests. Some of the results available in literature for both the single pile or the group of piles are discussed in the following.

Laloui et al. (1999, 2003 and 2006) report the details and the results of the first in situ experiment on a single energy pile carried out at the Ecole Polytechnique Fédérale de Lausanne (EPFL) in Switzerland. The test involved one of the 97 piles of a building located at the EPFL that, at the time of the test, was under construction. The soil was composed of 5 stratifications with the pile tip embedded in the stiff Molasse layer (Fig. 1.14a). The groundwater table was almost at the ground surface. The pile, 25.8m in length and 0.96÷1.17m in diameter (Amatya et al., 2012), was equipped with polyethylene tubes installed with U-shape. The 58 sensors employed to monitor the pile (vibrating-wire strain gauges, optical fibres, extensometers and a load cell) allowed to measure the vertical and radial strain, the temperature and the base load. The thermal load on the pile was applied in combination with mechanical loads, i.e. the dead weight of the building; in particular, at the end of the construction of each level, one cycle of heating and cooling was performed. The first test involved a temperature increase of about 21°C, while, for the remaining tests the temperature increase was about 15°C. The heating was applied in 12 days followed by 16 days of cooling in which the temperature decreased almost to the initial conditions. The variation of temperature resulted in a variation of the mobilized shaft friction with additional compressive axial force induced by the increase of temperature; the stiffer the soil, the higher the thermally-induced axial force. Indeed, the maximum value of the thermally-induced axial force was at the pile toe where the sandstone was found; at this depth the mechanical load was almost null. The progressively increase in the weight of the building turned out in an increasingly higher constraint for the pile-head movement; the high thermally-induced load at head was of the same order of magnitude of the mechanical load (Fig. 1.14c). The axial and radial thermal strains were thermo-elastic.

Bourne-Webb et al. (2009) describe the test performed on an isolated energy pile undertaken at the Lambeth College in UK. The in situ test was part of the construction project of a building resting on 143 energy piles of variable length. The pile tested was 23m long with a diameter in the range of 0.55÷0.61m. It was installed in the London clay surmounted by two thin layers of granular fill and sand and gravel (Fig. 1.14b). The groundwater table was located at about 3m from the ground surface.

The test setup involved also the drilling of a heat sink pile, four anchor piles and a borehole created to measure the ground temperature. The instrumentation used to record the strain, the temperature and the load was composed of vibrating-wire strain gauges, optical fibres, thermistors, linear variable differential transformers and a load cell. The pile was equipped with polyethylene pipe loops. Before the application of the cooling and heating phases, a mechanical load equal to the working load estimated at the design stage was applied to the pile head. After that, the temperature was first decreased by 20°C and then increased by 10°C with respect to the initial temperature. The cooling phase caused the doubling of the settlements measured at the end of the mechanical stage, while the following heating allowed to recover part of them. The axial strain profile recorded along the energy pile suggested the development of a tensile thermally-induced axial force during cooling and a compressive one during heating, the magnitude of the thermal load depending on the restraint at pile extremities. Indeed, unlike the test at the EPFL, no further load developed at head and the axial force at pile base underwent slight variation with respect to the mechanical phase (Fig. 1.14d). It is worth noting that in this case, after the cooling phase, the lower part of the pile experienced overall tensile axial force. As concerns the thermal field in the surrounding soil, at the borehole (0.5m away from the pile) the temperature was equal to the 50% of the pile temperature and, at the location of the anchor piles (2m away from the pile), it had almost the initial value. The isothermal contours generated from the available measurements, revealed that the thermal field was symmetric, proving reliability in the design assumption of the pile as an infinitely long line source.

Akrouch et al. (2014) show the results of a series of thermo-mechanical tension tests performed on an energy pile at the National Geotechnical Experimental Site at the Riverside campus of Texas A&M University. The tested pile, 5.5m long with a diameter of 0.18m, belonged to a group of 8 piles of which 6 were traditional piles. At the ground level, a 0.30m thick slab was casted; in order to guarantee no connection at the pile heads, the slab was shaped with 8 holes. The soil was made of very stiff high plasticity clays. The energy piles were equipped with a U-shape polyethylene loop. The instrumentation installed was composed of strain gauges, dial gauges, load cells and thermocouples. 5 tests were performed with different tension load applied at head along with a temperature variation of about +7°C. The data showed that, compared to the ultimate capacity, the thermally-induced force is less than the 1% each °C of temperature increase. Moreover, as a consequence of the temperature increase, an increase of the creep rate was found; the Authors extrapolated the load-settlement curve to assess the long term displacement (50 years of operation) obtaining settlements 2.35 times greater if compared to a foundation without energy piles. This is in accordance with the increase of the settlement in clay soils found via the laboratory tests. In order to reduce the differential settlements, it is suggested to use a symmetric configuration.

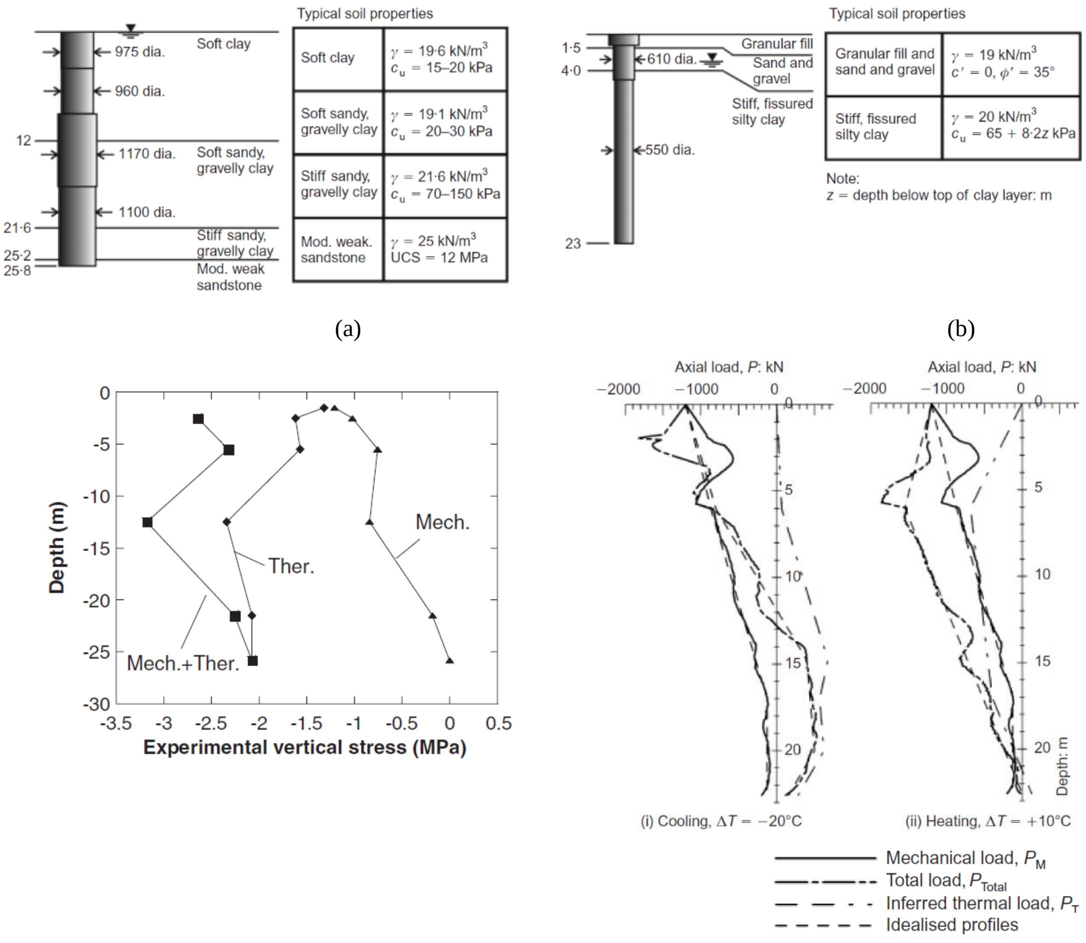

(a) (b)

(c) (d)

Figure 1.14. Soil properties and thermally-induced axial force distributions (after Amatya et al., 2012 and Laloui et al., 2006): (a, c) EPFL test and (b, d) Lambeth college test.

Sutman et al. (2015) performed a series of tests on three single energy piles, having different lengths (2 of them were 15.24m long, while the third was 9.14m) and same diameter of about 0.25m. The field tests were carried out in Richmond, Texas, in a site characterized by alternation of sandy and clayey strata with the groundwater table at 3.7m. The piles were equipped with a single loop of a polyethylene pipe and with optical fibre sensors, vibrating wire strain gages, linear variable differential transformers, thermistors and thermal integrity profile wires for monitoring strains, displacements and temperatures; piezometers were also installed. The thermal tests included 5 heating and cooling cycles over 5 weeks. The results are referred just to the pile temperature and axial strains at the end of the first cycle. It is shown that as a consequence of the average increase of 8°C in pile temperature, the soil underneath the longer piles partially restrained the free movements resulting in additional compressive loads (similar to what is observed by Goode and McCartney, 2015). Moreover, since the head of the energy piles was free to move, no thermally-induced axial force was observed.

The technology employed in the energy pile has also been tested in piles used for the ground improvement. You et al. (2016) report the data of a series of tests on single Cement Fly-ash Gravel (CFG) energy piles carried out in Beijing in China. The CFG drilled piles are made of a mix of cement, fly ash, gravel, sand and water; they are separated by the raft via a layer of mixed sand-gravel allowing a less degree of restraint at head. The CFG piles, 18m long with a diameter of 0.42m, were installed in a stratified soil composed by alteration of sandy silt, silty clay and gravel layers. The piles were equipped with high-density polyethylene pipes in W-shape, connected to the reinforcement cage. The reinforcement cage was used just to bound the pipes since it was not part of their design. Temperature sensors and vibrating-wire strain gauges were used to measure the temperature and the stains. Two tests were carried out to investigate the behaviour under thermal loads solely and under combined mechanical working load and thermal load, respectively. Moreover, to explore the effect of the temperature variations on the pile bearing capacity, static load tests at different pile temperature were performed. The mechanical load was applied though the use of a system of anchor piles and reaction beam. The application of thermal loads only (temperature variation of +8°C and -6.5°C in heating and cooling, respectively) resulted in non-uniform stresses along the pile; since the pile didn’t have strong restraints at the extremities, in accordance with the simplified schemes proposed by Bourne-Webb et al. (2013), the null point was located at the mid depth. As in Bourne-Webb et al. (2009), the combined mechanical and thermal loads resulted in an overall compressive axial force at the end of heating and in an overall tensile stress in the lower part of the pile at the end of cooling. Moreover, accumulation of settlements was found. In accordance with Goode and McCartney (2015), the tests at failure showed that the bearing capacity of the pile didn’t change significantly at higher temperature; a reduction of the pile capacity was encountered when the temperature was decreased.

Allani et al. (2017) presents the results of a field test on 5 screw energy piles carried out in Belgium. The piles, 11.5m long with outer and inner diameter equal to 0.56m and 0.36m, respectively, were embedded in a soil characterized by alternation of clay and sand. The circulation of the heat-carrier fluid was allowed using U-shape polyethylene pipes. Forces, displacements and temperature were measured using dynamometer, linear variable differential transformers and thermocouples, respectively. The thermal loading was preceded by the application of the mechanical load at pile head. As shown by Bourne-Webb et al. (2009) and by You et al. (2016), the temperature increase (+15°C) caused the increase of the axial force, while the decrease of the temperature (-12°C) resulted in tensile overall load at pile base.

Chen et al. (2017) investigated the performance of a single prestressed concrete energy pile with two thermal tests. The pile was 23m long with inner and outer diameter equal to 0.25m and 0.4m, respectively. The soil was made of stratifications of silty clay with the groundwater table located at about 0.5m from the surface level. The measurements were carried out using vibrating wire strain gauges and temperature sensors. The heat carried fluid was circulated inside 6 polyethylene pipes. Three tests were performed. During the first two tests the temperature of the fluid was increased and then maintained constant resulting in an increase of the pile temperature of about +30°C. The soil located 0.3m away from the pile experienced about the 43% of the temperature increase in the pile, while at 0.5m distance the variation become negligible. The axial load increased with increasing the temperature with different rates; moreover, similarly to Ng et al (2014b), a downward shift of the neutral plane was found. The last test involved a decrease of approximately -6°C for the pile. In this case, the thermally-induced axial force decreased linearly with decreasing the temperature.

Luo et al. (2017) carried out thermal response tests on two energy piles in a site located Xinyang city, China, characterized by layers of sandy clay and clay-rich sandstones; the groundwater table was located 4m below the surface level. The energy piles, 18.5m long with a diameter of 0.6m, were equipped with strain gauges and temperature sensors along with strain-integrated temperature sensors. The loops used were double U-shape high density polyethylene pipes. The experimentation consisted of different phases: the temperature of the ground was measured just allowing the fluid circulation inside the pipes; then, the temperature of the first pile was increased (about +13.5°C) to analyse the response of the single pile; a recovery of the ground temperature was simulated switching off the system; finally, a simultaneous cooling (about -7°C) of the two energy piles connected in parallel was performed. They found that the thermally-induced strains increased linearly with increasing the temperature showing an elastic behaviour with higher magnitude at the extremities due to the restraint conditions. As a consequence, in accordance with the simplified schemes proposed by Bourne-Webb et al. (2013), the thermally-induced stress was maximum in the central sections of the piles. Moreover, the temperature recorded in a borehole located 0.6m away from the piles showed that, with respect to the initial temperature, the maximum disturbance was equal to 4.1°C at a depth of 3m form the ground level.

Few data regarding field tests on energy pile groups are also available. McCartney and Murphy (2012) and Murphy and McCartney (2015) report the results of the first in-situ test on a group of energy piles carried out in Colorado, USA. 2 energy piles were tested, having a diameter equal to 0.91m and a length of 14.8m (foundation A) and of 13.4m (foundation B), respectively. They belonged to a group of 58 traditional drilled piles that was the foundation of an 8-storey building under construction. The two energy piles were coupled with a system of 40 ground-source heat pumps, 143m long. The soil was made of an urban fill layer, a sandy and gravel layer and a claystone bedrock. No groundwater table was found in the area of the foundation site. To measure strains and temperature, six vibrating wire strain gauges with thermistors were placed at different pile depths. U-shape polyethylene pipes were installed inside the piles. The maximum temperature variations recorded in the foundations were in the order of +14°C and -5°C depending on the operational period. The data of the monitoring after 658 days showed that the thermally-induced axial force was within the structural limits and the settlement were not expected to cause damage to the building. Heating and cooling cycles led to permanent effect on the axial strain profile. The stress profile was consistent with the restraint due to the building and the bedrock, showing greater load at pile head and base as already observed for the single pile tests aforementioned (Laloui et al., 2006; Bourne-Webb et al., 2009; Stewart and McCartney, 2013; Goode and McCartney, 2015; Sutman et al., 2015; You et al., 2016).

Mimouni and Laloui (2015) report the results of an in situ test on a group of 4 piles connected by a slab, performed at the EPFL, Switzerland (Fig. 1.15). The group of pile was part of the foundation of a water retention tank. Since the test site was 200m away from the single pile test site, the stratigraphy was similar to that described by Laloui et al. (1999 and 2003). The pile diameter was equal to 0.9m, while the length was 28m; U-shape polyethylene pipes connected in series were installed. Up to about 4m from the surface level the pipes were thermally insulated. The instrumentation used to monitor the test consisted in vibrating wire strain gauges, pressure cells, optical fibres, piezometers and thermistors. A free-head pile test was conducted before the building of the tank, involving one of the 4 piles. After the completion of the construction, each energy pile was tested while the remaining piles were inactive. Moreover, a final group test was carried out.

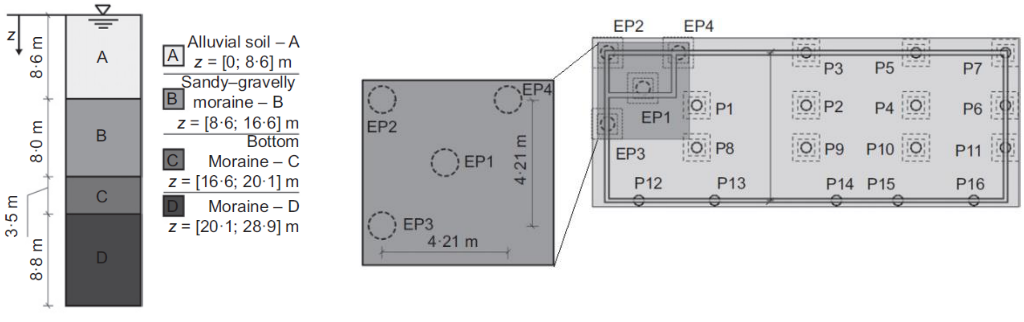

(a) (b)

Figure 1.15. Group test at the EPFL: (a) soil properties and (b) energy pile group layout (after Rotta Loria and Laloui, 2017a).

Since the interaction between energy and non-energy piles can affect the performance of the foundation, the purpose of the single pile tests was to investigate the behaviour of the foundation composed by thermally activated piles and traditional piles. The temperature variation during the single pile tests ranged between +6.5°C and +10°C and lasted 6 days, while a variation between +7.4°C and +9.1°C was found during the 16 days of the group test. For all the tests, the heating phase was followed by passive cooling. The tests on the single energy piles after the tank construction showed a greater thermally-induced load along pile length if compared with the free-head pile test; the pile base was almost unaffected by the presence of the tank. The active pile was subjected to a thermally-induced compression and to an upward head movement; this head movement pulled out the inactive piles inducing expansive strains. The data of the test on the pile group showed an increase of the degree of freedom with respect to the test on the single pile after the tank construction; a reduction of the differential displacement was also found. With reference to the same group, other experiments were carried out. Rotta Loria and Laloui (2017a) describe the results of a test performed after the construction of the tank, consisting of three phases: determination of the ground temperature, 5 months of single pile heating (+20°C) followed by 10 months of passive cooling. After 1 month of heating, i.e. when the temperature of the heated pile increased up to +15°C, a temperature increase was registered in the inactive piles too due to the heat conduction through the soil. Expansion of the heated pile (EP1) was recorded (Fig. 1.16, Test20EP1) except for the shallower portion in which contraction occurred because of the thermal insulation. The inactive piles were subjected to mechanical negative strains induced by the upward movement of the heated pile and the slab, and, after 1 moth, also to thermally-induced negative strains due to the increase of their temperature. The magnitude of these strains was found to be higher than the calculated expansion in free conditions. For all the piles, the axial load increased with increasing the temperature; the inactive piles are characterized by negative values in the early stage (i.e. when their temperature is practically undisturbed) and by an increase toward positive compressive values when their temperature increases. Rotta Loria and Laloui (2018a) report the results of a later group test in which one heating-passive cooling cycle (2 months of heating, with +20°C variation of the pile temperature, and 10 of passive cooling) was performed activating all the piles simultaneously (Test 20EPall). As for the other tests performed after the construction of the tank, in this case the piles were subjected also to mechanical loads. It was found that, because of the group effect, the same temperature variation induced additional strains to the pile EP1 (Fig. 1.16a) compared to the single pile test (Test 20EP1); as a consequence, the thermally-induced axial force gets lower in magnitude (Fig. 1.16b). As concerns the displacements, when the group is thermally activated, the upward movement increases of about the 158% with respect to the single pile test (Fig. 1.17).

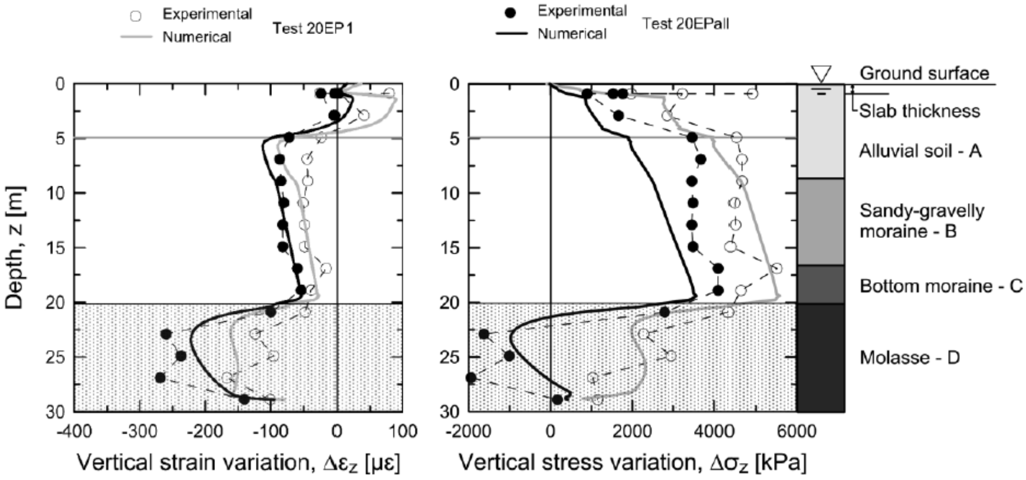

(a) (b)

Figure 1.16. Group test at the EPFL. Results of the single pile (Test20EP1) and the group pile (Test20EPall) tests on pile EP1 in terms of (a) vertical strain and (b) stress after heating (after Rotta Loria and Laloui, 2018a).

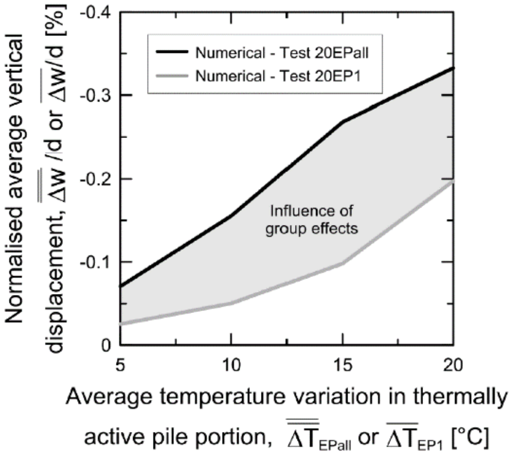

Figure 1.17. Group test at the EPFL. Average vertical displacements (after Rotta Loria and Laloui, 2018a).

The analysed field tests involved the study of different types of piles installed in different soils and, in all the cases, have shown that the variation of the stress and strain states inside the energy foundation is characterized by common features. In addition to the main issues already discussed as concerns the laboratory tests, it can be stated that:

- due to the presence of a structure connecting the pile heads, the thermally-induced force at head can be of the same order of magnitude of the mechanical load;

- the restraining condition at the base affects the behaviour of the end-bearing piles;
- during the cooling phase, overall tensile loads may be experienced at the base;
- the activation of other piles inside the group causes the increase of axial strain allowing the reduction of the thermally-induced axial forces; as a consequence, the displacement increases.

1.2.5. Theoretical studies

The analyses of the energy foundations can rely also on theoretical studies used as alternative tools to gain insight in the main features characterizing the behaviour of the geothermal structures that are expensive and time consuming to be explored solely via in situ or small scale tests. The theoretical studies can be carried out using numerical techniques (including the load-transfer and the continuum-based methods) and analytical approaches, allowing to investigate any configuration even under extreme loading conditions; they can be validated using the data available from the tests.

1.2.5.1. Load-transfer analyses

The load-transfer analysis consists in dividing the pile in a number of rigid elements connected to each other by springs representing the pile stiffness; moreover, elastoplastic springs, attached to each pile section, are used to model the soil stiffness both along the shaft and at the base. The pile-soil interface behaviour is represented via a load-transfer curve used to evaluate the local shaft friction and the pile-soil relative displacement along the shaft (t-z function); the relation between the stress and the displacement at pile base is also modelled via a load-transfer curve (q-z function). Knellwolf et al. (2011) used the load-transfer approach following Seed and Reese (1957) and Coyle and Reese (1966) to develop a design method validated on field data. They employed the t-z curves proposed by Frank and Zhao (1982). The method was based on the hypothesis of (i) neglecting the radial displacements of the pile due to the temperature variation, and of (ii) properties of the pile, soil and pile-soil interaction not changing with temperature. Based on the approach proposed by Knellwolf et al. (2011), the ThermoPile software was developed at the EPFL. The software computes the depth at which the null point is located by producing a number of solutions equal to the number of the discrete sections of the pile; the minimum difference in the equilibrium between the forces acting on the part of the pile above and below the considered section, allows to find the correct position of the null point. Anyway, the t-z curve used are bilinear, composed by two linear branches and a plateau equal to the ultimate resistance without a kinematic hardening criterion. Suryatriyastuti et al. (2014) proposed a cyclic t-z function with a hardening/softening mechanism. This function allowed to take into account the degradation of the pile-soil interface capacity due to two-way cyclic thermal loading. Moreover, the Authors developed a numerical tool employing the load-transfer method with the proposed t-z curve. The results of the one-dimensional analyses showed good agreement with more complex 3D analyses. Pasten and Santamarina (2014) developed a one-dimension load transfer formulation to study the thermoplastic cyclic effects induced by the long term activity of the single energy pile. In this way the accumulation of irreversible displacements could be estimated employing a simple linear elastic-perfectly plastic model for the interface. The numerical results showed that the mobilization of the side shear resistance caused a progressive accumulation of plastic displacements with decreasing rate depending on the applied mechanical load, on the value of the shaft resistance with respect to the ultimate pile resistance and on the amplitude of the thermal cycles. Chen and McCartney (2016) developed a thermo-mechanical load-transfer analyses calibrated on the results available from experiments in nonplastic soils and rocks. On the basis of these data, preliminary design charts were proposed. Sutman et al., (2019) performed a series of 2D thermo-mechanical cyclic finite element analyses defining the soil-pile interaction with load-transfer curves. These curves were derived experimentally, analytically and through empirical relations. The cyclic response was described using the Masing rules. The temperature of the soil was considered constant. The results showed a different behaviour depending on the load-transfer curve used; satisfactory results were obtaining calibrating these curves using the data from field tests. It is concluded that the use of monotonic analyses is not capable of predicting the thermally-induced displacements and the shaft mobilization caused by the cyclic changes.

1.2.5.2. Continuum-based method

The use of the load-transfer approach is a simple tool to analyse the energy foundations; clearly the simplified hypotheses on which it is based on, lead to some limitations. The continuum-based methods (i.e. the finite element method, FEM, and the finite difference method, FDM) offer the possibility to perform fully coupled thermo-hydro-mechanical (THM) analyses in transient regime employing any constitutive model to describe the soil behaviour, whereas they are more time-consuming. Moreover, with respect to field tests, the FEM and the FDM, validated on the available data, allow to investigate the response in each point of the system, while the data collected from experiments are related to the limited number of points in which the instrumentation is installed.

In the following, the results of some studies available in literature are discussed.

The first application of the FEM employing a THM model for saturated porous media was done by Laloui et al. (2006). They back analysed the results of the test on a single pile performed at the EPFL (see section 1.3.1) and found that the proposed

THM model was capable of reproducing the experimental results. Suryatriyastuti et al. (2012) analysed the behaviour of a single pile in sand using two interfaces, one with a cyclic constitutive law and the other with the perfect contact condition. The FDM was used. The pile was subjected to both mechanical and thermal loads. It was found that the contact type between pile and soil strongly affected the mechanical behaviour; in particular, the stresses and the displacements increased when the perfect contact was adopted. Yavari et al (2014) show that, instead of performing fully coupled THM analyses, the results of the field tests can be satisfactory reproduced by simply applying an equivalent thermal volumetric strain to the pile via a commercial FE code. Di Donna and Laloui (2014) used a FE code to carry out fully coupled THM analyses on a single pile and on a group of energy piles (activated simultaneously). The piles were installed in a clay soil that was modelled using an advanced constitutive model. After 10 years of simulated thermal cycles, it was found that the additional settlement occurred during the first cycle, while from the second cycle onward the behaviour was thermo-elastic. This result is contrast with the experimental evidence reported by Ng et al. (2014a) and Wu et al. (2018). As observed in some field tests (Bourne-Webb et al., 2009; You et al., 2016, Allani et al., 2017), the additional compressive stress during heating was admissible while the cooling steps caused tensile stress in the vicinity of the tip. Concerning with the group, the presence of a raft in contact with the ground determined the redistribution of the load between the piles and the development of a uniform settlement. Rotta Loria et al. (2015) evaluated the impact of different magnitude of mechanical and thermal loads on the behaviour of a single energy pile. FE analyses were performed after the calibration of the model on the results of a centrifuge test (Ng et al., 2014b). It was found that the null point moved upward with increasing the applied mechanical load at a constant value of the applied temperature variation. On the contrary, as in Chen et al. (2017), increasing the temperature variation turned out in a downward shift of the null point (Fig. 1.18).

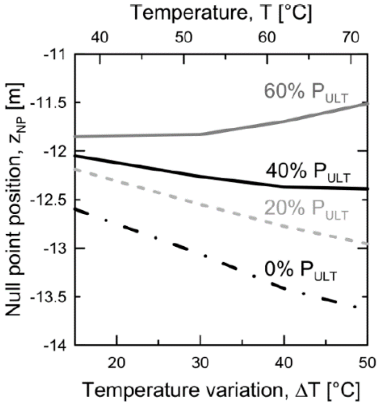

Figure 1.18. Null point position (after Rotta Loria et al., 2015).

Suryatriyastuti et al. (2015) performed FD analyses on a group of traditional and energy piles. During the cyclic temperature variation, the non-energy piles behaved in opposite way with respect to the energy piles. It is concluded that, the location of the energy piles inside the pile group is a crucial aspect as it affects the global behaviour of the group itself. Similar results were found by Di Donna et al. (2016) and Rotta Loria et al. (2016a). They calibrated the FE model using the results of the field test carried out at the EPFL on a group of energy piles (Mimouni and Laloui, 2015). The thermally-induced stresses were found to be of the same order of magnitude as that caused by the application of the mechanical loads. According to the results shown by Rotta Loria and Laloui (2018a), the presence of non-heated pile caused a higher axial force on the active pile if compared to the case in which all the piles are thermally-activated. This axial force decreased as a consequence of heat diffusion in the surrounding soil and, thus, in the other piles (Fig. 1.19). Therefore, the non-heated piles acted as a constraint; when their temperature started to variate because of the thermal conduction, this constraint reduced its effect. It was concluded that the most critical condition in terms of additional stress was the end of the heating phase and that non-uniform thermal loadings, typical of energy foundations in which not all the piles are energy piles, gave rise to more significant stresses and strains.

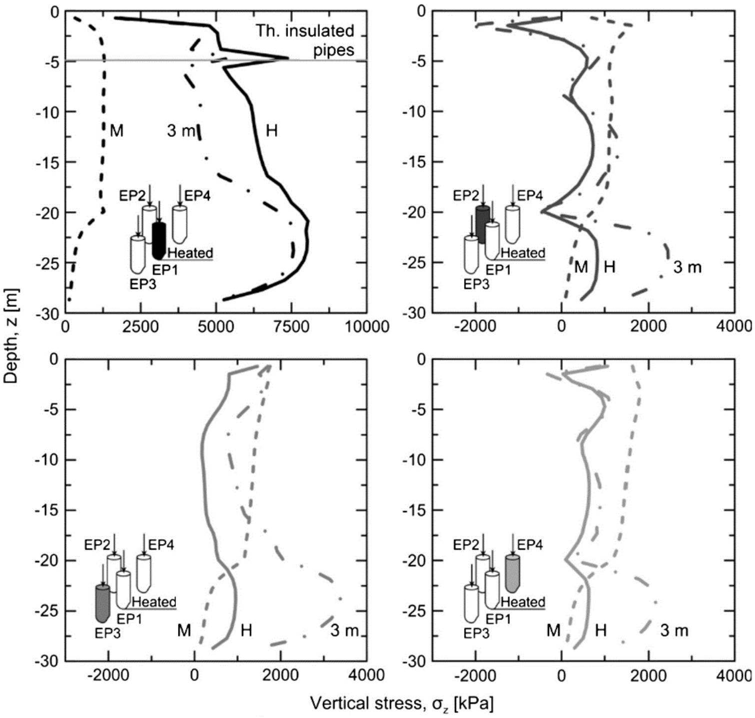

Figure 1.19. Vertical stress on piles EP1, EP2, EP3 and EP4 after the application of the mechanical load, M, the end of the temperature increase, H, and three months of continuous heating, 3m (after Di Donna et al., 2016).

Salciarini et al. (2017) carried out a parametric study with a FE code investigating the behaviour of a piled raft foundation with energy piles installed in clayey soils. It was found that the inactive piles were subjected to additional axial forces having the same order of magnitude as that of the energy piles. Moreover, largely spaced active piles underwent to an increase of the compression load during heating and to a decrease during cooling, while the opposite occurred for closely spaced piles. In the latter case, stronger interaction effects were found. Rui and Yin (2017) and Rui and Soga (2019) used an advanced constitutive model to back analyse the in-situ test performed at the Lambeth College (Bourne-Webb et al., 2009) via FE analyses. The results were found to be in good agreement with the data from the test. Moreover, from a parametric study it was found that the thermal expansion coefficient of the concrete and the position of the neutral plane, had a strong influence on the pile head movements and that the thermally-induced axial force increased with decreasing the thermal expansion coefficient of soil skeleton and water with respect to that of the pile. Adinolfi et al. (2018) used a FE code to analyse the long-term performance of energy piles simulating the operational mode into three different ways, i.e. with and without daily thermal cycles and with an average temperature. The daily cycles mode resulted as the most accurate one, even though the simpler application with the average temperature gave acceptable results. The thermally-induced stresses, displacements and pore water pressures were suggested to be taken into account into the design process. Similarly, Rammal et al. (2018) performed a series of FE analyses in which an isolated energy pile was subjected to temperature changes and to thermal cycles along with a simple mechanical calculation (i.e. imposing only the volumetric strain to the pile) neglecting the heat conduction. They showed that the latter simple scenario, reasonable for soils that do not experience thermal plastic strains, well reproduced the additional thermal axial forces.

Numerical studies employing the FEM have been carried out also to explore the main factors affecting the performance of the energy piles in terms of heat exchange. Batini et al. (2015) show that the W-shape configuration of the pipes is the most efficient. Increasing the pile length, the diameter and the fluid velocity resulted in an increase of the heat exchanged. Moreover, compared with the pure water, the use of antifreeze concentration in the heat carrier fluid had no influence on the rate of heat transferred. Cecinato and Loveridge (2015) highlight the importance of having a high number of pipes along with a turbulent flow condition inside the pipes.

1.2.5.3. Analytical approach

Another way to investigate the performance of a geotechnical systems is to rely on the analytical approach. The pile behaviour under mechanical loads has been widely explored using this analysis method. Accordingly, in recent years many efforts have been devoted to the study of the energy foundations employing this approach.

Rotta Loria and Laloui (2016b) evaluated the vertical displacement of the energy piles in group extending the interaction factor method to the case of thermal loads. Two identical energy piles subjected to the same uniform temperature change were analysed. The following simplified assumptions were made: no mechanical load at head is considered; the piles are free to move at head; the soil is a homogeneous, isotropic semi-infinite space that remains at a constant temperature; perfect contact is assumed at the interface; linear elastic behaviour is considered and thus, the principle of superimposition of effects can be used. In these hypothesis, the effects of the transmission of the thermally-induced displacement field on the adjacent pile were studied and the interaction factor for a pair of two piles was derived. The displacement field was obtained performing FE analyses. Moreover, the FE analyses were also used to propose design charts for the displacement interaction of the two piles, to analyse the group and to validate the proposed analytical approach. The charts refer to different mechanical, geometrical and thermal features, such as pile spacing, slenderness ratio, Poisson's ratio of the soil, pile-soil stiffness ratio, soil-pile thermal expansion coefficient ratio. Considering a general pile group, the thermally-induced displacement of the single pile and the interaction factor can be deduced via the charts, while the final group settlement is derived by exploiting the superimposition of effects using the analytical expression proposed in the work. On the same fashion, Rotta Loria and Laloui (2017b), in order to evaluate the displacement of the groups of energy piles under thermal solicitation, enhanced the formulation of the equivalent pier method. The analogy with the pier allows to model a group of piles with a single equivalent column characterized by the same pile length and equivalent diameter and by mechanical and thermal properties derived homogenising those of the piles and soil. The assumptions made were: no restraint and no applied mechanical load considered at the head; infinitely flexible slab; isotropic, homogeneous and uniform soil modelled as an elasto-plastic medium; the piles and equivalent pier behaving according to the linear thermo-elasticity; the temperature variation applied instantaneously to the piles and the pier, remaining constant with time; conduction allowed in the surrounding soil; the load-displacement behaviour of the pier described by using the one-dimensional load-transfer approach neglecting the radial displacements; the load-settlement curves not affected by the temperature variation. The novelty of the approach for the thermal case is in the equations proposed for the evaluation of the equivalent linear thermal expansion coefficient of the pier; they are based on the hypothesis that the thermal interaction between the piles of the group is negligible. The results obtained applying the pier method for the thermal problem were validated using the interaction factor method and the 3D FE analyses reported by Rotta Loria and Loloui (2016b); the comparison is shown in figure 1.20.

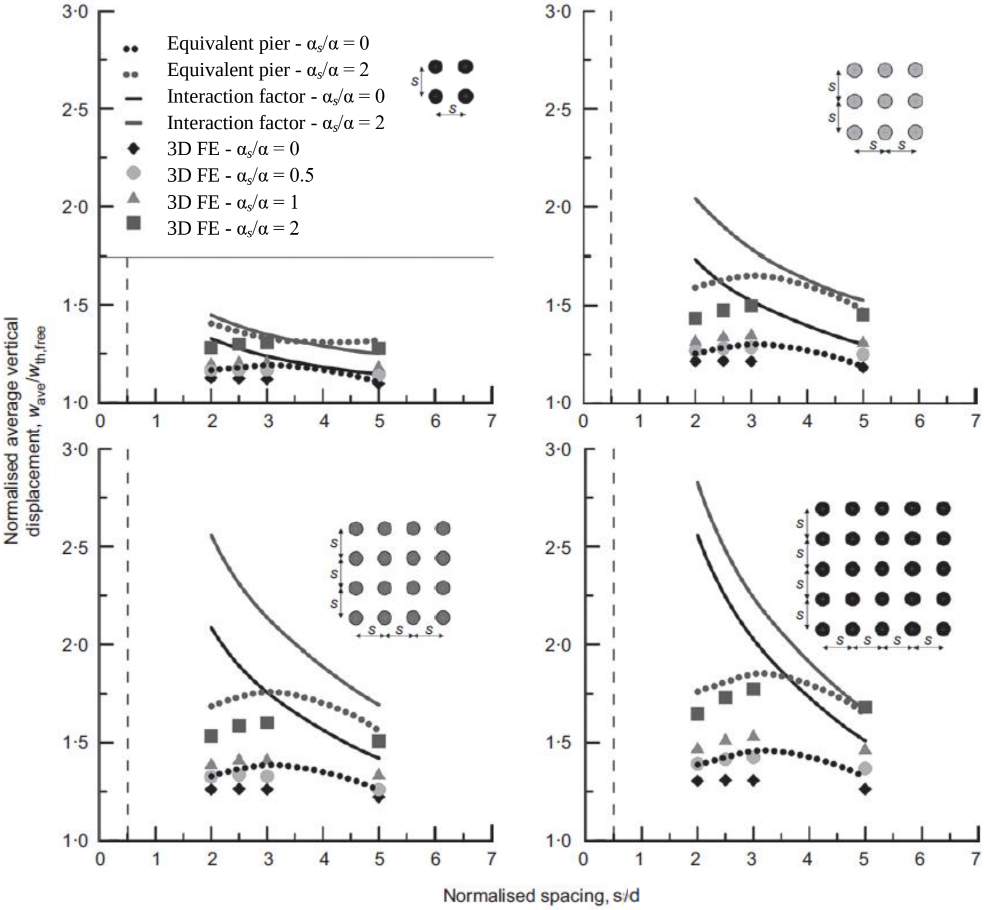

Figure 1.20. Comparison between the results of 3D FE analyses, the interaction factor method and the equivalent pier method considering different soil-pile thermal expansion coefficient ratio (α_s/α) and pile group configurations, 2x2, 3x3, 4x4 and 5x5 (after Rotta Loria et al., 2017b).

From figure 1.20 it is evident that, for low value of the normalized spacing, since the group settlement is evaluated based on the interaction among the pair, the interaction factor method fails in reproducing the evolution of the displacement curves.

In order to consider the displacement interaction between end-bearing energy piles, Rotta Loria and Laloui (2017c) extended the interaction factor method by Rotta Loria and Loloui (2016b) to the case of piles resting on a stiff soil layer. Based on the same assumptions and on the results of stationary finite element analyses, the Authors developed design charts for the evaluation of the interaction factor between two energy piles considering the impact of varying some design parameters (such as the slenderness ratio, the spacing between the piles, the stiffness ratio and so on). For a general pile group, the analytical approach follows the steps proposed by Rotta Loria and Loloui (2016b). Finally, the results were validated via 3D FE analyses. From the above studies, it was found that: the interaction factor is higher for the case of end-bearing pile compared to the floating pile groups; the displacement of the group is influenced by the number of piles in the group and a strong interaction between the piles causes larger displacements; the interaction factor between the two piles increases with increasing the slenderness ratio, the soil-pile thermal expansion coefficient ratio and with decreasing the spacing, the Poisson's ratio of the soil and the pile-soil stiffness ratio; moreover, if the piles are resting on a stiff layer, the interaction between the two piles increases with increasing the base-to-shaft ratio of the Young's modulus of the soil. The interaction factor and the equivalent pier methods are applied in combination with the results of FE analyses and, therefore, can be regarded as semi analytical approaches.

Rotta Loria et al. (2018b) developed two analytical models, i.e. the layer model and the continuous model, for the estimation of the thermally-induced displacement field from the source pile, the displacement of the receiver pile and the evaluation of the interaction factor. Anyhow, since closed-form solutions are not available for the thermal loads, the displacement and the shear stress along the pile shaft developed as a consequence of the temperature variation are derived via the FE method. Therefore, the FE results are used along with the analytical models as analyses tools. The fundamental assumptions are the same as that by Rotta Loria and Laloui (2016b). In the layer model the soil surrounding the pile is modelled with concentric cylindrical elements and the receiver pile is assumed to be a beam attached to springs along the shaft. For the continuous model, the shear stress at the interface is approximated with point loads located at the centre of the elements in which the pile is divided. The capabilities of the two models were validated by comparisons with FE analyses (Fig. 1.21).

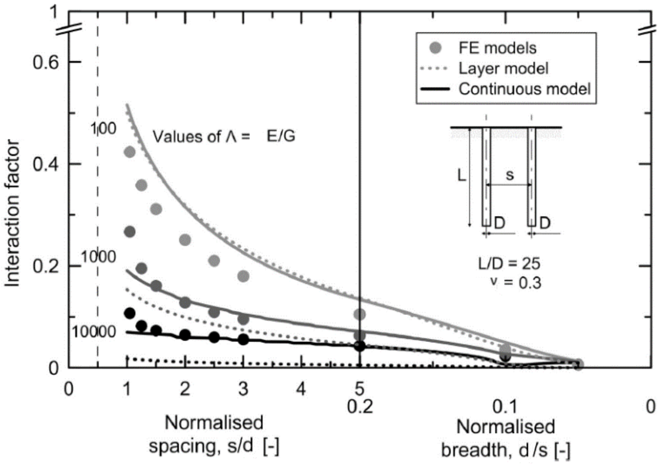

Figure 1.21. Comparison between the FE analyses and the analytical approach for the evaluation of the interaction factor (after Rotta Loria and Laloui et al., 2018b).

1.2.6. Concluding remarks

The researches carried out in recent years covered several issues related to the energy piles. One of the main effects of the thermal solicitation is the development of additional strains that are lower in magnitude if compared to the deformation of a free pile subjected to the same temperature variation. The difference between these strain distributions is a consequence of the restraint provided by the soil and the structure connecting the pile heads; the restrained strains turns into thermally-induced axial loads. If the pile is free to move at head, the heat exchange always implies a mere redistribution of load between the shaft and base. When the energy pile belongs to a group of piles connected by a raft in contact with the ground, the restraining condition changes and the total load at head may also significantly vary. The presence of other energy piles and/or traditional piles, give rise to interaction phenomena. In particular, the simultaneous temperature variation of an increasingly higher number of piles allows a reduction of the thermally-induced axial force; if only one pile is heated, the reduction of the thermally-induced axial force for the active pile is observed only if the traditional piles are affected by the thermal field generated by the energy pile. Field test and numerical analyses focused both on the analysis of the single pile and the groups with and without the application of the mechanical loads. In the majority of the cases a monotonic temperature variation was considered, or at least, one heating-cooling cycle was performed. Concerning with the cyclic performance in terms for axial force, few data are available. As regards the design suggestions, with reference to the Ultimate Limit State (ULS), the increase or decrease of the axial force due to the temperature variation seems to be a small percentage of the ultimate bearing capacity of the system and, considering the magnitude of the applied mechanical load, is of minor concern. Nevertheless, the redistribution of the load should be considered in practical applications. Robust design methods are not yet available and the safety factors usually employed in practice are too much on the side of safety.

The results of many laboratory tests showed that the behaviour of the energy piles in terms of cyclic displacements depends from the installation technique and the soil type. It was highlighted that for replacement piles, normally consolidated clays, lightly oversonsolidated clays and loose sands, cyclic accumulation of irreversible settlement can occur with decreasing rate cycle after cycle. These studies, along with numerical simulations and field tests, also indicated that, neglecting the interaction, the free-head energy pile experiences the maximum head movement and that the presence of inactive piles mitigates the accumulation phenomenon. In recent years, the analytical approach along with numerical analyses were used to derive theoretical methods for the study of the displacement interaction of a group of energy piles. Although the developed analytical approaches are very useful in practical applications as means to have first order values to employ in the design, they are based on simplified assumptions. For example, the influence of cyclic loading and the stiffening effect due to the presence of other piles are not taken into account. Considering the practical applications, the behaviour in terms of settlements should be carefully addressed since it affects the Serviceability Limit State (SLS) design.

To date, it is evident that more research is still needed to include some aspects that have not yet been fully covered.

In the present work the behaviour of the single pile was investigated using analytical and numerical approaches considering different restraint at head and the effect of the cyclic loading.

In the first part, a Winkler-type model is proposed to derive closed-form solutions applicable for the case of the thermally loaded piles. In particular, based on the linear elasticity, exact and approximate analytical solutions are developed for the evaluation of the vertical displacements, the shear stress and the axial force distributions. The derived solutions are very valuable both in the research field and for practical purposes.

In the second part, the numerical method is used for the evaluation of the cyclic performance of the energy piles in terms of thermally-induced axial force and settlements. The single energy pile is modelled in a 2D axisymmetric FE model. Both the free- and fixed-head conditions are considered. To study the effect of the thermally-induced collapse of the soil, the energy pile is installed in NC clay. A discussion comparing the predictive capabilities of the various constitutive models employed in the numerical analyses is provided.

In the final part, for monotonic thermal loading, the analytical approach is compared to the results of the numerical analyses and a procedure for the calibration of the springs is proposed.

2. Analytical solution for the design of thermal piles

At the current stage the analysis of the energy piles must be necessarily carried out through the use of numerical techniques (Knellwolf et al., 2011; Suryatriyastuti et al., 2012, 2014; Pasten and Santamarina, 2014; Yavari et al., 2014, Di Donna and Laloui, 2014; Chen and McCartney, 2016; Di Donna et al., 2016; Rotta Loria and Laloui, 2016a; Adinolfi et al., 2018; Rui and Yin, 2017; Rammal et al., 2018; Rui and Soga, 2019). Rotta Loria et al. (2018b) highlight that for piles subjected to a thermal load "the need to resort to numerical analyses … results from the lack of closed form solutions …, in contrast to their availability for isolated piles subjected to a mechanical load".

In order to fill this lack, exact analytical solutions are developed for the problem at hand, with reference to homogeneous and two-layered soils as well as for subsoil whose stiffness varies linearly with depth. For more general subsoil conditions, approximate energy solutions have been also derived. These solutions provide accurate results if compared against numerical and experimental data, and thus can help the practitioners in designing thermal piles by means of simple hand calculations (Iodice et al., 2020).

2.1. Proposed model

Consider a cylindrical pile subjected to a uniform temperature change ΔT. If the pile were not subjected to any restraint from the surrounding soil, it would experience a constant axial strain along its length equal to:

$$\varepsilon_{\Delta T}\left(z\right)=\alpha\,\Delta T \qquad (2.1)$$

where α is the coefficient of thermal expansion of the pile material and expansion is taken as positive. However, the soil acts as a mechanical restraint which opposes the elongation or shortening of the pile by applying shear stresses upon its external surface. The resulting thermal strain is therefore lower than $\varepsilon_{\Delta T}(z)$ and can be expressed through the following relation:

$$\varepsilon_p(z) = \frac{du_p(z)}{dz} = \alpha\,\Delta T - \frac{N(z)}{EA} \tag{2.2}$$

where E and A are the Young's modulus and cross-sectional area of the pile, respectively, u_p is the pile vertical displacement and N is the axial load induced by the temperature. The compressive axial loads are taken as positive.

The equation (2.2) can be written as:

$$N(z) = \alpha\,\Delta T\,EA - EA\frac{du_p(z)}{dz} \tag{2.3}$$

To account for the restraining effect of the surrounding soil a linear elastic model where the soil is represented through distributed springs of stiffness $k(z)$ [dimensions: FL^{-2}], and pile base and pile top are connected to concentrated springs of stiffness k_b and k_t [dimensions: FL^{-1}] (Fig. 2.1), is here proposed. Note that this is exactly the same model adopted by Randolph and Wroth (1978) for mechanical axial loads at pile top. The calibration of springs' stiffness as function of pile and soil properties is discussed later; however, k is of the order of twice the soil shear modulus and this first-approximation value is adopted in the subsequent graphs.

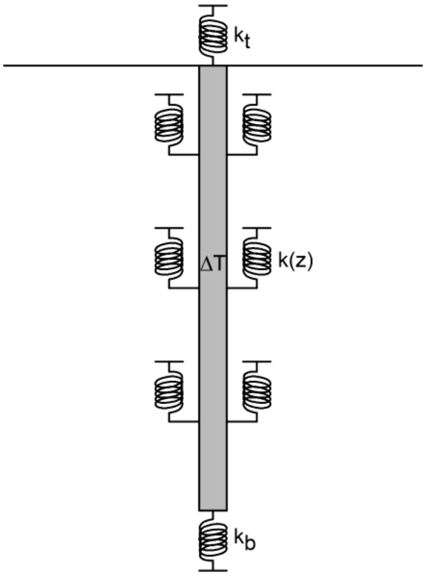

Figure 2.1. Proposed model.

The shear stress $\tau(z)$ acting upon pile surface is therefore proportional to the pile displacement according to the equation:

$$2\pi r_0 \tau(z) = -k(z)\cdot u_p(z) \tag{2.4}$$

where r_0 is the pile radius.

The derivative of the axial load is related to shear stress as follows:

$$\frac{dN(z)}{dz}=2\pi r_0\tau(z)=-k(z)\cdot u_p(z) \tag{2.5}$$

Upon substituting Eq. (2.3) into Eq. (2.5), the following second-order differential equation is obtained:

$$\frac{d^2u_p(z)}{dz^2}-\frac{k(z)}{EA}\cdot u_p(z)=0 \tag{2.6}$$

The solution to the above equation can be found imposing proper boundary conditions. In the following sections, the solution for the case on homogeneous and two-layer subsoil is presented; the details about the integration of the differential equation can be found in the Appendix I.

2.2.Exact solutions

2.2.1.Constant stiffness

If soil stiffness is constant with depth, Eq. (2.6) can be written as follows:

$$\frac{d^2u_p(z)}{dz^2}-\lambda_p^2u_p(z)=0 \tag{2.7}$$

where λ_p [dimensions: L^{-1}] is the pile-soil wave number:

$$\lambda_p=\sqrt{\frac{k}{EA}} \tag{2.8}$$

The pile axial load distribution can be found solving Eq. (2.7) by imposing proper boundary conditions as follows:

$$\begin{aligned} N(z)&=\alpha\,\Delta T\,EA\cdot\\ &\cdot\left(1-\frac{\cosh\left(\lambda_p(L-z)\right)+\Omega\left(\sinh\left(\lambda_p(L-z)\right)+\Theta\cosh\left(\lambda_pz\right)+\sinh\left(\lambda_pz\right)\right)}{(1+\Theta\Omega)\cosh\left(\lambda_pL\right)+(\Theta+\Omega)\sinh\left(\lambda_pL\right)}\right) \end{aligned} \tag{2.9}$$

where L is the pile length; the dimensionless parameters Ω and Θ are equal to:

$$\Omega=\frac{k}{\lambda_pk_b}=\frac{EA\lambda}{k_b} \tag{2.10}$$

$$\Theta=\frac{k_t}{\Omega k_b}=\frac{k_t}{EA\lambda_p} \tag{2.11}$$

and physically represent the ratios between the shaft or top stiffness and base stiffness (integrated over a characteristic pile-soil wave length), respectively. Note that values of Θ larger than 50 correspond, from an engineering viewpoint, to a perfect restraint.

It is very useful to define a mechanical slenderness, $\lambda_p L$, encompassing both pile geometry and pile-soil stiffness ratio. In absence of restraints at pile ends, this would be the unique dimensionless parameter controlling the maximum axial force induced by the thermal load. The presence of base and top springs introduces two additional parameters.

In figure. 2.2, the maximum thermal load along pile shaft, N_{max}, normalized by the (maximum) axial force the pile would have experienced if fully restrained at the ends, $\alpha \Delta T E A$, is plotted against the mechanical slenderness $\lambda_p L$ for different values of Θ and two extreme values of pile-soil stiffness ratio (with G being the soil shear modulus). The following aspects are noteworthy: (a) the thermally-induced axial force increases with $\lambda_p L$, tending to the value for a bar fully restrained at the ends when the pile length or soil stiffness approaches infinity and when the axial stiffness vanishes; (b) the presence of a restraint at pile top always results in an increase in the axial force; (c) for a given pair ($\lambda_p L$, Θ) the axial force is practically independent of the pile-soil stiffness ratio.

The depth at which the axial load is maximum corresponds to the depth at which the shear stress and pile displacement vanish, and can be found through the following equation:

$$z_{N=N\max} = z_{\tau=0} = \frac{1}{2\lambda_p} \ln\left(\frac{e^{\lambda_p L}\left(\Omega\left(e^{\lambda_p L} - 1\right) + e^{\lambda_p L} + \Theta\right)}{\Omega\left(e^{\lambda_p L} - 1\right) + \Theta e^{\lambda_p L} - 1} \right) \tag{2.12}$$

Figure 2.2b depicts the normalized depth of maximum axial force against mechanical slenderness; as for the axial force, there is no dependence from the pile-soil stiffness ratio. For a fully restrained pile ($\Theta = \infty$), it is simple to verify that the maximum axial load is at pile head ($z_{N=Nmax} = 0$). As the mechanical slenderness ratio approaches infinity, the maximum axial force is located at pile half length ($z_{N=Nmax} = L/2$).

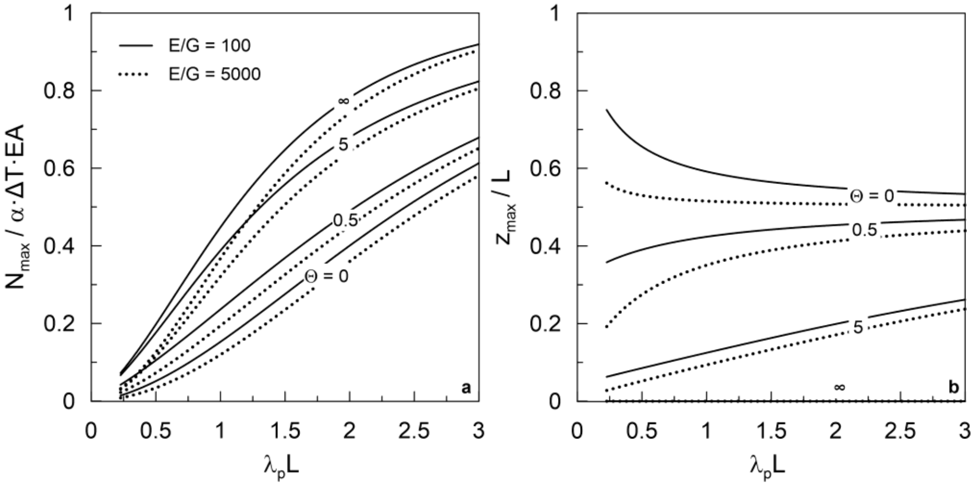

Figure 2.2. Constant stiffness soil. Variation of the (a) normalized axial load and (b) normalized depth with the mechanical slenderness for different values of Θ.

2.2.2. Two-layer soil

When a two-layer soil is considered, the axial load distribution has the following expression (the solution of the differential equation, as well as the expressions of the settlement and shear stress are reported in the Appendix I):

$$
\begin{aligned}
N_1(z) &= \alpha \, \Delta T \, EA \cdot \\
&\cdot \left(1 - \frac{\rho\Big(a_3\left(a_5 + \Omega_1 a_6\right) + \Omega_1\left(a_2 + \Theta \, a_1\right)\Big) + a_4\left(a_6 + \Omega_1 \rho^2 a_5\right)}{\rho a_3\Big(a_7\left(1 + \Theta\Omega_1\right) + a_8\left(\Omega_1 + \Theta\right)\Big) + a_4\Big(a_7\left(\Omega_1 \rho^2 + \Theta\right) + a_8\left(1 + \Theta\Omega_1 \rho^2\right)\Big)} \right) \\
N_2(z) &= \alpha \, \Delta T \, EA \cdot \\
&\cdot \left(1 - \rho \frac{a_9\Big(a_3 + \Omega_1\left(a_8 + \rho a_4 + \Theta a_7\right)\Big) - a_{10}\Big(a_4 + \Omega_1 \rho\left(a_3 - a_7 + \Theta a_8\right)\Big)}{\rho a_3\Big(a_7\left(1 + \Theta\Omega_1\right) + a_8\left(\Omega_1 + \Theta\right)\Big) + a_4\Big(a_7\left(\Omega_1 \rho^2 + \Theta\right) + a_8\left(1 + \Theta\Omega_1 \rho^2\right)\Big)} \right)
\end{aligned}
\qquad (2.13)
$$

where:

$$
\rho = \sqrt{\frac{G_2}{G_1}} \qquad (2.14)
$$

encompasses the ratio between the shear modulus of the deeper layer (G_2) and that of the shallower layer (G_1). The expressions of the dimensionless terms a_i can be found in the Appendix I. They involve the dimensionless parameter $\lambda_1 L$ (i.e. the mechanical slenderness referred to the first layer), and the dimensionless interface depth defined as:

$$\zeta = \frac{h_1}{L} \tag{2.15}$$

h_1 being the thickness of the shallower layer.

In figure 2.3 the normalized axial load is plotted for a free and a fully-restrained head pile, by varying the problem parameters.

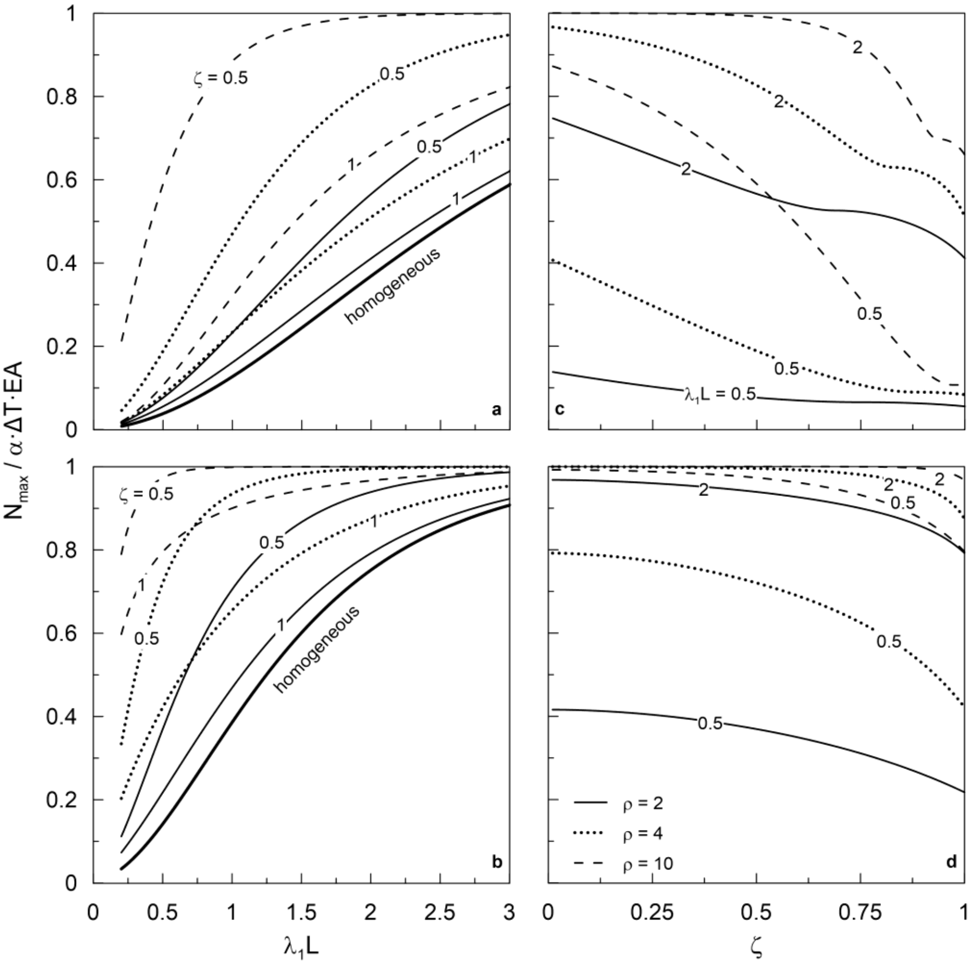

Figure 2.3. Two-layer soil. Variation of the normalized pile axial load with the mechanical slenderness for different values of ζ and ρ: (a) Θ = 0; (c) Θ =∞. Variation of the normalized pile axial load with the dimensionless interface depth for different values of $\lambda_1 L$ and ρ: (b) Θ = 0; (d) Θ = ∞. In all graphs, E / G=1000.

N_{max} understandably increases with increasing $\lambda_1 L$ and ρ, and for decreasing values of ζ. Note that for end-bearing piles ($\rho > 2$, $\zeta \cong 1$) of ordinary length ($\lambda_1 L > 1$) the induced axial force is at least 80% of the maximum value (see graph c) and thereby the thermal load for this category of piles is particularly detrimental, yet it may be of lesser importance if compared to the (high) mechanical loads.

The depth of maximum axial force is depicted in figure 2.4. It is noted for most cases encountered in practice that N_{max} occurs in the second (stiffer) layer.

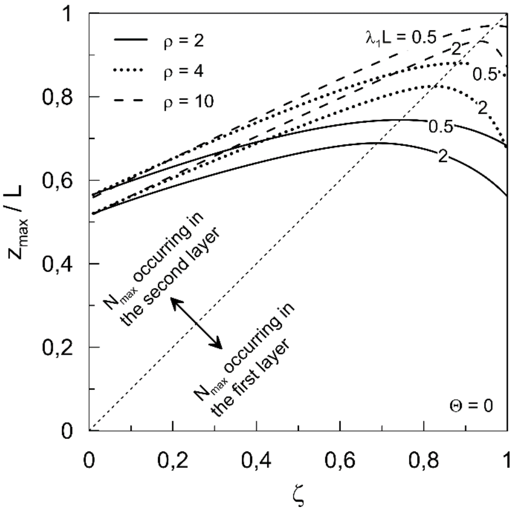

Figure 2.4. Two-layer soil. Variation of the normalized depth with the dimensionless interface depth for different values of $\lambda_1 L$ and ρ.

2.2.3. Linear stiffness profile (Gibson soil)

Equation (2.6) for a soil whose stiffness varies proportionally with depth can be written as follows:

$$\frac{d^2 u_p(z)}{dz^2} - \mu^3 u_p(z) = 0 \tag{2.16}$$

where

$$\mu = \sqrt[3]{\frac{\bar{k}_G}{EA}} \tag{2.17}$$

is the pile-soil wave number [dimensions: L^{-1}] for a Gibson soil profile (i.e. assuming $k = \bar{k}_G z$).

The axial forces at the pile head and base are given by:

$$\begin{aligned}
N_{z=0} = {} & \alpha\,\Delta T\,EA\cdot \\
& \cdot 3^{\frac{1}{6}}\Theta\left(\bar{\Omega}\left(I_{-\frac{2}{3}}\left(\frac{2}{3}(\mu L)^{\frac{3}{2}}\right)\sqrt{\mu L}-\frac{3^{\frac{2}{3}}}{\Gamma\left(\frac{1}{3}\right)\sqrt{\mu L}}\right)+I_{\frac{1}{3}}\left(\frac{2}{3}(\mu L)^{\frac{3}{2}}\right)\right)\cdot \qquad (2.18a) \\
& \cdot\left[\begin{aligned} & 3^{\frac{1}{6}}\Theta\left(I_{-\frac{2}{3}}\left(\frac{2}{3}(\mu L)^{\frac{3}{2}}\right)\bar{\Omega}\sqrt{\mu L}+I_{\frac{1}{3}}\left(\frac{2}{3}(\mu L)^{\frac{3}{2}}\right)\right)+ \\ & +\frac{2\pi}{\Gamma\left(\frac{1}{3}\right)^{2}}\cdot\left(I_{-\frac{4}{3}}\left(\frac{2}{3}(\mu L)^{\frac{3}{2}}\right)\bar{\Omega}\sqrt{\mu L}+I_{-\frac{1}{3}}\left(\frac{2}{3}(\mu L)^{\frac{3}{2}}\right)\left(\frac{\bar{\Omega}}{\sqrt{\mu L}}+1\right)\right)\end{aligned}\right]^{-1}
\end{aligned}$$

$$\begin{aligned}
N_{z=L} = {} & \alpha\,\Delta T\,EA\cdot \\
& \cdot 3^{\frac{1}{6}}\left(I_{\frac{1}{3}}\left(\frac{2}{3}(\mu L)^{\frac{3}{2}}\right)\Theta-\frac{3}{\Gamma\left(\frac{1}{3}\right)\sqrt{\mu L}}\right)+\frac{2\pi}{\Gamma\left(\frac{1}{3}\right)^{2}}\cdot I_{-\frac{1}{3}}\left(\frac{2}{3}(\mu L)^{\frac{3}{2}}\right)\cdot \qquad (2.18b) \\
& \cdot\left[\begin{aligned} & 3^{\frac{1}{6}}\Theta\left(I_{-\frac{2}{3}}\left(\frac{2}{3}(\mu L)^{\frac{3}{2}}\right)\bar{\Omega}\sqrt{\mu L}+I_{\frac{1}{3}}\left(\frac{2}{3}(\mu L)^{\frac{3}{2}}\right)\right)+ \\ & +\frac{2\pi}{\Gamma\left(\frac{1}{3}\right)^{2}}\cdot\left(I_{-\frac{4}{3}}\left(\frac{2}{3}(\mu L)^{\frac{3}{2}}\right)\bar{\Omega}\sqrt{\mu L}+I_{-\frac{1}{3}}\left(\frac{2}{3}(\mu L)^{\frac{3}{2}}\right)\left(\frac{\bar{\Omega}}{\sqrt{\mu L}}+1\right)\right)\end{aligned}\right]^{-1}
\end{aligned}$$

where:

$$\bar{\Omega}=\frac{\bar{k}_G}{\mu k_b}=\frac{EA\mu}{k_b} \qquad (2.19)$$

Θ has the same expression for the case of homogeneous soil except using Eq. (2.19) for $\bar{\Omega}$; $I_i(2/3(\mu L)^{3/2})$ is the first kind modified Bessel function of i-th order and argument $2/3(\mu L)^{3/2}$; $\Gamma(1/3)$ is the Gamma function evaluated at 1/3.

In figure 2.5a the normalized axial load is plotted against the mechanical slenderness μL for different values of Θ and two extreme values of pile-soil stiffness ratio (with $\bar{G}$ being the gradient of the soil shear modulus with depth).

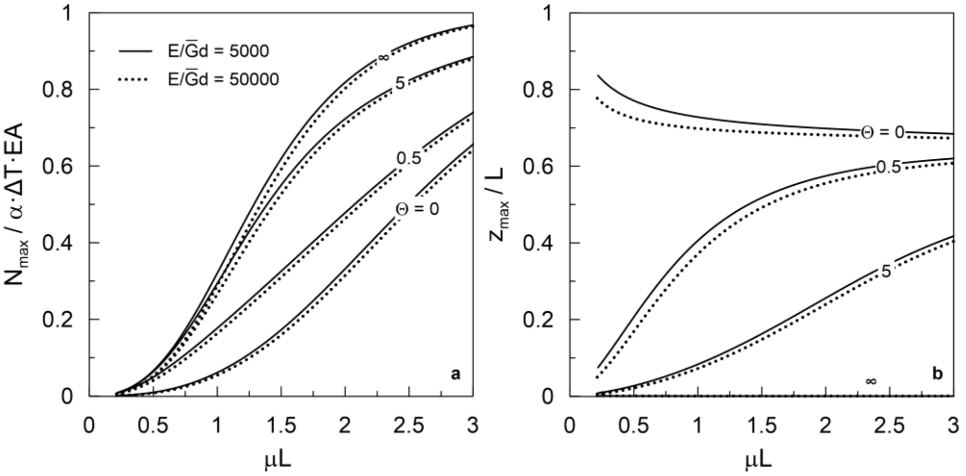

Figure 2.5. Gibson soil profile: Variation of (a) normalized axial load and (b) depth with the mechanical slenderness μ*L* for different values of Θ.

As for the case of the homogeneous soil, it can be seen that the mechanical slenderness successfully merges geometrical and mechanical properties of pile and soil. The same statement holds for the normalized depth plotted against the mechanical slenderness μ*L* (Fig. 2.5b).

The above solution, on one hand possesses the undeniable advantage of being exact, while on the other hand may face some reluctance from practitioners who are often not familiar with the Bessel functions which, however, are implemented even in spreadsheets.

In order to simplify the problem, an iterative procedure to derive the equivalent homogeneous soil leading to the same maximum axial force as the Gibson soil has been developed. The procedure allows to estimate the depth z_h at which the axial load for the Gibson soil is equal to that of the homogeneous soil. Once known this depth, it is possible to evaluate the axial force of the Gibson soil using the simple Eq. (2.9).

The steps followed to obtain z_h are listed below:

- choice of an arbitrary value of z_h, $(z_h)_1$;

- estimation of $(E_p / \bar{G}\, z_h)_1$ from the following equation:

$$\frac{E_p}{\bar{G}\, z_h} = \left(\frac{E_p}{\bar{G}\, d}\right)^{2/3} \left(\frac{z_h}{L} \cdot \mu L\right)^{-1} \left(\frac{2\delta}{\pi}\right)^{2/3} \tag{2.20}$$

where δ is a coefficient for the calibration of spring stiffness. Its evaluation is addressed in paragraph 2.3.2;

- evaluation of the axial load $(N)_1$ from the Gibson soil solution;
- estimation of $(\lambda_p L)_1$ from eq. (2.9)
- estimation of $(z_h)_2$ from the following equation:

$$\lambda_p L = \left(\frac{z_h}{L}\right)^{1/2} (\mu L)^{3/2} \tag{2.21}$$

- comparison between $(z_h)_1$ and $(z_h)_2$.

The results obtained using the iterative procedure are reported in figure 2.6 in terms of z_h/L versus the mechanical slenderness, μL, for different values of the degree of freedom, Θ, and stiffness ratio, $E_p / \bar{G}\, d$; it can be noted that the influence of the stiffness ratio on the value assumed by z_h/L is negligible.

After estimating z_h/L from figure 2.6, it is possible to evaluate the associated $\lambda_p L$ from Eq. (2.21) and, thus, to use Eq. (2.9). The comparison between the use of the analytical and the approximate solution is plotted in figure 2.7.

In the following sections a more general approximate solution will be developed for practical use. In this sense, the exact solutions reported above are prone to be used as benchmark for future research, since a comparison with models involving nonlinear springs would not require a specific selection of the spring stiffness as function of the soil shear modulus. On the contrary, the approximate solutions turn to be more suitable for practical applications, considering that they are developed for more general subsoil and that even the small error is totally cancelled out since the spring stiffness is directly calibrated on these simpler solutions.

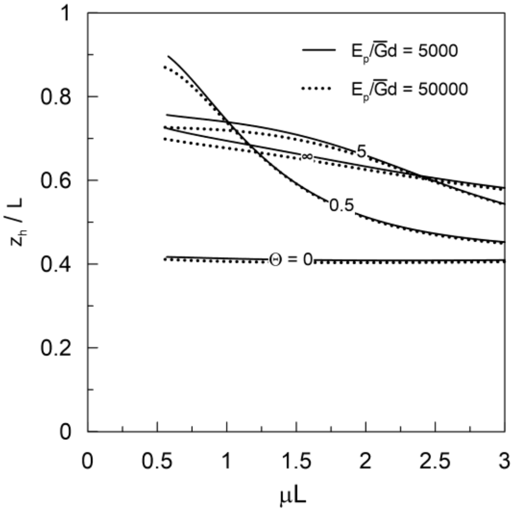

Figure 2.6 Gibson soil profile. Variation of the normalized depth load with the mechanical slenderness ratio for different values of Θ and $E_p / \bar{G}\, d$.

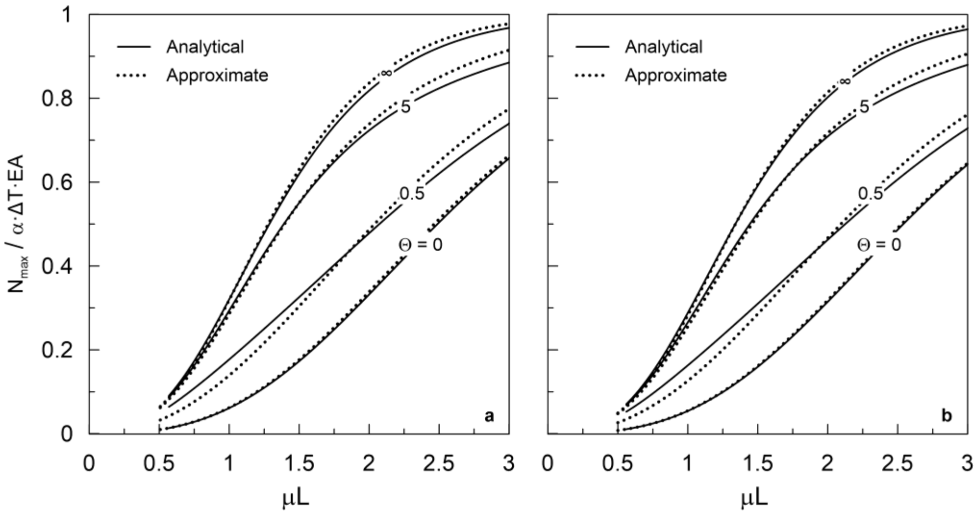

Figure 2.7. Gibson soil profile. Comparison between analytical and approximate solution: (a) $E_p/\bar{G}d$ = 5000 and (b) $E_p/\bar{G}d$ = 50000.

2.3. Approximate solutions

With the aim of obtaining an approximate solution for the problem at hand, it is possible to refer to a simplified displacement profile and then exploit the principle of virtual work.

The displacement of the pile induced from the thermal load is here approximated through a linear function of the depth. It is convenient to express the pile displacement as follows:

$$u_p(z) = L\,\bar{u}_l\,\Phi(z) \tag{2.22}$$

where $\bar{u}_l$ is the displacement at pile tip normalized by pile length; Φ(*z*) is the shape function:

$$\Phi(z) = \frac{\frac{z}{L} - \bar{z}_N}{1 - \bar{z}_N} \tag{2.23}$$

with $\bar{z}_N$ being the depth corresponding to zero pile displacement normalized by pile length.

In the realm of the principle of virtual work, both the virtual and real displacements are assumed to be described by Eq. (2.22).

To enlarge the domain of potential practical applications, reference is made to a general subsoil with a stiffness profile given by the following relation:

$$G(z)=G_L\left(a+(1-a)\left(\frac{z}{L}\right)^b\right) \tag{2.24}$$

where G_L is the soil shear modulus at pile tip and a, b are two coefficients regulating the stiffness profile. The principle of virtual work assures that the work done by the top, base and shaft loads equals the work done by the axial force, due to the variation of the pile temperature, both associated to the displacement pattern in Eq. (2.22). The latter statement can be written for the problem at hand, in a dimensionless form, as follows:

$$\begin{aligned}&\Theta_L\,\Omega_L\,\bar{u}_0^2+\bar{u}_l^2+\int_0^L \lambda_L\Omega_L\left(a+(1-a)\left(\frac{z}{L}\right)^b\right)\bar{u}_l^{\,2}\,\Phi^2(z)\,dz=\\&=\Omega_L\bar{u}_l\,\frac{\Phi'}{\lambda_L}\left(\alpha\,\Delta T-L\,\bar{u}_l\,\Phi'\right)\end{aligned} \tag{2.25}$$

where $\bar{u}_0$ is the displacement at pile head normalized with respect to pile length; λ_L, Ω_L, Θ_L are obtained from Eqs. (2.8), (2.10) and (2.11) respectively using Eq. (2.24) for soil shear modulus and Φ' is the derivative of the shape function with respect to z.

In addition, the equilibrium along the vertical direction assures that:

$$\Theta_L\,\Omega_L\,\bar{u}_0+\bar{u}_l+\int_0^L \lambda_L\Omega_L\left(a+(1-a)\left(\frac{z}{L}\right)^b\right)\bar{u}_l\,\Phi(z)\,dz=0 \tag{2.26}$$

Eqs. (2.25) and (2.26) can be solved simultaneously for the two unknowns $\bar{u}_l$ and $\bar{z}_N$, whose expressions are reported in the Appendix I. Once the displacement profile is known, it is possible to derive the axial force distribution as follows:

$$\begin{aligned}&N(z)=EA\lambda_L L\bar{u}_l\cdot\\&\cdot\frac{2\Theta_L\bar{z}_N-\lambda_L z\left(a\left(\frac{z}{L}-2\bar{z}_N\right)+2(1-a)\left(\frac{z}{L}\right)^b\left(\frac{z}{L(2+b)}-\frac{\bar{z}_N}{1+b}\right)\right)}{2\left(1-\bar{z}_N\right)}\end{aligned} \tag{2.27}$$

Expressions for special cases are reported in the Appendix I in terms of axial force and shear stress.

Energy solutions have been obtained for axially-loaded (Crispin et al. 2019) as well as laterally-loaded (Karatzia and Mylonakis 2016) piles. However, the application of this method to thermally-loaded piles leads to much more accurate solutions since, contrary to the case of piles loaded at the top, approximating the displacement profile by a linear function results in an error of minor concern. This is evident in figure 2.8, where a comparison between FE-derived displacement profile and the one given by Eq. (2.22) is reported for different kind of subsoils.

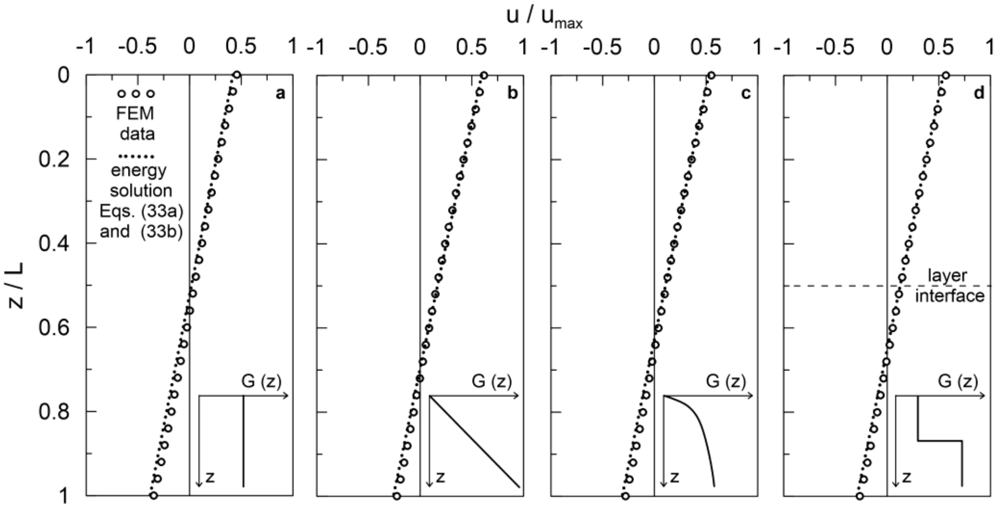

Figure 2.8. Energy solution. Comparison between FEM data and proposed solution for free-head pile: (a) constant stiffness soil; (b) Gibson soil profile; (c) proportional stiffness profile; (d) two-layer soil.

2.3.1. Multi-layer soil

Referring to a multi-layer soil with constant stiffness within each layer, the virtual work and the vertical equilibrium equations can be written as follows:

$$k_t L^2 \bar{u}_0^2 + k_b L^2 \bar{u}_l^2 + \frac{\bar{u}_l^2}{3\left(1-\bar{z}_N\right)^2}\sum_{m=1}^{n} k_m \left(\left(z_m - L\bar{z}_N\right)^3 - \left(z_{m-1} - L\bar{z}_N\right)^3\right) = \\ = \frac{L\bar{u}_l EA}{1-\bar{z}_N}\left(\alpha\Delta T - \frac{\bar{u}_l}{1-\bar{z}_N}\right) \tag{2.28}$$

$$k_t L\bar{u}_0 + k_b L\bar{u}_l + \frac{\bar{u}_l}{2\left(1-\bar{z}_N\right)}\sum_{m=1}^{n} k_m \left(z_m^2 - z_{m-1}^2 - 2L\bar{z}_N \left(z_m - z_{m-1}\right)\right) = 0 \tag{2.29}$$

where the third term represents the contribution of the shear stress acting along the pile shaft for each n-th layer, k_m being the spring stiffness of layer m; z_m and z_{m-1} are the depths of the bottom and top interfaces of layer m.

By solving Eqs. (2.28) and (2.29) it is possible to obtain the two unknown $\bar{u}_l$ and $\bar{z}_N$; the axial force and the shear stress distributions have the following expressions:

$$N_i\left(z\right)=-k_t L\bar{u}_0-\frac{\bar{u}_l}{2\left(1-\bar{z}_N\right)}\begin{pmatrix} k_i\left(z^2-z_{i-1}^2-2L\bar{z}_N\left(z-z_{i-1}\right)\right)+ \\ +\sum_{m=1}^{i-1}k_m\left(z_m^2-z_{m-1}^2-2L\bar{z}_N\left(z_m-z_{m-1}\right)\right) \end{pmatrix} \tag{2.30}$$

$$\tau_i\left(z\right)=-\frac{\bar{u}_l}{4\pi r_0\left(1-\bar{z}_N\right)}k_i\left(z-z_{i-1}-L\bar{z}_N\right) \tag{2.31}$$

where z_{i-1} is the depth of the top interface of layer i.

2.3.2. Spring stiffness

In the proposed model the soil surrounding the pile is represented through a series of linear elastic springs whose elastic constant $k(z)$ is proportional to the soil shear modulus $G(z)$ through a coefficient δ:

$$k\left(z\right)=\delta\cdot G\left(z\right) \tag{2.32}$$

Spring stiffness has been widely investigated for the case of mechanical axial loads at the pile top (Coyle and Reese, 1966; Randolph and Wroth, 1978; Mylonakis, 2001), so that such Winkler-type models well-reproduce continuum solutions.

To calibrate the value of δ for the thermally-loaded piles, a number of Finite Element analyses have been carried out by means of the commercial software ANSYS®. Different configurations have been considered, varying soil stiffness distribution and pile size. Both free-head and restrained-head piles have been analysed. A total of 480 analyses have been carried out, involving values of L/d = 20, 30, 40 and 50 (where d is the pile diameter), $E/G_{L/2}$ = 250, 500, 1000 and 2000 (with $G_{L/2}$ being the soil shear modulus at z = $L/2$), Poisson's ratio ν = 0.3, 0.4 and 0.49 as well as 4 different subsoils (b = 0; a = 0 and b = 1; a = 0 and b = 0.5; a = 0.5 and b = 1). 2D axisymmetric 8-noded elements have been employed to mesh the model. As outcome of a sensitivity study, the elements vertical size has been set to 0.25 d, while the model dimensions are 100 diameters in height and 200 diameters in width. Perfect bounding between pile and soil has been considered. The lateral boundary of the model is restrained against vertical displacement.

By imposing the equality between the maximum axial force derived by the numerical analyses and the one furnished by the above energy solutions, the following simple expressions for δ are found:

$$\delta=x_1\cdot e^{\left[-x_2\cdot\frac{L}{d}\cdot\left(\frac{E}{G_{L/2}}\right)^{-x3}\right]} \tag{2.33}$$

where the coefficients x_i depend on the imposed boundary conditions. For free-head pile, fixed-head pile and restrained soil surface, fixed-head pile and free soil surface, the equation 2.33 has the following expressions, respectively:

$$\delta = 4 \cdot e^{\left[-0.075 \cdot \frac{L}{d} \cdot \left(\frac{E}{G_{L/2}}\right)^{-\frac{1}{5}}\right]} \tag{2.33a}$$

$$\delta = 3.5 \cdot e^{\left[-0.25 \cdot \frac{L}{d} \cdot \left(\frac{E}{G_{L/2}}\right)^{-\frac{1}{3}}\right]} \tag{2.33b}$$

$$\delta = 2.2 \cdot e^{\left[-0.2 \cdot \frac{L}{d} \cdot \left(\frac{E}{G_{L/2}}\right)^{-\frac{1}{3}}\right]} \tag{2.33c}$$

Figure 2.9 reports the comparison between the numerically-derived δ and the above expressions. Also shown in the graphs are the values obtained by Randolph and Wroth's expression (i.e., assuming $\delta = 2\pi/\ln(r_m/r_0)$, r_m being the magical radius), emphasizing the need for a calibration of δ on the specific problem of the thermal load.

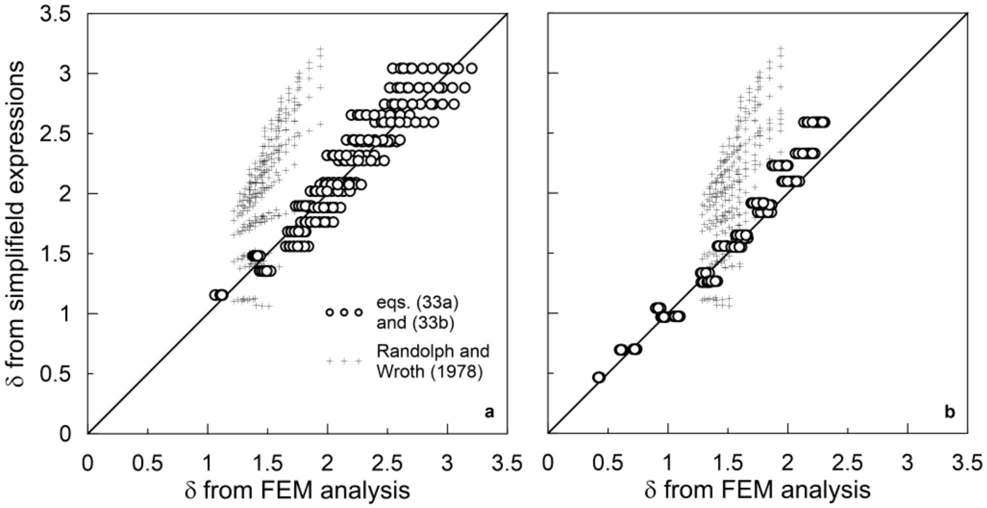

Figure 2.9. Spring stiffness calibration. FEM data, proposed equations and expression from Randolph and Wroth (1978) work, for (a) free head pile and (b) restrained-head pile.

Employing the above values for δ, the results from the energy solution are compared to the rigorous FE analyses for the case of constant stiffness and stiffness proportional to depth (Figs. 2.10 and 2.11).

The role of δ in the accuracy of the solution is instead explored in figure 2.12, with reference to values equal to half and twice the optimum value $\overline{\delta}$ from Eqs. (2.33). From such graphs, it is inferred that δ (as well as the soil shear modulus) has a major effect on the thermally-induced axial force, yet the energy solutions well reproduce numerical data when the proposed formulae for spring stiffness are employed. The prominent role of the stiffness for axially-loaded piles as opposed to the case of lateral load is due to the exponent of soil stiffness in the pile-soil wave number (= 0.5 for axial, 0.25 for lateral load).

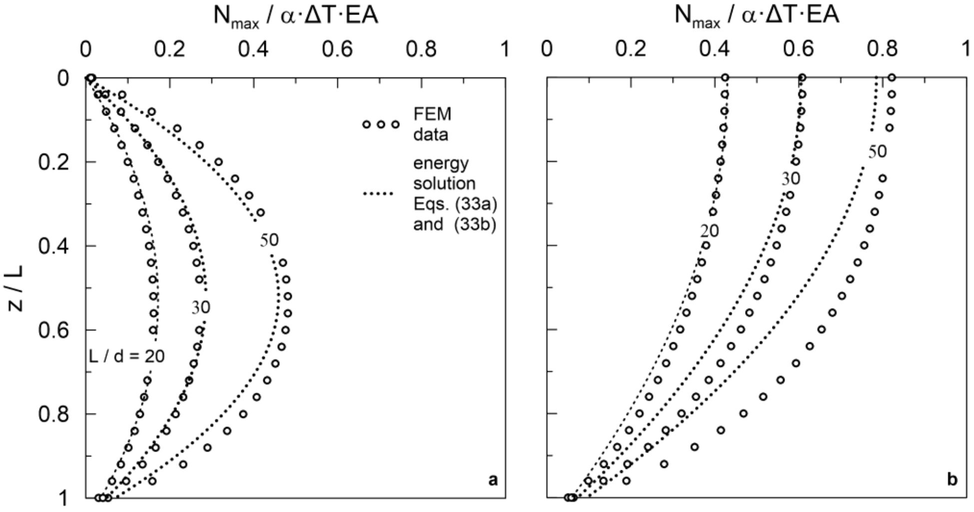

Figure 2.10. Comparison between FE and analytical energy solution for constant stiffness soil with $E/G_{L/2}$ = 1000: (a) free-head and (b) restrained-head pile.

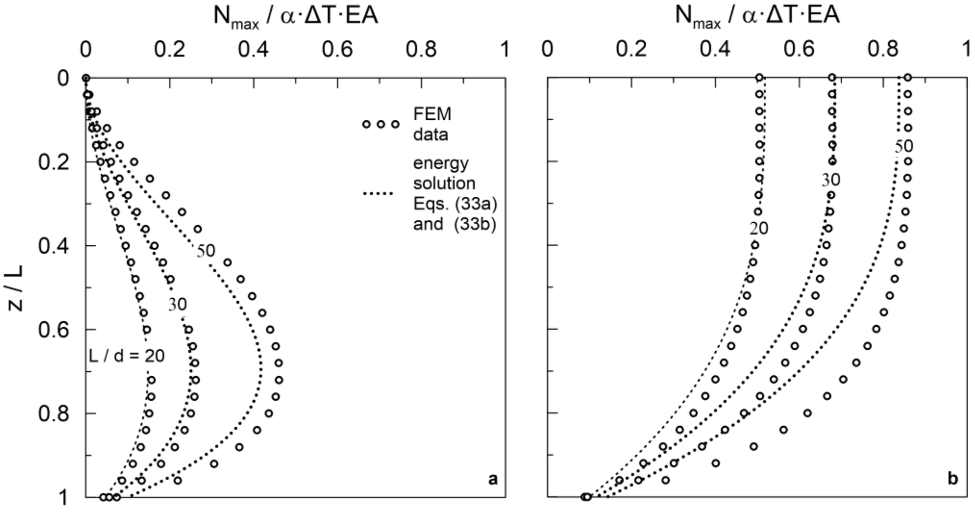

Figure 2.11. Comparison between FE and analytical energy solution for proportional stiffness soil with $E/G_{L/2}$ = 1000: (a) free-head and (b) restrained-head pile.

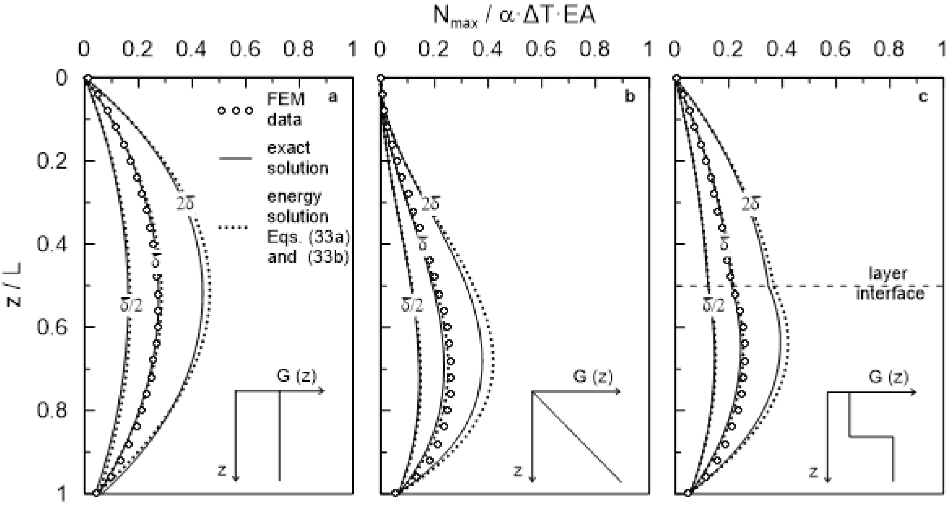

Figure 2.12. Effect of δ on the analytical solutions for free-head piles: (a) constant stiffness soil; (b) proportional stiffness soil profile; (c) two-layer soil. All the cases possess the same average soil stiffness.

2.3.3. Comparison with experimental data

The performance of the analytical solutions has been verified by comparison with field test data. Notably, two tests have been considered: one was performed at the Lambeth College of London, UK, in clay soils (Bourne-Webb et al., 2009), whereas the other one was executed in sandy soils at the EPFL of Lausanne in Switzerland (Laloui et al., 2003; Laloui et al., 2006).

The pile tested in the London clay was 23m long with a diameter of 0.61m up to 5m and of 0.55m for the remaining pile length. The London clay was surmounted by a 4 m-thick layer of Made Ground and River Terrace Deposits (Fig. 2.11). Details of the test set-up can be found in in the original paper. The pile had no restraint at its head, while the ground initial temperature was 20°C. A constant mechanical vertical load of 1200 kN was first applied. The cooling phase took place in 31 days followed by a heating phase of 12 days; the pile was cooled down to about 0°C and heated up to approximately 30°C. Finally, daily thermal cycles were also performed over 3 days' time. The temperature distribution along the pile shaft was recorded through the use of thermistors and Optical Fibre Sensors (OFS) at the end of the first cooling and heating phases. To capture both the mechanical and the thermal behaviour of the pile, OFS and Vibrating Wire Strain Gauges (VWSG) were used. The available strain data refers to measurements just after the application of the constant load of 1200 kN (solely mechanical strains) and of the first cooling and heating phases (thermo-mechanical strains). The distribution of thermal strain is obtained taking the difference between the aforementioned two profiles (Amatya et al., 2012). The axial load can be deduced using Eq. (2.3), in which the first term is the thermal strain that the pile would experience if free to displace, $\varepsilon_{\Delta T}$, and the second is the actual thermal strain developed during the loading process, ε_p (Fig. 2.13a). After the first cooling phase, since the measured data showed that in the first 4m below the ground surface the pile experienced thermal strain larger than $\varepsilon_{\Delta T}$, they have been neglected. Note that the temperature was not constant along the pile. The energy solution has been employed to reproduce the results of the first cooling phase. Due to the lack of information about the soil stiffness, data from literature have been used. In particular, according to Vardanega and Bolton (2011), the clay shear modulus at low strain has been considered to vary proportionally to the undrained shear strength s_u, $G(z) = 320.7\ s_u$. For pile stiffness and soil strength parameters, reference is made to Amatya et al. (2012). The pile diameter has been considered to be 0.55m for all the pile length. A value of δ equal to 2 has been derived from Eq. (2.33a). Figure 2.11b depicts the prediction of the analytical solution as compared to the measurements of the OFS. It can be noticed that the simple proposed approach is capable of capturing the overall behaviour of the pile under thermal load.

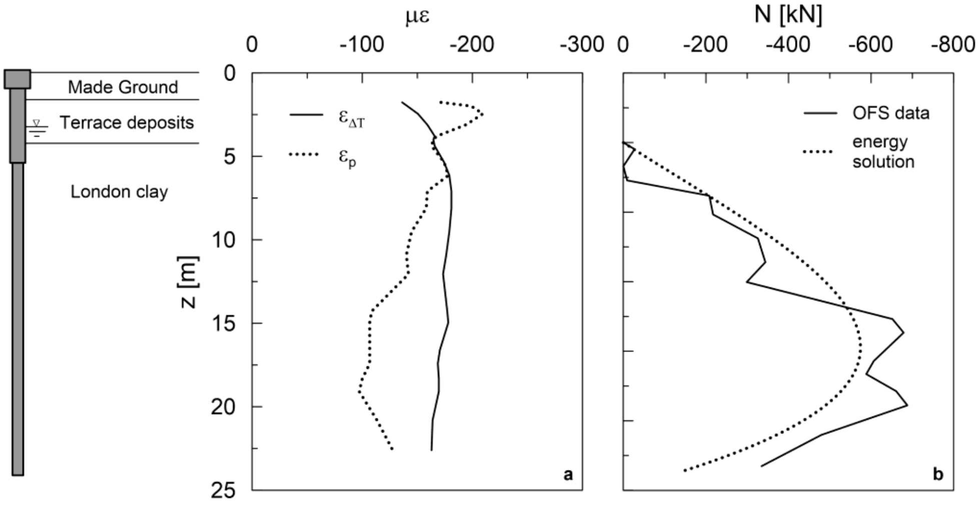

Figure 2.13. The Lambeth College test: (a) comparison between free and thermal strain at the end of the first cooling phase, OFS data; (b) comparison between field data and energy solution.

The tests performed at the EPFL involved a building under construction founded on a piled raft foundation in which one pile, equipped with heat exchanger pipes, underwent a series of thermo-mechanical tests. The pile group was installed in a multi-layer soil composed of 5 different strata of sandy deposits (Fig. 2.14). Pile length and average diameter were 25.8m and 1.05m respectively. Further details are reported in the original work. Reference is made here to test number 7 in which the temperature of the pile was increased up to 13.4°C. The tested pile was fully instrumented with optical fibres and extensometers. The thermal loads were applied in presence of a mechanical load of about 1300 kN; the pile head was restrained by the presence of the building connected to other piles. A heating process over 12 days followed by 16 days of passive cooling was applied. To consider the degree of restraint at pile head, the proposed energy solution has been applied considering two extreme cases: free- and restrained-head pile. The values of δ derived from Eqs. (2.33a) and (2.33b) are 2.45 and 1.75 respectively. The shear modulus has been evaluated form the bulk modulus data reported by the authors using a Poisson's ratio of 0.3. The results have been compared to the field data and to the data obtained by a fully coupled thermo-hydro-mechanical analysis (Laloui et al., 2006) through a FE software (Fig. 2.14). Despite its simplicity, the energy approach has proven to be effective, since experimental data place in the middle between the free- and restrained-head conditions. Note that the simple analytical results are very close to the complex FE results.

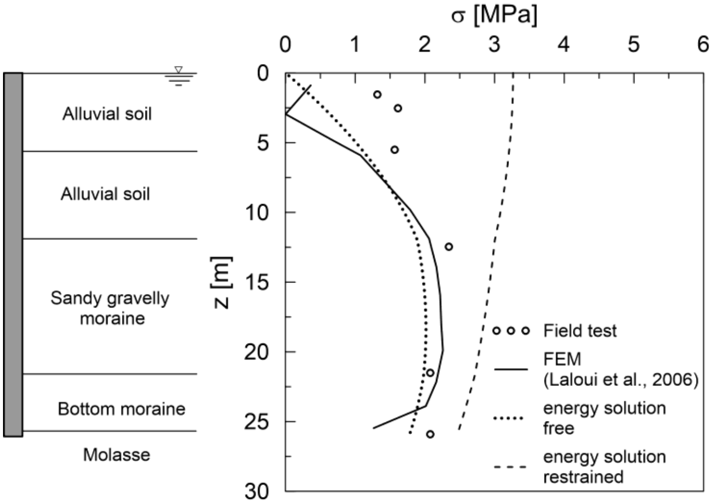

Figure 2.14. The Lausanne test: comparison between field data and results from numerical and analytical solution.

3.Constitutive modelling

In Chapter 2 the analytical approach has been used for the evaluation of the thermally-induced axial load. On one hand, exact solutions are provided for idealized soil profiles. On the other hand, simpler approximate solutions, applicable to any multilayer soil, are derived. While the first kind of solutions, being exact, may be used by researchers to validate future more complex models (like non-linear springs with p-y curves), the latter type of solutions is expected to be utilized by practitioners to get a first-order value of the thermally-induced axial force to be considered in ULS checks. Nevertheless, since the proposed solutions relies upon an equivalent linear approach, it is not possible to catch the cyclic behaviour especially in terms of accumulated displacements. To this end, numerical analyses employing advanced constitutive models have been carried out to investigate the effects of the thermal cycles on the global performance of a single energy pile subjected to mechanical and cyclic thermal loads.

The classical elasto-plastic models are developed in the frame of the perfect or hardening plasticity theory and are able to describe the non-linear and irreversible behaviour of soil in monotonic loading conditions. Nevertheless, they are not capable of properly describing the accumulation of irreversible strain and pore water pressures caused by cyclic loading and have some limitations in providing memory of the previous loading history.

In recent years, in order to improve the predictive capabilities of the conventional constitutive models, new approaches have been developed. Among these, the kinematic hardening and the Bounding Surface plasticity theories are based on a generalization of the classical plasticity theory. In the kinematic hardening plasticity, the yield surface is a function of the stress state, of the scalar internal state variables and of the back stress tensor. The back stress evolution is responsible of the translation of the yield surface. This movement is limited by an external Bounding Surface similar in shape to the yield surface, that separates the possible from the impossible stress states. In the Bounding Surface plasticity, the Bounding Surface is subjected to hardening as the yield surface in the plasticity theory but, in contrast, there is no elastic region and irreversible strains can occur for stress states inside it.

An alternative approach consists in the use of the Hypoplastic theory with internal state variables formulated as an extension of the Hypoelastic theory, whose main features are the absence of the kinematic decomposition of strain and the incremental non-linearity.

In the present work, the Mohr Coulomb, the Modified Cam-Clay and the Hypoplastic models for clay have been chosen to describe the soil behaviour. The first two models are developed in the framework of the classical plasticity, i.e. perfect plasticity and hardening plasticity theories, respectively. The convenience of using the Hypoplastic model is related to two main reasons. The mathematical formulation of the model is accessible on the website www.soilmodels.com in a validated version ready to be used in the ABAQUS code; given that the scope of the present work was not the implementation of a constitutive model and that the software available for the FE analyses was ABAQUS, these features were considered for the selection of the model as a priority. Moreover, the model can be simply enhanced with the thermal formulation, capable of reproducing the NC clay behaviour described in Chapter 1, by modifying the available isothermal version. Finally, as a simple reference model, the Linear Elastic model, has also been used.

The comparison of the results obtained employing the different models aims at highlighting that the use of advanced constitutive models in the case of cyclic loading and NC clay is the only option to qualitatively reproduce the behaviour observed via experiments. Indeed, while in the case of monotonic thermal loading the use of simpler constitutive models with effective moduli allows realistic estimations of the observed behaviour, in cyclic loading it is needed to employ more sophisticated models.

In the following, the structure of the constitutive models used is reported (where not specified, the stresses are considered as effective in terms of the Terzaghi principle, Terzaghi, 1923).

In the last section, the thermo-hydro-mechanical formulation for porous media is presented.

3.1.Elasticity

In the Linear Elastic model, the total stress, $\boldsymbol{\sigma}$, is defined from the total elastic strain, $\boldsymbol{\varepsilon}_e$, according to the following relation:

$$\boldsymbol{\sigma} = \boldsymbol{D}_e \boldsymbol{\varepsilon}_e \tag{3.1}$$

where $\boldsymbol{D}_e$ is the fourth-order elasticity tensor. The simplest way to define the linear elastic behaviour is the isotropic case, in which the elastic properties of the elastic tensor are completely defined by the Young’s modulus E and the Poisson’s ratio ν.

In the FE analyses, the isotropic Linear Elastic model has been used; in the following it will be referred with the label E.

3.2. Theory of plasticity

The classical theory of plasticity (Zienkiewicz et al., 1999) is based on the hypothesis of kinematic decomposition of the strain rate tensor in an elastic reversible part, $\dot{\boldsymbol{\varepsilon}}_e$, plus a plastic irreversible one, $\dot{\boldsymbol{\varepsilon}}_p$:

$$\dot{\boldsymbol{\varepsilon}} = \dot{\boldsymbol{\varepsilon}}_e + \dot{\boldsymbol{\varepsilon}}_p \tag{3.2}$$

The tension rate, $\dot{\boldsymbol{\sigma}}$, is related to the elastic strain rate through the use of the elastic tangent stiffness, $\boldsymbol{D}_e$, that is a fourth-order tensor function of the current stress state:

$$\dot{\boldsymbol{\sigma}} = \boldsymbol{D}_e(\sigma)\dot{\boldsymbol{\varepsilon}}_e = \boldsymbol{D}_e(\sigma)\left(\dot{\boldsymbol{\varepsilon}} - \dot{\boldsymbol{\varepsilon}}_p\right) \tag{3.3}$$

The elastic domain is defined using the yield surface $f(\boldsymbol{\sigma},\boldsymbol{q})$, $\boldsymbol{q}$ being the vector of the state variable. The irreversibility of the mechanical response is taken into account by imposing that the state of the point $(\boldsymbol{\sigma},\boldsymbol{q})$ belongs to the convex region:

$$\mathbb{C}_\sigma := \left\{(\boldsymbol{\sigma},\boldsymbol{q}) \mid f(\boldsymbol{\sigma},\boldsymbol{q}) \le 0\right\} \tag{3.4}$$

The evolution of the plastic strain rate can be expressed via the following flow rule:

$$\dot{\boldsymbol{\varepsilon}}_p = \dot{\gamma}\frac{\partial g}{\partial \boldsymbol{\sigma}}(\boldsymbol{\sigma},\boldsymbol{q}) \tag{3.5}$$

where $g(\boldsymbol{\sigma},\boldsymbol{q})$ is the plastic potential and $\dot{\gamma}$ is the plastic multiplayer. The hardening law defines the evolution of the internal state variables:

$$\dot{\boldsymbol{q}} = \dot{\gamma}\boldsymbol{h}(\boldsymbol{\sigma},\boldsymbol{q}) \tag{3.6}$$

where $\boldsymbol{h}(\boldsymbol{\sigma},\boldsymbol{q})$ is a given function. The plastic multiplayer $\dot{\gamma}$ must satisfy the Kuhn-Tucker conditions:

$$\dot{\gamma} \ge 0, \qquad f(\boldsymbol{\sigma},\boldsymbol{q}) \le 0, \qquad \dot{\gamma} f(\boldsymbol{\sigma},\boldsymbol{q}) = 0 \tag{3.7}$$

These conditions assure that the plastic strain are allowed solely for stress state on the yield surface. The plastic multiplayer is obtained from the consistency condition $\dot{\gamma} f(\boldsymbol{\sigma},\boldsymbol{q}) = 0$ and from Eqs. (3.3) and (3.5) as follows:

$$\dot{\gamma} = \frac{1}{k_p}\left\langle \frac{\partial f}{\partial \boldsymbol{\sigma}} \cdot \boldsymbol{D}_e \dot{\boldsymbol{\varepsilon}}_e \right\rangle \tag{3.8}$$

where $\langle \ \rangle$ are the Macaulay brackets, the symbol " $\cdot$ " indicates the inner product and k_p is:

$$k_p := \frac{\partial f}{\partial \boldsymbol{\sigma}} \cdot \boldsymbol{D}_e \frac{\partial g}{\partial \boldsymbol{\sigma}} + H_p \geq 0 \tag{3.9}$$

being $H_p(\boldsymbol{\sigma},\boldsymbol{q})$ the scalar function defined as the hardening modulus:

$$H_p := -\frac{\partial f}{\partial \boldsymbol{q}} \cdot \boldsymbol{h} \tag{3.10}$$

The hardening of the material is associated to positive value of H_p; negative values of the hardening modulus means softening, while $H_p = 0$ represent the case of perfect plasticity.

Using Eqs. (3.3), (3.5) and (3.8) it follows:

$$\dot{\boldsymbol{\sigma}} = \boldsymbol{D}_{ep} \dot{\boldsymbol{\varepsilon}} \tag{3.11}$$

where:

$$\boldsymbol{D}_{ep} := \boldsymbol{D}_e - \frac{h(\dot{\gamma})}{k_p} \left(\boldsymbol{D}_e \frac{\partial g}{\partial \boldsymbol{\sigma}} \right) \otimes \left(\frac{\partial f}{\partial \boldsymbol{\sigma}} \boldsymbol{D}_e \right) \tag{3.12}$$

the symbol "$\otimes$" indicates the dyadic product of the two tensors; $h(\dot{\gamma})$ is the Heaviside function, equal to 1 if $\dot{\gamma} \geq 0$ and to 0 in the other cases.

It is possible to define the unit tensors $\boldsymbol{n}$ and $\boldsymbol{n}_g$ that are the unit normal to the yield surface and to the plastic flow, respectively:

$$\boldsymbol{n} := \left\| \frac{\partial f}{\partial \boldsymbol{\sigma}} \right\|^{-1} \frac{\partial f}{\partial \boldsymbol{\sigma}} \tag{3.13}$$

$$\boldsymbol{n}_{\mathrm{g}} := \left\| \frac{\partial g}{\partial \boldsymbol{\sigma}} \right\|^{-1} \frac{\partial g}{\partial \boldsymbol{\sigma}} \tag{3.14}$$

It follows that Eqs. (3.5), (3.8) and (3.12) can be written as follows:

$$\dot{\boldsymbol{\varepsilon}}_{\mathrm{p}} = \dot{\lambda} \boldsymbol{n}_{\mathrm{g}} \tag{3.15}$$

$$\dot{\lambda} = \frac{1}{\hat{k}_p} \langle \boldsymbol{n} \cdot \boldsymbol{D}_e \dot{\boldsymbol{\varepsilon}} \rangle \tag{3.16}$$

$$\boldsymbol{D}_{ep} := \boldsymbol{D}_e - \frac{h(\dot{\lambda})}{\hat{k}_p} \left(\boldsymbol{D}_e \boldsymbol{n}_{\mathrm{g}} \right) \otimes \left(\boldsymbol{n} \boldsymbol{D}_e \right) \tag{3.17}$$

where:

$$\hat{k}_p := \boldsymbol{n} \cdot \boldsymbol{D}_e \boldsymbol{n}_g + \hat{H}_p \tag{3.18}$$

$$\hat{H}_p := \left(\left\| \frac{\partial f}{\partial \boldsymbol{\sigma}} \right\| \left\| \frac{\partial g}{\partial \boldsymbol{\sigma}} \right\| \right)^{-1} H_p \tag{3.19}$$

According to the plastic multiplayer (Eqs. (3.8) and (3.16)) the switch between elastic and plastic behaviour is regulated by the sign of the inner product $\boldsymbol{n} \cdot \boldsymbol{D}_e \dot{\boldsymbol{\varepsilon}}$.

The classical plasticity theory assumes a wide elastic region inside which the strains are completely reversible. All the stress states inside the yield surface are characterized by elastic strains until the loading path approaches the yield surface. The development of irreversible plastic strains is allowed solely for stress states on the yield envelope.

In the following, the Mohr-Coulomb and the Modified Cam-Clay equations used by the FE code ABAQUS are reported.

3.2.1. Mohr-Coulomb model

The Mohr-Coulomb model is an elastic perfectly plastic model developed in the framework of the plasticity theory. The elastic part of the model is described via the Eq. (3.1); in the analyses, isotropic linear elasticity is assumed. The yield surface is based on the shear criterion known as the Mohr-Coulomb yield criterion; for a general 3D stress state it can be written in terms of the three stress invariants (p, q, θ) as follows:

$$F = R_{mc} q - p' \tan \varphi - c = 0 \tag{3.20}$$

where R_{mc} is a function of the Lode angle and of the friction angle; p' is the mean effective stress; q is the deviatoric stress; c is the cohesion of the material; φ is the friction angle of the material, controlling the shape of the yield surface in the deviatoric plane. In the space of the principal stresses, the deviatoric plane is perpendicular to the hydrostatic axis; on this plane, the projections of the three principal axes are at an angle of 120° between each other and the mean effective stress is constant. R_{mc}, p' and q can be expressed as follows:

$$R_{mc}(\theta, \varphi) = \frac{1}{\sqrt{3} \cos \varphi} \sin\left(\theta + \frac{\pi}{3}\right) + \frac{1}{3} \cos\left(\theta + \frac{\pi}{3}\right) \tan \varphi \tag{3.21}$$

$$q = \sqrt{\frac{3}{2}} \|\boldsymbol{s}\| \tag{3.22}$$

$$p' = \frac{1}{3} \operatorname{tr}(\boldsymbol{\sigma}) \tag{3.23}$$

In Eq. (3.21) θ is the Lode angle, while in Eq. (3.22) ***s*** is the deviatoric stress tensor. They are defined as follows:

$$\cos(3\theta)=\left(\frac{r}{q}\right)^3 \tag{3.24}$$

$$\boldsymbol{s}=\boldsymbol{\sigma}-p'\mathbf{1} \tag{3.25}$$

where r is the third invariant of the deviatoric stress tensor and **1** is the second-order identity tensor. r is defined as:

$$r^3=\frac{9}{2}\mathrm{tr}\left(\boldsymbol{s}^3\right) \tag{3.26}$$

The plastic potential is described with the following hyperbolic function:

$$G_m=\sqrt{\left(\varepsilon c|_0\tan\psi\right)^2+\left(R_{mw}q\right)^2}-p\tan\psi \tag{3.27}$$

where ε defines the rate at which the asymptote is approached by the plastic potential function; $c|_0$ is the initial cohesion yield stress; ψ is the dilation angle; R_{mw} is a function of the Lode angle and of the friction angle and it is expressed as follows:

$$R_{mw}\left(\theta,\bar{e}\right)=\frac{4\left(1-\bar{e}^2\right)\cos^2\theta+\left(2\bar{e}-1\right)^2}{2\left(1-\bar{e}^2\right)\cos\theta+\left(2\bar{e}-1\right)\sqrt{4\left(1-\bar{e}^2\right)\cos^2\theta+5\bar{e}^2-4\bar{e}}}R_{mc}\left(\frac{\pi}{3},\varphi\right) \tag{3.28}$$

where:

$$\bar{e}=\frac{3-\sin\varphi}{3+\sin\varphi} \tag{3.29}$$

is the deviatoric eccentricity;

$$R_{mc}\left(\frac{\pi}{3},\varphi\right)=\frac{3-\sin\varphi}{6\cos\varphi} \tag{3.30}$$

The plastic potential is continuous and smooth and ensures that the flow direction is always uniquely defined.

In the following, the Mohr-Coulomb model will be referred with the label MC.

3.2.2. Modified Cam-Clay model

The Modified Cam-Clay model (Roscoe and Burland, 1968) is based on the hardening plasticity theory and is developed in the framework of the Critical State Soil Mechanics (Roscoe et al., 1958; Schofield and Wroth, 1968).

Reference is made to the (1+e)-ln$p$' plane, where e is the void ratio (Fig. 3.1).

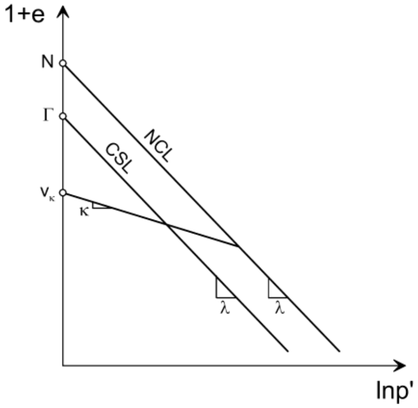

Figure 3.1. (1+*e*)-ln*p*' plane.

In figure 3.1 the normal consolidation line (NCL) is represented along with the unloading-reloading lines and the critical state line (CSL). The NCL is the representation of the yield surface for q=0 on the (1+e)-ln$p$' plane; it has the following expression:

$$1+e=\mathrm{N}-\lambda\ln\left(\frac{p'}{p'_{ref}}\right) \tag{3.31}$$

where N is the value of (1+e) at a mean effective stress equal to the reference pressure p'_{ref} (1kPa) and λ is the slope of the NCL (swelling index). If the initial state of a sample lies on the NCL, the soil is normally consolidated (NC) otherwise it is overconsolidated (OC). It is possible to define the overconsolidation ratio as follows:

$$OCR=\frac{p'_c}{p'_0} \tag{3.32}$$

where p'_c is the preconsolidation pressure, i.e. the maximum mean effective stress the soil has experienced during its past history, and p'_0 is the initial stress state of the soil. NC samples are characterized by OCR=1, while OC soils by OCR>1.

If the soil is OC the initial state of the soil lies on the unloading-reloading line that governs the behaviour inside the yield surface, assumed to be elastic; its expression is:

$$1+e=v_k-\kappa\ln\left(\frac{p'}{p'_{ref}}\right) \tag{3.33}$$

where v_κ is the value of (1+e) on the specific unloading-reloading line at a mean effective stress equal to the reference pressure p'_{ref} and κ is the slope of the unloading-reloading line (compression index).

The final state of the sample is on the CSL for which the deviatoric stress and the volumetric strain remain constant with increasing the axial strain (critical state). The CSL is a straight line in the (1+*e*)-ln*p*' and *q*-*p*' planes; its expressions are:

$$\left(1+e\right)_f = \Gamma - \lambda \ln\left(\frac{p'}{p'_{ref}}\right) \tag{3.34}$$

$$q_f = M p'_f \tag{3.35}$$

where the subscript f indicates the final state of the sample, Γ is the value of (1+*e*) at a mean effective stress equal to the reference pressure p'_{ref}; M is the slope of the CSL in the *q*-*p*' plane and it is a function of the friction angle at the critical state φ_c according to the following expression:

$$M = \frac{6\sin\varphi_c}{3+\sin\varphi_c} \tag{3.36}$$

In the FE code ABAQUS the elasto-plastic and the hardening behaviour are characterized as follow.

As concerns the elastic response, it is modelled by assuming that the elastic part of the change in volume of the material is proportional to the logarithm of the mean effective stress via the following relation:

$$\frac{\kappa}{1+e_0}\ln\left(\frac{p'_0+p'^{el}_t}{p'+p'^{el}_t}\right) = J^{el} - 1 \tag{3.37}$$

where e_0 is the initial void ratio; p'^{el}_t is the elastic tensile strength of the material; J^{el} is the elastic part of the volume ratio between the current and the reference configurations.

The shear modulus can be derived specifying the value of the Poisson's ratio:

$$G = \frac{3\left(1-2\nu\right)\left(1+e_0\right)}{2\left(1+\nu\right)\kappa}\left(p'+p'^{el}_t\right)J^{el} \tag{3.38}$$

The yield surface is a function of the three stress invariants as follows:

$$\frac{1}{\beta^2}\left(\frac{p'}{a_y}-1\right)^2 + \left(\frac{t}{M a_y}\right)^2 - 1 = 0 \tag{3.39}$$

where β is a constant whose value depends from the dry and the wet side of the critical state line; a_y is the size of the yield surface; t is expressed as follows:

$$t = \frac{1}{2} q \left(1 + \frac{1}{K} + \left(1 - \frac{1}{K} \right) \cos 3\theta \right) \tag{3.40}$$

where K is the ratio of the flow stress in triaxial tension to the flow stress in triaxial compression; a value of K between 0.79 and 1 is required.

The plastic strain rate is defined via an associated flow rule.

The size of the yield surface can change according to the following exponential hardening law:

$$a_y = a_{y0} \exp\left[\left(1 + e_0\right) \frac{1 - J^{pl}}{\lambda - \kappa J^{pl}} \right] \tag{3.41}$$

where a_{y0} is the initial size of the yield surface; J^{pl} is the inelastic volume change.

In the following, the Modified Cam-Clay model will be referred with the label MCC.

3.3.Advanced constitutive models

In recent years a new approach to the constitutive modelling has been proposed as a generalization of the hypoelasticity theory by Truesdall (1956). Unlike the elasto-plasticity (i) there is no kinematic decomposition of the strains and (ii) the tangent stiffness tensor is continuously dependent on the direction of the strain increment, i.e. the Hypoplastic models are incrementally non-linear. The most general form of the constitutive equation can be derived from the incrementally non-linear model of the second order.

The theory of hypoplasticity is referred to a special class of incrementally non-linear models developed by Kolymbas (1991). The rate form of the constitutive equation in full tensorial notation has the following expression:

$$\dot{\boldsymbol{T}} = \mathscr{L} : \boldsymbol{D} + \boldsymbol{N} \left\| \boldsymbol{D} \right\| \tag{3.42}$$

where the symbol “:” indicates the inner product with double contraction, $\dot{\boldsymbol{T}}$ is the objective stress rate, $\mathscr{L}$ is a fourth-order tensor, $\boldsymbol{N}$ is a symmetric second-order tensor both function of the current state of the material, and $\boldsymbol{D}$ is the Euler’s stretching tensor. The non-linearity is accounted via the scalar quantity $||\boldsymbol{D}||$.

To have a geometric representation of the property of the constitutive equation in rate form, it is possible to use the stress response envelope (SRE) by Gudehus (1979). The SRE can be defined as the image in the stress rate space of a unit sphere in the strain rate space, derived via the Eq. (3.42). In the case of triaxial conditions, the SRE can be plotted in the $\dot{\sigma}_a$ - $\sqrt{2}\dot{\sigma}_r$ plane (the Rendulic plane), where σ_a and σ_r are the principal axial and radial component of the stress, respectively. In figure 3.2 the

SRE for a hypoplastic material is reported. The unit circle in the $\dot{\varepsilon}_a$ - $\sqrt{2}\dot{\varepsilon}_r$ plane (Fig. 2.3a) become an ellipse in the Rendulic plane, not centered in the origin (Fig. 2.3c). This can be explained considering that the effect of the linear operator $\mathscr{L}$ is to transform the unit circle in the ellipse centered at the origin of the stress rate plane, while the non-linear $\boldsymbol{N}\|\boldsymbol{D}\|$ part causes the translation of the ellipse in a direction defined by $\boldsymbol{N}$. Therefore, in the final configuration the SRE is not symmetric with respect to the axis origin. This non-symmetry is the graphic representation of the incremental non-linearity.

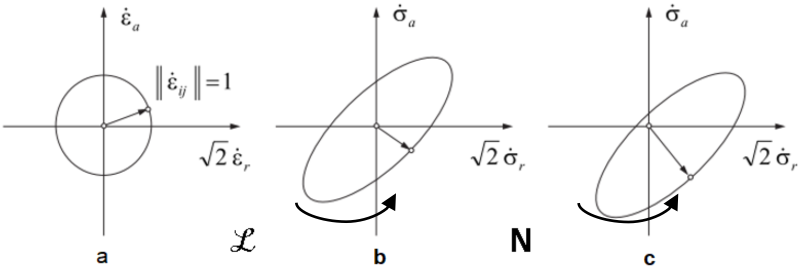

Figure 3.2. Graphical representation of the hypoplastic constitutive equation adapted after Tamagnini and Viggiani (2002): (a) unit circle in the strain rate space; (b) effect of the linear term; (c) effect of the non-linear term.

3.3.1. Hypoplastic model for clays

The hypoplastic model for clays (Mašín, 2005, 2013 and 2014) is an advanced incrementally non-linear constitutive model based on the Critical State Soil Mechanics developed specifically for fine-grained soils. The model by Mašín (2013) is presented herein.

The constitutive equation (3.42) has the expression proposed by Gudehus (1996):

$$\dot{\boldsymbol{T}} = f_s\left(\mathscr{L} : \boldsymbol{D} + f_d \boldsymbol{N}\left\|\boldsymbol{D}\right\|\right) \tag{3.43}$$

where f_s and f_d are the barotropy and picnotropy factors controlling the influence of the mean stress and of the relative density, respectively.

The asymptotic state boundary surface is incorporated in the model assuming that it changes in size with variable void ratios but not in shape. The NCL is considered as a straight line in the ln(1+e)-ln p' plane; therefore, its expression is:

$$\ln\left(1+e\right) = \mathrm{N}^* - \lambda^* \ln\left(\frac{p'}{p'_{ref}}\right) \tag{3.44}$$

where N^* is the value of ln(1+e) at a mean effective stress equal to the reference pressure p'_{ref} (assumed equal to1kPa) and λ^* is the slope of the NCL.

The Hvorslev's equivalent pressure, p'_e, that measures the size of the asymptotic state boundary surface, is expressed as follows:

$$p'_e = p'_{ref} \exp\left[\frac{\mathrm{N}^* - \ln(1+e)}{\lambda^*}\right] \tag{3.45}$$

Considering that the asymptotic state boundary surface doesn't change in shape during a proportional asymptotic loading, it follows that the stress tensor $\boldsymbol{T}$ normalized by p'_e remains constant. Therefore, it is possible to derive an alternative expression for the hypoplastic model:

$$\dot{\boldsymbol{T}} = f_s \mathscr{L} : \boldsymbol{D} - \frac{f_d}{f_d^A} \mathscr{A} : \boldsymbol{d} \|\boldsymbol{D}\| \tag{3.46}$$

where:

$$\boldsymbol{N} = -\frac{\mathscr{A} : \boldsymbol{d}}{f_s f_d^A} \tag{3.47}$$

$$\mathscr{A} = f_s \mathscr{L} + \frac{\boldsymbol{T}}{\lambda^*} \otimes \mathbf{1} \tag{3.48}$$

f_d^A is the value of f_d at the asymptotic state boundary surface; $\boldsymbol{d}$ is the asymptotic direction of the strain rate.

The model components to define are: $\mathscr{L}$, f_s, f_d, f_d^A, $\boldsymbol{d}$.

The tensor $\mathscr{L}$ is expressed as a function of the parameter ν regulation the shear stiffness:

$$\mathscr{L} = \boldsymbol{I} + \frac{\nu}{1+2\nu} \mathbf{1} \otimes \mathbf{1} \tag{3.49}$$

The barotropy factor, f_s, is expressed via the following equation:

$$f_s = \frac{3p'}{2}\left(\frac{1}{\lambda^*} + \frac{1}{\kappa^*}\right)\frac{1-2\nu}{1+\nu} \tag{3.50}$$

κ^* is the slope of the unloading-reloading line in the $\ln(1+e)$-$\ln p'$ plane.

For the picotropy factor, f_d, the following relation holds:

$$f_d = \left(O_c \frac{p'}{p'_e}\right)^{\alpha_f} = \left(\frac{O_c}{OCR}\right)^{\alpha_f} \tag{3.51}$$

OCR is the overconsolidation ratio defined from the Hvorslev's equivalent pressure:

$$OCR = \frac{p'_e}{p'} \tag{3.52}$$

O_c controls the position of the critical state line in the ln(1+e)-lnp' plane with respect to the isotropic NCL and, thus, is the value of *OCR* at the critical state; its value is fixed to 2.

α_f controls the irreversibility of the deformation inside the asymptotic state boundary surface; it is expressed as follows:

$$\alpha_f = \frac{\ln\left[\frac{\lambda^* - \kappa^*}{\lambda^* + \kappa^*}\left(\frac{3 + a_f^2}{a_f\sqrt{3}}\right)\right]}{\ln O_c} \tag{3.53}$$

κ^* being the slope of the unloading-reloading line in the ln(1+e)-lnp' plane; a_f is given from the following relation:

$$a_f = \frac{\sqrt{3}\left(3 - \sin\varphi_c\right)}{2\sqrt{2}\sin\varphi_c} \tag{3.54}$$

f_d^A is calculated as follows:

$$f_d^A = \left(O_c\right)^{\alpha_f}\left(1 - F_m\right)^{\alpha_f/\omega} \tag{3.55}$$

where F_m is the Matsuoa-Nakai factor that is equivalent to the mobilized friction angle, φ_m, corresponding to the Matsuoa-Nakai failure criterion:

$$F_m = \frac{9I_3 + I_1 I_2}{I_3 + I_1 I_2} \tag{3.56}$$

where the stress invariants are:

$$I_1 = \mathrm{tr}\boldsymbol{T} \tag{3.57}$$

$$I_2 = \frac{1}{2}\mathrm{tr}\left[\boldsymbol{T} : \boldsymbol{T} - \left(I_1\right)^2\right] \tag{3.58}$$

$$I_3 = \det \mathbf{T} \tag{3.59}$$

ω is expressed as follows:

$$\omega = -\frac{\ln\left(\cos\varphi_c\right)}{\ln O_c} + a_{y1}\left(F_m - \sin^2\varphi_c\right) \tag{3.60}$$

with a_{y1} being a model parameter controlling the shape of the asymptotic state boundary surface; a fixed value equal to 0.3 can be used.

In summary, the hypoplastic model for clays requires the calibration of the 5 parameters: φ_c, N^*, λ^*, κ^* and ν.

The basic hypoplastic model is capable of predicting non-linear soil behaviour in both loading and unloading. Nevertheless, it is incapable of predicting very small strain stiffness and the effects of the recent history; moreover, in cyclic loading condition, since the response of each cycle is equal to that of the first cycle, ratcheting is predicted. To include these two effects and the response to cyclic loading, the hypoplastic models can be enhanced with the intergranular strain concept. At the beginning of the loading process, it is assumed that there is no rearrangement of the grain and that the deformation of the soil is due to the elastic deformation of the skeleton plus the reversible deformation of the intergranular strain layer. The grains rearrangement takes place after the development of a certain amount of strain and is irreversible. In the approach proposed by Niemunis and Herle (1997) the intergranular strain is a second-order symmetric tensor, $\boldsymbol{\delta}$; the rate form is given by the following equation:

$$\dot{\delta} := \begin{cases} \left(\boldsymbol{I} - \vec{\delta} \otimes \vec{\delta}\,\bar{\rho}^{\beta_r}\right) : \boldsymbol{D} & \text{for } \vec{\delta} : \boldsymbol{D} > 0 \\ \boldsymbol{D} & \text{for } \vec{\delta} : \boldsymbol{D} \leq 0 \end{cases} \tag{3.61}$$

where $\boldsymbol{I}$ is the fourth-order unit tensor; $\vec{\boldsymbol{\delta}}$ and $\bar{\rho}$ are the direction and the normalized magnitude of the intergranular strain tensor, respectively; β_r is a model parameter controlling the rate of the intergranular strain evolution and, therefore, the stiffness degradation curve. $\vec{\boldsymbol{\delta}}$ and $\bar{\rho}$ are defined as follows:

$$\vec{\delta} := \begin{cases} \dfrac{\delta}{\|\delta\|} & \text{for } \delta \neq 0 \\ 0 & \text{for } \delta = 0 \end{cases} \tag{3.62}$$

$$\rho := \frac{\delta}{\|R\|} \tag{3.63}$$

where R is a model parameter indicating the maximum value of the intergranular strain.

Eq. (3.42) can be written as follows:

$$\dot{\boldsymbol{T}} = \mathscr{M} : \boldsymbol{D} \tag{3.64}$$

where $\mathscr{M}$ is the forth-order tangent stiffness tensor of the material. It is expressed as follows:

$$\mathcal{M} = \left[\rho^{\chi} m_T + \left(1-\rho^{\chi}\right) m_R\right]\mathcal{L} + \begin{cases} \rho^{\chi}\left(1-m_T\right)\mathcal{L}:\vec{\boldsymbol{\delta}}\otimes\vec{\boldsymbol{\delta}} + \rho^{\chi}\boldsymbol{N}\otimes\vec{\boldsymbol{\delta}} & \text{for}\,\vec{\boldsymbol{\delta}}:\boldsymbol{D}>0 \\ \rho^{\chi}\left(m_R-m_T\right)\mathcal{L}:\vec{\boldsymbol{\delta}}\otimes\vec{\boldsymbol{\delta}} & \text{for}\,\vec{\boldsymbol{\delta}}:\boldsymbol{D}\leq 0 \end{cases} \tag{3.65}$$

where m_T, m_R and χ are additional model parameters. χ controls the interpolation between the reversible elastic and the non-linear hypoplastic response.

The intergranular strain concept has been modified by Wegener and Herle (2014). They found that the original intergranular strain formulation overpredicted the accumulation of the strains and excess pore water pressures during drained and undrained cyclic loading, respectively. To overcame this problem, they introduced a new model parameter, ϑ, to replace the exponent χ in the non-linear part of the hypoplastic equation. Thus, the Eq. (3.65) reads:

$$\mathcal{M} = \left[\rho^{\chi} m_T + \left(1-\rho^{\chi}\right) m_R\right]\mathcal{L} + \begin{cases} \rho^{\chi}\left(1-m_T\right)\mathcal{L}:\vec{\boldsymbol{\delta}}\otimes\vec{\boldsymbol{\delta}} + \rho^{\vartheta}\boldsymbol{N}\otimes\vec{\boldsymbol{\delta}} & \text{for}\,\vec{\boldsymbol{\delta}}:\boldsymbol{D}>0 \\ \rho^{\chi}\left(m_R-m_T\right)\mathcal{L}:\vec{\boldsymbol{\delta}}\otimes\vec{\boldsymbol{\delta}} & \text{for}\,\vec{\boldsymbol{\delta}}:\boldsymbol{D}\leq 0 \end{cases} \tag{3.66}$$

Increasing the value of ϑ respect to χ allow to reduce the cyclic accumulation that is ruled by the non-linear part of the hypoplastic equation.

Mašín (2014) proposed another modification. With equation (3.66) the dependency of the stiffness from the stress state cannot directly be controlled by the user of the model via a parameter. To include this dependency, it is possible to back-calculate m_R from A_g and n_g, taken from a non-linear small strain stiffness distribution, G_0, in accordance with experimental data for clay:

$$G_0 = p'_r A_g \left(\frac{p}{p_r}\right)^{n_g} \tag{3.67}$$

where p'_r is the reference stress (often considered equal to 1kPa), and A_g and n_g are parameters. Moreover, it convenient calculate m_T as follows:

$$m_T = m_{rat} m_R \tag{3.68}$$

where m_{rat} is a new model parameter representing the ratio between the initial shear stiffness after a 90° change in the strain path direction, G_{90}, and G_0. If the experimental data are not available, a value of 0.7 is recommended as a default value.

In summary, the intergranular strain parameters to calibrated are 6: A_g and n_g control the magnitude of G_0; m_{rat} represents the ratio G_{90} / G_0; R, β_r, χ and ϑ control the size of the elastic range, the rate of evolution of the intergranular strain tensor, the interpolation between the reversible elastic and non-linear hypoplastic responses and the accumulation of strains or stresses in cyclic loading paths, respectively.

In the following, the Hypoplastic model for clay will be referred with the label Hypo or H.

3.3.2. Thermal term: implementation and validation

To model the accumulation of non-recoverable volumetric contraction, the hypoplastic model for clays (Mašín, 2013) has been enhanced (Mašín and Khalili, 2012; Ma et al., 2017) with a thermal formulation using the concept of the shakedown already implemented for cyclic mechanical loading. In drained conditions, NC clays reach a stable structure after few thermal cycles; in the model this stabilization is attained when the soil status lays on the thermal stabilization line, TSL. The TSL is a straight line in the ln(1+*e*)-ln*p*' plane with slope (k_T) lower than λ^* (Fig. 3.3).

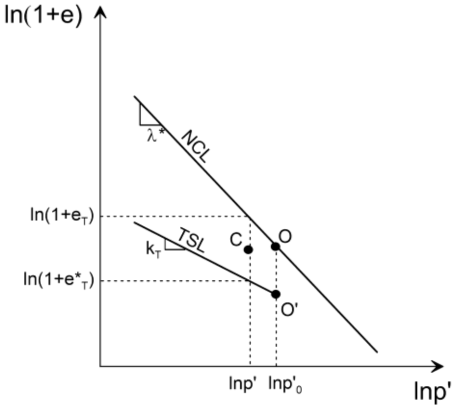

Figure 3.3. TSL line in ln(1+*e*)-ln*p*' plane (modified after Ma et al., 2017).

The proposed approach is based on the following hypotheses: (i) both the NCL and TSL are sensible to the temperature variation, when temperature increases they shift downward; (ii) the accumulation of irreversible volumetric contraction continues with decreasing rate until the soil status reaches the TSL; (iii) during cooling there is no accumulation and the strains are completely recoverable. From the latter, it follows that, since the soil skeleton and the voids have a proportional volumetric deformation (Khalili et al., 2010; Mašín and Khalili, 2012), the cooling causes a contraction of the soil but not a variation of the voids

To better understand how the model works, reference is made here to figure 3.4 where the qualitative behaviour of a NC soil specimen heated and cooled down cyclically at a constant effective stress is reported. In isothermal condition ($T=T_{in}$), the NCL and TSL intersect at the soil status (point 0). When the specimen is heated ($T=T_{fin}$), the TSL shifts more than the NCL and the soil status remains on the NCL (point 1); as a consequence, volumetric contraction is accumulated with a variation in the void ratio $\Delta\ln(1+e)_1$. The specimen is cooled and its temperature is brought back to the initial conditions (point 2); according to the hypothesis (iii), no additional strain is accumulated and both the NCL and the TSL return in their original position. In the following heating, the TSL and the NCL shift downward again and the behaviour remains elastic until TSL crosses the soil status (point 2). After that, accumulation of additional volumetric contraction, $\Delta\ln(1+e)_2 < \Delta\ln(1+e)_1$, takes place; the soil status moves downward and its distance from the TSL reduces (point 3).

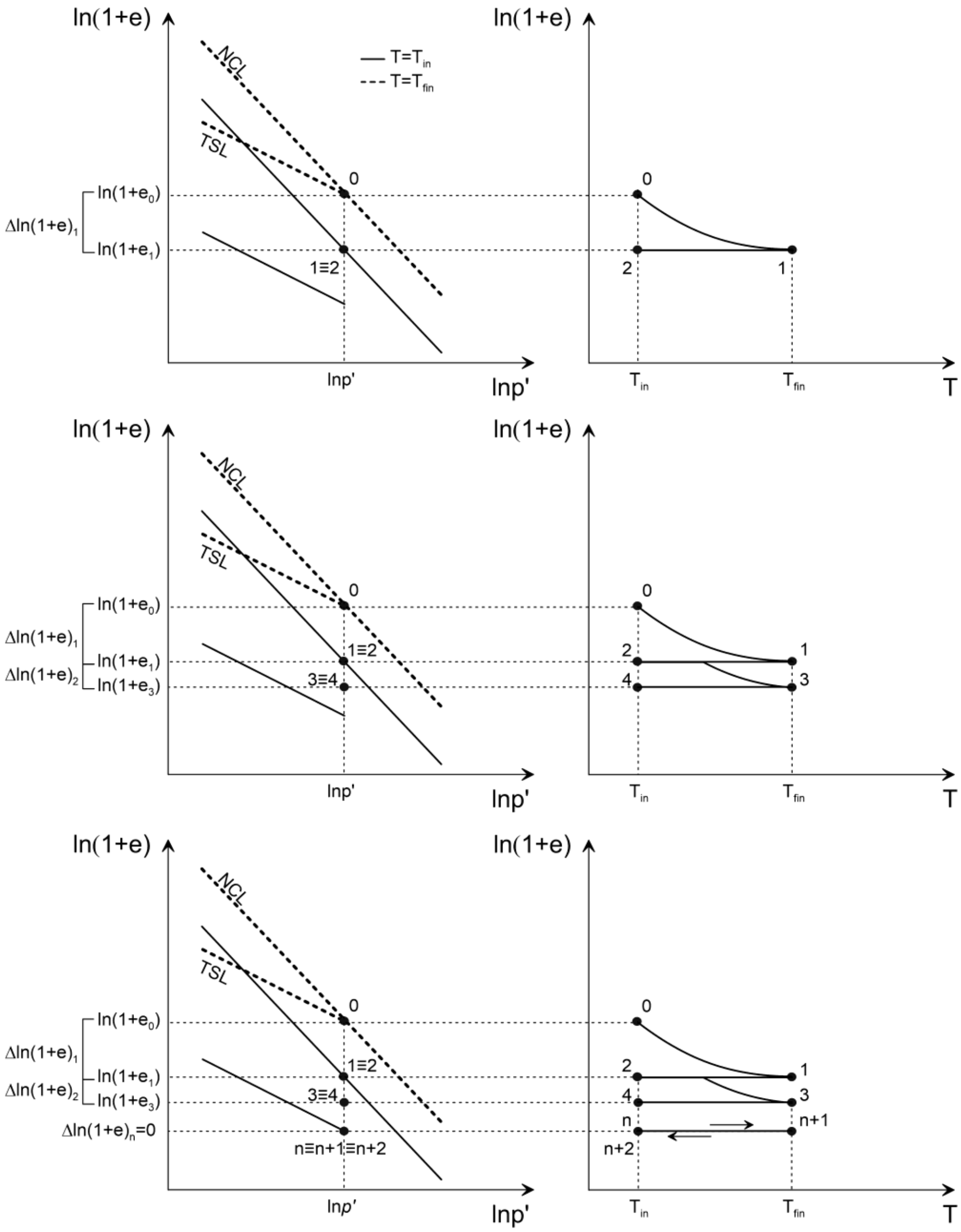

Figure 3.4. Clay volumetric behaviour with the hypoplastic model with thermal formulation (modified after Ma et al., 2017).

In the cooling phase no further strains develop (point 4). During the following heating volumetric contraction continues to build-up but at a reduced rate; after n cycles, the soil status reaches the TSL and the overall response gets stable with no further accumulation of strains.

The thermo-hypoplastic model is not available in the ABAQUS library, nevertheless it is possible to use an external routine where any user-defined model can be implemented in Fortran language (UMAT). The basic version of the Hypoplastic model has been already implemented for ABAQUS via a UMAT subroutine and is accessible from the SoilModels website. This version includes the intergranular strain concept, the anisotropy and softening behaviour of the clay. The last two components of the model are beyond the interest of the present research and, therefore, they will be not activated throughout this study.

In order to use the thermal version of the model, the thermal term has been added by the writer; the details are described in the Appendix II. For its implementation, the equations reported by Mašin and Khalili (2012) and Ma et al. (2017) have been followed.

The hypoplastic equation with the thermal formulation is written as follows:

$$\dot{\boldsymbol{T}} = f_s \left[\mathscr{L} : \left(\boldsymbol{D} - \boldsymbol{D}^{TE} \right) + f_d \boldsymbol{N} \left\| \boldsymbol{D} - \boldsymbol{D}^{TE} \right\| \right] + f_u \boldsymbol{H}_T \tag{3.69}$$

$\boldsymbol{D}^{TE}$ being the strain rate tensor due to thermal volumetric change of soil particles, f_u the collapse potential factor and $\boldsymbol{H}_T$ a second-order constitutive tensor.

The strain rate tensor, $\boldsymbol{D}^{TE}$, is calculated as follows:

$$\boldsymbol{D}^{TE} = \frac{\mathbf{1}}{3} \beta_s T \tag{3.70}$$

where β_s is the volumetric thermal expansion coefficient of the solid particles and T is the temperature. The thermal part is coupled with the mechanical part through the void ratio and the void ratio rate is calculated as follows:

$$\dot{e} = (1+e)\,\mathrm{tr}\left(\boldsymbol{D} - \boldsymbol{D}^{TE} \right) \tag{3.71}$$

The NCL depends from the temperature through the parameters N^* and λ^*:

$$\ln(1+e) = \mathsf{N}^*(T) - \lambda^*(T) \ln\left(\frac{p'}{p'_{ref}} \right) \tag{3.72}$$

$$\mathsf{N}^*(T) = \mathsf{N}^* + n_T \ln\left(\frac{T}{T_0} \right)$$

(3.73)

$$\lambda^*(T) = \lambda^* + l_T \ln\left(\frac{T}{T_0}\right) \tag{3.74}$$

where n_T and l_T are two parameters of the thermal model controlling the shift and the slope of the NCL respectively and T_0 is the reference temperature, i.e. the initial temperature of the soil.

The TSL has the following expression (Fig. 3.3):

$$\ln(1+e) = \ln(1+e_{0'}) - k_T \ln\left(\frac{p'}{p'_0}\right) \tag{3.75}$$

where ln(1+$e_{0'}$) is calculated as follows:

$$\ln(1+e_{0'}) = \ln(1+e_0) + c_T n_T \ln\left(\frac{T}{T_0}\right) \tag{3.76}$$

c_T is a parameters of the thermal model regulating the accumulation of the volumetric contraction after the first thermal cycle. When the temperature is lower than the reference temperature, $e_{0'}$ is fixed equal to e_0 (Fig. 3.3).

The collapse potential factor f_u, controls the thermally induced irreversible contraction and can be expressed as follows:

$$f_u = \left\langle \frac{e - e_T^*}{e_T - e_T^*} \right\rangle^{\gamma_T} \tag{3.77}$$

where γ_T is a parameters of the thermal model regulating the rate of irreversible volumetric contraction, e_T is the void ratio on the NCL and e^*_T is the void ratio on the TSL at the current mean effective stress.

The second order tensor, $\boldsymbol{H}_T$, is expressed as follows:

$$\boldsymbol{H}_T = c_i \frac{\boldsymbol{T}}{T\lambda^*} \left(n_T - l_T \ln\frac{p'_e}{p'_{ref}} \right) \langle \dot{T} \rangle \tag{3.78}$$

c_i being:

$$c_i = \frac{\left(\lambda^* + \kappa^*\right)\left(O_c^{\alpha_f} - f_d\right) + 2\kappa^* f_d}{\left(\lambda^* + \kappa^*\right)\left(O_c^{\alpha_f} - f_d\right) + 2\kappa^* f_d^A} \tag{3.79}$$

In summary, the additional parameters of the thermal part are: n_T, l_T, k_T, c_T, γ_T and T_0.

In the following, the hypoplastic model for clay with thermal formulation will be referred with the label Hypo-T or HT.

To validate the implementation of the model, the results of a triaxial test on a saturated clay have been used. Campanella and Mitchell (1968) performed an isotropic consolidation test at constant temperature of about 18°C on a normally consolidated specimen of remoulded illite using a triaxial apparatus. The applied total stress was 400kPa and the back pressure was kept at 200kPa resulting in an effective isotropic stress of 200kPa. After the consolidation phase, the specimen temperature was changed over a wide range from about 4°C to about 60°C with a total of three heating and cooling cycles. The drainage was allowed during all the test. The model parameters have been calibrated by Ma et al. (2017) and are reported in table 3.1. The mechanical part includes the basic parameter of the hypoplastic model without the activation of the intergranular strain; the thermal part refers to the thermal term introduced in the advanced part of the model. The simulations with the ABAQUS code have been performed considering the drained conditions; therefore, in the current analyses, the thermal expansion coefficient of the water doesn't play any role. Moreover, to better fit the contraction in the first heating, a simulation with a lower value of n_T has also been carried out (table 3.1, set-2). During the first temperature variation the soil specimen stress state remains on the NCL and, consequently, its volumetric contraction is entirely determined by n_T. Since the scope is to improve the prevision of the first contraction, all the other parameters are fixed to the value of the first simulation (set-1).

Mechanical parameters			Thermal parameters		
	set - 1	set – 2		set - 1	set - 2
φ [°]:	22	22	α_s [°C^{-1}]:	$1.17 \cdot 10^{-5}$	$1.17 \cdot 10^{-5}$
ν [-]:	0.23	0.23	T_0 [°C]:	18	18
λ^* [-]:	0.092	0.092	n_T[-]:	-0.009	-0.01
κ^* [-]:	0.027	0.027	k_T [-]:	0.04	0.04
N^* [-]:	1.178	1.178	c_T [-]:	0.4	0.4
			γ_T [-]:	0.1	0.1

Table 3.1. Model parameters used to simulate the drained triaxial test by Campanella and Mitchell (1968).

Figure 3.5 shows the comparison between the data available from the triaxial test and the two simulations performed. The best fit is obtained with the second set of parameters.

Campanella and Mitchell (1968) reported also the results of a triaxial test in undrained condition. Indeed, for the same specimen, the drainage was closed and two thermal cycles were performed. The data are plotted in figure 3.6 showing that the pore pressure-temperature relation is hysteretic with closed loop. It is worth noting that, in undrained condition, the excess pore water pressure develops because of the higher value of the thermal expansion coefficient of the water than that of the soil skeleton; moreover, the NC specimen would contract and this contraction is contrasted by the expansion of the water which must thus adsorb a larger pressure.

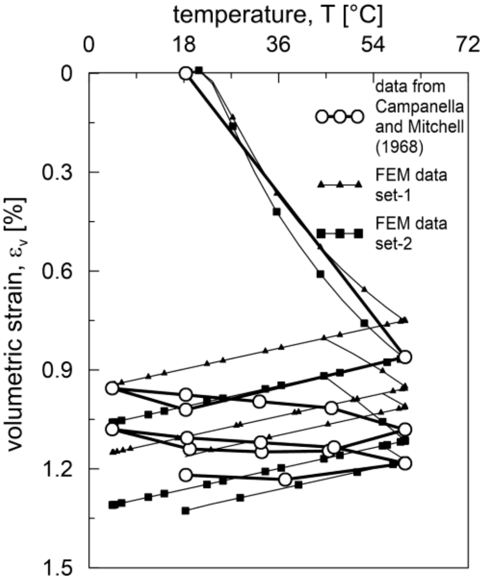

Figure 3.5. Comparison between triaxial test in drained condition and FE simulations.

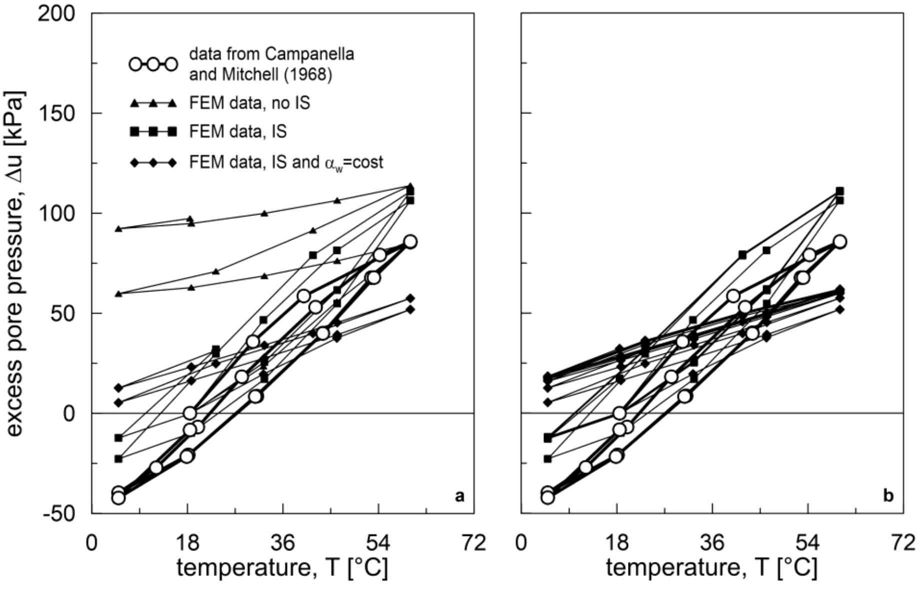

Figure 3.6. Comparison between triaxial test in undrained condition and FE simulations.

The thermal expansion coefficient of the water is a function of the temperature itself; this dependency is reported in figure 3.7.

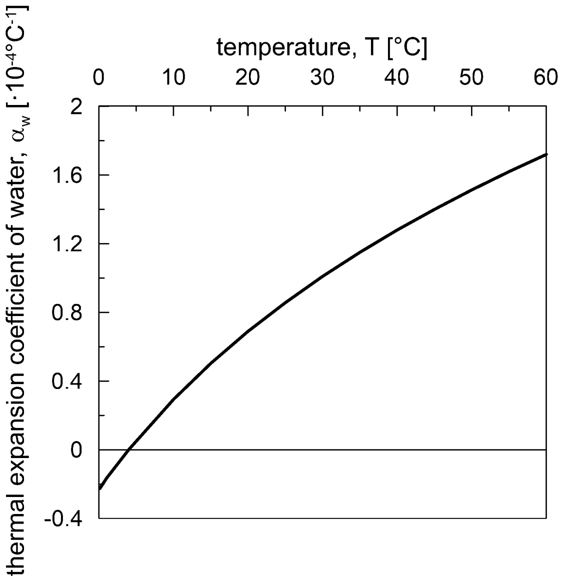

Figure 3.7. Variation of thermal expansion coefficient of water with temperature.

If a simulation with the ABAQUS code is run taking into account the variability of the thermal expansion of the water and using the thermal parameters reported in table 3.1 (set-2), there is no possibility to capture the overall behaviour in undrained conditions (Fig. 3.6a, FEM data, no IS). In fact, after the first heating, the excess pore pressure has a tendency to cumulate cycle after cycle and no hysteresis is observed. To reproduce the actual behaviour with the model at hand, it is necessary to calibrate the intergranular strain part of the model (IS). The calibration was carried out by trial and error on the available data on the parameters A_g and n_g. The parameter used are reported in table 3.2. The results of the FE analysis with the calibrated intergranular strain part show that the model can reproduce quite well the observed behaviour (Fig. 3.6a, FEM data, IS). In figure 3.6b the result of a seven cycles analysis is also reported (FEM data, IS); this has been done to be sure that the hysteretic behaviour is captured by the model after multiple cycles. It is evident that, after a small accumulation in the first cycle, a closed loop behaviour is observed from the second cycle onward. If the intergranular strain is used and the thermal expansion coefficient of the water is taken constant to the value corresponding to the initial temperature (18°C), the hysteretic behaviour is reached within few cycles and a slight accumulation of the excess pore pressure is obtained (Fig. 3.6, FEM data, IS and α_w constant).

Intergranular strain parameters	
R [-]:	$5 \cdot 10^{-4}$
A_g [-]:	70
n_g [-]:	1
β_r [-]:	0.08
χ [-]:	0.9
m_{rat} [-]:	0.5
ϑ [-]:	10

Table 3.2. Intergranular strain parameters used to simulate the undrained triaxial test by Campanella and Mitchell (1968).

A better evaluation of the model parameters would require ad hoc laboratory tests performed with devices equipped for the non-isothermal conditions. Because no such results are available for the problem at hand, the trial and error procedure has been the only option to assess the capability of the model to reproduce the experimental evidence. Moreover, in the case of energy piles, temperature changes are applied to a structure interacting with the ground and therefore shear strength tests with thermal variation would provide a better validation for the constants to use in the chosen constitutive model. Nevertheless, the scope of the FE analyses carried out in this study is to evaluate the potential of advanced constitutive models over the classical models in reproducing the behaviour found via experimentation. For this reason, the qualitative point of view acquires more importance than the quantitative analysis. Once demonstrated that the use of advanced models is crucial to catch the cyclic behaviour, the accurate calibration of the input parameters would improve the results from a quantitative point of view.

3.4. Thermo-hydro-mechanical coupling

The soil is a porous medium composed by grains, water and gasses, for which the mechanical, hydraulic and thermal responses are coupled; indeed, its mechanical behaviour is affected by the pore water pressure regime and by the temperature field (that is also responsible of the pore pressure variation). In the following, the thermo-hydro-mechanical formulation for porous media is written in the hypothesis of small deformations and of pores filled with water (i.e. the soil is saturated).

The equilibrium equation can be written as follows:

$$\nabla \cdot \boldsymbol{\sigma} + \rho_g \boldsymbol{b} = \mathbf{0} \tag{3.80}$$

where the symbol “$\nabla\cdot$” is the divergence of the total stress tensor **σ**, ρ_g is the bulk density of the material, ***b*** is the body force vector (gravity) per unit mass and **0** is the null vector. The hydro-mechanical coupling is introduced via the Terzaghi (1923) formulation:

$$\boldsymbol{\sigma} = \boldsymbol{\sigma}' + u\mathbf{1} \tag{3.81}$$

where **σ'** is the effective stress tensor, *u* is the pore water pressure. The density of the soil is a function of the density of the grains, ρ_s, and of the density of the water, ρ_w:

$$\rho_g = n\rho_w + (1-n)\rho_s \tag{3.82}$$

n being the porosity of the soil equal to the ratio of the volume of the voids over the total volume. Therefore, Eq. (3.80) can be written as follows:

$$\nabla\cdot\boldsymbol{\sigma}' + \nabla u + \rho\boldsymbol{b} = \mathbf{0} \tag{3.83}$$

where the symbol “∇” in the second term is the gradient of the pore water pressure.

The mass conservation equation is expressed as follows:

$$\left(n\frac{1}{K_w} + (1-n)\frac{1}{K_s}\right)\dot{u} + \left(n\beta_w + (1-n)\beta_s\right)\dot{T} + \mathrm{div}\,\boldsymbol{v} = 0 \tag{3.84}$$

where $\dot{u}$ is the pore pressure rate; $\dot{T}$ is the temperature rate; $1/K_w$ and $1/K_s$, β_w and β_s, are the compressibilities and the volumetric thermal expansion coefficients of the water and solid skeleton, respectively; ***v*** is the relative velocity of the pore water with respect to solid skeleton expressed by the Darcy’s law. The thermo-hydraulic coupling is associated to the variation of the mass of soil and water cause by a variation of the pore water pressure and the temperature accounted by the first and the second term of Eq. (3.84), respectively. The other terms are related to the exchange of water between the outside and the reference volume. The Darcy ‘s low is expressed as follows:

$$\boldsymbol{v} = -\frac{1}{\mu_w}\hat{\boldsymbol{k}}\left(\nabla u + \rho_w\boldsymbol{b}\right) \tag{3.85}$$

where μ_w is the dynamic viscosity of the pore water and $\hat{\boldsymbol{k}}$ is the intrinsic permeability of the solid skeleton, the hydraulic conductivity being:

$$\boldsymbol{k} = \frac{\hat{\boldsymbol{k}}\rho_w\boldsymbol{b}}{\mu_w} \tag{3.86}$$

The dependence of the hydraulic conductivity from the temperature is related to the dynamic viscosity and to the density (Thomas and King, 1994):

$$\mu_w = 0.6612\left(T-229\right)^{-1.562} \tag{3.87}$$

$$\rho_w = \rho_{w0}\left(1+\frac{1}{k_w}\dot{u}-\beta_w\dot{T}\right) \tag{3.88}$$

where the viscosity and the temperature are expressed in Pascal per second and in Kelvin respectively and ρ_{w0} is the density of the water at the reference temperature. The hydraulic conductivity, $\boldsymbol{k}$, controls the rate of seepage of water through the pores. If the load on the soil is applied slowly with respect to the rate of seepage, the volume of the soil changes with constant pore pressure and this situation is referred as drained condition. In contrast, if the loading phase is quicker than the rate of seepage, the water pressure changes and the volume of the soil remains constant; this situation is referred as undrained and is characterized by the occurrence of volume changes as a consequence of the dissipation of the excess pore pressure. In non-isothermal problems the undrained condition is related to the water content inside the soil volume, i.e. is the mass of the reference volume that remains constant rather than the volume itself (Aversa et al., 1993). Indeed, in undrained condition, during heating or cooling the volume of the soil changes as a consequence of the temperature variation but the water cannot flow outside the volume and its mass stays constant.

As concern the heat transfer in the saturated soil, it involves the conduction, the convection and the radiation mechanisms (Fig. 3.8). The conduction occurs through the solid skeleton and the water filling the pores; the convection is related to the presence of a groundwater flow; with respect to the other mechanisms, the radiation contribution is negligible. The heat transferred by conduction is expressed by the Fourier's law:

$$\boldsymbol{q_{cond}} = -\lambda_{th}\nabla T \tag{3.89}$$

where λ_{th} is the thermal conductivity of the soil:

$$\lambda_{th} = n\lambda_{th,w} + \left(1-n\right)\lambda_{th,s} \tag{3.90}$$

$\lambda_{th,w}$ and $\lambda_{th,s}$ being the thermal conductivity of the water and solid skeleton, respectively.

The heat flux by convection is expressed as follows:

$$\boldsymbol{q_{conv}} = \rho_w c_{p,w}\boldsymbol{v}\nabla T \tag{3.91}$$

where $c_{p,w}$ is the specific heat of water.

The energy conservation equation has the following expression:

$$\rho c_p \dot{T} + \nabla\cdot\boldsymbol{q_{cond}} + \boldsymbol{q_{conv}} = 0 \tag{3.92}$$

ρc_p being the soil heat capacity, with c_p expressed as follows:

$$c_p = nc_{p,w} + (1-n)c_{p,s} \tag{3.93}$$

where $c_{p,s}$ is the specific heat of the solid skeleton.

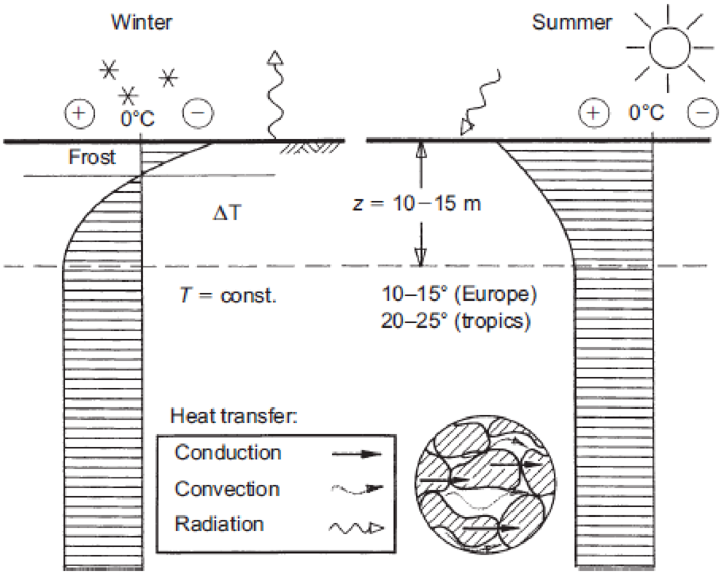

Figure 3.8. Heat transfer mechanisms (from Brandl, 2006)

4.Finite Element analyses

Energy piles are subjected to mechanical loads transmitted at the top by the superstructure as well as to cyclic variation of their temperature. Numerical techniques can be employed to study the performance of these foundations in terms of axial force and displacements. To this end, a single energy pile installed in NC clay and subjected to a vertical mechanical load and to 5 thermal cycles has been modelled using the ABAQUS code.

Although some laboratory tests (e.g., Ng et al., 2014a; Wu et al., 2018) have analysed the cyclic performance of the energy pile in terms of settlements, as discussed in Chapter 1, the studies available in literature are mainly focused on the effect of the monotonic increase of the temperature or, at least, of the single cycle. In particular, the case of a pile installed in soils subjected to volumetric collapse has not yet been fully investigated (except for Di Donna and Laloui, 2014, that analysed the cyclic behaviour only with reference to the vertical displacements).

In this sense, the use of numerical analyses with appropriate constitutive models, allows to explore the performance in terms of thermally-induced axial force and settlements as a consequence of the combined loading conditions. Indeed, the constitutive models usually employed are based on the classical theory of plasticity, while the analyses of the cyclic behaviour might require the use of more sophisticated models. In order to understand the predictive capabilities of the constitutive models commonly used in practical application and available in the libraries of many FE codes, comparison with advanced constitutive models implemented in external subroutines (UMAT) have been carried out.

The comparison between the results obtained employing the different models aims at highlighting that, in the case of energy piles subjected to cyclic solicitation, the use of advanced constitutive models is the only way to qualitatively predict the cyclic behaviour observed in the real applications. Nevertheless, the advantage of achieving detailed results is counterpoised to the effort paid for the calibration of a larger amount of parameters.

In the following sections the code used for the simulations and the FE model of the pile are introduced. Then, the calibration of the constitutive models used to reproduce the soil behaviour is reported.

The results of the FE analyses are discussed in Chapter 5.

4.1.ABAQUS code

The numerical analyses have been performed with the code ABAQUS Standard v6.14.

The ABAQUS Standard software is a general purpose finite element program suited for, among the others:

- Static and dynamic stress-displacement analyses;
- Steady-state and transient heat transfer processes uncoupled or coupled with the stress-displacement analysis;
- Steady-state and transient pore fluid flow and stress analyses in fully or partially saturated porous media.

One of the main advantages is the possibility to perform coupled analyses such as the fully coupled thermo-hydro-mechanical calculations in which the heat transfer equation is solved in addition to and in a fully coupled manner with the continuity and the mechanical equilibrium equations.

Among the others, the following constitutive models are available:

- Elastic models: linear elasticity; porous elasticity; hypoelasticity; hyperelasticity;
- Inelastic models: elastic perfectly plastic models (such as von Mises, Drucker-Prager, Mohr-Coulomb); elasto-plastic models with isotropic and kinematic hardening (such as the Modifiel Cam-Clay models); concrete damaged plasticity;
- User material: user-defined mechanical material behaviour can be provided by means of an interface that allows to add to the basic library any mechanical constitutive model. The implementation of the constitutive model is possible via the user subroutine UMAT where the constitutive model is required to be programmed in Fortran language.

As concerns the available elements, among the others, it is possible to choose between the following:

- Continuum elements: these elements are used for 1D, 2D, 3D and axisymmetric analyses; degrees of freedom for displacements, pore pressure and temperature are available depending on the type of the analysis; they differ for number of nodes and integration techniques;
- Structural elements: such as membrane, truss, beam, shell and frame;
- Special-purpose elements: such as spring, dashpot, surfaces and joint; user-defined elements can be programmed in external subroutine, EUL, in Fortran language.

Finally, an interactive environment is also available, ABAQUA/CAE; it can be used to create finite element models, submit ABAQUS analyses, monitor and diagnose jobs, and evaluate results.

The simulations presented herein were run at the University of Cambridge on a multiprocessor computer allowing shared and distributed memory parallel processing.

4.2.FE model: problem definition

The single energy pile modelled in the simulations has a slenderness ratio of *L/d* = 50; its geometrical, mechanical and thermal features are reported in table 4.1

Pile	
L [m]:	25
d [m]:	0.5
E [GPa]:	30
ν [-]:	0.2
γ_c [KN/m^3]:	25
T_0 [°C]:	15
α_c [°C^{-1}]:	$8.5 \cdot 10^{-6}$
$\lambda_{th,c}$ [W/mK]:	2
$c_{p,c}$ [J/kgK]:	1200

Table 4.1. Energy pile features.

The model is axisymmetric and its dimensions are 50x50m (Fig. 4.1). The axial symmetry of the problem allows to conveniently consider a 2D model, resulting in a relevant saving in the computational efforts. The soil is fully saturated with the groundwater table at the ground surface. A structured mesh with 4-node axisymmetric quadrilateral elements has been employed for both the pile and the soil. The pile is a non-porous elastic medium; the elements used are of the type CAX4T, i.e. 4-node axisymmetric thermally coupled quadrilateral, bilinear displacement and temperature elements. The total number of elements is 1000; they have a base of 0.05m and a height of 0.125m. The soil is modelled with elements of the type CAX4PT, i.e. 4-node axisymmetric quadrilateral, bilinear displacement, bilinear pore pressure, bilinear temperature elements. This allows to perform fully coupled thermo-hydro-mechanical analyses. The total number of elements used for the soil is 27956. Since the mesh has been strongly refined at the interface and in the vicinity of the pile base, the elements used have a variable geometry. At the pile-soil interface, the same dimensions of the pile elements are used up to a distance of 1*d*; from this point onward, the base of the elements is progressively increased up to 2.50m at 50m (Fig. 4.1). For a length of 2*d* above and of 6*d* below pile the tip, the dimensions of the elements are 0.05x0.05m. In the lower part of the mesh, the height of the elements has been progressively increased up to 1m at 50m (Fig. 4.1). A sensitivity analysis showed that for the loading conditions and constitutive models adopted, these modelling choices do not significantly alter the results.

At the interface perfect contact between pile and soil is modelled with the use of tie constrains. Indeed, the energy pile is installed in a clay for which the degradation phenomenon is of minor concern and the increase of temperature improves the interface strength; moreover, since the clay is normally consolidated, the thermally induced consolidation phenomenon helps reducing the degradation during shearing (Di Donna and Laloui, 2015b).

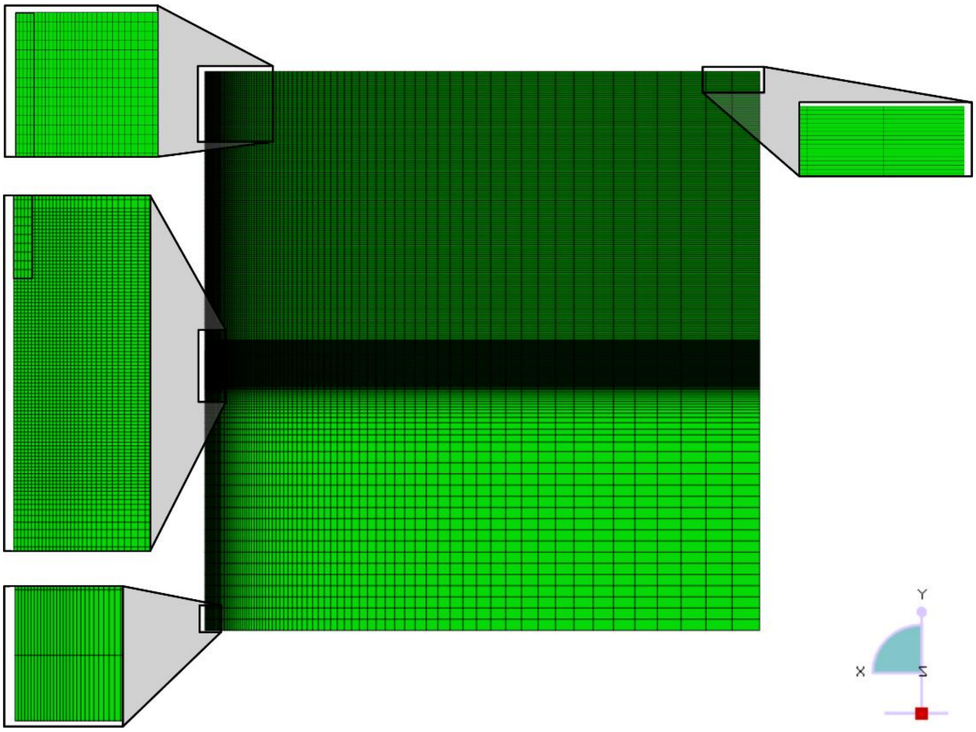

Figure 4.1. Mesh of the Finite Element model.

The pile and the soil have a constant initial temperature T_0 = 15°C.

Concerning with the boundary conditions, the following restriction have been applied in terms of displacements, pore pressure/water flux and temperature/heat flux:

- left boundary (axisymmetric axis): horizontal displacement, water flux and heat flux restrained;

- bottom part of the model: vertical displacement restrained; constant pore water pressure (hydrostatic value u = 500kPa); constant temperature (initial value T_0);
- right boundary: horizontal displacement restrained; constant pore water pressure (hydrostatic distribution); constant temperature (initial value T_0);
- upper part of the model: constant pore water pressure (hydrostatic value u = 0kPa); constant temperature (initial value T_0).

The first step of the analysis is a geostatic step. In this step the equilibrium between the external and internal forces is verified. The loading phase starts with a mechanical step in which a mechanical load is applied at pile head. In order to obtain the performance of the system at different loading conditions, two levels of mechanical load have been simulated. The choice of the load level is discussed in the results section. The application of the mechanical load is in drained conditions resulting in no excess pore water pressures at the end of the loading stage; it follows that the subsequent variation of pore water pressure can be related only to the thermal loads. The temperature variations are applied cyclically according to a temperature path over one year: the pile temperature is changed in one day and kept constant for 5 months followed by a thermal rest of 1 month; then it is reversed. During the rest phase the pile temperature is not constant along the shaft because it varies according to the thermal boundary conditions. Figure 4.2 shows the temperature variation at pile head during one-year cycle. 5 thermal cycles have been performed.

The hypoplastic and the MCC models allow a variation of the stiffness with the effective stress. In the analyses with the Linear Elastic and the MC models, to allow a similar stiffness increase with depth, the soil has been divided in layers with a height of 2 meters, each of them characterized by a constant stiffness corresponding to the value at the centre of the layer.

Two groups of analyses have been performed where pile head is either completely free to move or fully restrained.

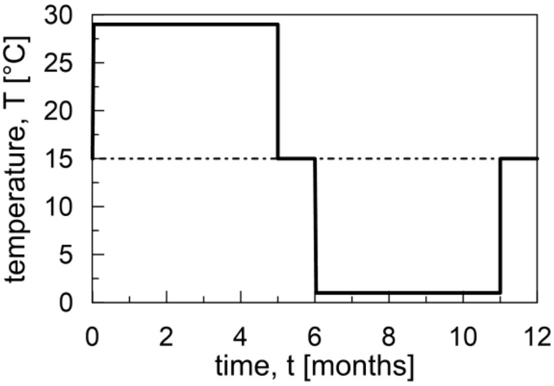

Figure 4.2. One-year temperature variation at pile head.

4.3. Model calibration

The FE analyses are carried out for a single energy pile installed in a NC clay. The constitutive models used to reproduce the behaviour of the soil are the Linear Elastic model, the Mohr-Coulomb model, the Modified Cam-Clay model and the Hypoplastic model without and with the thermal formulation.

Since a robust calibration of the Hypo model is available for the London clay, the parameters of the other models have been chosen using the Hypo model as a benchmark. In this way the results of the FE analyses of the single pile can be reliably compared. In particular, the classical models are calibrated on the hypoplastic parameters considering that (i) the Linear Elastic stiffness has to be referred to an effective value of shear modulus and (ii) for the MCC model there is no parameter that takes into account the stiffness at small strain and the model has to be calibrated using the 5 mechanical parameters of the basic Hypoplastic model.

The Hypo model is also employed to simulate a set of drained and undrained triaxial test via the FEM; the results using the other models are also reported.

4.3.1. Mechanical parameters

The thermo-hypoplastic model consists of a mechanical and a thermal part. The mechanical part includes the basic parameters and the intergranular strain concept (as anticipated, in this study anisotropy and softening behaviour are not considered). The mechanical constants of the model have been calibrated by the authors for many clayey soils (Mašín, 2019). A complete set of parameters is available for the London clay (table 4.2). These parameters are based on a robust calibration and have been used to model the soil in this work.

Basic parameters		**Intergranular strain parameters**	
φ [°]:	21.9	R [-]:	$5 \cdot 10^{-5}$
ν [-]:	0.23	A_g [-]:	270
λ^* [-]:	0.1	n_g [-]:	1
κ^* [-]:	0.02	β_r [-]:	0.08
N^* [-]:	1.26	χ [-]:	0.9
		m_{rat} [-]:	0.5
		ϑ [-]:	n.c.

Table 4.2. Parameters calibrated for London clay.

It is known that London clay is heavily overconsolidated; to reproduce the behaviour of a normally consolidated clay some considerations have been made. First of all, the soil state has been initialized entering the overcondolidation ratio rather than the initial void ratio in the set of parameters required by the UMAT implementation; then, the parameters A_g and n_g of the interganular strain have been calibrated following Viggiani and Atkinson (1995). For reconstituted normally consolidated London clay they suggest the values of A_g and n_g reported in table 4.3.

A_g [-]:	400
n_g [-]:	0.76

Table 4.3. A_g and n_g calibrated for NC London clay.

The MC friction angle, φ, and Poisson's ratio, ν, are simple to calibrate since they can be taken directly from the strength parameters used for the hypoplastic model. The dilatancy angle, ψ, has been set to 0. Concerning with the stiffness, an effective value of the shear modulus has been selected in order to reproduce the same settlement of the pile under working load conditions for both the MC the hypoplastic models (details are reported in paragraph 5.1.). To this aim, the small strain stiffness used for the intergranular strain part has been divided by a factor of 2.1. For the stiffness and the Poisson's ratio of the E model the same values of the MC model have been adopted.

The MCC model can be completely defined by the use of 5 mechanical parameters that have the same meaning of that of the hypoplastic model. In fact, both models incorporate the critical state theory with one main difference. In the MCC the NCL and the CSL are linear in the (1+*e*)-ln*p*' plane while in the hypoplastic formulation they are linear in the ln(1+*e*)-ln*p*' plane. The parameters of the MCC can be derived from that of the hypoplastic model considering that the void ratio, *e*, is the same at a depth of 10m and for a mean effective pressure equal to the reference value of 1kPa. It follows that:

$$\mathsf{N} = \exp\left(\mathsf{N}^*\right) \tag{4.1}$$

$$\lambda = \frac{\lambda^*\left(\mathsf{N} - (1+e)\right)}{\mathsf{N}^* - \ln(1+e)} \tag{4.2}$$

$$\kappa = \frac{\kappa^*\left(v_k - (1+e)\right)}{v_k{}^* - \ln(1+e)} \tag{4.3}$$

The parameters used are summarized in table 4.4. Note that the soil is normally consolidated and, therefore, the void index varies with depth.

In all the analyses, the permeability of the soil, k_w, is set to a value of 10^{-10} m/s while the saturated soil unit weight, γ_{sat}, is equal to 20 kN/m^3.

Moh-Coulomb		Modified Cam-Clay	
φ [°]:	21.9	φ [°]:	21.9
ν [-]:	0.23	ν [-]:	0.23
		λ [-]:	0.286
		κ [-]:	0.048
		N [-]:	3.52

Table 4.4. Mechanical parameters for MC and MCC models.

To compare the response of the calibrated models with reference to the single element, triaxial tests at constant temperature have been simulated via the ABAQUS code. Three NC samples have been isotropically consolidated at different pressures; in the following deviatoric phase, the drained and the undrained conditions have been both simulated is two separate tests. The results are plotted in terms of deviatoric stress versus axial deformation (q-ε_a, Fig. 4.3) and deviatoric stress versus mean effective stress (q-p', Fig. 4.4).

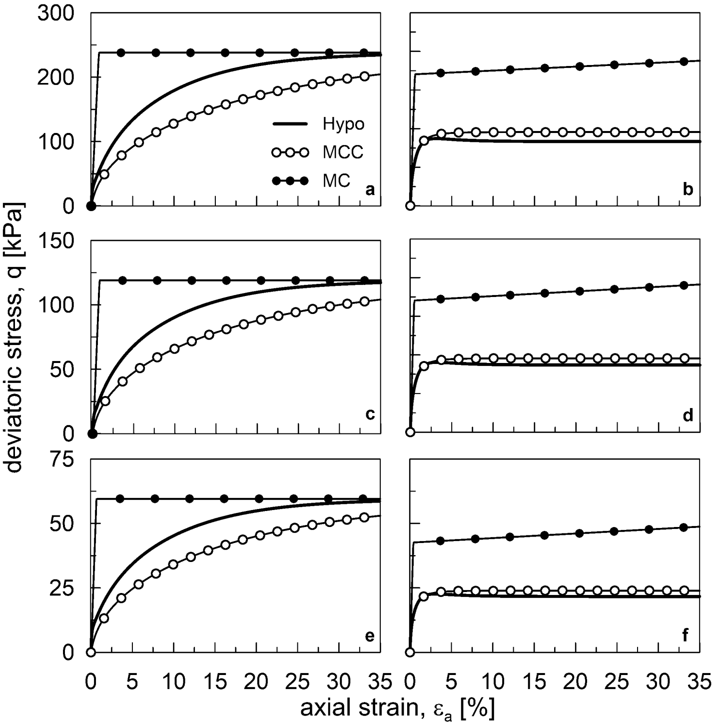

Figure 4.3. Data from simulation of drained (a, c, e) and undrained (b, d, f) triaxial test.

In drained condition, it can be noted that (i) the capacity is almost the same regardless of the model employed, (ii) the hypoplastic model is characterized by a high stiffness in the very small strain range before the intergranular strain attains its maximum value, (iii) since there is no parameter able to account for the behaviour at the early stage of the loading process, the MCC shows a much lower stiffness, (iv) compared to the other models, the MC response is quite stiff and the ultimate resistance is achieved at very small strains. In undrained condition the loading paths in the *q*-*p*' plane reveal a quite different behaviour; as expected, the pore pressures developed with the MC are lower than that with the other models and, therefore, for this case the undrained resistance is almost doubled.

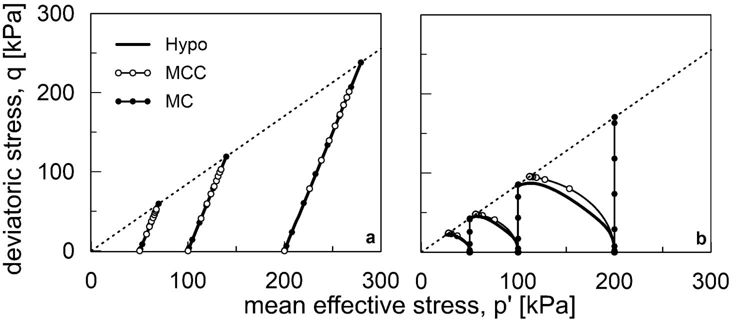

Figure 4.4. Drained (a) and undrained (b) load paths.

The simulated laboratory tests show dissimilarities in the model response in terms of both shear strength and stiffness. It is likely that these differences at the element scale might not be negligible in the global performance of the pile-soil system since the overall behaviour comes from the integration of the local responses along the pile shaft and at pile base.

4.3.2. Thermal parameters

Concerning with the thermal part of the thermo-hypoplastic model, no specific data are available for the thermal calibration of London clay. Therefore, suggestions by Ma et al. (2017) have been followed.

The additional thermal parameters are five:

- n_T controls the shift of the NCL; a careful assessment of this parameter is crucial for reliable results; indeed, as shown in figure 3.5 even a small variation of this parameter has a major influence on the results;
- since the influence of the temperature on the slope of the NCL is negligible, the parameter l_T can be set to 0;
- k_T controls the slope of the TSL and should be larger than the slope of the unload-reload line, κ^*. A proper calibration of k_T requires a set of thermal tests with different *OCR*s. Nevertheless, as a starting point, Ma et al. (2017) suggest to adopt a value lager than κ^* and in the range of 0.01÷0.015;
- c_T account for the accumulation of irreversible volumetric contraction after the first heating; in order to calibrate it, a test until stabilization is required. Based on the published experimental results (Campanella and Mitchell 1968;

Vega and McCartney 2014; Di Donna and Laloui 2015a), Ma et al. (2017) suggest to adopt a value in the range of 0.4÷0.5;

- γ_T controls the rate of irreversible volumetric contraction; based on the sensitivity analysis conducted by Ma et al. (2017), the accumulation stabilized within five thermal cycles when its value is set to 0.1. This is in accordance with the experimental results (Vega and McCartney, 2014).

The thermo-hydro-mechanical coupling is a strongly non-linear problem; the use of a temperature dependent thermal expansion coefficient of water adds further non-linearities to this rather complex analysis. In order to reduce the computational efforts, the thermal expansion coefficient of the water, α_w, is taken constant throughout the analyses and equal to the value at the initial temperature. Table 4.5 reports the adopted values along with the other constants used for the characterization of the soil thermal properties.

Thermal term		**Thermal properties**	
n_T [-]:	-0.01	α_s [°C^{-1}]:	$1.5 \cdot 10^{-5}$
l_T [-]:	0	T_0 [°C]:	15
k_T [-]:	0.04	λ_{th} [W/mK]:	1.5
c_T [-]:	0.4	c_p [J/kgK]:	1000
γ_T [-]:	0.1	α_w [°C^{-1}]:	$5 \cdot 10^{-5}$

Table 4.5. Thermal parameters.

5.Results and discussion

Fully coupled thermo-hydro-mechanical analyses have been performed to study the behaviour of a single energy pile using five different constitutive models. Free-head or fixed-head conditions are the two constraints considered at pile head, while two different levels of mechanical vertical load have been applied to account for working (30% R_t) or close-to-failure conditions (80% R_t).

The analysis of the single energy pile with different constitutive models allows a comparison between the performance of the pile in terms of settlements and axial force. In particular, the use of increasingly complex constitutive models points out that in cases of nonlinear fully coupled thermo-hydro-mechanical analyses, simpler models might fail to account for all the main actors of the process.

Hereafter, the response in terms of load-settlement curve is reported and a discussion about the restraint at pile head is provided; then, with reference to the thermo-mechanical load, comparisons at the global scale are presented and, to better understand the overall behaviour, the local response along the pile shaft and at the base is also shown.

5.1.Mechanical loading phase

The bearing capacity of a pile foundation can be assessed via field loading tests in real scale, tests on prototypes, numerical techniques or with the use of empirical and analytical formulae. In the following, reference will be made to the latter as they are commonly used in practice.

When the pile is subjected to an axial load Q applied at its head, the equilibrium along the vertical direction assures that (Fig. 5.1):

$$Q + W = Q_s + Q_b \tag{5.1}$$

where W is the pile self-weight, Q_s and Q_b are the shaft and the base loads respectively.

The shaft and the base loads reach their maximum values (resistance or ultimate value or capacity) following two different mechanisms: sliding along the shaft, for which small relative displacements between pile and soil are generally required (not depending on the pile diameter d, of the order of few tens of millimetres);

compression at pile base, for which greater displacements are required (depending on the pile diameter *d*, typically not lower than 10% *d*). It follows that generally the shaft bearing capacity is attained well before the base bearing capacity.

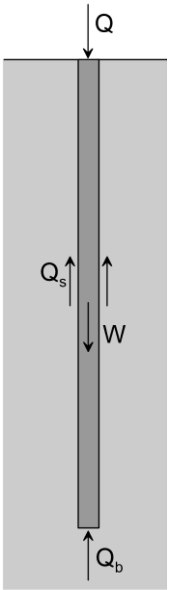

Figure 5.1. Equilibrium along vertical direction of a pile subjected to an axial load *Q*.

With approaching failure, Eq. (5.1) can be written as follows:

$$R_t = R_c + W = R_s + R_b \tag{5.2}$$

where R_t is the overall bearing capacity.

The shaft contribution R_s can be evaluated as:

$$R_s = \pi d \int_0^L q_s(z)\,dz \tag{5.3}$$

where q_s is the unit shaft resistance.

In drained conditions, q_s can be computed as follows:

$$q_s(z) = \bar{k} \tan\delta_f \, \sigma'_z \tag{5.4}$$

where $\bar{k}$ is the earth pressure coefficient whose value depends on the soil properties and on the pile technology; δ_f is the friction angle between pile and soil; σ'_z is the effective vertical stress.

In undrained conditions:

$$q_s(z) = \bar{\alpha}\, s_u(z) \tag{5.5}$$

where $\bar{\alpha}$ is a coefficient ranging between 0 and 1, depending on soil and pile properties while s_u, is the undrained shear strength.

The base bearing capacity R_b has the following expression:

$$R_b = \frac{\pi d^2}{4} q_b \tag{5.6}$$

where q_b is the unit base resistance.

In drained conditions, q_b can be computed as follows:

$$q_b = \sigma'_{z,L} N_q + c' N_c \tag{5.7}$$

where $\sigma'_{z,L}$ is the vertical effective stress at the depth $z = L$; N_q can be evaluated following Berezantzev et al. (1961); N_c is related to N_q by the expression:

$$N_c = \left(N_q - 1\right) \cot\text{an}\varphi \tag{5.8}$$

In undrained conditions, q_b can be computed as follows:

$$q_b = \sigma_{z,L} + 9\, s_u \tag{5.9}$$

where $\sigma_{z,L}$ is the vertical total stress and N_c can be set equal to 9 (Skempton, 1951).

In the numerical analyses, the mechanical loading phase is modelled in drained condition; therefore, to determine a conventional value of the pile bearing capacity, the formulae in drained conditions have been used. As stated before, this choice allows relating the variation of the pore water pressure occurring during the thermal phases to the thermal loads only. Moreover, passing from undrained to drained conditions, the shaft capacity of the pile is not expected to vary significantly and, in clay soils for usual values of pile slenderness, the increase in tip capacity with time is not a relevant portion of the overall capacity. However, the aim of this calculation is merely to define a conventional factor of safety, FS, and a different evolution of R_t would just result in a different value of FS. By considering a bored wished in place pile, the earth pressure coefficient is assumed to be k_0 = 1-sinφ while the friction angle between pile and soil is equal to φ. The soil mechanical parameters and the value of the bearing capacity factors are summarized in table 5.1, along with the calculated bearing capacity of the pile in drained conditions.

The load-settlement curve has been derived through a FE analysis, exploring different responses as coming from the different soil models (MC, MCC and Hypo). In figure 5.2 the ratio of the load, Q, and the bearing capacity estimated with the analytical formulae, R_t, is plotted against the dimensionless ratio w/d, w being the head settlement. According to what is generally assumed in practice, the ultimate load deriving from the load-settlement curve, R_{FEM}, can be taken as the pile head load corresponding to a pile head settlement w = 10% d.

c [kPa]:	0
$\overline{k}$ [-]:	0.63
δ_f [°]:	21.9
N_q [-]:	5
R_t [kN]:	1490

Table 5.1. Pile bearing capacity.

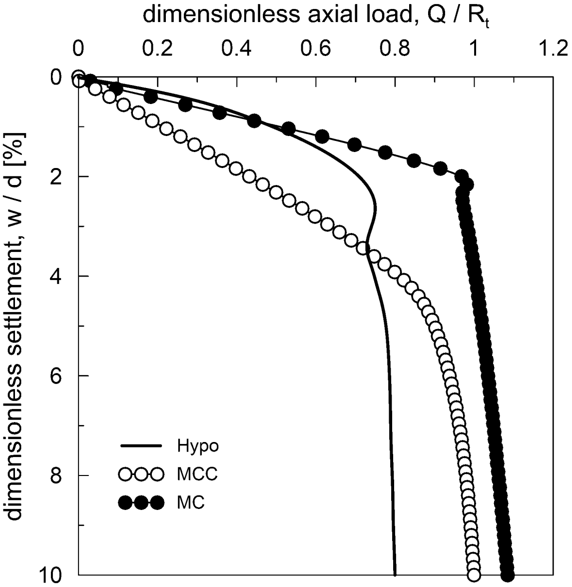

Figure 5.2. Load settlement curves from different soil models.

While the MC and the MCC show a quite similar response at large displacements (i.e., similar pile capacities), the Hypo model certainly attains lower value. It has to be noted that the soil stiffness used for the MC model has been calibrated in order to give the same settlement as for the Hypo model at a load level of $Q/R_t \sim 40\%$ (i.e., $FS = R_t/Q \sim 2.5$).

Considering, as an example, a soil element along the pile shaft at a depth of 6m, it is possible to represent the load paths in terms of the stress invariants q and p' (Fig. 5.3). For the MC model, q and p' increase with increasing the load until the yield surface is reached; after that, the stress path moves backward with a reduction of both q and p'. With the MCC, the path shows an initial decrease of the mean effective stress while the deviatoric stress increases; the load path tends to the critical state line. The response of the Hypo model is mainly dominated by a stronger decrease of the mean effective stress with a final value of the deviatoric stress almost unchanged.

In figure 5.4 the stress path is plotted in the deviatoric plane. In terms of the third invariant, the Lode angle varies during the loading phase decreasing from the initial value corresponding to the triaxial compression, 60°. Compared to the other models, for the Hypo model this reduction is more evident. The final value of the Lode angle is 30°, 45° and 49° respectively for the Hypo, the MCC and the MC models. These dissimilarities at local scale determine a quite different response in terms of the global performance of the pile.

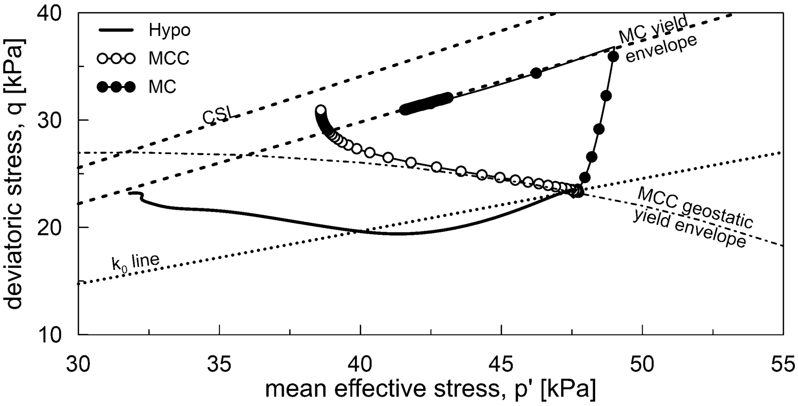

Figure 5.3. Load paths in *q-p'* plane.

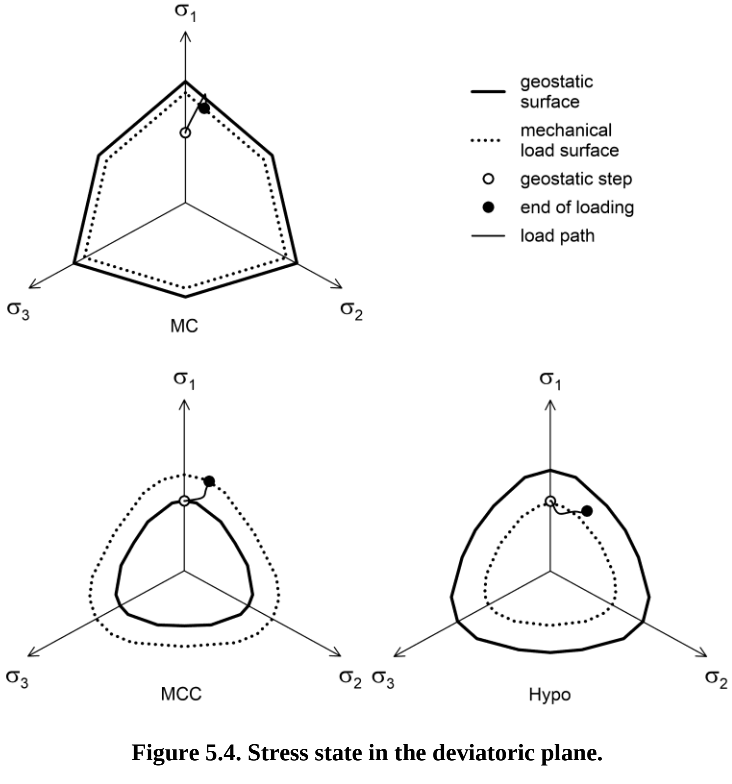

Figure 5.4. Stress state in the deviatoric plane.

The level of mechanical load to employ in the thermo-hydro-mechanical analyses has been selected with reference to the conventional pile capacity evaluated with the analytical formulae, R_t, and it has been chosen in order to represent specific conditions:

- working conditions, Q/R_t = 30%, corresponding to a global factor of safety FS = 3.3 as for conventional pile design;
- close-to-failure conditions, Q/R_t = 80%, corresponding to a global factor of safety FS = 1.25 as for piles as settlement reducers.

In figure 5.2 the FE analysis results for the Hypo model show that the capacity of the pile is about the 80% of the conventional capacity evaluated with the formulae; for this reason, when the Hypo model is employed, a mechanical load equal to the 60% R_t has been considered rather than the 80% R_t. In table 5.2, for each model, the applied mechanical load level is reported with respect to the conventional capacity, R_t, and to the capacity obtained through the FE analyses at a w = 10%d, R_{FEM}.

	Q/R_{FEM}		
Q/R_t	MC	MCC	Hypo
30%	28%	30%	38%
60%	-	-	75%
80%	74%	80%	-

Table 5.2. Mechanical load levels.

5.2.Thermal loading phase

As detailed in paragraph 5.2., the mechanical loading phase is followed by a thermal stage in which the temperature of the pile is varied during the year for a total of 5 thermal cycles. In the following, the choice of the boundary conditions imposed at pile head is discussed and the thermal field generated during the cyclic variation of the temperature is presented. Then, the response using increasingly complex models, accounting for the effect of non-linearity, irreversibility and cyclic behaviour under thermal loading, is reported. For each constitutive model, the behaviour of the foundation is analysed at both global and local scales. In particular, the global response gives an idea of the performance in terms of settlements and axial load, whose maximum values can affect the choices at the design stage for both mechanical and thermal loads; while the analysis of the local response allows a more thorough understanding of the system global performance.

5.2.1. Free- and fixed-head pile condition

Piles are usually connected by a raft at their top. Consider an energy foundation in which the piles have the same geometrical and mechanical features and are sufficiently spaced not to be affected from the thermal field generated by the neighbour piles. If the raft is not in contact with the ground and all the piles are thermally activated, the whole structure moves up and down following the expansion and contraction of the piles. Since all the piles experience the same temperature variation simultaneously, no extra axial force develops at head whereas settlements may grow cycle after cycle. Therefore, each pile can be seen as a single energy pile free to move at head. On the other hand, if only one pile is thermally activated and the raft is in contact with the ground, the other piles, connected to the active pile by the raft, contrast the pile elongation and shortening with their axial stiffness; as a consequence, the head movement is prevented and extra force develops. The stronger the constrain imposed to the energy pile the larger the thermally-induced axial force. In this configuration, the active pile can be seen as a single pile restrained at head; moreover, if the raft stiffness and the number of inactive piles are sufficiently large, the head movements can be considered as fully restrained.

With reference to a piled raft foundation in which not all the piles are thermally-activated, the axial force can be evaluated employing the analytical approach proposed in Chapter 2. In particular, the exact analytical solutions for the cases of homogeneous and Gibson soils have been used to calculate the axial force at the head of a pile surrounded by inactive piles, N_{head}, and the axial force at the head of a fixed-head energy pile, N_{fixed}, for comparison.

To account for the restraint at head due to the presence of non-energy piles, k_t has been estimated from the stiffness of the group neglecting the contribution of the raft since the increment of the global stiffness would have been of the 10% at most (Clancy and Randolph, 1993). In particular, the stiffness of the inactive piles has been evaluated from the axial stiffness of the single pile (Randolph and Wroth, 1978) considering the interaction effect (Butterfield and Douglas, 1981). As a first approximation, the efficiency of the group has been calculated as $(n_{inactive\ piles})^{0.5}$, where $n_{inactive\ piles}$ is the number of inactive pile

In figure 5.5a the ratio N_{head} / N_{fixed} is reported as a function of $n_{inactive\ piles}$, over the number of active piles, $n_{active\ piles}$, for different pile-soil stiffness ratios and pile geometry. It can be noted that: (i) the case in which all the piles are activated, i.e. $n_{inactive\ piles}$ / $n_{active\ piles} = 0$, is characterized by $N_{head} = 0$; (ii) when one pile is inactive per each active pile, the load at head is about 0.5 N_{fixed}; (iii) it is necessary a number of 5 inactive piles per each active pile, to have N_{head} / N_{fixed} varying in the range 0.75÷0.8. In figure 5.5b the same curve is plotted for the case of the London clay modelled in the FE analyses.

It can be concluded that, in most practical applications involving piled rafts with energy piles, the load at head is very close to N_{fixed}, while a group of active piles behaves as a free-head pile.

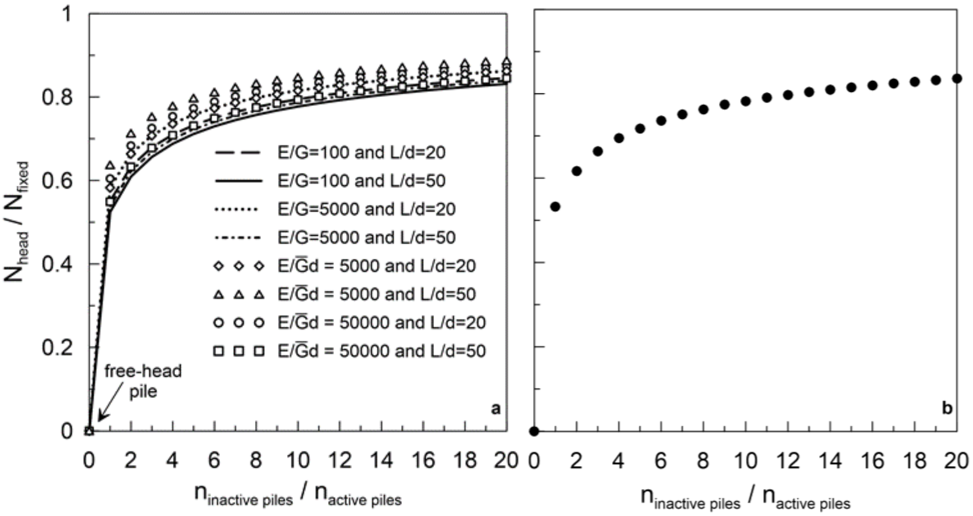

Figure 5.5. Axial load variation at pile head with respect to the number of inactive piles: a) homogeneous and Gibson soil, b) London clay.

In general, the geometrical configuration of the system, the stiffness and mechanical properties and the number of active piles can be very different from the ideal configurations aforementioned. The performance of the system is strongly related to the interaction between the piles, especially in terms of heat diffusion in the soil toward the non-energy piles. As a result of the transient conduction process, the degree of restraint can decrease in time since the inactive piles can be affected by the temperature field generated by the active pile, allowing a reduction of the axial load and the increase of the settlements. Regarding the latter, it has to be noted that, the interaction factor, ratio between the additional displacement due to the adjacent pile and the displacement of the single isolated pile, is approximately lower than 0.1 when the ratio *s/d* (i.e. pile spacing over pile diameter) is higher than 3 (Rotta Loria et al., 2016a). Therefore, considering that usually not all the piles of a foundation are energy piles, it can be neglected. It follows that the real behaviour of energy foundations in terms of thermally-induced axial force and settlements lies in between the two aforementioned limiting conditions. Further comments on the restraint imposed at head will be provided in section 5.2.7.

In the present analyses, to simulate the case of no thermally-induced axial load at head and cyclic settlements, numerical analyses modelling a free-head energy pile have been carried out. Moreover, to assess the maximum value of the axial load, a single energy pile blocked at head has been also modelled.

5.2.2. Thermal field

The mechanical loading stage is followed by an increase of pile temperature up to 29°C (Fig. 5.6). During the heating phase, only the soil in the vicinity of the shaft and the base reaches the maximum imposed temperature, while the remaining part is undisturbed and its temperature corresponds to the initial value of 15°C.

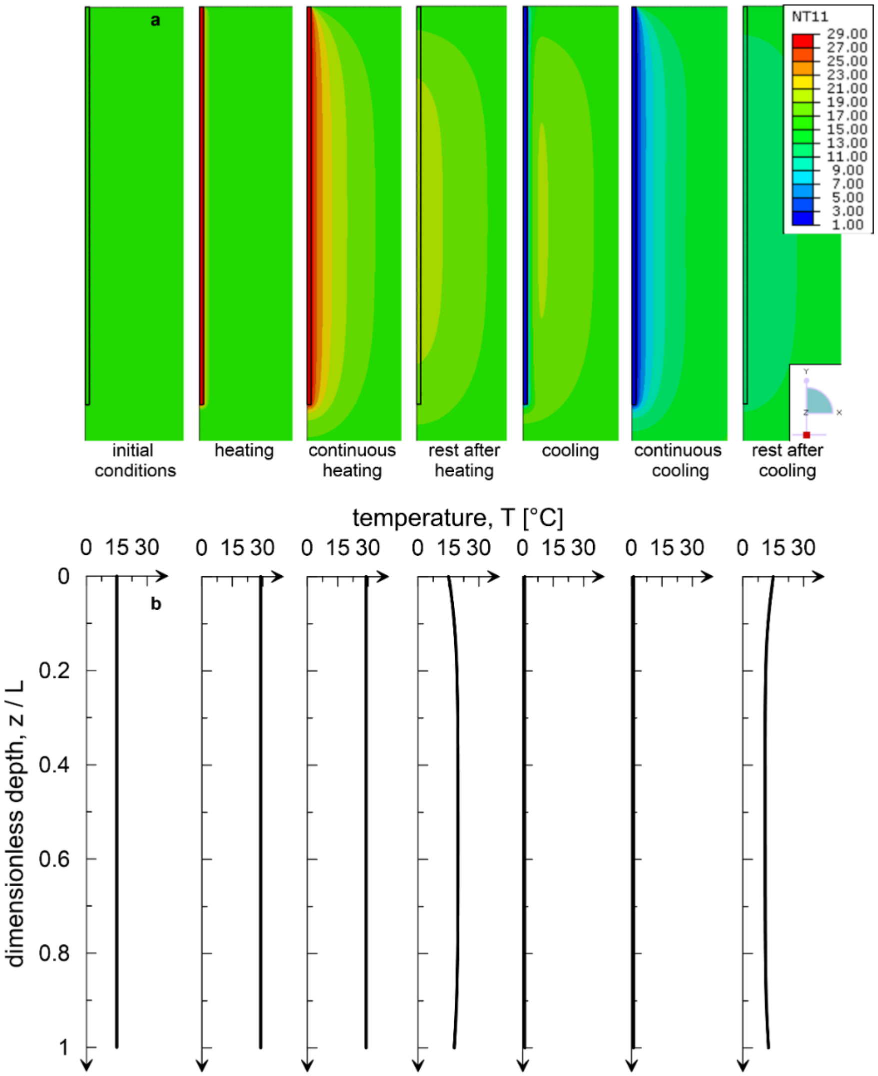

Figure 5.6. Temperature distribution in the I cycle: a) pile and soil, b) along the pile.

The heat conduction takes place mostly during the following phase in which the temperature of 29°C is kept constant for 5 months. Therefore, in this phase of continuous heating, the heat flux affects an increasingly wide portion of the soil surrounding the pile (Fig. 5.6a). After that, a rest step is simulated in which no temperature is imposed and a thermal equilibrium is reached according to the boundary conditions of the model. This implies that the pile temperature decreases with time, except at its top where the boundary condition imposes a fixed value of 15°C (Fig. 5.6b); along the shaft, the temperature ranges between 19°C and 15°C.

The following step is characterized by a decrease of the pile temperature up to 1°C. The cooling phase influences just the soil in the vicinity of the pile. In fact, as for the continuous heating, the heat conduction plays a major role only when the value of 1°C is kept constant for 5 months (continuous cooling). Then, a new rest phase is performed in which the pile gets a variable temperature, equal to 15°C at head, slightly lower in the central sections (about 11°C) and at base (Fig. 5.6b).

At the end of the first cycle the temperature distribution in the pile and in the soil is different from the initial conditions in which T_0 = 15°C everywhere (Fig. 5.7). As a consequence, the second cycle starts from a different temperature scenario that corresponds to the rest phase after the continuous cooling of the first cycle. Likewise, the cycles from the third onward start from the rest phase of the previous cycle and are characterized by similar initial conditions as that of the second cycle (Fig. 5.7).

Since in the present analyses the heat transmission is solely by conduction, the thermal variation imposed to the pile lead to a thermal field that is the same regardless of the constitutive model chosen to simulate the soil behaviour.

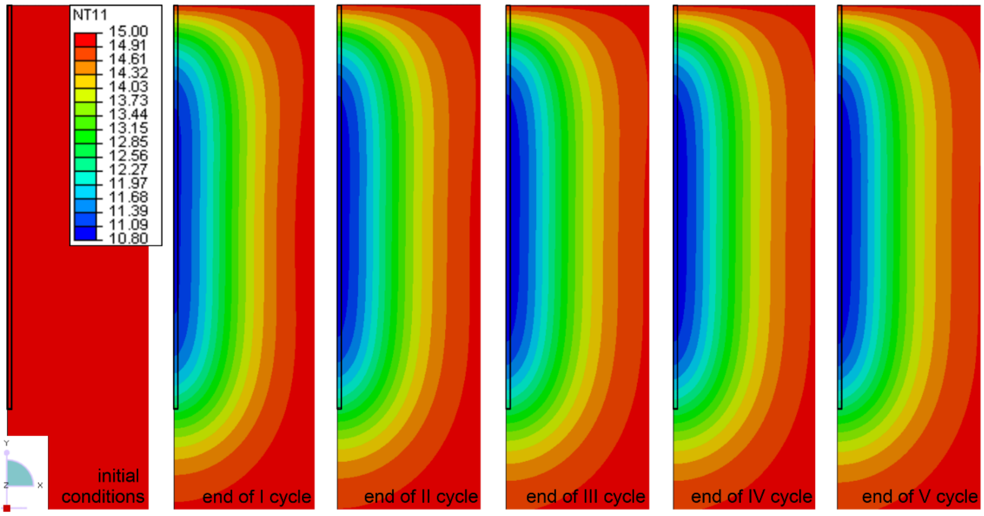

Figure 5.7. Temperature variation [°C].

5.2.3. Elastic model

5.2.3.1. Free-head pile

Starting from the simplest model, it is possible to have a reference solution in the realm of elasticity. It is worth noting that, since the model is elastic, the overall performance of the pile is qualitatively the same regardless of the applied mechanical load at pile head, the only difference being in the magnitude.

In figures 5.8 and 5.9 the variation of the axial force throughout the first thermal cycle is reported. The data shown are referred to the free-head pile for the applied mechanical load levels of 30% R_t and 80% R_t, respectively. As in the analytical solution provided in Chapter 2, the performance of energy piles in terms of axial loads is mainly ruled by the difference of temperature and the stiffness mismatch between pile and soil.

When the pile is heated its free expansion is partly prevented by the surrounding soil; this implies a thermally-induced axial compression along the pile shaft and at its base, that sums up with the mechanical axial load. The expansion of the pile results into an opposite movement of its two extremities: on one hand, the upper part of the pile moves upward causing the development of negative skin friction; on the other hand, the lower part moves downward and the additional skin friction has the same direction as that due to the mechanical axial loads. As a consequence, along pile length there is a depth characterized by zero thermally-induced strain, the null point. If the restraints existing at pile head and tip are the same, the null point is located at the pile mid length. In figure 5.10 it is possible to notice that, for the elastic analysis, since the stiffness of the soil is increasing with depth and no constraint is imposed at head, the position of the null point is closer to the pile tip and corresponds to about 17.25m.

As the process goes on, owing to heat conduction, a wider portion of the soil follows the pile movement leading to a decrease of the thermally-induced force and, hence, of the overall force. From figures 5.8a, and 5.9a it is evident that the thermally-induced compression is maximum at the beginning of the heating since solely the soil in the vicinity of the pile experiences the same temperature variation as the pile itself (Fig. 5.5a), while the remaining part has a temperature corresponding to the initial one.

In the rest step, the thermal equilibrium is reached according to the thermal boundary conditions of the model, which lead to the reduction of the temperature of both pile and soil comparable to the initial increment. It follows that the thermally-induced axial force profile places to the left of that induced by the mechanical load.

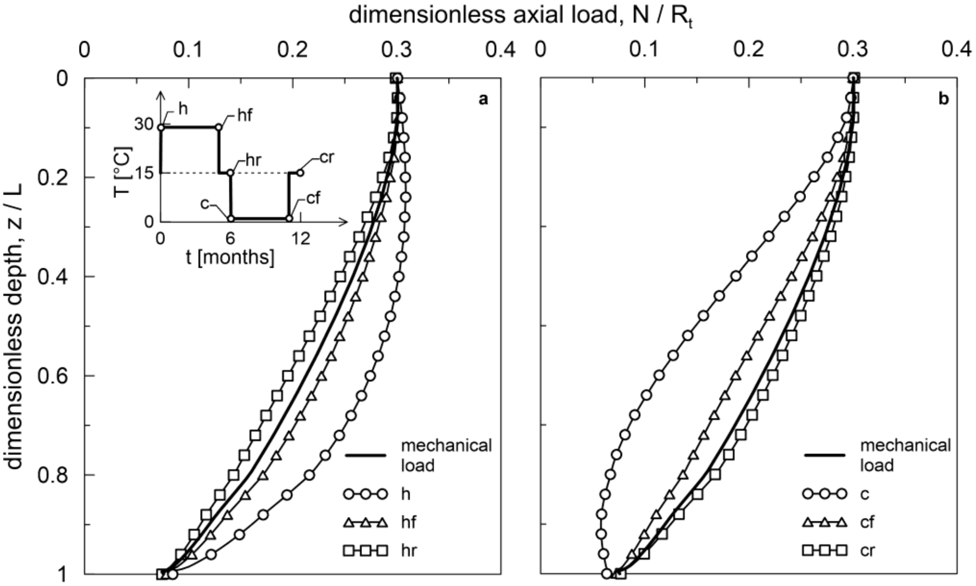

Figure 5.8. Axial load distribution in the I cycle, free-head pile (E model, *Q* = 30% *R_t*).

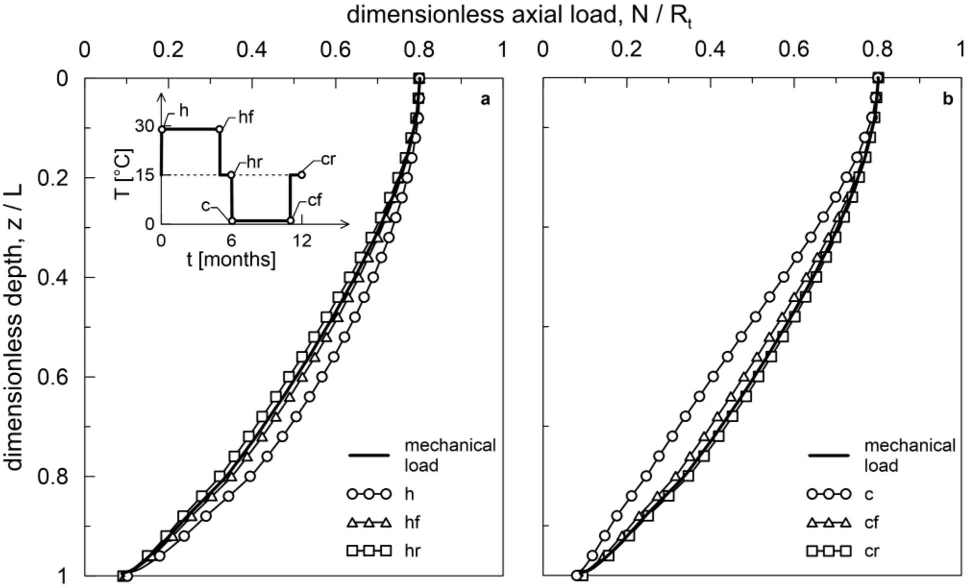

Figure 5.9. Axial load distribution in the I cycle, free-head pile (E model, *Q* = 80% *R_t*).

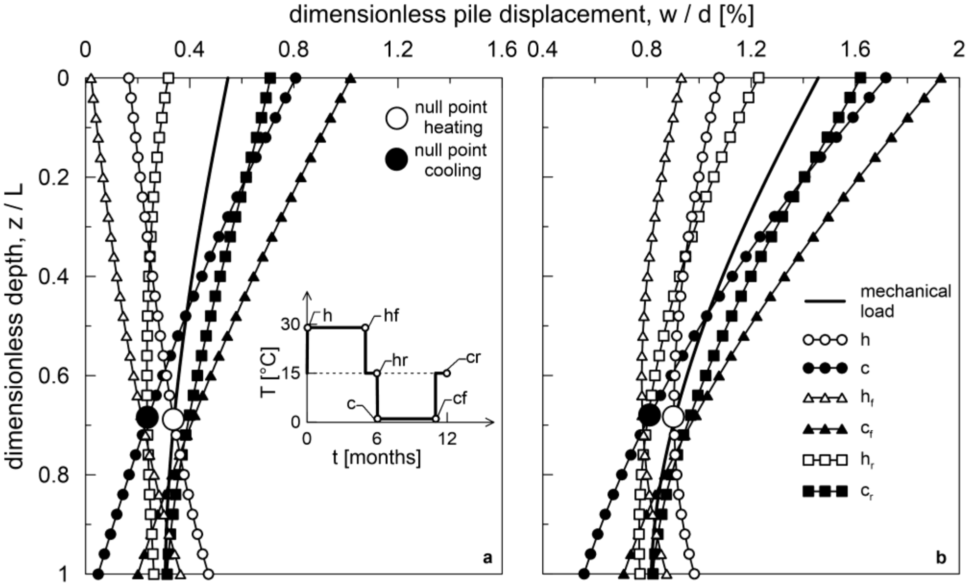

Figure 5.10. Dimensionless displacement of the pile along its length in the I cycle, free-head pile (E model, a: *Q* = 30% *R_t* and b: *Q* = 80% *R_t*).

The effect of temperature reversal on the axial load is reported in figures 5.8b and 5.9b. During cooling, the upper part of the pile moves downward with development of positive skin friction, while the lower part goes upward showing negative skin friction (Fig. 5.10). The soil opposes to pile shortening and the generated tensile stress determines the reduction of the axial load. The null point is located at the intersection between the displacement profiles of the rest after heating and the cooling steps, at a depth of about 17.25m. As in the continuous heating phase, during continuous cooling the temperature decrease involves further portion of the soil and, therefore, the tensile thermally-induced axial force reduces leading to an increase of the total axial force. A further increase is encountered in the following thermal rest phase, in which the pile temperature, although variable with depth, grows up. This final configuration attained at the end of the first cycle is different from the configuration at the end of the mechanical loading phase and represents the starting point of the second cycle.

As shown in figures 5.8 and 5.9, for the free-head pile, the overall axial load distributions in heating and cooling phases are the maximum and minimum load that the pile experiences during the individual thermal cycle. From here onward, reference is made just to these maximum and minimum profiles.

As concerns the cyclic behaviour, in figure 5.11 the settlements along pile length are reported for the I, the II and the V cycles. Since the model is elastic, the position of the null points remains the same.

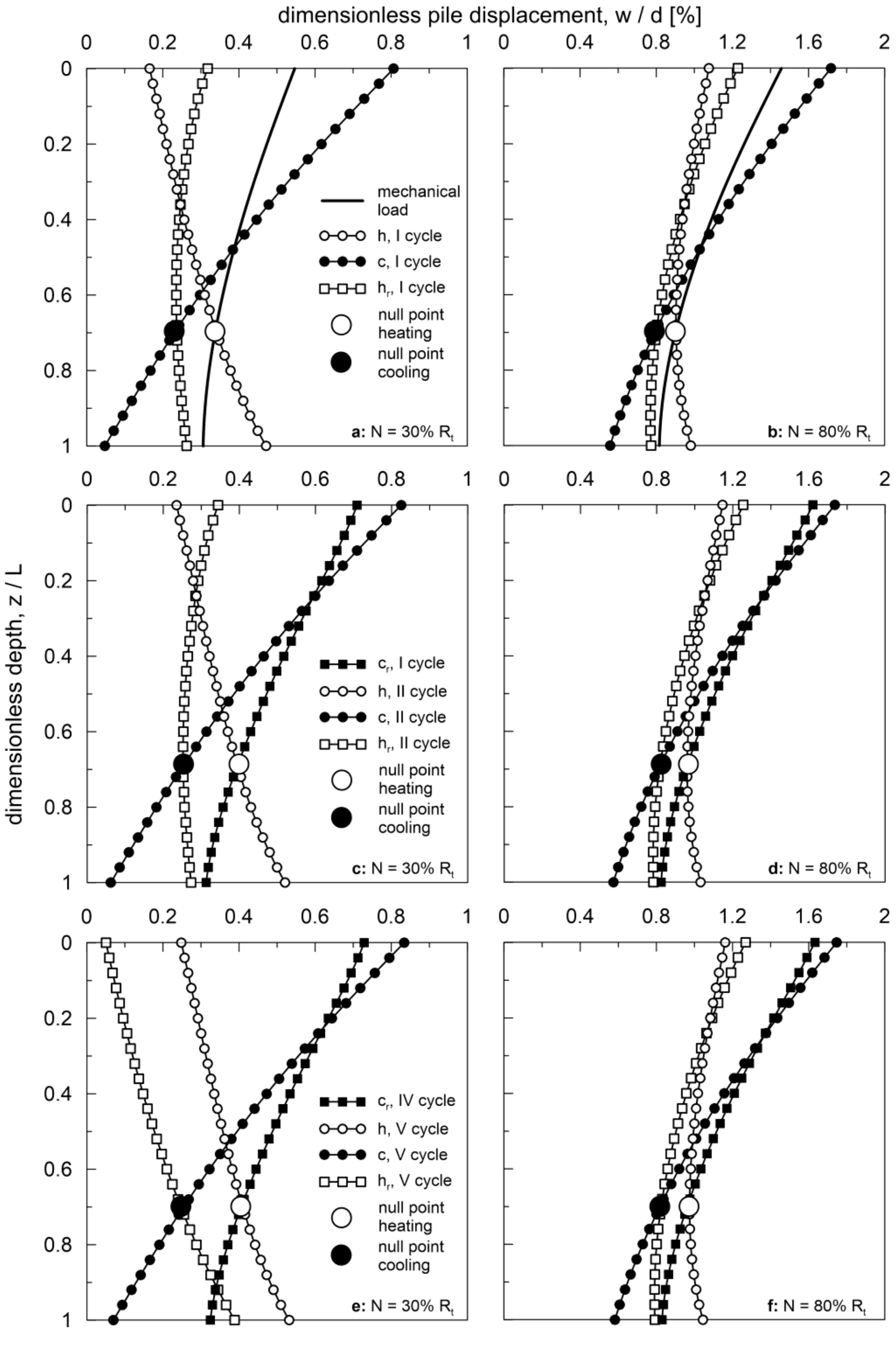

Figure 5.11. Dimensionless displacement of the pile along its length in the I, II and V cycles, free-head pile (E model).

The axial load profiles and the settlements after performing multiple cycles are reported in figures 5.12. and 5.13. The slight difference appearing in the values of the first and the other cycles is due to the different initial condition. The highest thermally-induced loads are equal to about 6% R_t and -8% R_t for heating and cooling, respectively. During the heating phase, when the applied mechanical load is equal to 30% R_t, the maximum axial force is located along the shaft rather at head and is equal to the 32% R_t; while when the applied mechanical load is 80% R_t, the maximum force remains at head. During cooling, the thermally-induced tensile load lead to an overall compressive axial force whose maximum value is at head.

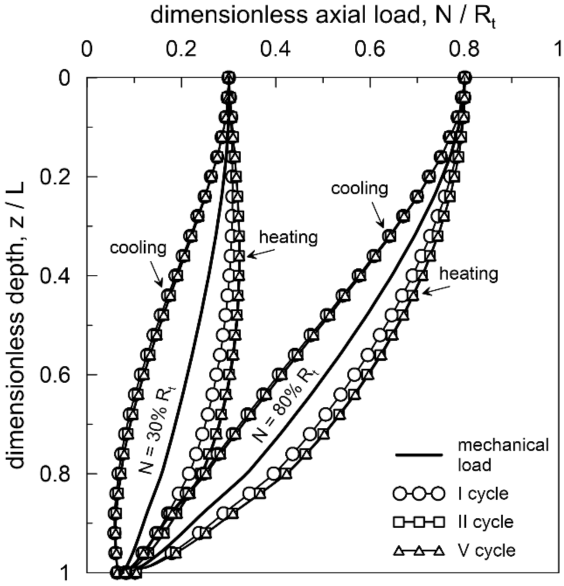

Figure 5.12. Axial load distribution in the I, II and V cycles, free-head pile (E model).

Regarding the displacements, during the heating phase, the pile head moves upward recovering part of the settlement experienced after the application of the vertical load. In the continuous heating, while further portions of the soil are solicited by temperature change, additional upward movements occur. The rest phase, characterized by a decrease of pile temperature, is, therefore, dominated by downward movements. The opposite behaviour of the pile is expected to occur during the next six month of reverse temperature condition. Since the model is elastic, no accumulation of irreversible settlement is possible from cycle to cycle; the pile head moves up and down cyclically experiencing the same displacement. At the end of the mechanical loading phase the pile settlements are equal to 0.57% *d* and to 1.48% *d* for the load levels of 30% R_t and 80% R_t, respectively. The maximum and minimum values of the thermally-induced settlement are recorder during the continuous cooling and continuous heating, their magnitude being about ± 0.50% *d*.

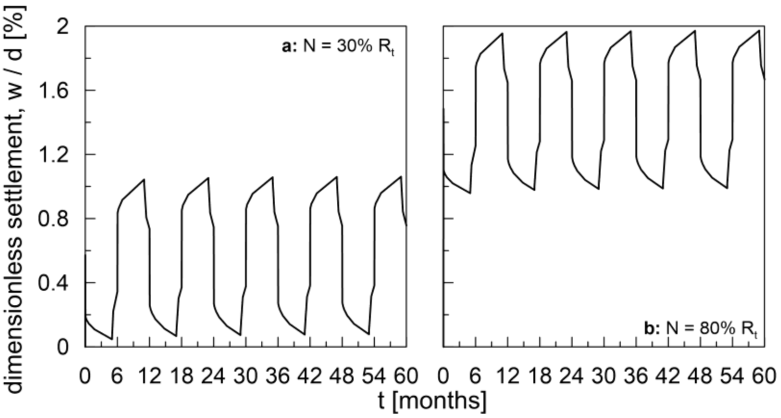

Figure 5.13. Dimensionless global settlement, free-head pile (E model).

It can be noted that, since the thermally-induced axial force and settlement are the same for both load levels, the higher the applied mechanical load, the lower the impact of the temperature variation on the axial force profile and on the displacement at head.

The performance of the pile can be analysed in detail looking at the local scale. In particular, the local response of the pile has been explored at 4 different depths. The pile has been divided in 4 parts of equal lengths; the elements under investigation are located at the pile-soil interface and underneath pile base at the following depths: 6.25m, 12.50m, 18.75m and 25m.

Compressive loads and volumetric contraction are taken as positive.

The behaviour in terms of excess pore pressure and volumetric strain has been analysed in figures 5.14 and 5.15. Reference is made to the applied mechanical load of 80% R_t.

The magnitude of the excess pore pressure depends on the element position with respect to the surface level. The following relation holds (Campanella and Mitchell, 1968):

$$\Delta u = \frac{n \Delta T \left(\alpha_w - \alpha_s\right) + \alpha_{st} \Delta T}{m_v + n m_w} \tag{5.10}$$

where, n is the porosity of the soil; ΔT is the applied temperature variation; α_s and α_w are the thermal expansion coefficient of soil grains and water, respectively; α_{st} is the physic-chemical coefficient that takes into account the volumetric strain due to the temperature induced change of the interparticle forces; m_v and m_w are the compressibility of soil structure and of water, respectively. In the present study, all the models employed, except for the thermo-hypoplastic model, are not capable to account for the physic-chemical effects. Since $m_v >> m_w$, the compressibility of water can be neglected. Therefore, in saturated soils, the excess pore pressure generated by the temperature variation are associated to the fact that the thermal expansion coefficient of water is bigger than that of soil grains. Anyway, the excess pore pressure is proportional to ΔT and increases with increasing the soil stiffness. Since the stiffness employed in the model varies with the stress state of the soil and, therefore, with depth, the maximum value of the excess pore pressure is expected to occur in the vicinity of pile tip. As shown in figure 5.14 this is confirmed by the results of the finite element analyses; in fact, the excess pore pressure attains the highest values when the applied temperature variation is maximum, with a magnitude that increases with depth (8kPa, 14kPa, 17kPa and 44kPa from the topmost element to the element underneath the tip). Looking at the single cycle, just before the temperature reversal, the excess pore pressure is dissipated and no accumulation is possible from one cycle to the other. The maximum excess pore pressure compared with the local effective vertical stress σ'_{v0} develops at 6.25m; this ratio $\Delta u/ \sigma'_{v0}$ decreases with increasing depth.

As regards the volumetric behaviour, at the end of the mechanical phase, the elements along pile shaft undergo compression decreasing with depth; from the top to the bottom, values of about 0.03%, 0.012% and 0.01% are shown (Fig. 5.15a, b, c). The maximum compression of 0.3% is attained underneath pile base (Fig. 5.15d). When the temperature increases, volumetric expansion develops with different magnitude depending on the position of the element. The elements along pile shaft are subjected to about the -0.09% of expansion, while the element at the base experiences a lower dilation equal to -0.04%, because its expansion is contrasted by the downward movement of pile tip. In continuous heating, as dissipation of positive pore pressure takes place (Fig. 5.14), contraction along pile shaft develops; about the 0.025% of the previous expansion is recovered. Underneath the tip, contraction takes place first, followed by a slight expansion due to temperature spread in the surrounding soil; in this step, the overall compression is of about the 0.018%. During the rest phase, the reduction of the temperature is followed by the development of further compression with values equal to 0.059%, 0.052% and 0.05% along the shaft and to 0.004% at the base. The following cooling phase is characterized by compression of about 0.13% along the shaft and 0.05% underneath pile tip, that gets progressively lower in magnitude when cooling is maintained for 5 months as a consequence of the negative pore pressure dissipation. During the continuous cooling the expansion along the shaft reaches the value of -0.04%, while at the base the value of -0.012% is observed. The further expansion following the final rest phase is equal to -0.062%, -0.056%, -0.054% and -0.003% for the elements located at 6.25m, 12.50m, 18.75m and 25m, respectively. It can be concluded that the elements along the shaft are characterized by volumetric contraction and expansion of the same order of magnitude, while at pile base expansion is mostly prevented.

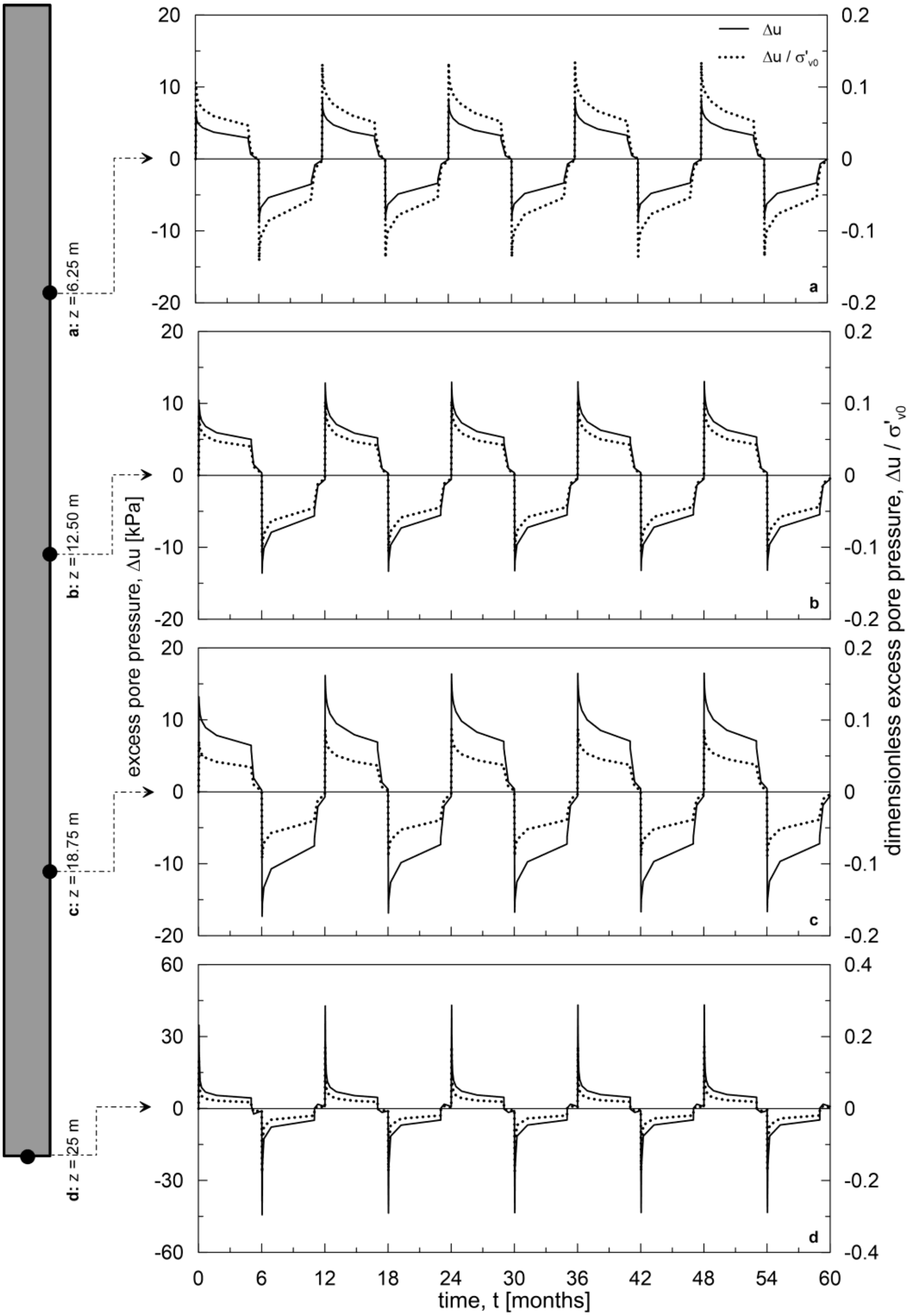

Figure 5.14. Excess pore pressure, free-head pile (E model, Q = 80% R_t).

During the following cyclic variations of the temperature, closed loops are experienced. In particular, the overall maximum expansion and compression are attained during the heating and cooling phases respectively, their values being equal to -0.08% and 0.15% at 6.25m, -0.09% and 0.12% at 12.5m and -0.09 and 0.11% at 18.75m. The element at 25m is characterized by compressive volumetric strains solely; the maximum value is attained at the end of the cooling phase and is equal to about 0.33%. The end of each cycle lead to positive overall values of the volumetric strain; in particular, with respect to the end of the mechanical phase, the compressive strain is increased of the 47%, 107%, 123% along the shaft, while it remains almost constant underneath the tip.

After the application of the mechanical load, the shear strain and the local settlement (Fig. 5.16) are equal to 0.52% and 1.24% *d* at 6.25m, 0.44% and 1.04% *d* at 12.5m and 0.39% and 0.88% *d* at 18.75m. Above the null point, upward movements along with reduction of the shear strain are experienced during heating and rest after cooling. Compared to the mechanical step, the highest variation of the shear strain occurs in heating and cooling, while, for the local settlement, after 5 months of maintained heating and cooling (±8% and ±28%, ±5% and ±18% for the elements located at 6.25m and 12.5m respectively). Below the null point, the shear strain and the settlements reduce during the rest after heating and the cooling; for the element at 18.75m, the maximum variations with respect to the mechanical phase, are equal to ±9% and ±10%, respectively. Underneath pile tip the behaviour is dominated by volumetric strains and cyclic settlements (0.82% *d* after the application of the mechanical load with a variation of ±28%) with basically no development of shear components.

Figure 5.17 shows the loading paths in the q-p' plane. For sake of clarity, labels are reported for the first and the last cycles. For all the elements, the starting point of the loading path is the geostatic step. In the geostatic step, the point representative of the initial state is located on the k_0 line, whose slope is equal to $3(1- k_0) / (1+2\ k_0)$. Along the shaft, an increase in temperature corresponds to a decrease of the mean effective stress due to the development of positive pore pressure and to a variation of the deviatoric stress depending on position of the element. In fact, for the elements above the null point q decreases, while the element below the null point are characterized by the increase of q. The opposite occurs when the temperature is reversed. It is important to note that the rest after heating means a decrease of pile temperature if compared with the heating, while the rest after cooling causes the increase of the temperature with respect to the cooling stage. Underneath pile tip, q and p' increase during heating and decrease during cooling.

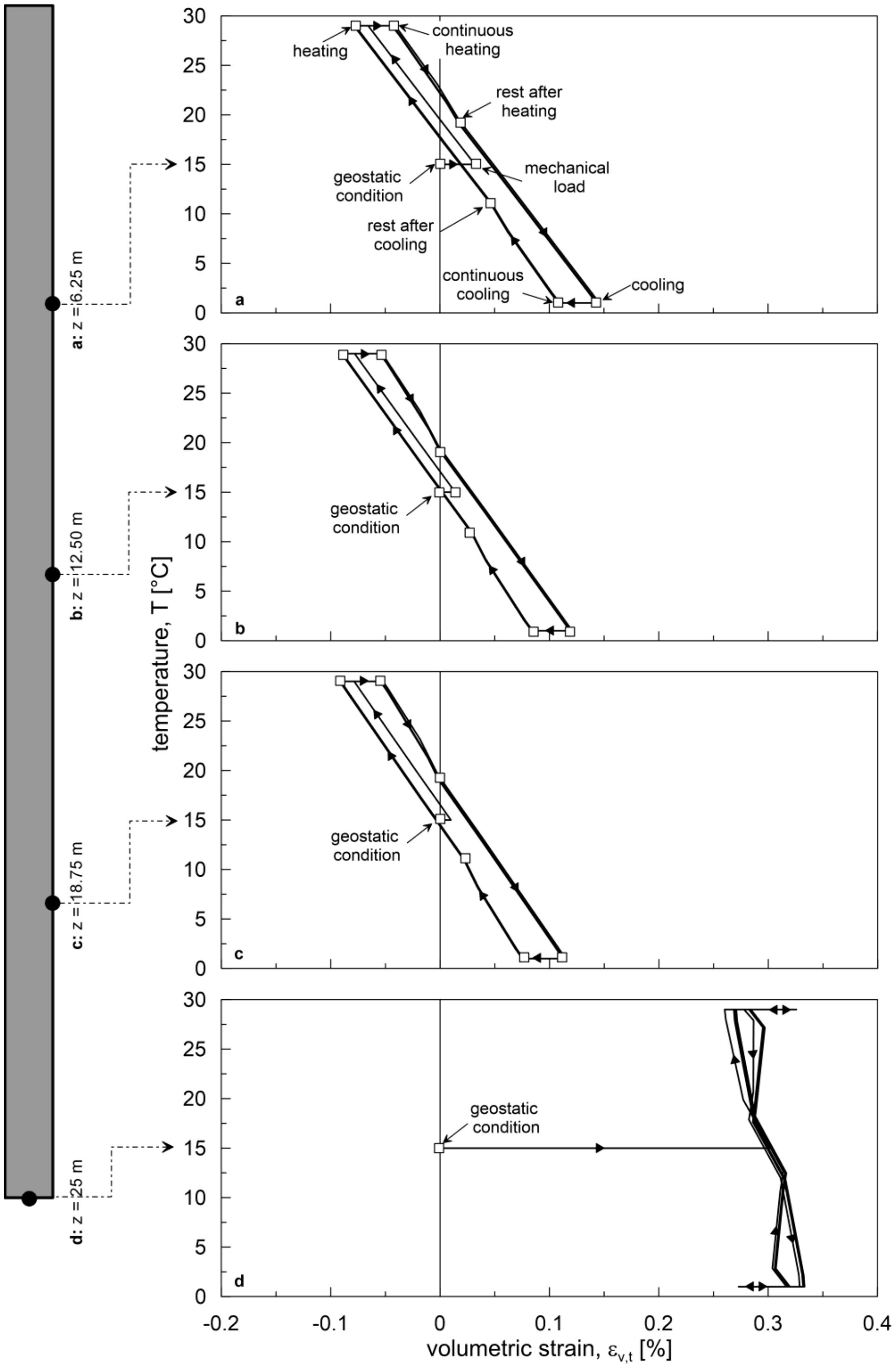

Figure 5.15. Volumetric strain, free-head pile (E model, *Q* = 80% *R*$_t$).

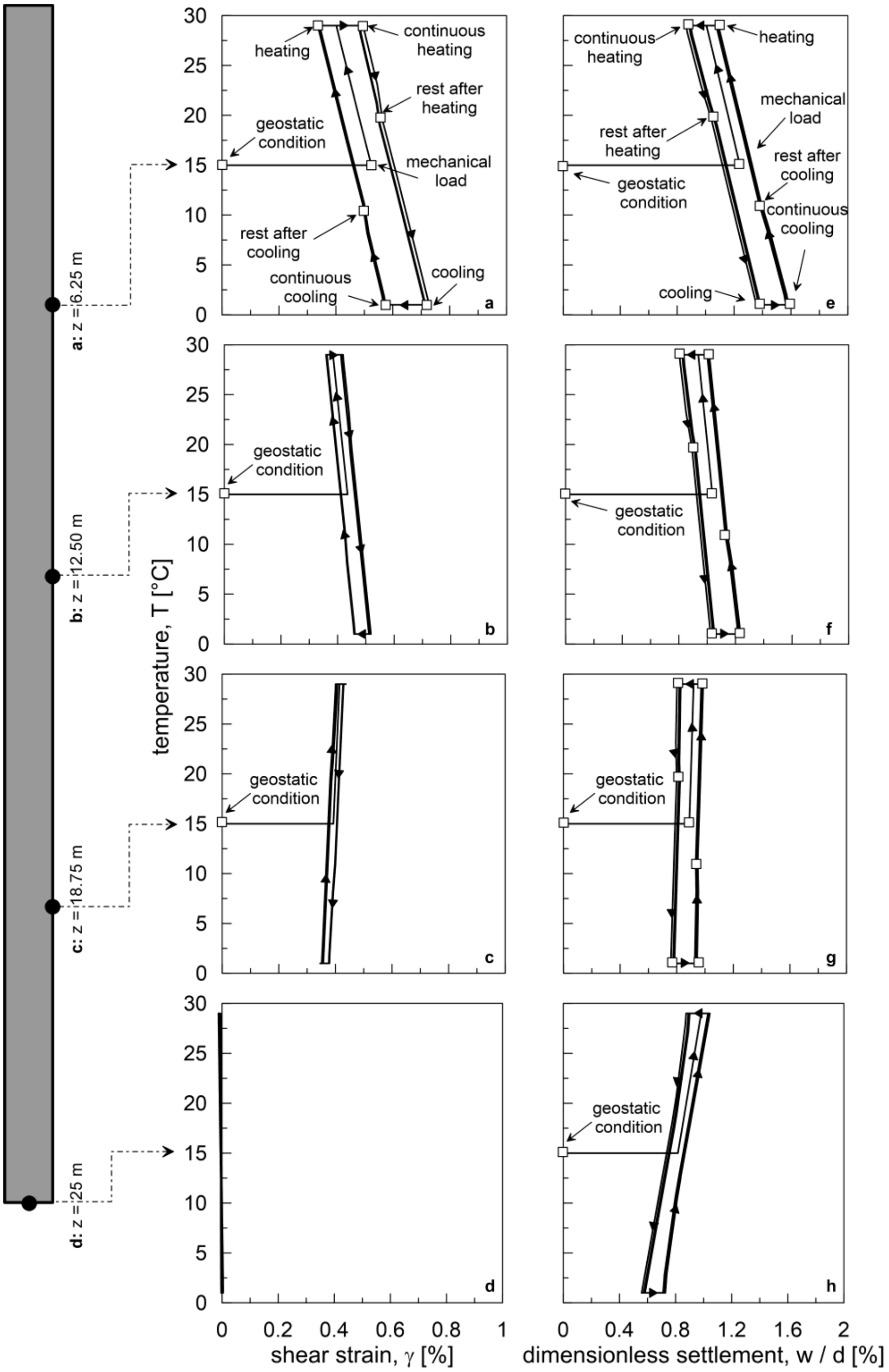

Figure 5.16. Shear strain and local settlement, free-head pile (E model, Q = 80% R_t).

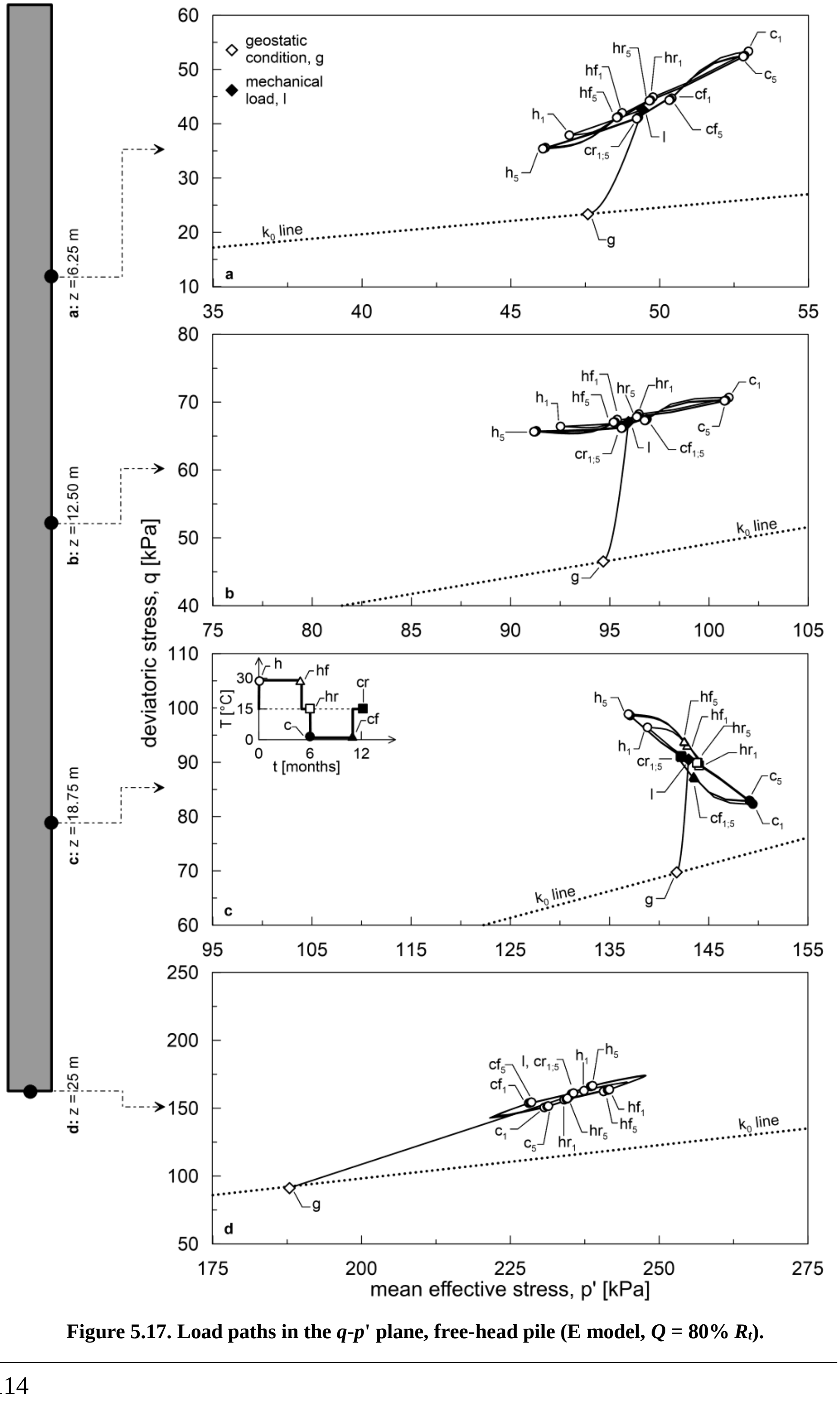

Figure 5.17. Load paths in the *q*-*p*' plane, free-head pile (E model, *Q* = 80% *R*$_t$).

The Linear Elastic model can’t reproduce the effect of plasticity; except for the first cycle, each element is subjected to loading condition that are identical cycle after cycle and, therefore, the loading path moves across the same points cyclically. As a result, there is no difference in the global performance from one cycle to the others.

5.2.3.2. Fixed-head pile

In this section the results related to the single fixed-head pile are analysed. The soil elements nearby the surface are not subjected to any restraint, while the pile head movements due to the thermal load is set to zero.

When the temperature of the pile is increased, the pile elongation is partially prevented by the presence of the soil. As a consequence, compressive axial load develops that sums up with the mechanical load (Figs. 5.18a and 5.19a). After 5 months of continuous heating, due to the heat conduction in the surrounding soil, the axial load at pile head increases (Figs. 5.18a and 5.19a). Indeed, the increase of the soil temperature in farther regions determines a reduction of the restrained upward movement of the pile inducing additional compressive load at head. An opposite behaviour is shown at the tip where the global downward movement induces the reduction of the axial force. The reduction of the thermally-induced axial force is also observed during the rest phase after the continuous heating (Figs. 5.18a and 5.19a).

When the cooling is activated, distinction must be made between the cases in which the mechanical load level corresponds to the 30% and the 80% of the pile bearing capacity. Indeed, if the applied load at pile head is equal to the 30% R_t, the axial force in the deeper section of pile shaft, although still compressive, becomes close to zero (Fig. 5.18b). For both load levels, the continuous cooling induces a further decrease of the axial load at pile head and a slight increase nearby pile base; the same observations as for the continuous heating phase hold. At the end of the first cycle the overall axial force increases and remains lower than that experienced during the mechanical phase.

The highest and lowest values of the load at pile head are observed when the temperature is kept constant for 5 months.

Since the pile is fully restrained at head, the null point is always located at pile head (Fig. 5.20).

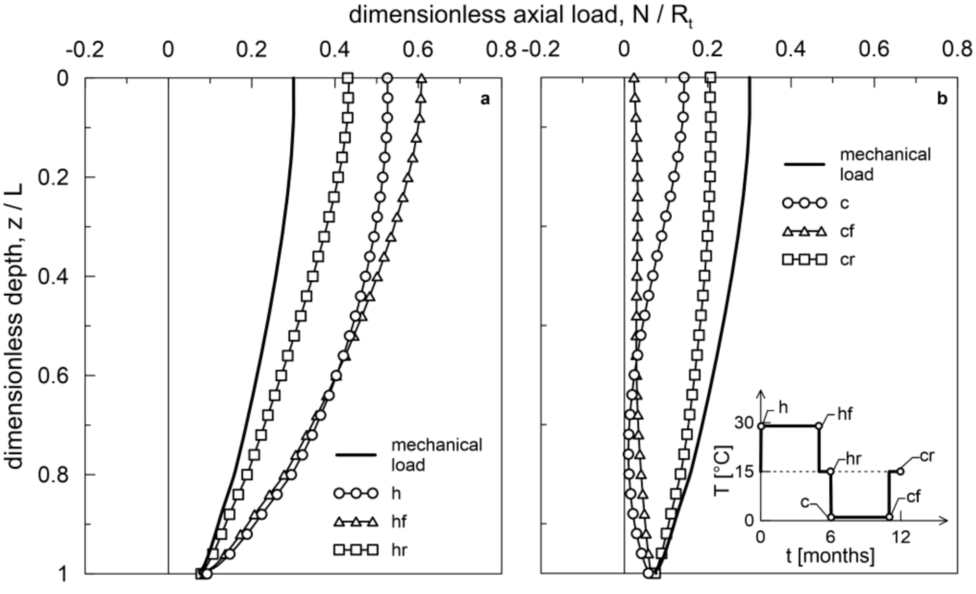

Figure 5.18. Axial load distribution in the I cycle, fixed-head pile (E model, Q = 30% R_t).

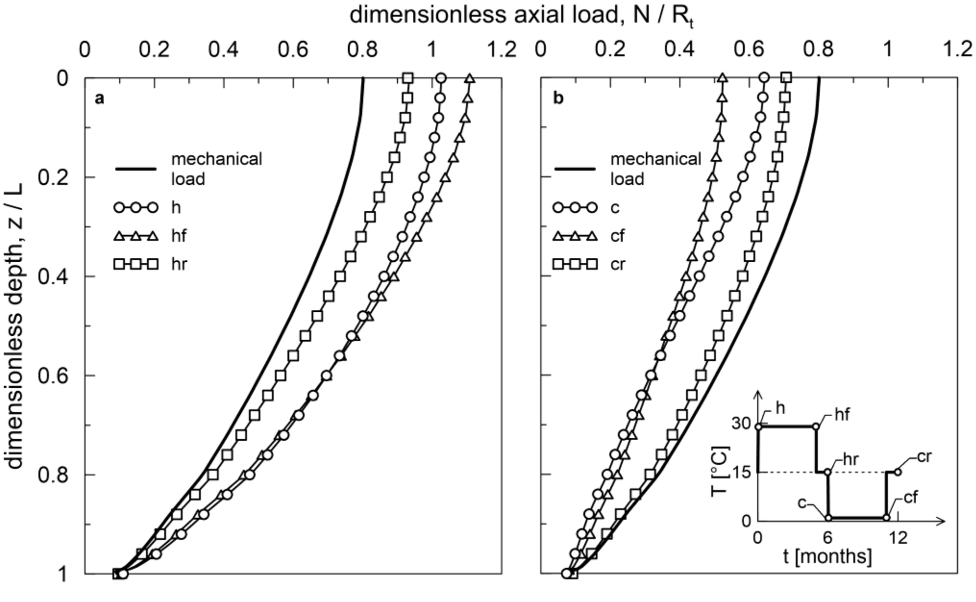

Figure 5.19. Axial load distribution in the I cycle, fixed-head pile (E model, Q = 80% R_t).

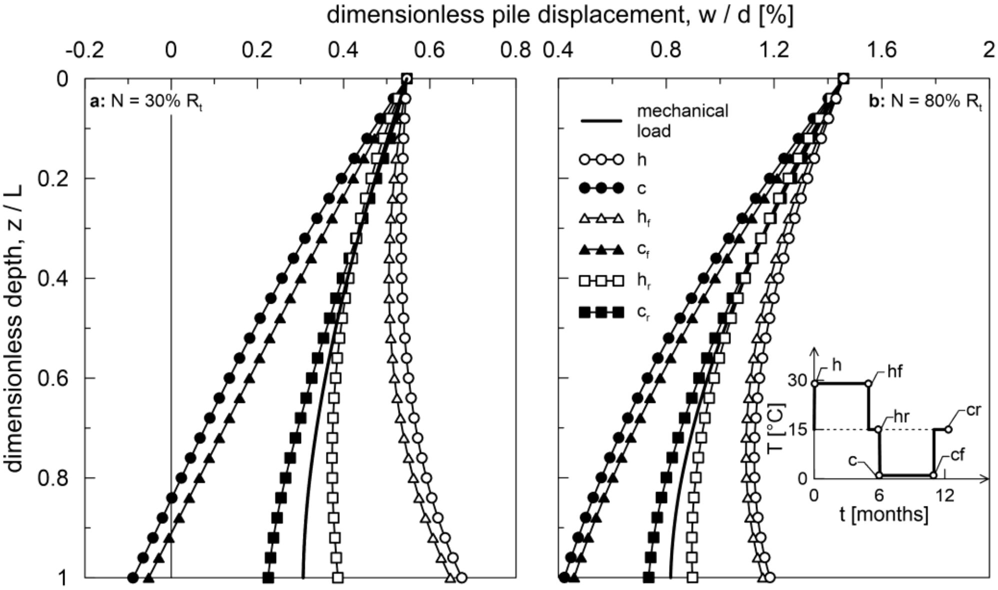

Figure 5.20. Dimensionless displacement of the pile along its length in the I cycle, fixed-head pile (E model).

In figure 5.21 the axial load distribution is reported for the heating, cooling, continuous heating and continuous cooling of the first, second and fifth cycles. As for the free-head pile, the second cycle starts with a different initial condition in terms of temperature, if compared with the first cycle; for this reason, a slight difference in the axial loads is encountered. For both load levels, the highest thermally-induced forces are equal to about ±30% R_t for continuous heating and cooling, respectively. It is worth noting that when the applied load is 80% R_t, the overall load during continuous heating becomes equal to 1.1 R_t; indeed, since the soil constitutive model is linear elastic, failure can never be reached.

In figure 5.22 the settlements along pile length are shown for the heating and cooling steps of the first, second and fifth cycles. At the end of the mechanical loading phase the settlement at pile base is 0.3% *d* for 30% R_t, and 0.8% *d* for 80% R_t. The distributions of the settlement in the various cycles are superimposed. The maximum increase and decrease are found in the heating and cooling phases. For both load levels, these values are equal to ±0.37% *d*.

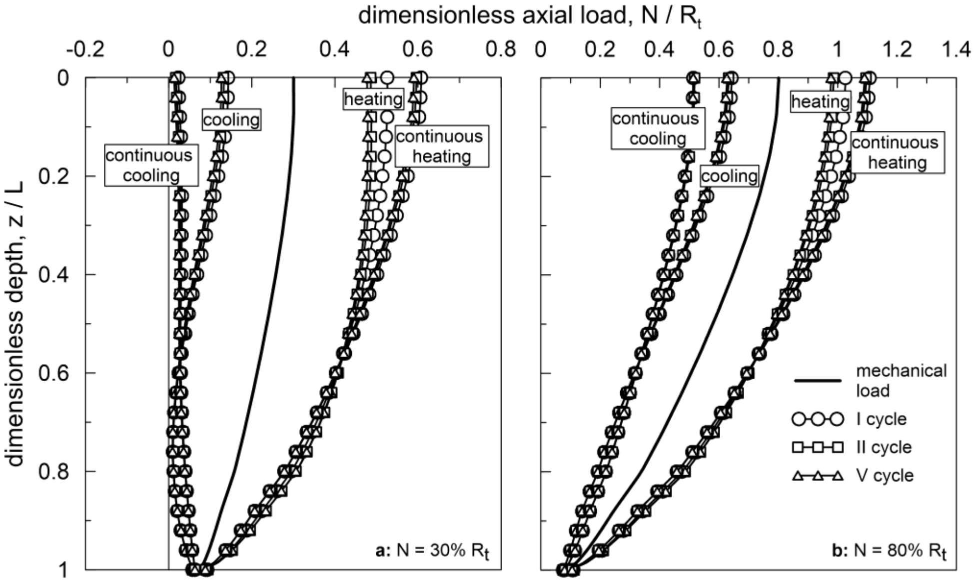

Figure 5.21. Axial load distribution in the I, II and V cycles, fixed-head pile (E model).

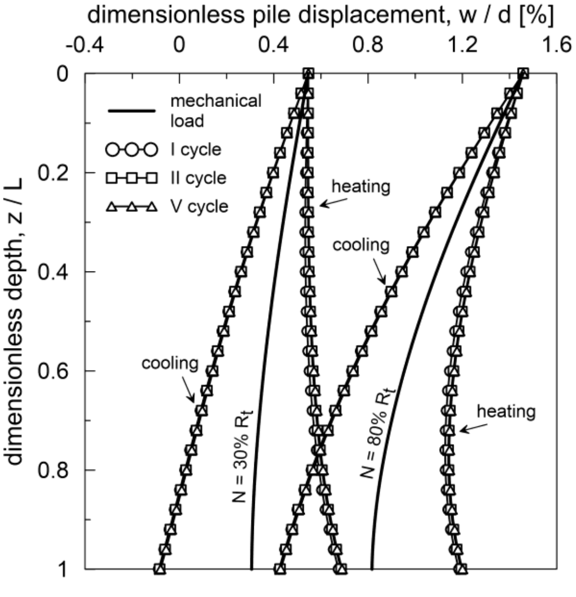

Figure 5.22. Dimensionless displacement of the pile along its length in the I, II and V cycles, fixed-head pile (E model).

5.2.4. Mohr-Coulomb model

5.2.4.1. Free-head pile

In the discussion of the results obtained employing the MC model, distinction must be made between the cases in which the mechanical load level corresponds to the 30% and the 80% of the pile bearing capacity. In the figures reported herein, the axial distribution is shown just for the heating and cooling phases that represent the steps in which the axial load is maximum and minimum, respectively.

When the pile is subjected to the 30% of the its bearing capacity, the overall performance is close to the one explored in the case of the Elastic model. The shallow elements experience plasticity but their paths do not affect the overall performance. In fact, as for the Linear Elastic model, the highest thermally-induced forces are equal to about 6% R_t and -8% R_t for heating and cooling, respectively; the maximum overall axial force is observed along the shaft and is equal to the 32% R_t (Fig. 23). The null point in heating and cooling of the first cycle is located at about 17.25m; its position remains practically constant during the following cycles (Fig. 5.24a, c and f). As concerns the head movements, at the end of the mechanical loading phase the pile settlement is equal to 0.57% *d*. The maximum and minimum values of the thermally-induced settlement during the continuous cooling and continuous heating are about ± 0.5% *d* (Fig. 5.25a).

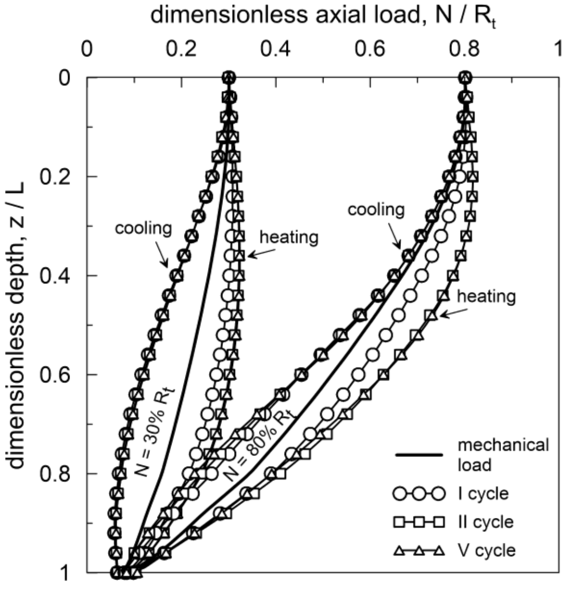

Figure 5.23. Axial load distribution in the I, II and V cycles, free-head pile (MC model).

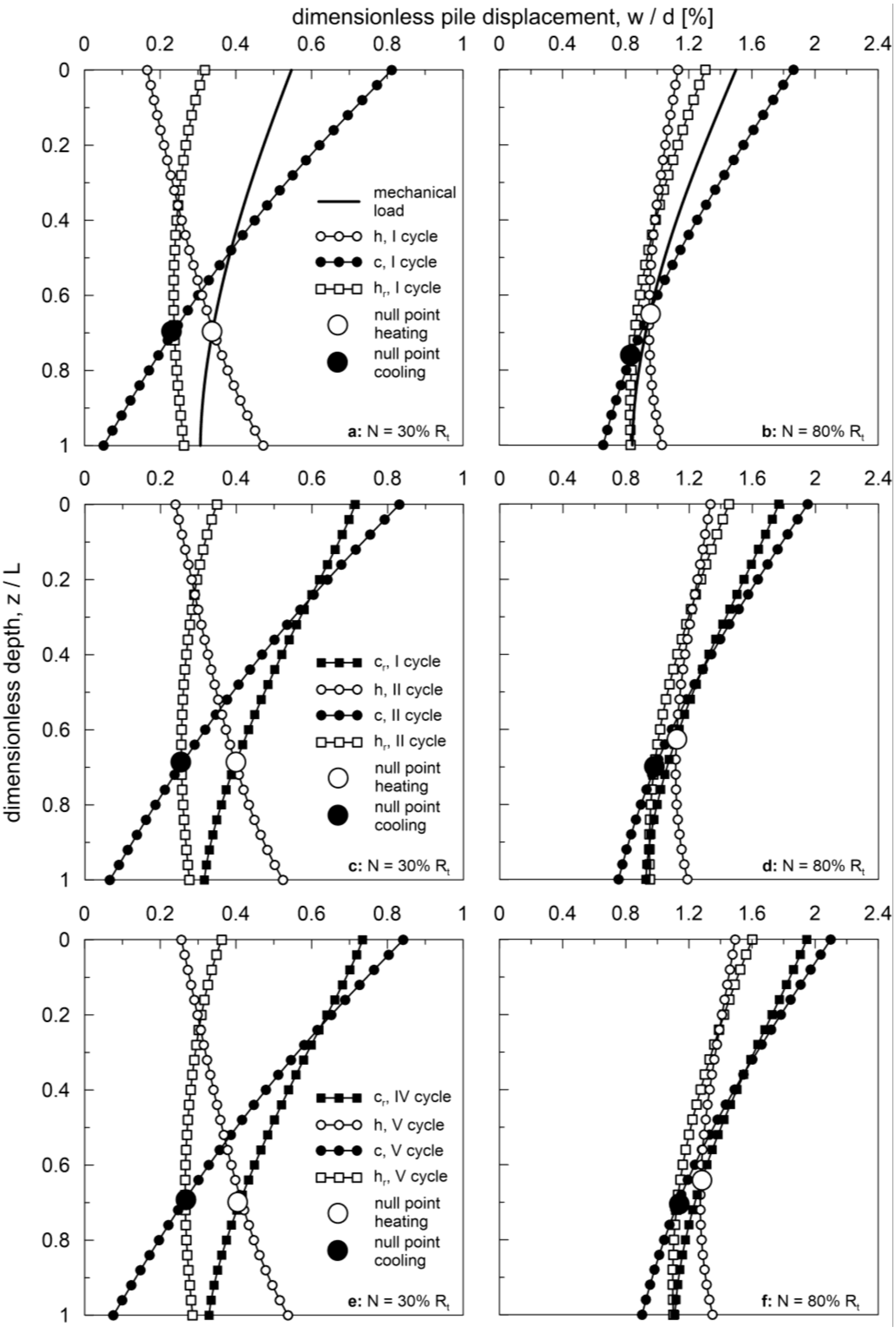

Figure 5.24. Dimensionless displacement of the pile along its length in the I, II and V cycles, free-head pile (MC model).

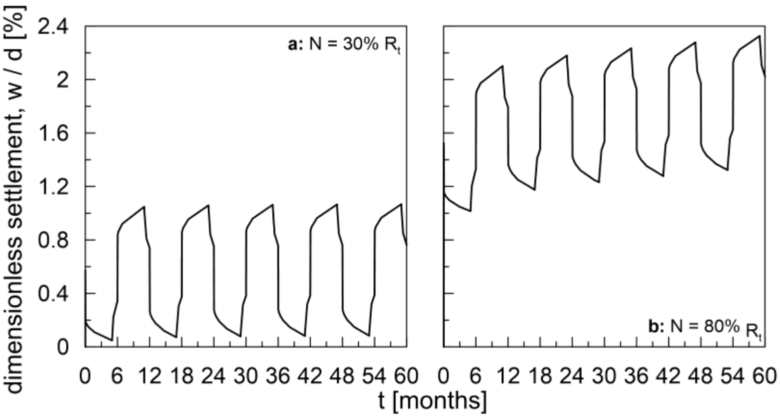

Figure 5.25. Dimensionless global settlement, free-head pile (MC model).

When the applied load is equal to the 80% R_t, the highest thermally-induced forces are equal to about 5.5% R_t and -6% R_t for heating and cooling. Differently from the elastic results in which the maximum total load is located at head, in this case the increase of the axial force along the shaft gives rise to an overall value of 82% R_t (Fig. 5.23). The higher applied load level at head causes the development of plastic shear strains, since the mechanical loading phase, involving points located in progressively deeper sections. The total shear strains are equal to 2% at 6.25m, to 0.46% at 12.5m and to 0.42% at 18.75m, while the plastic component is about 1.5% at 6.25m and 12.5m and is null at 18.75m (Fig. 5.26). Underneath pile tip the shear behaviour can be neglected. During the heating phase, the point located above the null point (5.25m and 12.5m) are characterized by unloading and, therefore, by a decrease of the total strain (the reduction is equal to about -0.10% and -0.04% in the first cycle, slightly increasing cycle after cycle). In the lower part of the pile the increase of the temperature turns into loading, i.e. in the increase of γ_t that can be responsible of the yielding of more points. In this case, the point located at 18.75m experience a total strain of 0.44% with no plastic component. As a consequence of the development of plastic shear strains, with respect to the elastic case, the null point shifts upward to guarantee the equilibrium; its location is at about 16.5m (Fig. 5.24a). When the temperature is reversed, the behaviour is opposite; the total strain and the plastic component in the first cycle are equal to 5.4% and 4.9% at 6.25m and to 0.79% and 0.74% at 12.5m while they remain almost constant for the element at 18.75m. As the ultimate shear resistance of the shallower points is reached since the application of the mechanical load, during cooling the overall axial load in the vicinity of the surface level can't be lower than that experienced at the end of the mechanical loading. This is evident from figure 5.23 where, at shallow depths, the thermally-induced axial load is almost null.

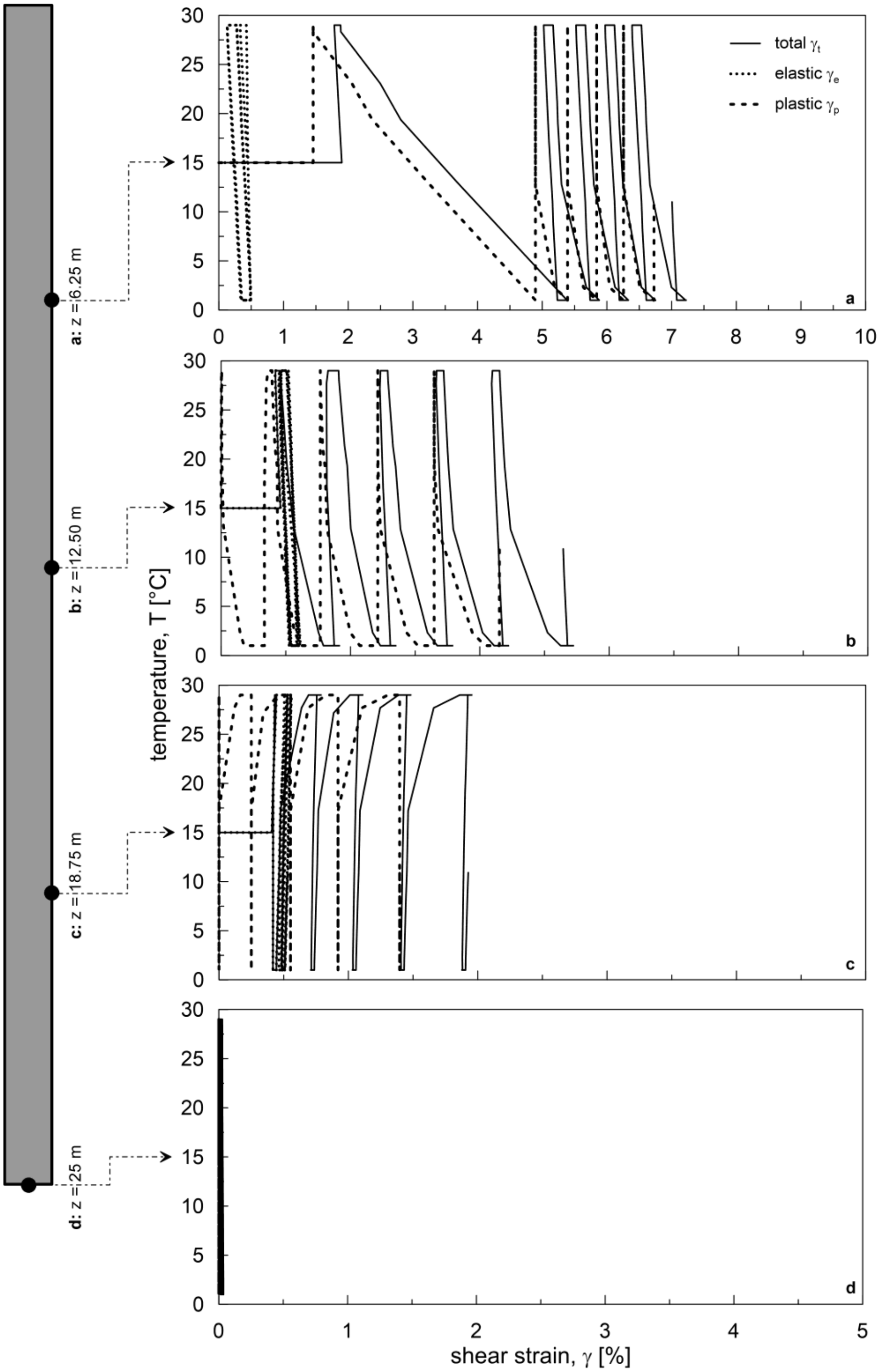

Figure 5.26. Shear strain components, free-head pile (MC model, Q = 80% R_t).

The increase of the shear strain in the upper sections of the pile causes a downward movement of the null point, that, in the cooling phase of the first cycle is located at 18.9m (Fig. 5.24a). Anyway, in the following cycles its position remains almost unchanged (Fig. 5.24b and c). In summary, the maximum development of plastic shear strain occurs with decreasing the temperature for the elements above the null point (Fig. 5.26a and b) and as a consequence of the temperature increase for those below the null point (Fig. 5.26c). As a result, the shear strains are accumulated cycle after cycle.

Looking at the relative pile-soil movement (in figure 5.27 the results are shown at the end of the third cycle and hold for all the steps), the pile settles more than the surrounding soil.

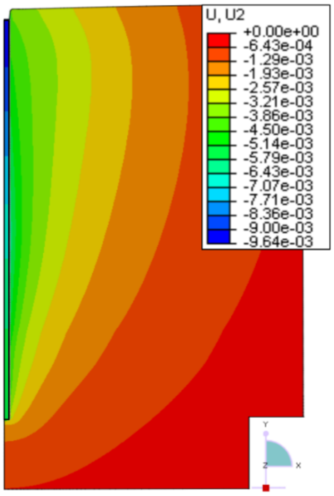

Figure 5.27. Vertical displacements [m] at the end of third cycle, free-head pile (MC model, Q = 80% R_t).

As concerns the pile displacement, the overall settlement after the application of the mechanical load is about 1.52% *d* (Fig. 5.25b) and decreases with depth (0.85% *d* underneath pile tip) if looking at the local scale (Fig. 5.28). In accordance with the shear strain profiles, each increase of temperature induces upward movement for the elements located above the null point, downward movements for that located below the null point (Fig. 5.28) and vice versa when the temperature is decreased. The minimum head settlement is equal to 1.02 % *d* and occurs at the end of the first continuous heating (Fig. 5.25b), while, after continuous cooling the maximum settlement experienced is equal to 2.1% *d*. Therefore, during the first thermal cycle, the settlement is increased of about the 38% with respect to that of the mechanical load. After 5 thermal cycles, the maximum increase is 52%.

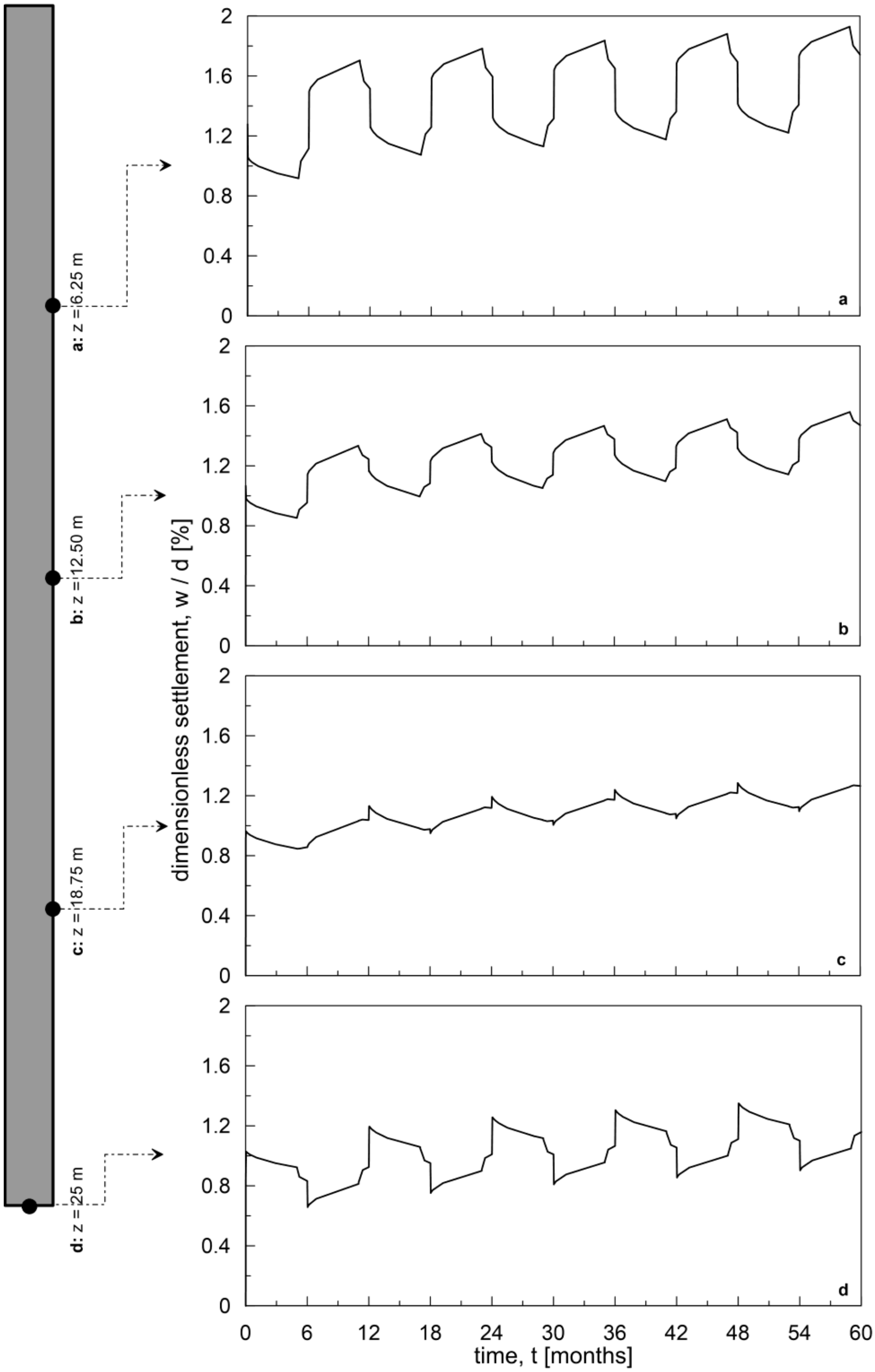

Figure 5.28. Local settlement, free-head pile (MC model, Q = 80% R_t).

The accumulation of the displacements in the case of higher applied mechanical load is explained with the fact that the soil elements experience local paths lying mostly on the yield surface; this is shown in figure 5.29 (for sake of clarity, labels are used only for the geostatic and mechanical loading phases, and for the steps of I and V cycles). The analysed behaviour is referred to few elements located at the pile soil interface; the local response of these elements integrated along the pile length explains the global performance.

In the geostatic condition the state of each element lies on the k_0 line. When the mechanical load is applied, the path of the element at 6.25m in the q-p' plane (Fig. 5.29a) moves almost vertically with development of positive volumetric strain (0.02%, Fig. 5.30a), until it reaches the yielding envelope. From this state onward, the path moves leftward on the yield surface, and therefore both q and p' decrease and the element expands (-0.9%). Before reaching the yield surface, the invariant p' remains basically constant but q changes; looking at the deviatoric plane, the points representative of the stress state of the element moves toward the yield surface with values of the Lode angle different from that of the geostatic step (Fig. 5.31a, b). In the geostatic step, the horizontal components of stress are equal and lower in magnitude if compared with the vertical component; therefore, the stress state is triaxial and the Lode angle is equal to 60°. At the end of the mechanical loading process, the Lode angle decreases up to about 49°. During heating, expansion takes place (-0.19%) and the point moves inside the elastic region; positive excess pore water pressures are generated (7kPa, Fig. 5.32a). During continuous heating and during the first thermal rest, due to the dissipation of the excess pore water pressures, contraction develops (-0.12%) and the path moves again on the yielding surface up to the cooling stage. The temperature reversal implies the contraction of the element (0.02%) followed by the development of negative excess pore pressures (9kPa) that dissipate during continuous cooling determining expansion (less than -0.01%); therefore, the path moves again inside the yield surface. During the final rest phase the element expands (-0.7%) and the pore pressures are completely dissipated. The minimum value of the Lode angle is of about 47.6° corresponding to the state at 5 months of continuous heating. The element state at the end of the first cycle is highlighted in figure 5.29a with the label *cr1*. At this stage, it is evident that the state of the point in terms of q, p' and Lode angle is quite different from that at the end of the application of the mechanical load. Therefore, when the second cycle starts, the point follows a different stress path. Anyway, expansion and contraction happens in the same phases and dissipation of excess pore water pressures is always guaranteed. The only state in which the soil yields corresponds to the cooling phase. From the second cycle onward, the loading paths are almost superimposed. During the cycles, the maximum and minimum values of the thermally-induced pore pressure are about ±9kPa; the overall volumetric behaviour is basically hysteretic with the maximum expansion being equal to -0.19% (heating), while the maximum compression being 0.03% (cooling).

During the application of the mechanical load, the element located at 12.5m remains within the elastic range; after that, the stress path moves mostly on the yield surface experiencing plasticity (Fig. 5.29b). As for the element at 6.25m, during both the mechanical loading and the thermal solicitation the Lode angle is not constant and decreases from the initial value of 60° experienced in the geostatic condition (Fig. 5.31). The volumetric behaviour is dominated by expansion. In particular, the expansion developed during the first continuous cooling ($\Delta\varepsilon_{v,t}$ = -0.06%) exceeds the contraction of the first continuous heating ($\Delta\varepsilon_{v,t}$ = 0.02%) and, since there is no compensation, the first cycle doesn't close. As a consequence, the volumetric strain profile moves toward higher negative values (Fig. 5.30b); anyway, the expansion of the continuous cooling step decreases cycle after cycle. It is worth noting that the stress path tends to move leftward, i.e., the mean effective stress reduces along with the deviatoric invariant. The maximum and minimum excess pore pressure is attained during the cycles following the first (12kPa and -16kPa) and is completely dissipated at the end of each cycle (Fig. 5.32b).

At 18.75m the mechanical load is such that the element state is quite distant from the yield surface. Nevertheless, during the thermal cycles, the stress path hit the yield envelope and moves on it during each heating phase except for the first one (Fig. 5.29c). In fact, for the elements below the null point, the heating can be considered as a loading phase, while the cooling as an unloading step. As the thermal solicitation goes on, the overall effect is that the load path moves leftward cyclically. Therefore, the mean effective stress reduces and overall volumetric expansion develops (Fig. 5.30c). Since this element is located along the shaft, the Lode angle reduces during the loading process with respect to the geostatic phase. The maximum and minimum thermally-induced pore pressures are equal to 14kPa and to -17kPa and are dissipated at the end of each cycle (Fig. 5.32c).

The element at 25m is located underneath pile tip. Even though expansion is encountered during the heating and the continuous cooling phases, the overall volumetric behaviour is compressive and expansion is completely recovered (Fig. 5.30d). As expected, the maximum volumetric strains are developed at pile base; from the value of 0.4% the total volumetric strain increases up to bout the 0.6% after 5 thermal cycles. At this depth, the stress path is always in the elastic region and moves rightward in the q-p' plane (Fig. 5.29d). Considering a cycle, the state of the point at a specific thermal phase, is different from that in the following cycle at the same thermal phase. Since the stress path crosses different states, the local settlements increase cycle after cycle (Fig. 5.28d). Therefore, these settlements are not caused by plastic deformations rather they are the result of not superimposed stress paths. The Lode angle remains equal to 60° throughout the loading phase (Fig.

5.32). The maximum and minimum excess pore pressure are registered at this depth and are equal to 57kPa and to -42kPa; dissipation occurs at the end of each thermal cycle (Fig. 5.32d).

In figure 5.33 the volumetric strain components are reported. At each depth, the volumetric behaviour is characterized by a plastic component that is less significant or null compared to the elastic one. The excess irreversible pore pressure depends on the volumetric irreversible strains that have a very low value; therefore, dissipation takes place during each cycle with no accumulation.

Differently from the linear elastic analyses, the use of the MC model allows to account for plasticity. The main effects of plasticity are: (i) the redistribution of the axial load due to the progressive yielding of the elements along the shaft and, consequently the upward (during heating) or downward (during cooling) movement of the null point; (ii) the higher overall axial load during the cooling phase caused by the mobilisation of the ultimate shear resistance mainly for the points in the vicinity of pile head; (iii) the variation of cyclic settlements due to local loading paths that moves mostly on the yield envelop.

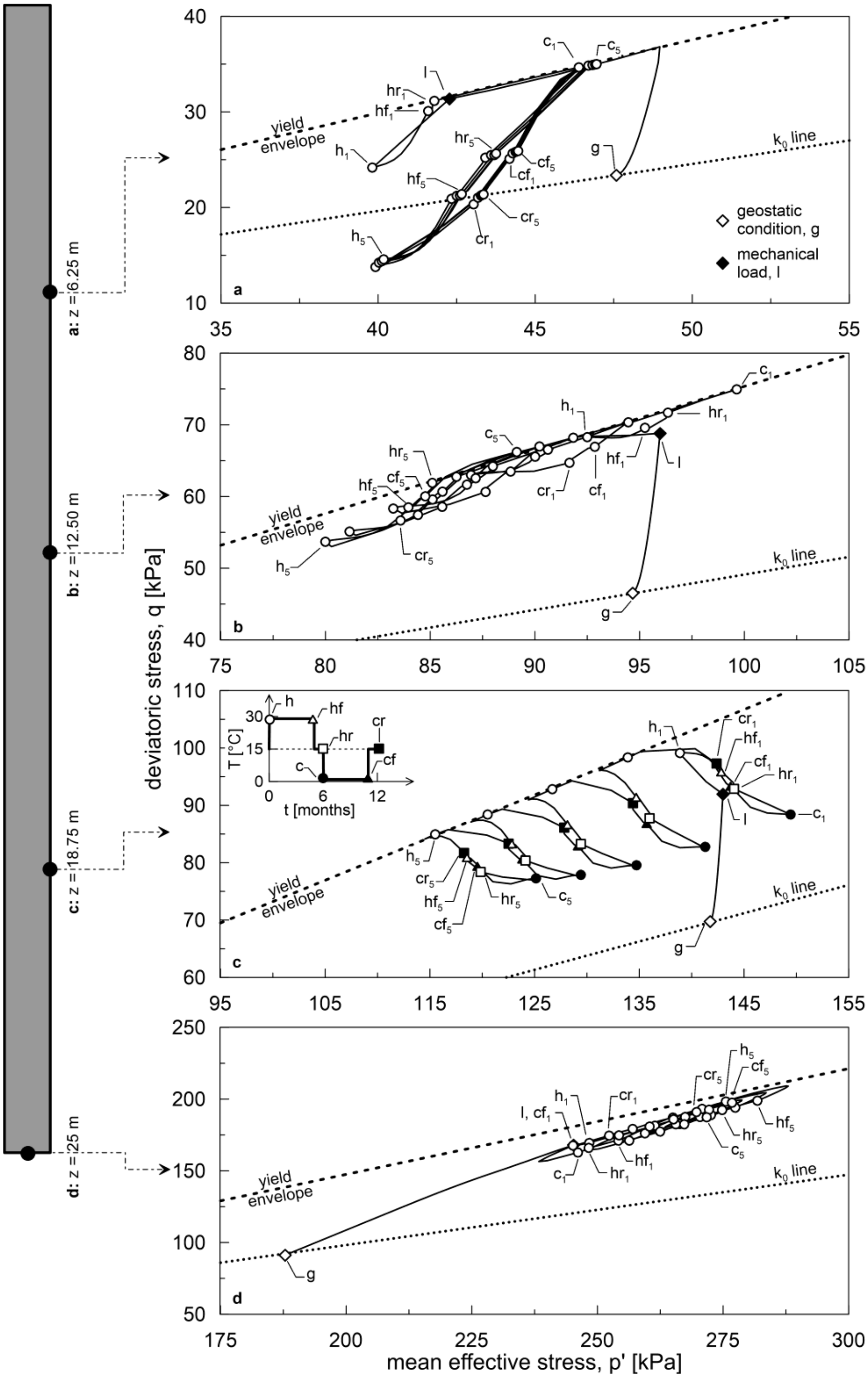

Figure 5.29. Load paths in the *q*-*p*' plane, free-head pile (MC model, *Q* = 80% *R*$_t$).

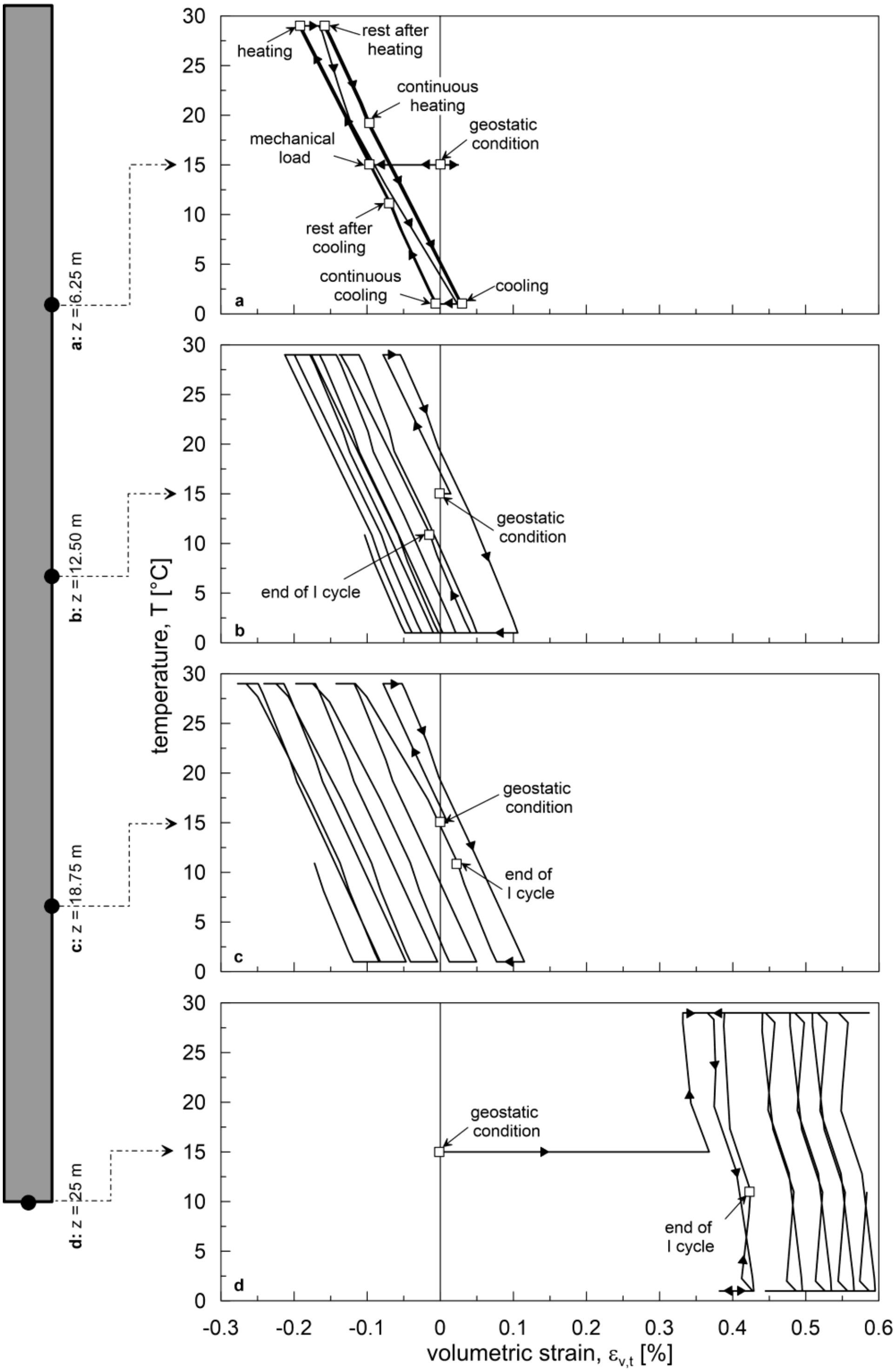

Figure 5.30. Volumetric strain versus temperature, free-head pile (MC model, *Q* = 80% *R$_t$*).

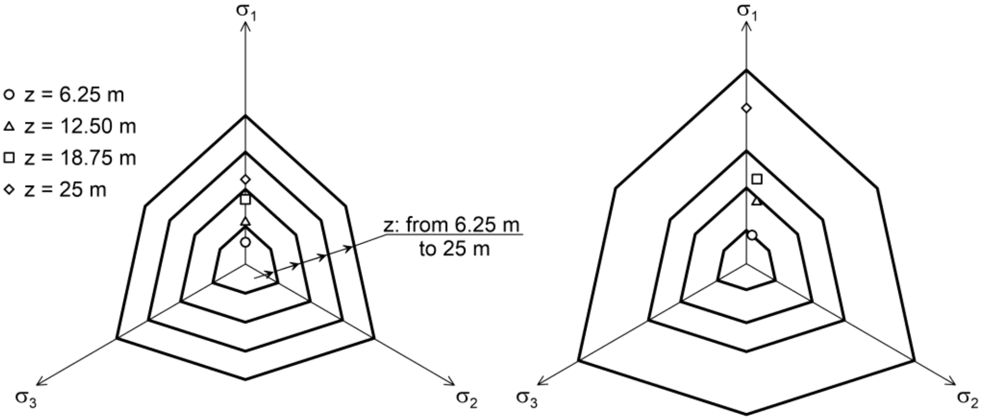

a: geostatic condition **b:** mechanical loading

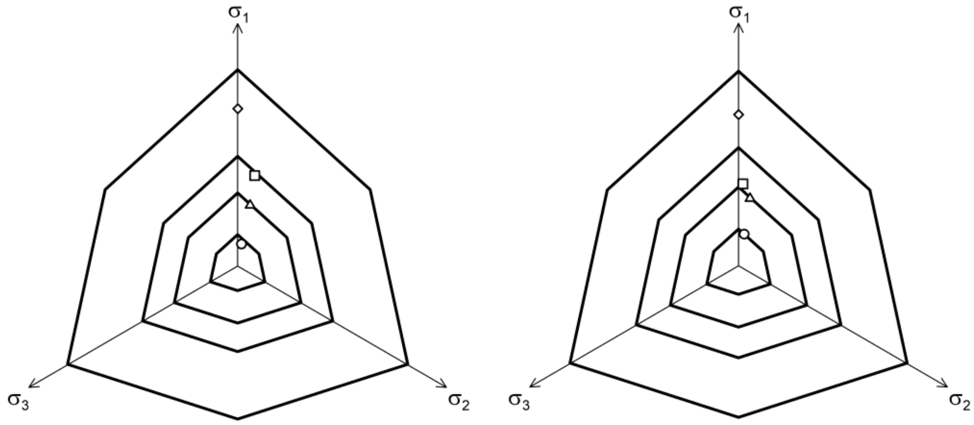

c: heating, I cycle **d:** cooling, I cycle

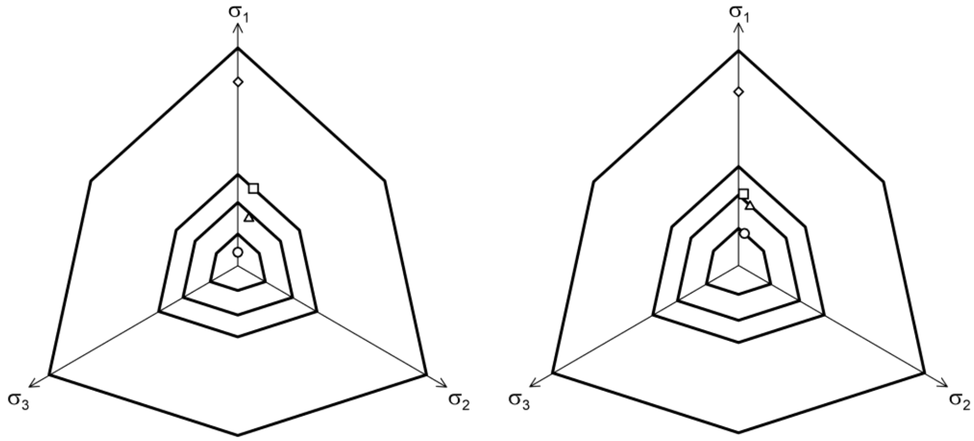

e: heating, V cycle **f:** cooling, V cycle

Figure 5.31. Stress state in the deviatoric plane, free-head pile (MC model, *Q* = 80% *R*$_t$).

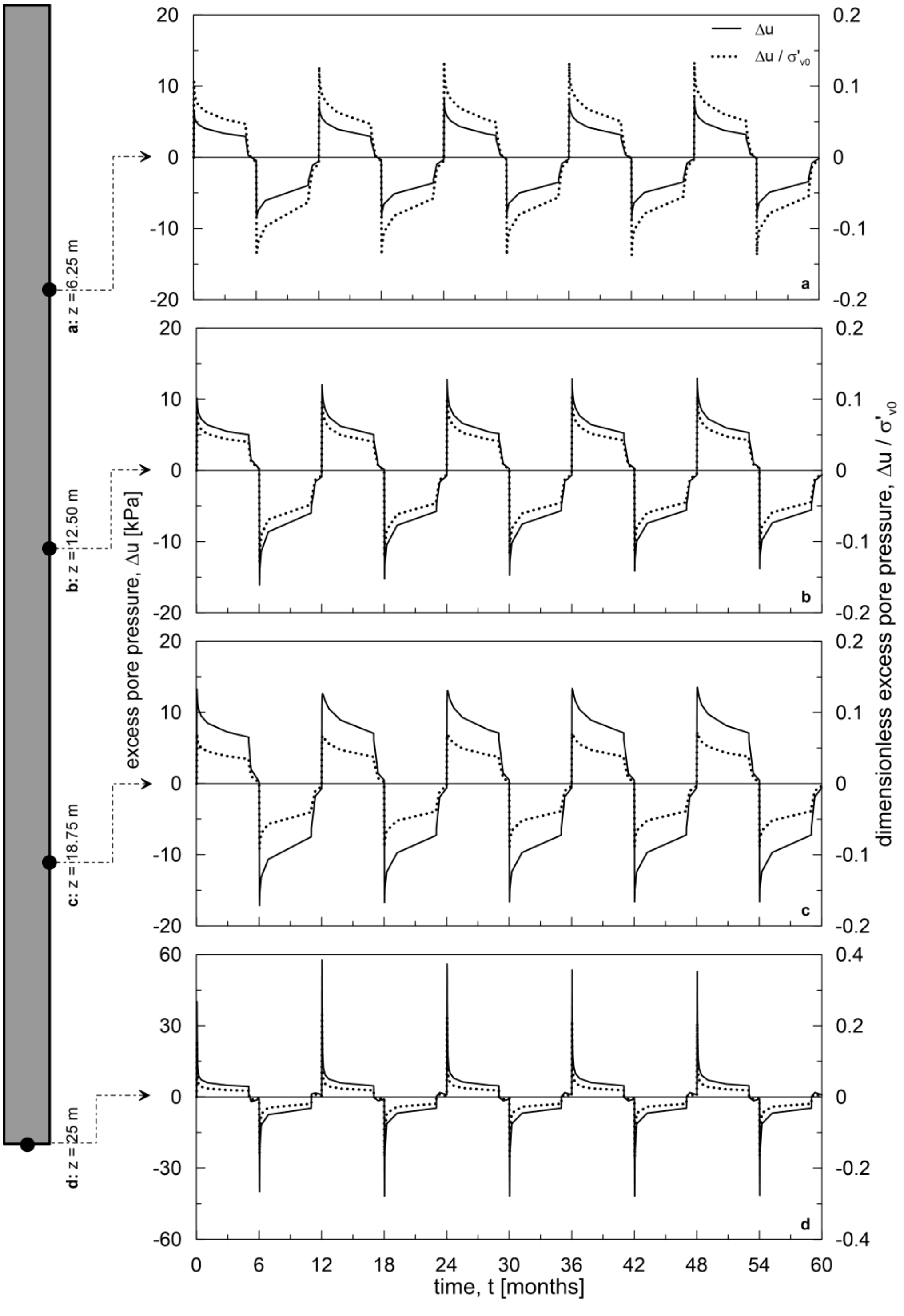

Figure 5.32. Excess pore pressures, free-head pile (MC model, Q = 80% R_t).

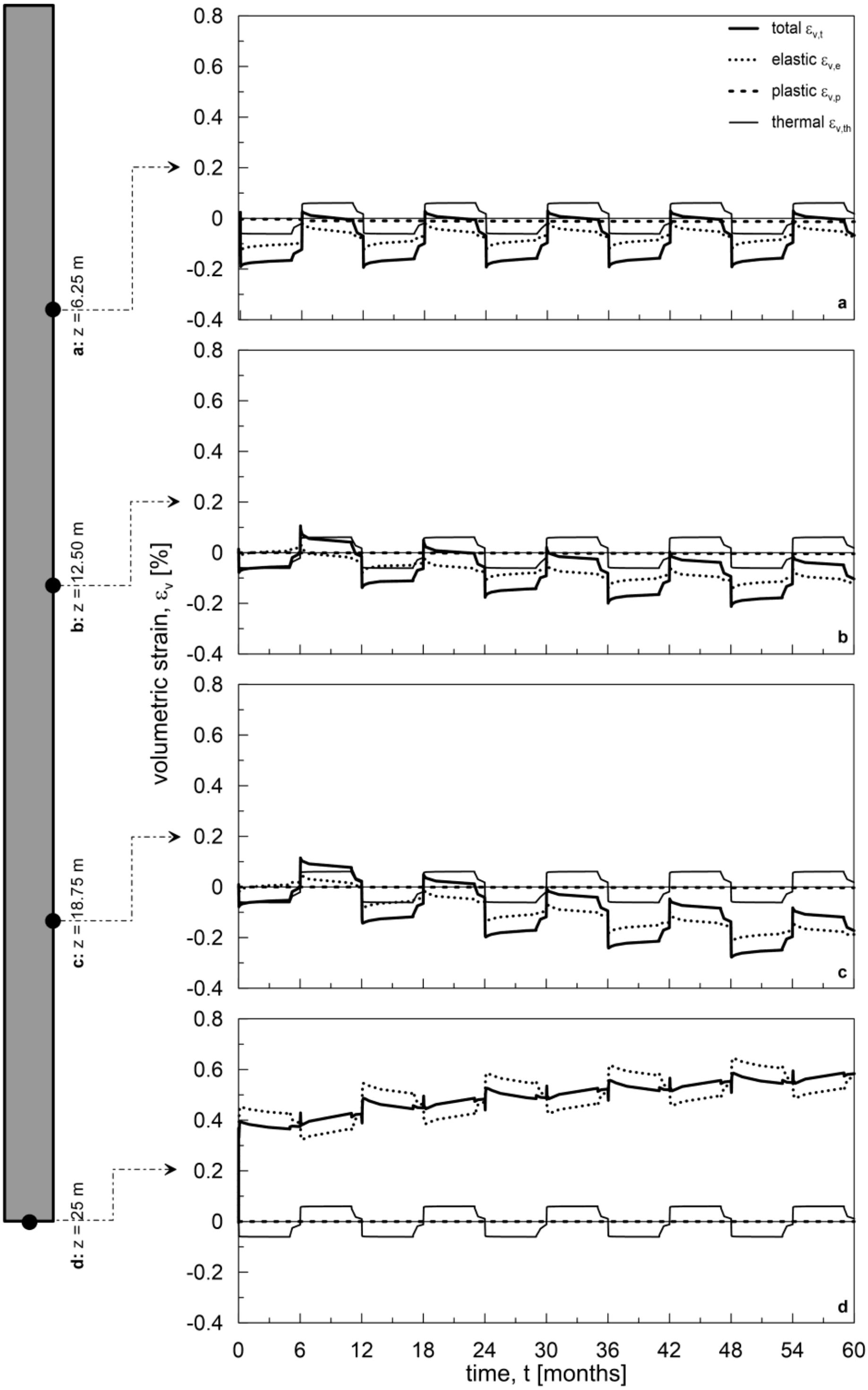

Figure 5.33. Volumetric strain components, free-head pile (MC model, Q = 80% R_t).

5.2.4.2. Fixed-head pile

When the applied mechanical load is the 30% of the pile bearing capacity, the response of the MC model in terms of axial load is the same as that obtained with the elastic model (Fig. 5.34a). Therefore, with respect to the mechanical loading phase, the highest thermally-induced forces are equal to about ±30% R_t for continuous heating and continuous cooling, respectively.

If the applied mechanical load is equal to the 80% of the ultimate capacity (Fig. 5.34b), the ultimate shear stress is reached by an increasingly number of points located along pile shaft. As a consequence, when the temperature increase is kept constant for 5 months, the increase of the axial force is lower than that experienced employing the elastic model and is equal to about 10% R_t, the overall being the 90% R_t. As for the free-head pile, during the continuous cooling the reduction of the shear stress in the upper sections with respect to the cooling, allows some elements to move inside the elastic region; the maximum tensile thermally-induced axial force is equal to about -48% R_t with an overall value of 31% R_t. The lower magnitude of the overall axial force if compared with the elastic analysis is due to the development of the plasticity.

It is worth noting that, the increase of the load during the continuous heating is limited by the shear strength of the elements. For this reason, with increasing the applied mechanical load, the difference between the maximum thermally-induced axial force at head in heating and continuous heating becomes negligible.

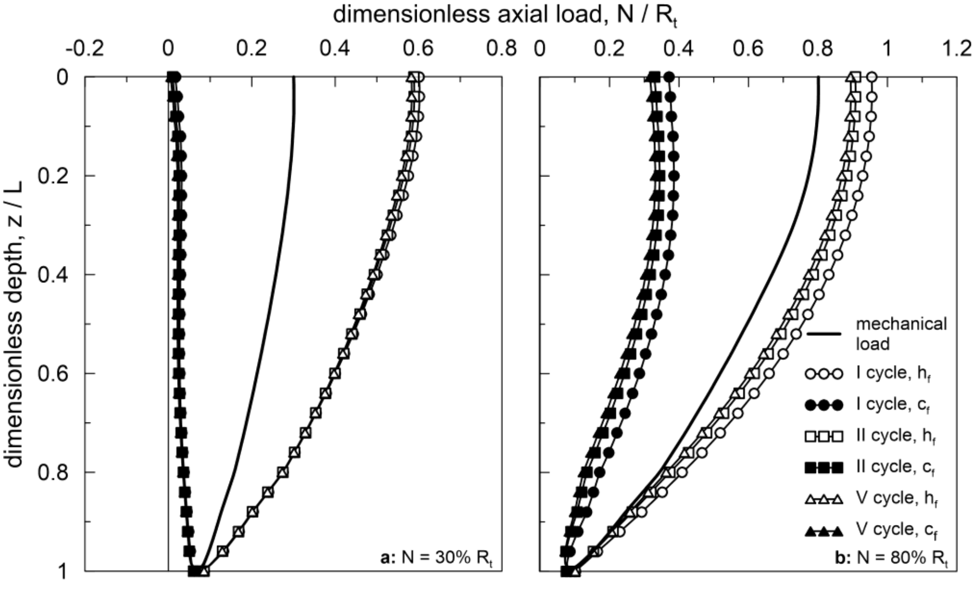

Figure 5.34. Axial load distribution in the I, II and V cycles, fixed-head pile (MC model).

5.2.5. Cam-Clay model

5.2.5.1. Free-head pile

The results of the analyses employing the MCC model are reported in figure 5.35 in terms of axial load. As for the MC model, when the mechanical load is equal to the 30% of the bearing capacity of the pile, the global response of the system in terms of axial force and settlements is qualitatively the same as the elastic analysis. The highest thermally-induced forces are equal to about 2.5% R_t and -3.5% R_t for heating and cooling respectively; the increase of the axial force along the shaft with increasing the temperature, causes an overall axial force equal to 31% R_t. During the first cycle the null points of heating and cooling are located at about 17m and 17.9m respectively (Fig. 5.36a). Using the MCC model implies that, since the soil is NC, the initial state is on the yield surface. This initial condition has an influence on the position of the null point in the first cycle. As for the other models, during the other cycles the null point remains at 17.25m (Fig. 5.36c and e). As concerns the head movements, at the end of the mechanical loading phase the pile settlement is equal to about 1.4% *d*. The maximum and minimum thermally-induced displacement develop at the end of the continuous cooling and continuous heating phases, respectively; their values are equal to about ± 0.54% *d* (Fig. 5.37a).

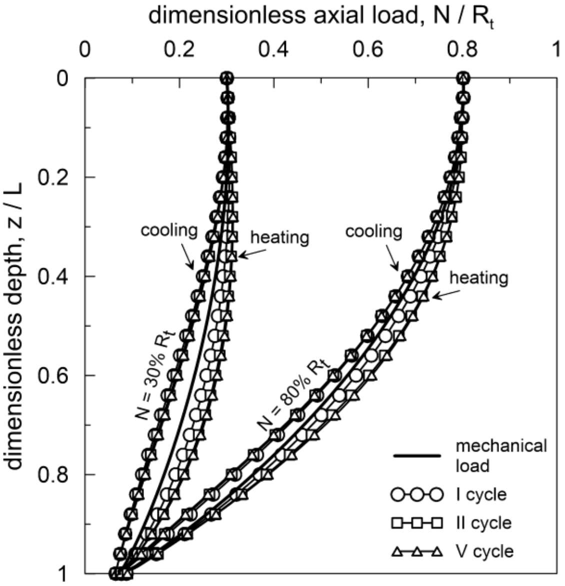

Figure 5.35. Axial load distribution in the I, II and V cycles, free-head pile (MCC model).

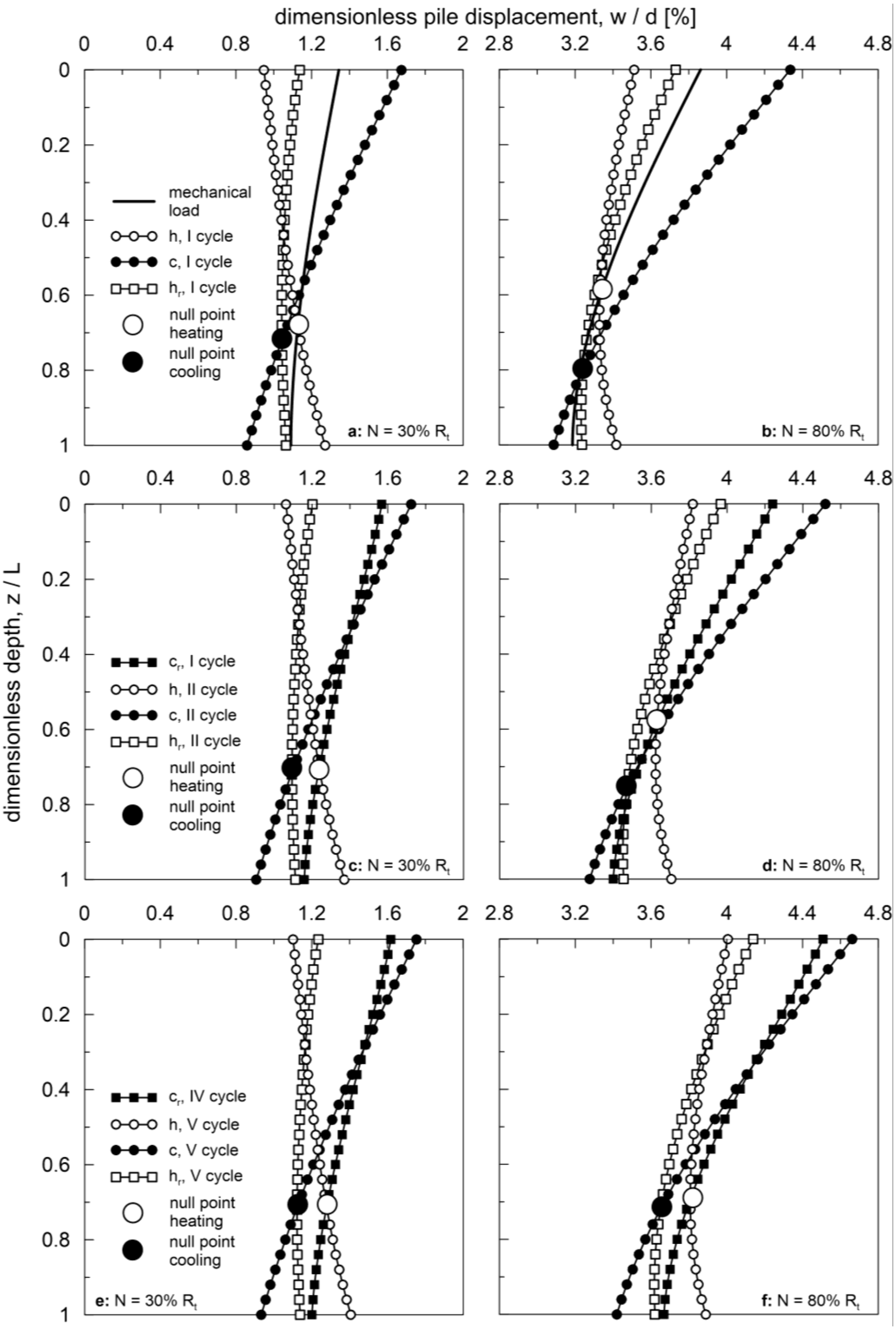

Figure 5.36. Dimensionless displacement of the pile along its length in the I, II and V cycles, free-head pile (MCC model).

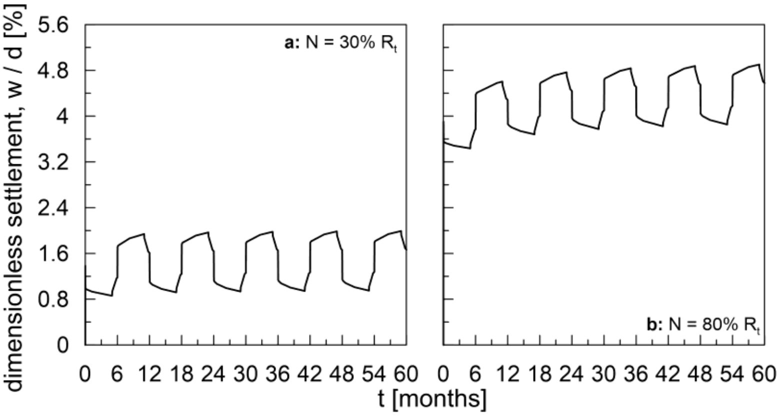

Figure 5.37. Dimensionless global settlement, free-head pile (MCC model).

As shown in Chapter 5, the parameters of the MCC model have been calibrated on the 5 basic parameters of the hypoplastic model. It follows that, compared to the other models, the stiffness of the soil is considerably lower. Since the stiffness of the pile is the same in all the analyses, when the MCC model is used, the ratio between pile and soil stiffness is higher. This leads to a higher value of the axial force due to the mechanical load and to a lower value of the thermally-induced axial force. In fact, one of the parameters controlling the magnitude of the axial force derived from thermal solicitations is the stiffness ratio. For the same reason, settlements are larger in magnitude; nevertheless, the trend is the same as for the other models.

When the mechanical load corresponds to 80% of the pile ultimate resistance, the thermally-induced axial force is equal to about the 1.8% and the -2% R_t for heating and cooling respectively (Fig. 5.35); the maximum overall axial force is located at head. The shear behaviour is characterized by plastic component since the application of the mechanical load; the total and the plastic shear strains are equal to 2.6% and 1.5% at 6.25m, to 2% and 0.95% at 12.5m, to 1.87% and 0.85% at 18.75m (Fig. 5.38). The highest thermally-induced plastic shear strains develop during the continuous heating, rest after heating and cooling phases at 6.25m and at 12.5m; whereas, at 18.5m the highest plastic component is found during the other three steps of the thermal cycle. For the element located underneath pile tip the shear strains can be neglected.

To summarize, as the loading process goes on, the shear strains tend to increase along pile shaft and the pile settles more than the surrounding soil (Fig. 5.39); this is in accordance with the global increase in settlement cycle after cycle (Fig. 5.37b).

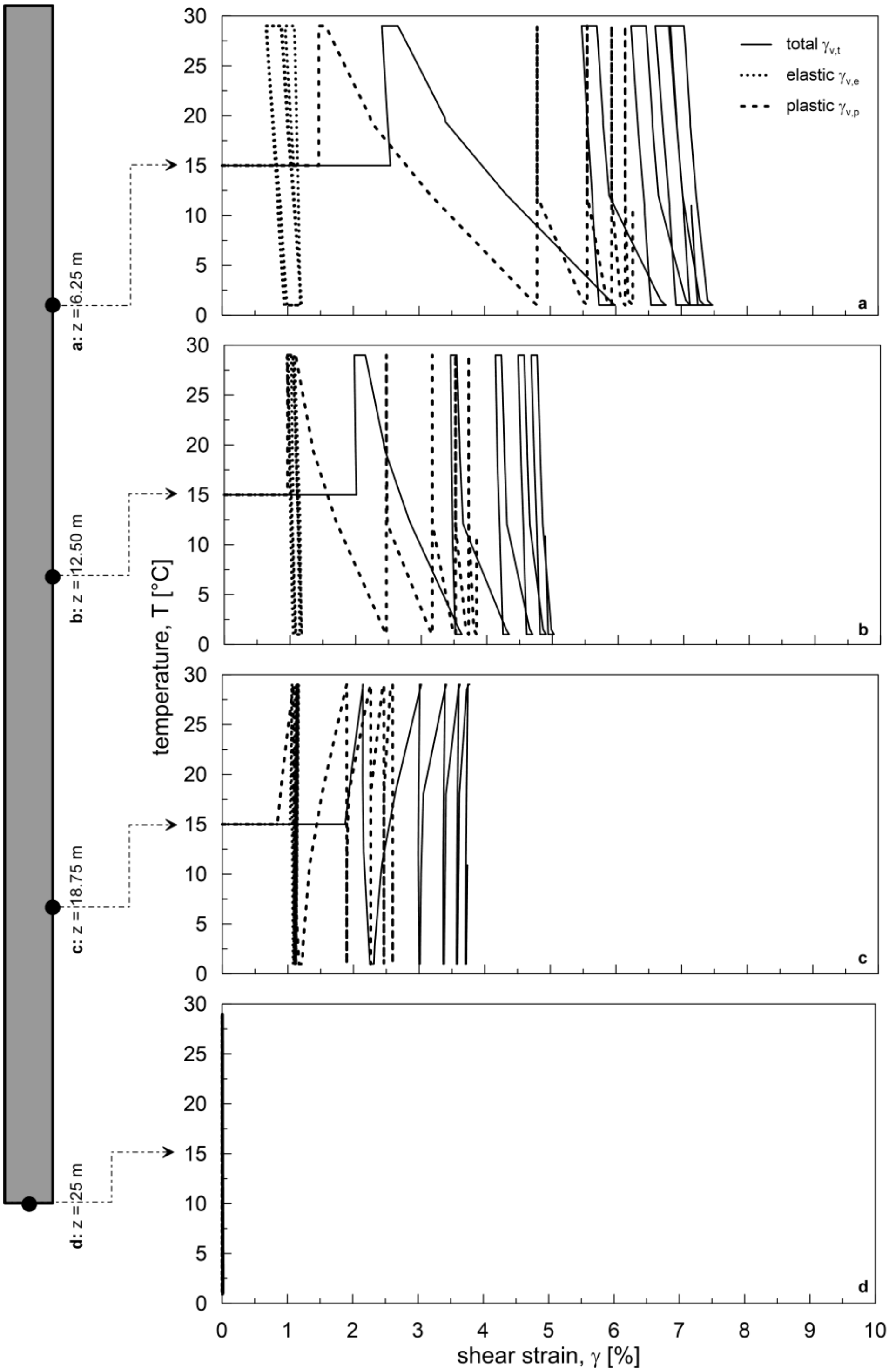

Figure 5.38. Shear strain, free-head pile (MCC model, *Q* = 80% *R*$_t$).

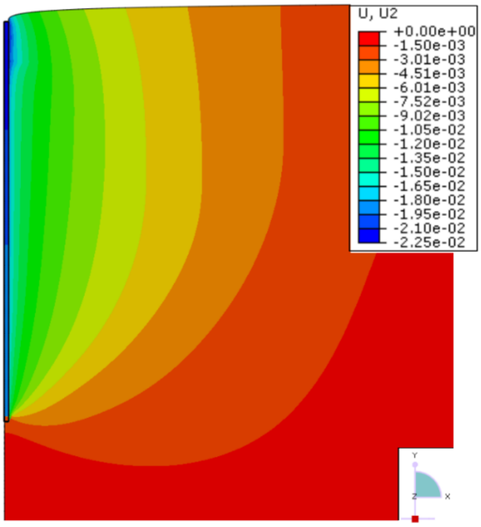

Figure 5.39. Vertical displacements [m] at the end of third cycle, free-head pile (MCC model, *Q* = 80% R_t).

The evolution of the shear strain affects the position of the null point. As for the MC model, on one hand, the redistribution of the load after the heating phase causes the upward movement of the null point, whose location is found at about 15m; on the other hand, during cooling, the progressive yielding of the element determines the downward movement of the null point that, at the end of the first cycle, can be found at about 19.9m (Fig. 5.36b). In the following cycles the position of the null point remains almost constant. It is worth noting that during the increase of temperature, as the applied mechanical load increases, a shallower null point is required to cope with the yielding of the shallower elements due to the mechanical loading. At the same time, the soil located in the vicinity of pile tip is subjected to an increase of the mobilized shear stress and yielding can occur in some points; the equilibrium requires a downward movement of the null point. The final position is determined by the balance between these two phenomena. Likely, when the temperature is reversed, the upper part of the pile is characterized by the increase of the shear stress that may cause the yielding of some points along the pile shaft; however, the cooling phase is applied after the heating phase in which the shear stress in the upper part of the pile is reduced compared to the mechanical stage and a progressive yielding of the points nearby pile tip might have occurred. Again, the position of the null point is determined considering that the redistributions of the load along the shaft must satisfy the vertical equilibrium in the cooling phase.

As concerns the head movements, the displacement experienced at the end of the mechanical phase is equal to about 3.9% *d* (Fig. 5.37b) and decreases with depth (3.2% *d* at pile tip, Fig. 5.40).

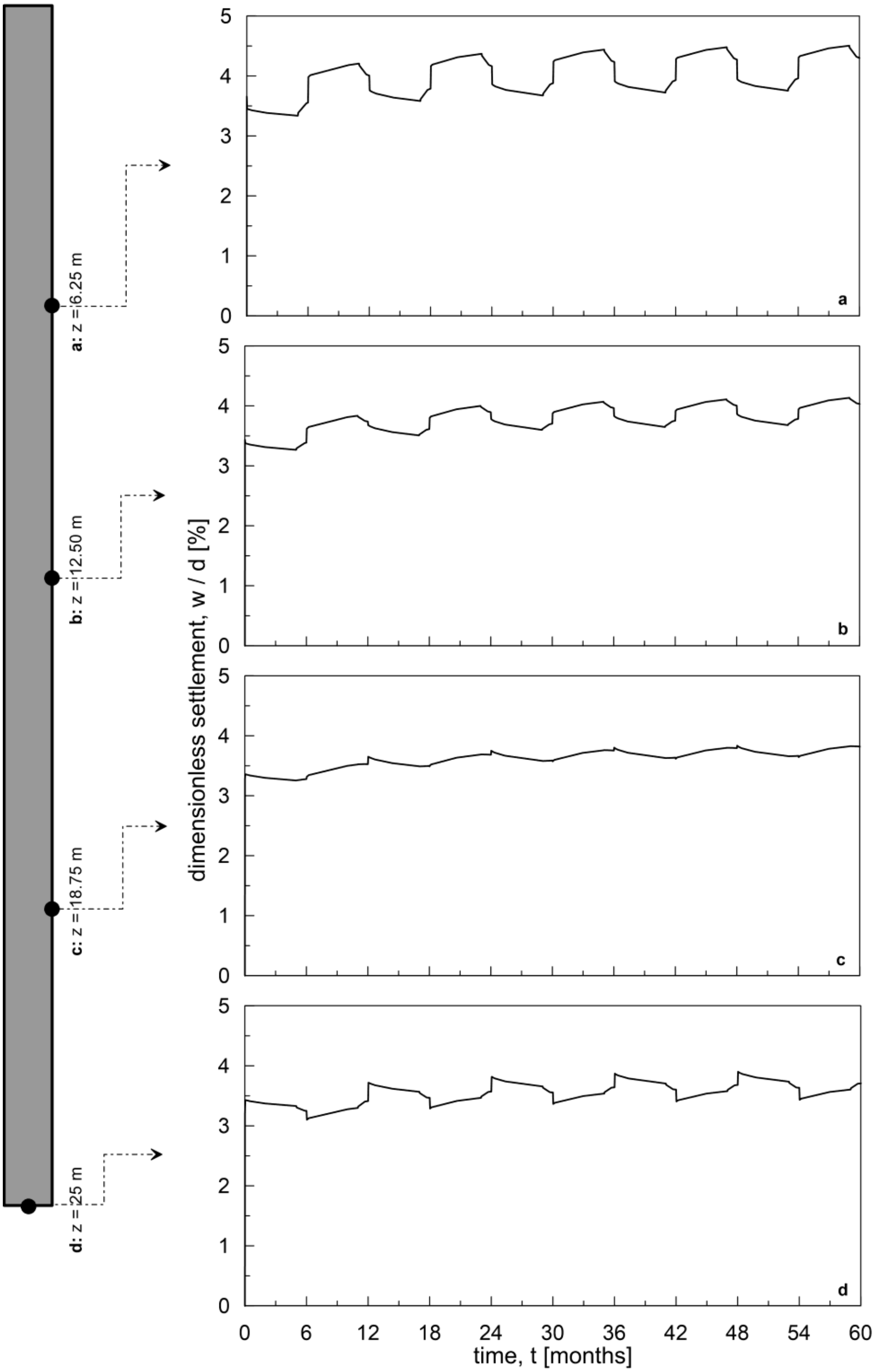

Figure 5.40. Local settlement, free-head pile (MCC model, Q = 80% R_t).

Since the pile displacements are slightly increasing cycle after cycle, the maximum settlement occurs in the continuous cooling phase of the fifth cycle (4.9% *d*), whereas the minimum settlement is recorded during the continuous heating phase of the first cycle (3.43% *d*). Compared to the mechanical load, the settlement increases of about the 26% after 5 cycles. At the local scale the upward or downward movements of the elements depends on their position with respect to the null point (Fig. 5.40). As for the MC model, the soil elements experience load paths characterized by different initial states cycle after cycle and, as a consequence, in the case of higher applied mechanical load, permanent displacements are observed from one cycle to the other.

With the MCC model, since the soil state is normally consolidated, in the geostatic step the point representative of the elements initial state is located at the intersection between the yielding surface and the k_0 line. For the elements along the shaft the preconsolidation pressure remains practically constant and, therefore, the size of the yielding ellipse is almost the same throughout the loading phases. For sake of clarity, in figure 5.41 only the yield surface related to the geostatic step is represented.

During the application of the mechanical load, the loading paths of the elements located at 6.25m and at 12.50m are characterized by the decrease of the mean effective stress and the increase of the deviatoric invariant (Fig. 5.41a and b) with development of positive volumetric strains (1% and 0.25%, Fig. 5.42a and b). Looking at the deviatoric plane, the Lode angle is equal to 60° in the geostatic step and decreases to about 46° at 6.25m and to 47° at 12.5m (Fig. 5.43). During heating, the contraction derived from the application of the mechanical load is partially recovered (-0.001% and -0.08%); the points move inside the elastic region and a positive pore pressure develops (2.7kPa and 5kPa, Fig. 5.44a and b). In the continuous heating, in the first rest phase and in the cooling phase, further contraction takes place (0.33% and 0.18%); the positive excess pore pressure is dissipated and is followed by negative values due to the cooling (-3.5kPa and -6.5kPa). The loading path is characterized by yielding. A slight difference between the behaviour of these two elements appears at continuous cooling of the first cycle. In fact, for the element at 6.25m contraction develops (0.38%), maybe due to temperature diffusion in the soil, whereas for the element at 12.50m, the initial contraction is followed by expansion with a complete recover of the develop compressive strain (0.18%). Expansion controls the volumetric behaviour in the second rest phase with a reduction of the compressive overall strains (0.31% and 0.11%). In this last two steps the load path moves inside the yield surface and complete dissipation of pore pressure takes place. From the second cycle onward, the loading paths are almost superimposed.

The element located at 18.75m is characterized by a stress path the moves tangentially to the yield envelope in the uppermost part of the ellipse with decreasing the mean effective stress and increasing the deviatoric stress (Fig. 5.41c). As for the other elements, the Lode angle reduces during the loading process with respect to the geostatic phase. The volumetric strain trend is practically hysteretic with maximum expansion and contraction during heating and cooling respectively (-0.1% and 0.15%, Fig. 5.42c). The maximum and minimum thermally-induced pore pressure are dissipated at the end of each cycle (±9kPa, Fig. 5.44c)

The element below the pile toe is subjected to compression with roughly no significant expansion during the single phases (up to about 2.8%, Fig. 5.42d). The geostatic yield surface expands at the end of the drained loading phase; therefore, the value of the preconsolidation pressure becomes bigger. In the next steps the preconsolidation pressure remains approximately constant and the loading path lies on the yield surface with almost no variation in the value of the mean effective and deviatoric stresses (Fig. 5.41d). The Lode angle remains equal to 60° throughout the loading phase (Fig. 5.43). The maximum and minimum excess pore pressure are registered at this depth and are equal to about ±28kPa; dissipation occurs at the end of each thermal cycle (Fig. 5.44d).

Along the shaft, the plastic component of the volumetric strain develops since the application of the mechanical loads (0.36% at 6.25m, 0.26% at 12.5m and 0.23% at 18.75m, Fig. 5.45) and increases during the thermal solicitation (0.87% at 6.25m, 0.64% at 12.5m and 0.46% at 18.75m). The element at 25m experiences high irreversible strains during the mechanical loading phase (1.65%), while during the thermal cycles, the plastic component varies slightly (1.95%).

Although the MC and the MCC models show some dissimilarities in the behaviour at the local scale, the global performance is qualitatively the same (not quantitatively if considering that the calibration of the MCC model resulted in a lower value of the soil stiffness).

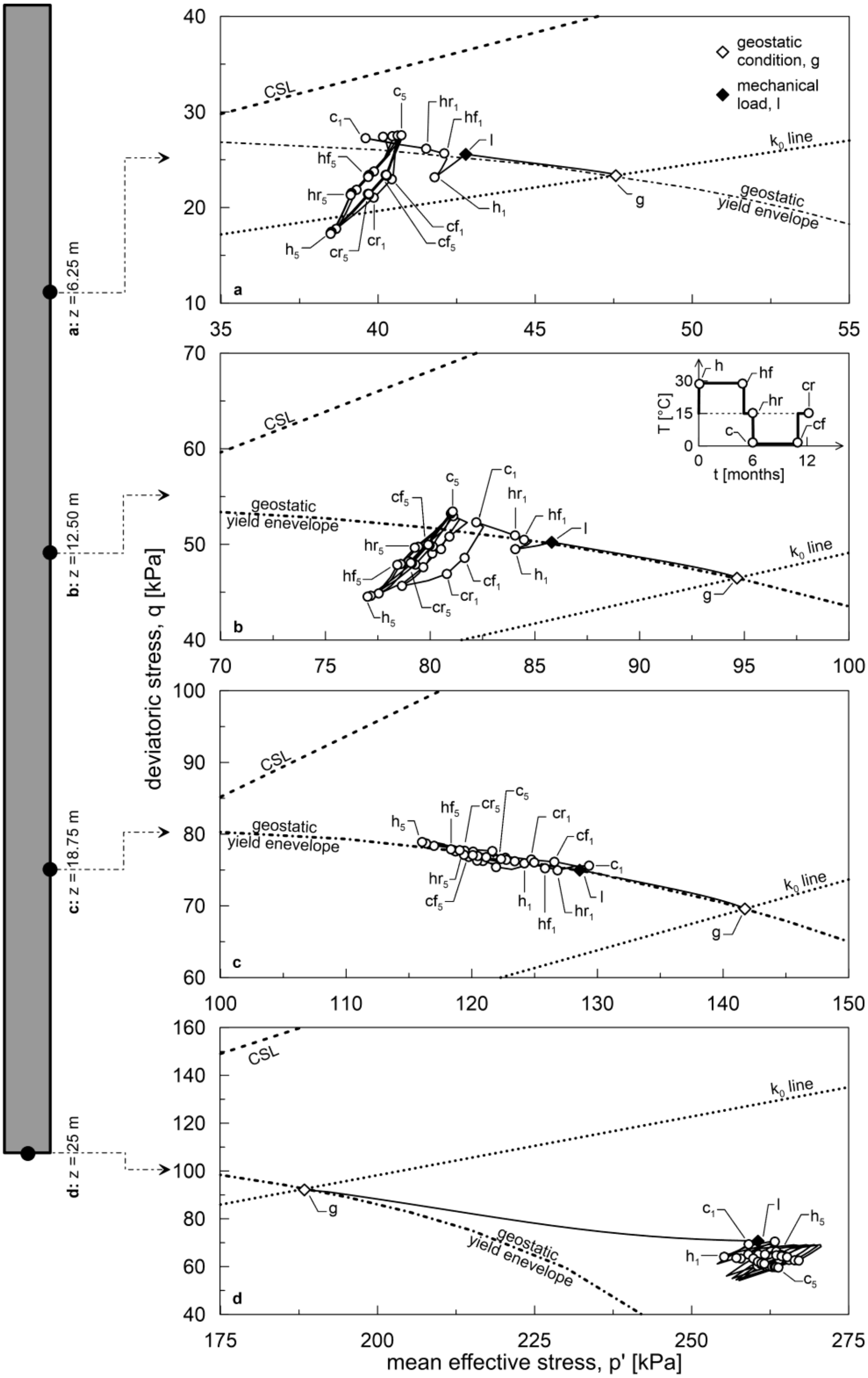

Figure 5.41. Load paths in the q-p' plane, free-head pile (MCC model, $Q = 80\% R_t$).

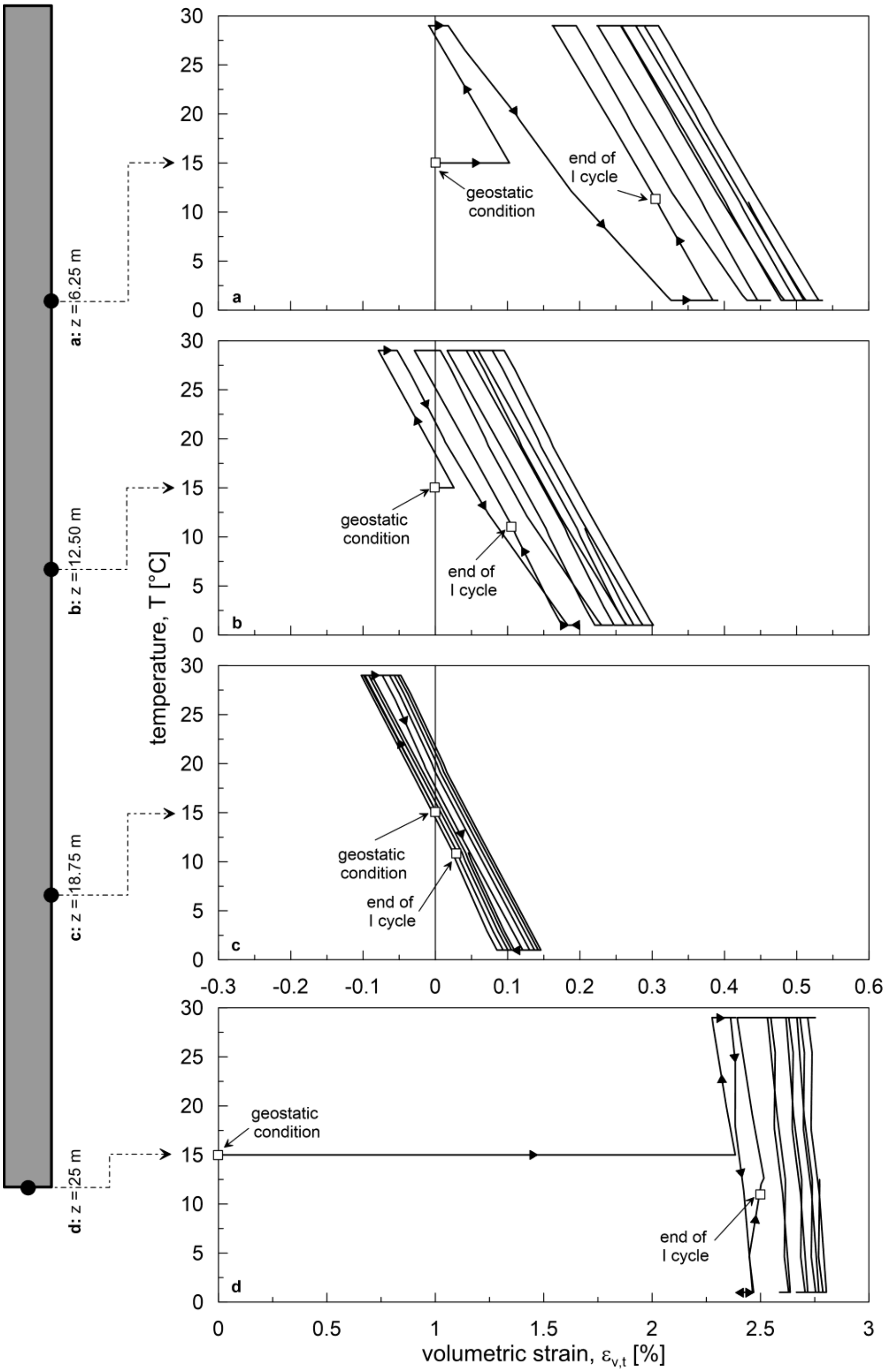

Figure 5.42. Volumetric strain versus temperature, free-head pile (MCC model, Q = 80% R_t).

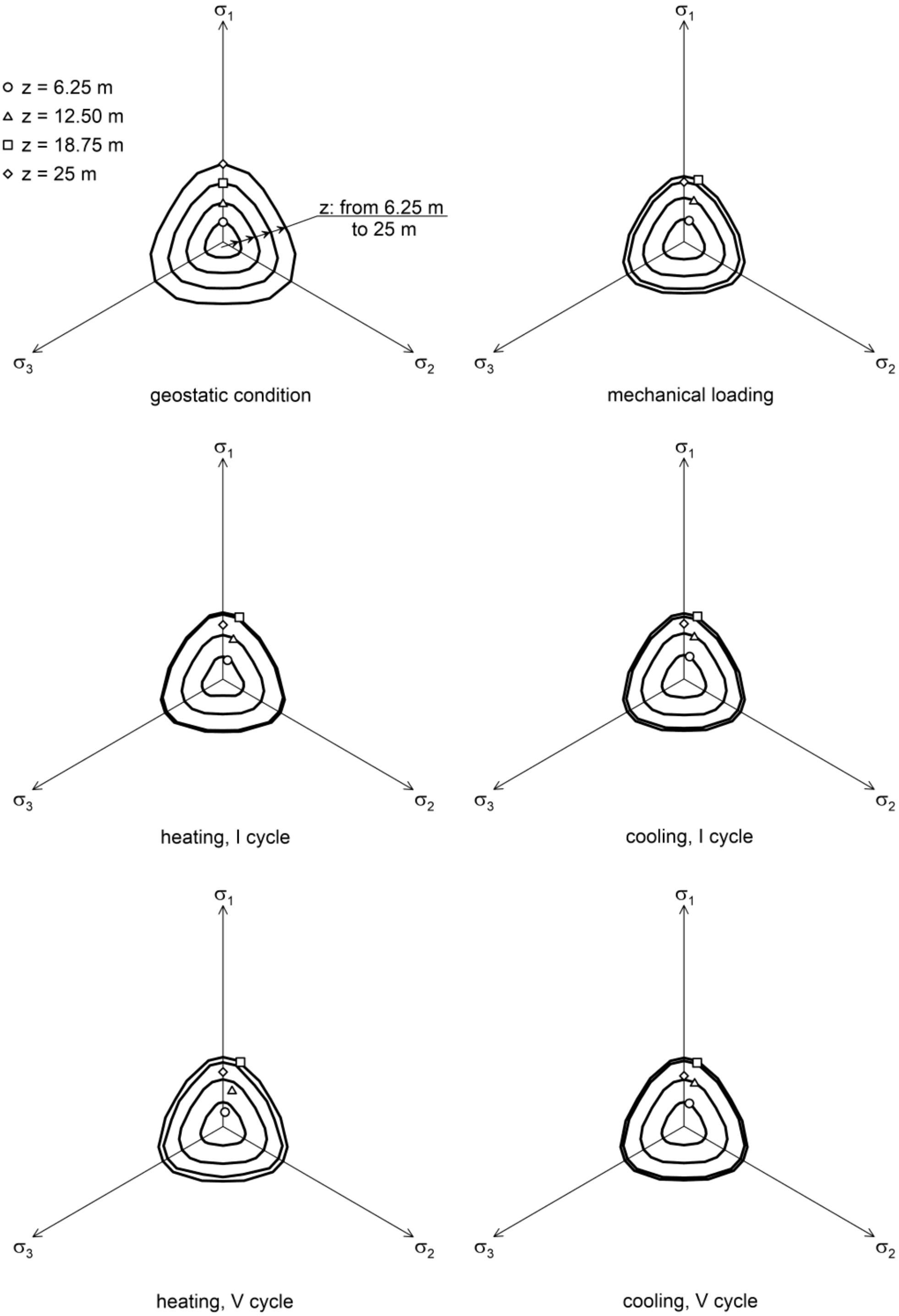

Figure 5.43. Stress state in the deviatoric plane, free-head pile (MCC model, Q = 80% R_t).

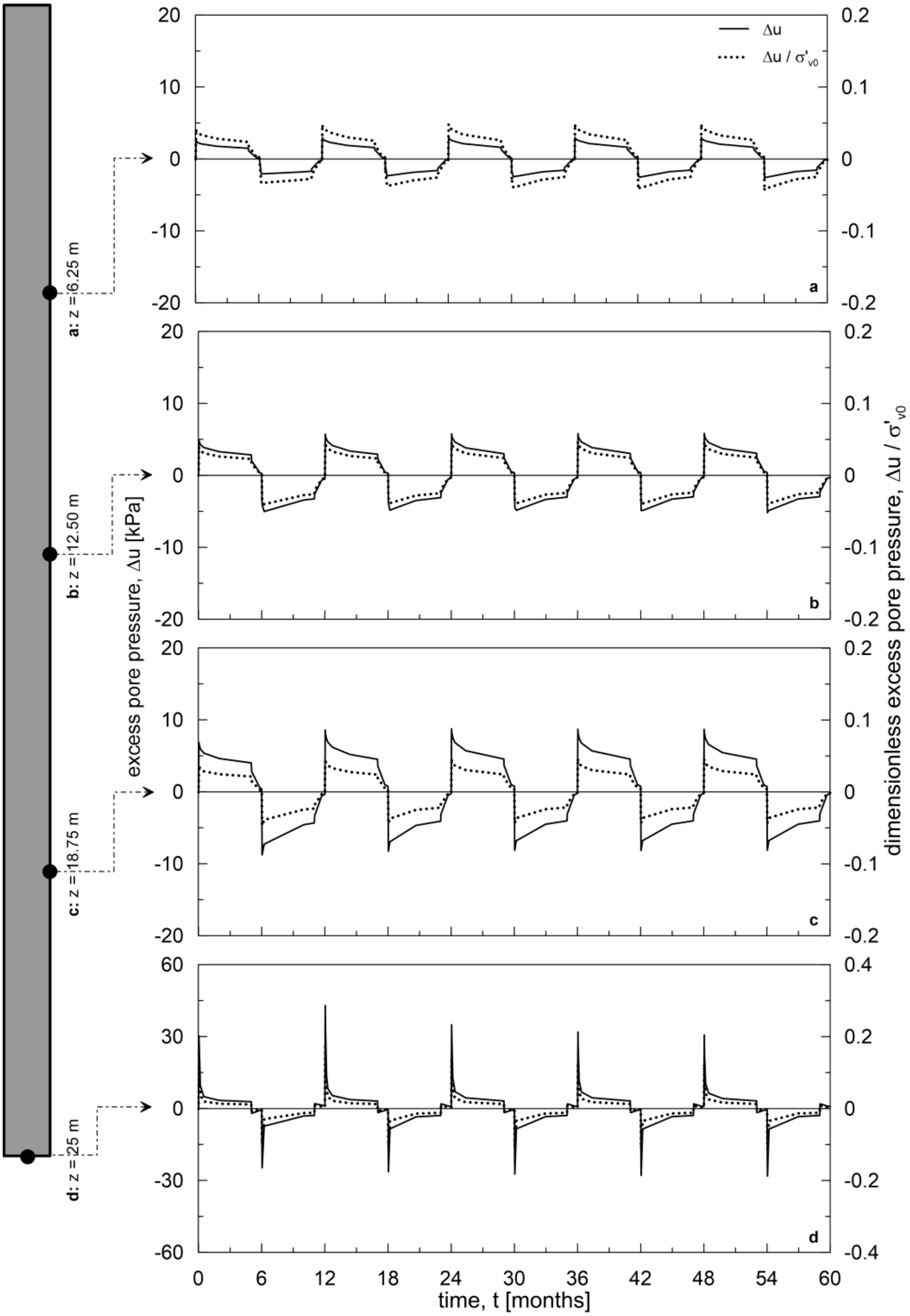

Figure 5.44. Excess pore pressures, free-head pile (MCC model, Q = 80% R_t).

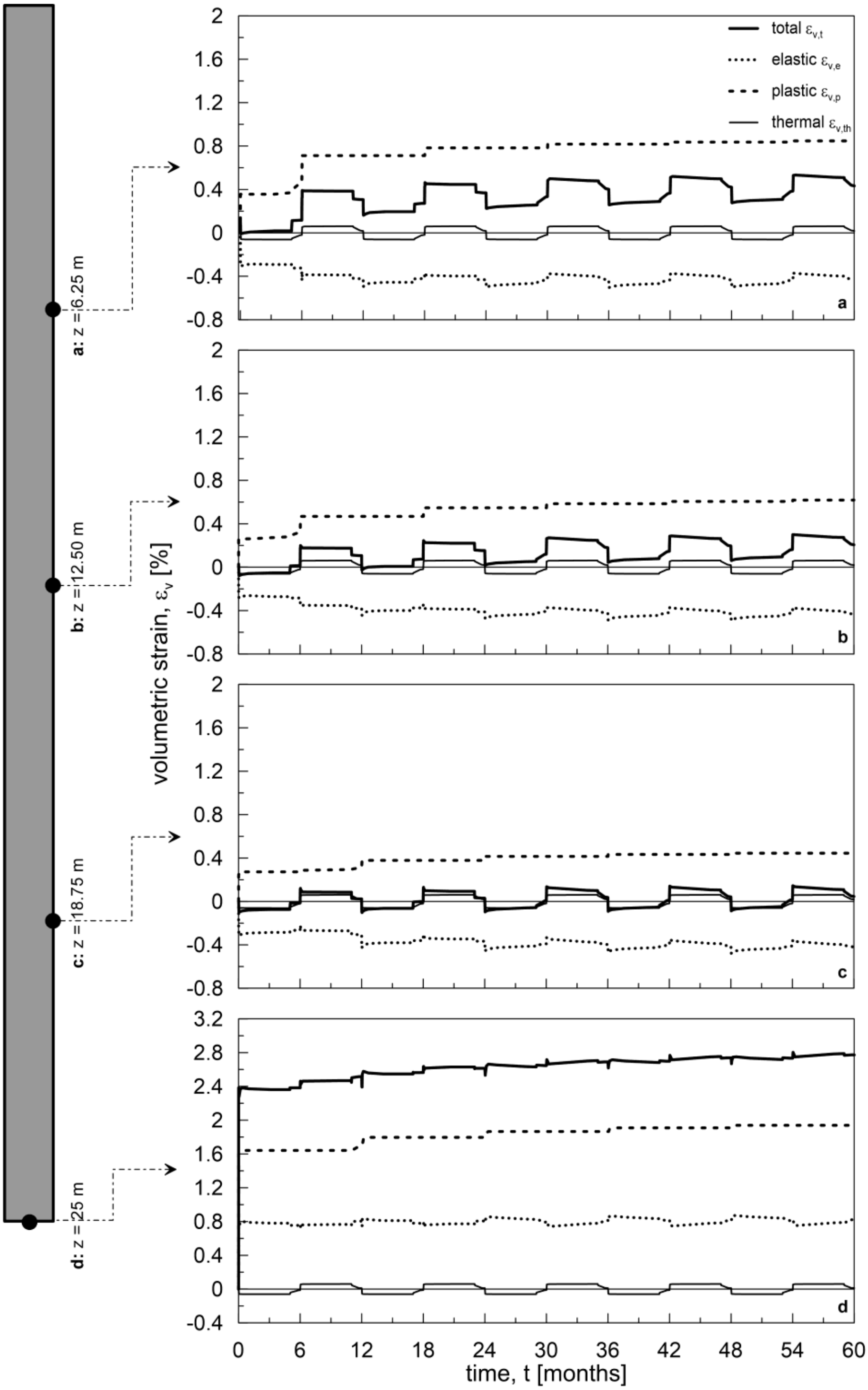

Figure 5.45. Volumetric strain components, free-head pile (MCC model, Q = 80% R_t).

5.2.5.2. Fixed-head pile

The axial load distribution obtained employing the MCC model is reported in figure 5.46. Due to the lower shear stiffness, the compressive and tensile thermally-induced axial force are lower in magnitude compared to that obtained with the MC model. When the applied mechanical load is the 30% of the pile bearing capacity, the response of the model is such that the overall values of the axial force are equal to 43% R_t and 9% R_t for continuous heating and continuous cooling respectively; therefore the highest thermally-induced forces are equal to about 13% R_t and -21% R_t. Contrary to the E and MC models, using the MCC model implies that the NC clay experiences plasticity from the geostatic condition; for this reason the magnitude of the thermally-induced load depends on the sign of the applied thermal variation.

As for the MC model, the plasticity plays a major role if the mechanical load is the 80% R_t. In the continuous heating phase, the thermally-induced axial force at head is equal to about 5% R_t, the overall force being 85% R_t. When the thermal load is reversed the tensile thermally-induced force is equal to about the -28% R_t with an overall value of 52% R_t.

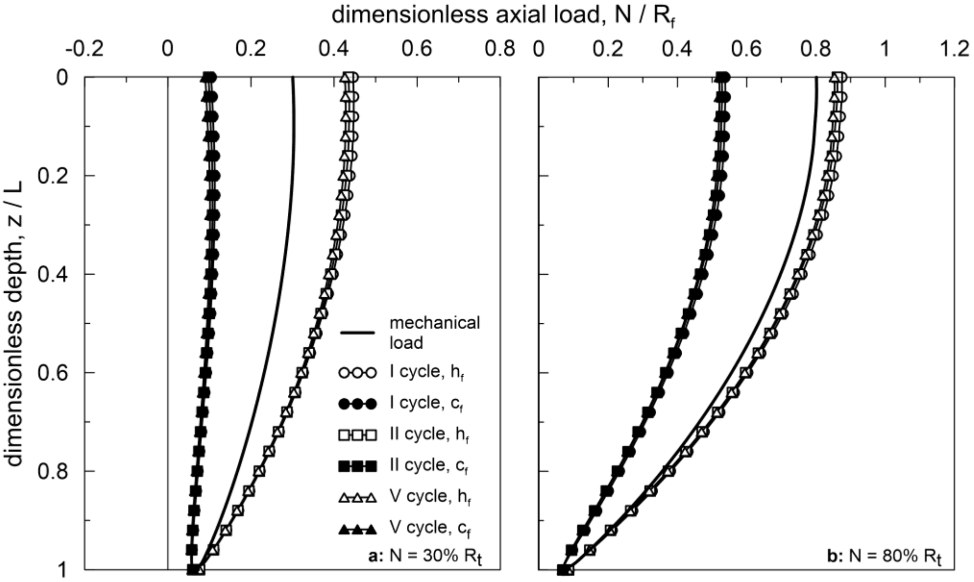

Figure 5.46. Axial load distribution in the I, II and V cycles, fixed-head pile (MCC model).

5.2.6. Hypoplastic and thermo-hypoplastic model

5.2.6.1. Free-head pile

Unlike the elasto-plastic models, in the hypoplastic model there is no kinematic decomposition of the strain rate tensor in the elastic reversible and plastic irreversible counterparts. The introduction of the intergranular strain concept assures that at the beginning of the loading process the deformation of the soil is reversible and comes from the elastic deformations of the grains and the intergranular strain layer (see also Section 4.3.1). This additional component of the model is capable of predicting high stiffness at small strain.

In the strain space, the size of the elastic range is governed by the parameter *R*; moreover, for continuous loading, when the normalized length of the intergranular strain, $\bar{\rho} = ||\delta||/R$, attains the unitary value, the stiffness is no more elastic, rather the response is hypoplastic. Contours of $\bar{\rho}$ are reported in figure 5.47 for both levels of applied mechanical load; it is evident that along the pile shaft and at its base $\bar{\rho} = 1$. Since no temperature variation occurs at this stage, the response is the same for both the hypoplastic and the thermo-hypoplastic models. As the thermal load is applied, the behaviour of the soil in the vicinity of the pile remains hypoplastic and a further portion of the soil is affected by the variation of $\bar{\rho}$. When the thermal term is activated, a slight difference in the trend of the contours is visible; as an example, in figure 5.48 the distribution of $\bar{\rho}$ is reported for the heating and cooling steps of the second cycle and at the end of the cycle itself, for an applied mechanical load of 30% of the pile bearing capacity. This difference is due to the fact that, in the thermo-hypoplastic model, the temperature variation has an influence on the constitutive response of the soil.

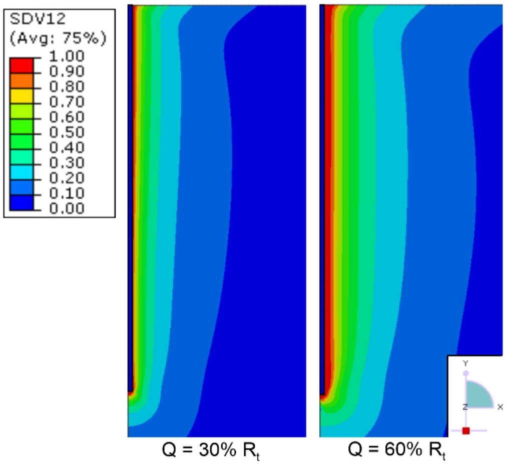

Figure 5.47. Contours of $\bar{\rho}$ at the end of the mechanical loading stage (H and HT models).

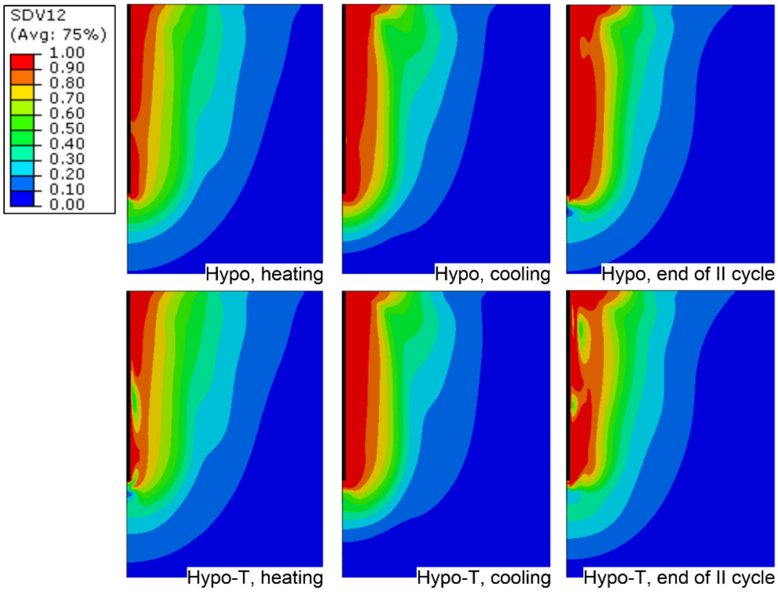

Figure 5.48. Contours of $\overline{\rho}$ in the heating and cooling steps of the II cycle and at the end of the II cycle (H and HT models, Q = 30% R_t).

Contrary to the MC and the MCC models, the response of the hypoplastic and the thermo-hypoplastic models is always outside the elastic region. As a consequence, the difference in the output related to the load levels of 30% R_t and 60% R_t is mainly quantitative. In the ensuing, the results in terms of axial load and global settlements are reported for both load levels, while the analysis of the behaviour at the local scale is shown the solely for the case of 30% R_t.

The axial load distribution is reported in figure 5.49. For both models, the highest and lowest thermally-induced forces are recorded during heating and cooling of the first cycle and are equal to about 6% R_t and -4% R_t for the load level of 30% R_t, and to about 3% R_t and -3% R_t for the load level of 60% R_t. The axial load envelope moves rightward cycle after cycle with decreasing rate. The maximum overall load during the fifth cycle is located along the shaft and is equal to 36% R_t (Hypo) and 34% R_t (Hypo-T) for the load level of 30% R_t, and to 63% R_t (Hypo) and 61% R_t (Hypo-T) for the load level of 60% R_t.

As for the other models, the redistribution of the load after the first heating phase causes the upward movement of the null point, whose location is found at about 15.4m (12.8m) and 15.2m (10.7m), for the H and the HT models, respectively (Fig. 5.50a and b; Fig. 5.51a and b), and applied load equal to 30% R_t (60% R_t). During the first cooling, the downward movement of the null point is such that it is placed at 18.4m (19.4m) and at 18.1m (19.1m), for the H and the HT models, respectively, and applied load equal to 30% R_t (60% R_t). In the analyses employing the HT model, the shallower position of the null points is due to the different development of the non-linearity during the thermal solicitation, in particular during the increase of the temperature; clearly the behaviour in heating affects the response in the next steps. In the subsequent cycles, the null point is interested by a progressively downward offset (Fig. 5.50c, d, e and f; Fig. 5.51c, d, e and f).

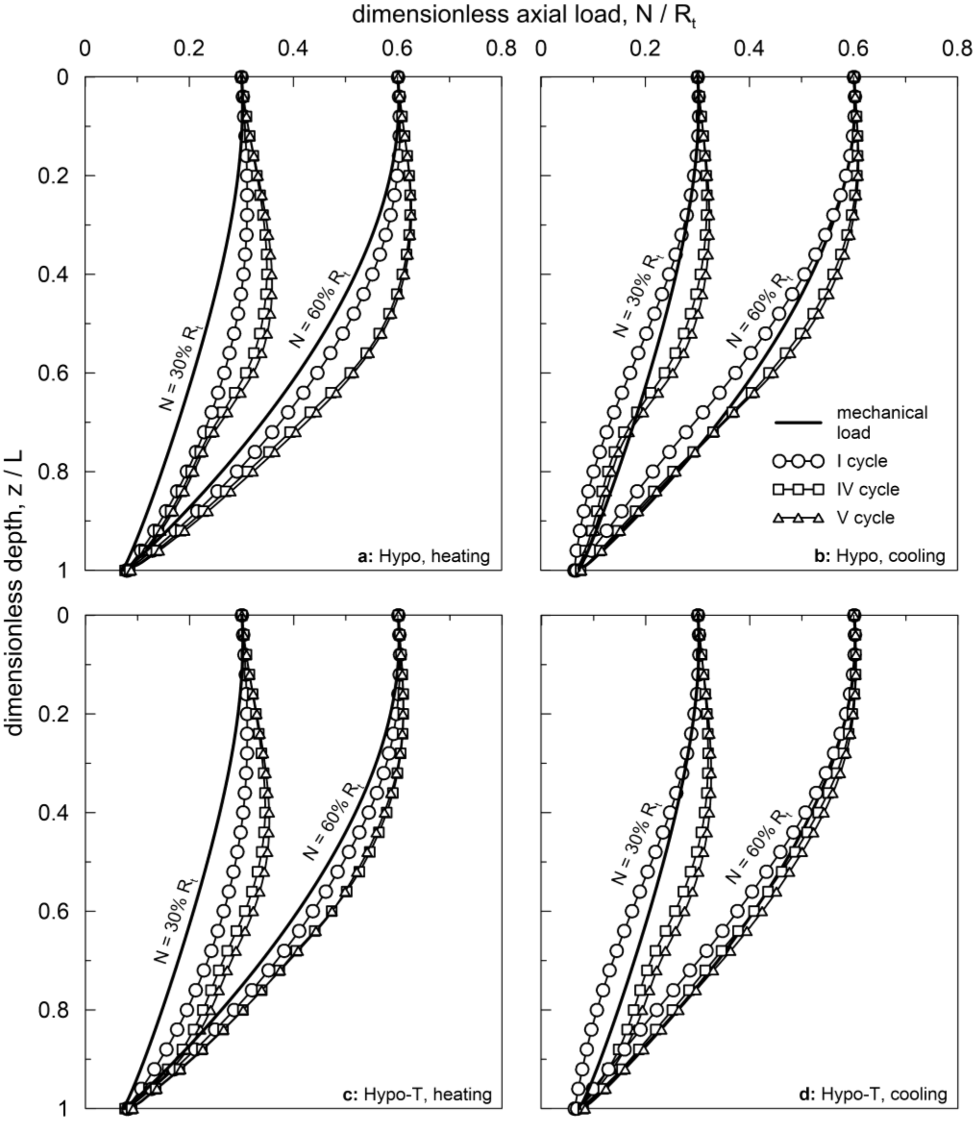

Figure 5.49. Axial load distribution in the I, IV and V cycles, free-head pile (Hypo and HT models).

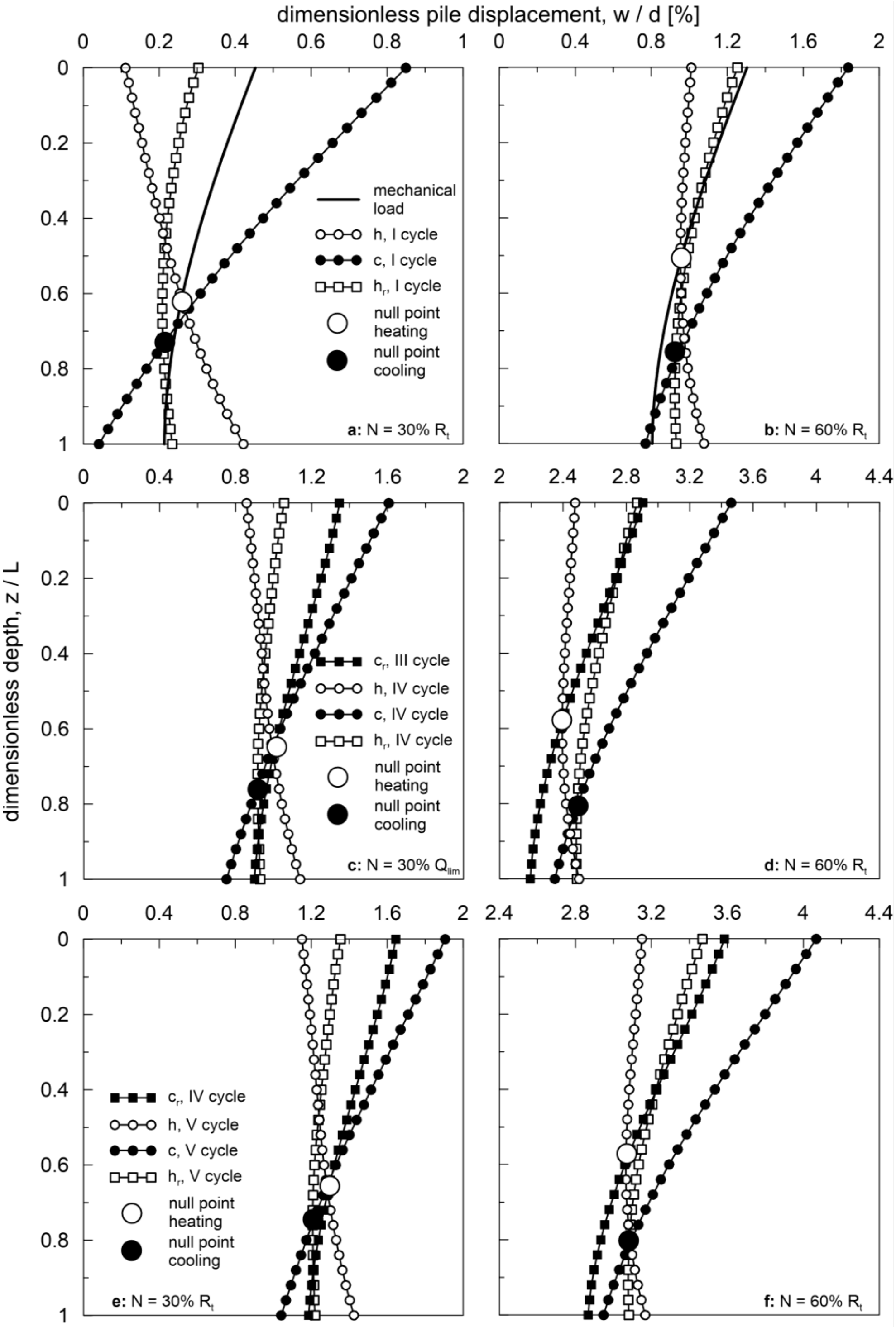

Figure 5.50. Dimensionless displacement of the pile along its length in the I, II and V cycles, free-head pile (Hypo model).

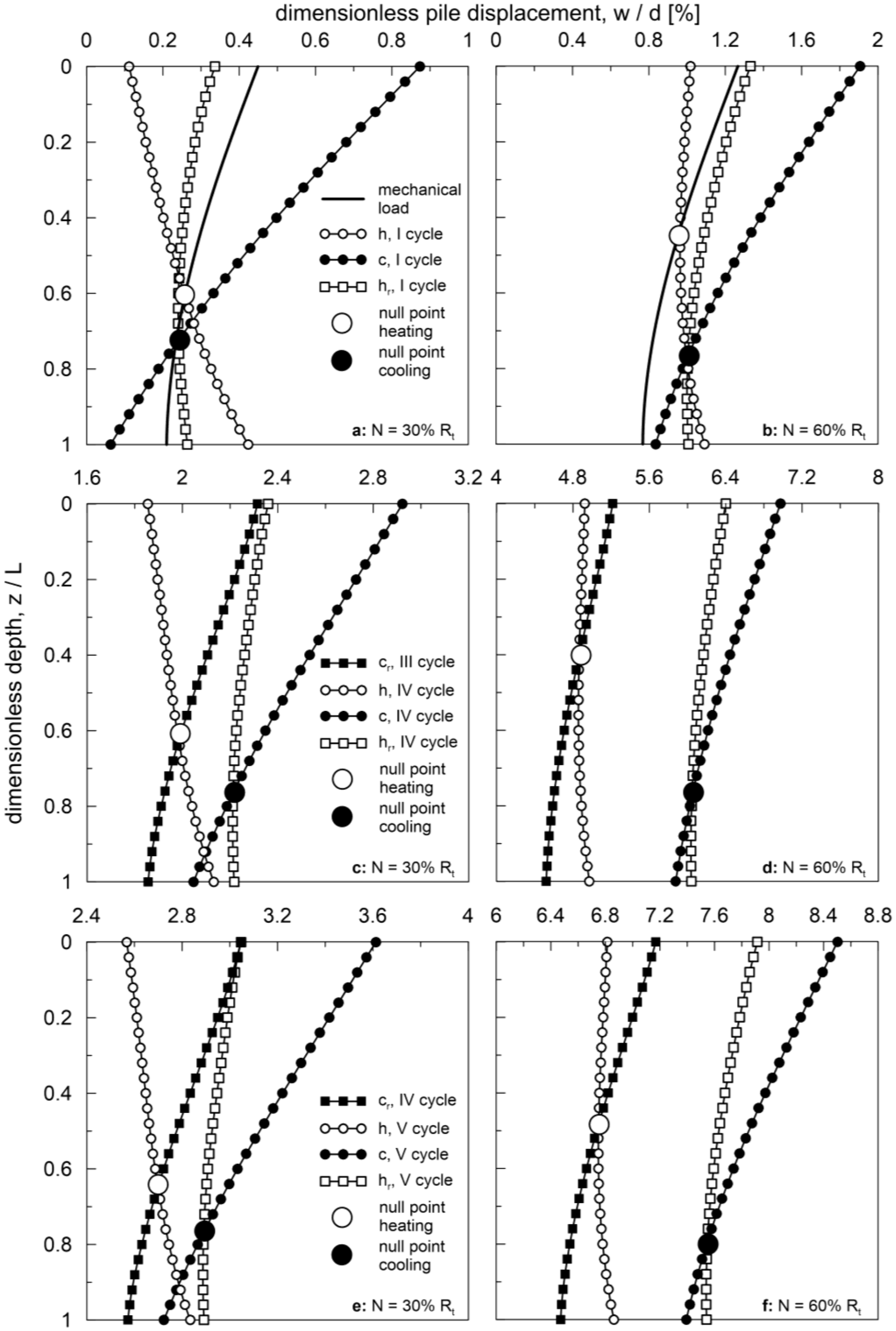

Figure 5.51. Dimensionless displacement of the pile along its length in the I, II and V cycles, free-head pile (HT model).

With reference to the axial load profiles, it can be noticed that thermally-induced load is not affected by the activation of the thermal term. The thermal term takes into account the volumetric collapse of the soil as a consequence of the temperature increase. Therefore, since the contraction of the soil would induce a further restraint to the pile expansion, a difference in the thermally-induced axial force should have been expected during the heating, continuous heating and rest after cooling phases.

Regarding the heating phase, solely the soil in the vicinity of the pile experiences a temperature variation. In this case, all the elements along the shaft and at the base are subjected to volumetric expansion recovering (entirely or in part) the contraction of the mechanical loading phase. In figures 5.52 and 5.53 the behaviour at the local scale is reported for 30% R_t, for the H and HT models, respectively. In particular, the element located at 6.25m experiences a final volumetric strain of -0.06% (H) and -0.07% (HT), the element at 12.5m of -0.09% (both H and HT), the element at 18.75m of -0.09% (H) and -0.08% (HT), the element at 25m of 0.05% (H) and 0.04% (HT). It can be observed that the response of the hypoplastic model with the activation of the thermal term is in agreement with the behaviour found employing the hypoplastic model. In fact, in the thermo-hypoplastic model, the volumetric collapse of the clay is prevented by the impossibility of water to flow outside the element; given to its incompressibility, the expansion of the water controls the volumetric response. More specifically, since the thermal expansion coefficient of the water is higher than that of the soil skeleton, the increase of the temperature determines the development of positive excess pore pressure. Moreover, the soil would contract and this contraction is contrasted by the expansion of the water which must thus adsorb a larger pressure to guarantee the compatibility of volumetric deformations. Therefore, in undrained or close to undrained conditions, the excess pore pressure is higher in magnitude if the thermo-hypoplastic model is used. This is evident comparing figure 5.54 with figure 5.55. The excess pore pressure is equal to 6kPa (H) and 8kPa (HT) at 6.25m, to 9kPa (H) and 12kPa (HT) at 12.5m, to 11kPa (H) and 16kPa (HT) at 18.75m, to 50kPa (H) and 60kPa (HT) at 25m.
As a consequence of the prevented volumetric collapse, in this step the volumetric behaviour is almost the same for both models, and, therefore, the restraint exerted by the soil doesn’t change significantly leading to no major differences in the load distribution. Moreover, the higher the positive excess pore pressure, the lower the mean effective stress (discussed later on) and consequently the mobilized shear stiffness. This last effect is also responsible of the differences found in the position of the null point.

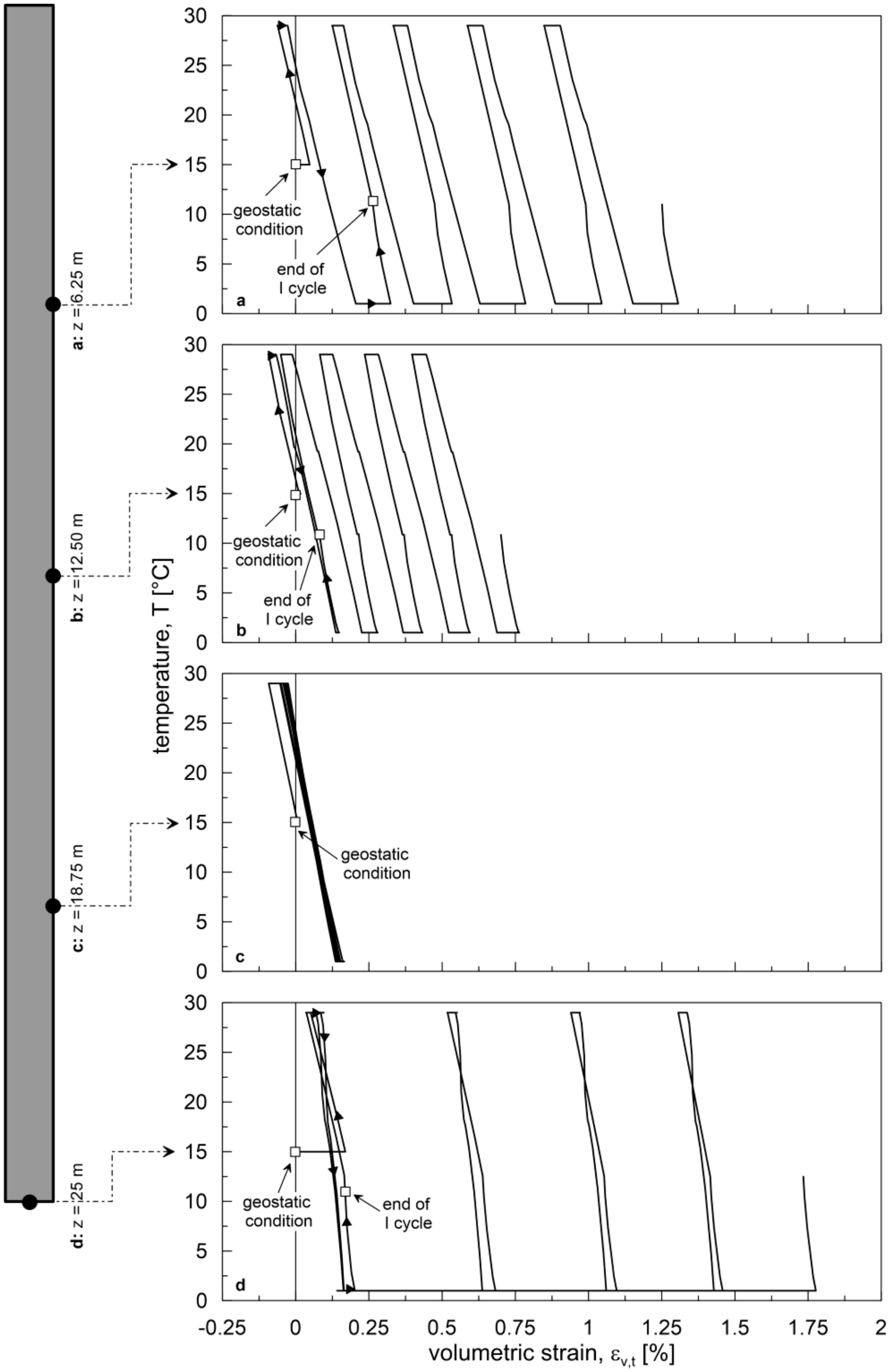

Figure 5.52. Volumetric strain versus temperature, free-head pile (H model, *Q* = 30% *R_t*).

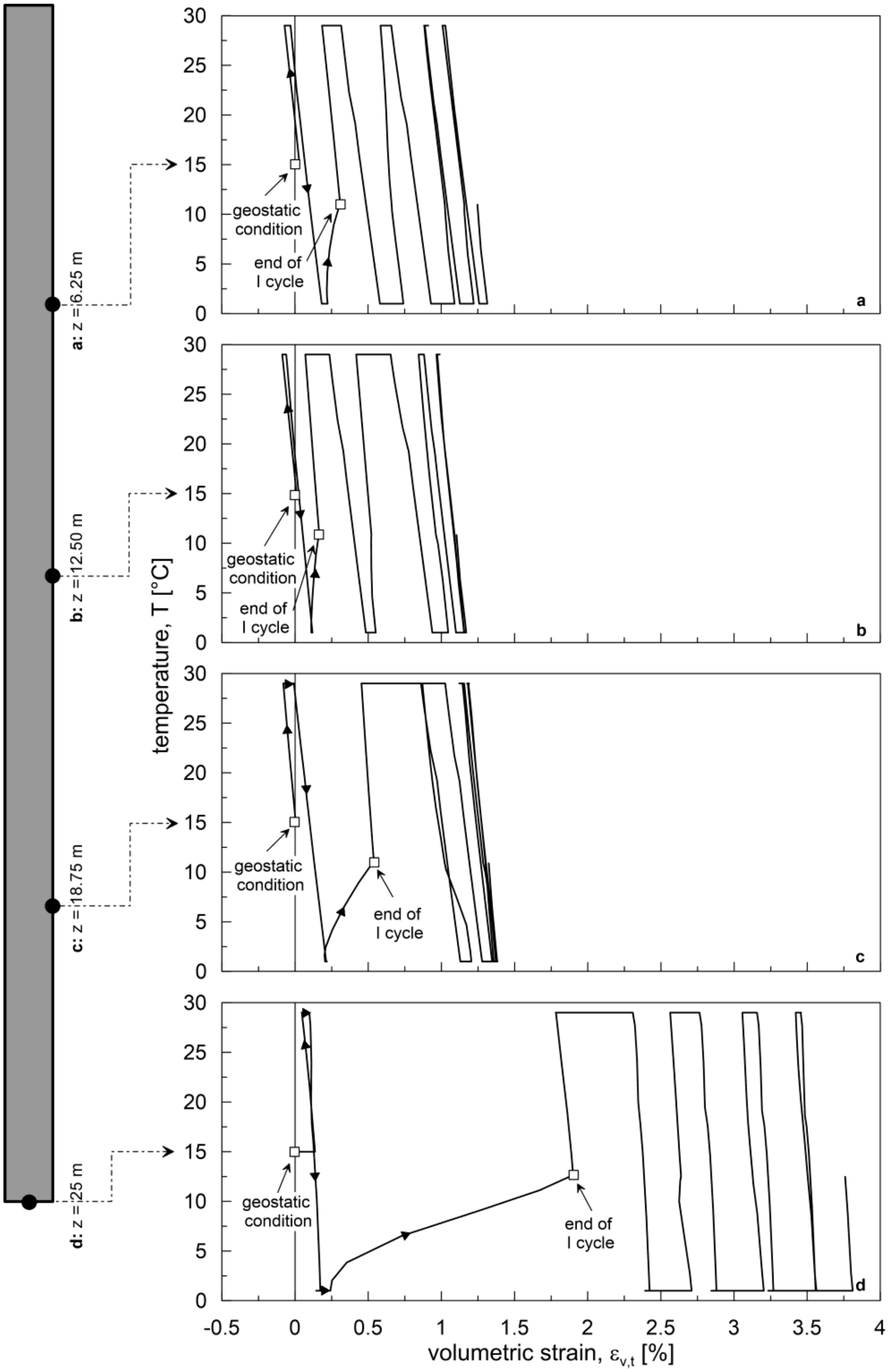

Figure 5.53. Volumetric strain, free-head pile (HT model, *Q* = 30% *R*$_t$).

The continuous heating phase is characterized by the increase of the temperature in further portion of the soil and by the contraction of the elements due to the partial dissipation of the positive excess pore pressure. Compared to the hypoplastic model ($\Delta\varepsilon_v$ = 0.03%, 0.025%, 0.04% and 0.035% from the top to the bottom, respectively), the highest contraction develops using the thermo-hypoplastic model ($\Delta\varepsilon_v$ = 0.04%, 0.03%, 0.07% and 0.05%). Anyhow, the two models show similar results and no differences are found in the load distribution.

The main difference in terms of volumetric behaviour between the hypoplastic and the thermo-hypoplastic model is found in the thermal rest phase after the first cooling. From figure 5.52, expansion takes place as a consequence of the temperature increase; the volumetric strain developed in this step ($\Delta\varepsilon_{v,t}$) are equal to -0.06% at 6.25m and at 18.75m, -0.07% at 12.5m, -0.035% at 25m. For the same reason, increase of the excess pore pressure is found (the final values are 1.4kPa at 6.25m, almost 0kPa at 12.5m, -1.3kPa at 18.75m and 1.3kPa at 25m). On the contrary, if the thermo-hypoplastic model is used, the highest percentage of volumetric contraction develops (Fig. 5.53). The rest phase after cooling follows the continuous cooling phase in which the soil is interested by negative or null excess pore pressures (almost 0kPa at 6.25m, -2kPa at 12.5m, -4kPa at 18.75m, -3kPa at 25m). Therefore, differently from the heating phase, the soil surrounding the pile is mostly characterized by the decrease of pore pressure with respect to the hydrostatic condition; as a consequence, a flux of water towards farther elements with lower pore pressure is possible and volumetric collapse can occur. Moreover, since no thermal condition is imposed to the pile, the increase of the temperature in the pile and in the soil next to the pile is simultaneous in accordance to the thermal boundary conditions of the model; the result is that, as discussed earlier, the axial load profile is almost the same of that resulting employing the hypoplastic model. Finally, the thermal collapse causes additional development of positive excess pore pressure with final values being lower than the excess pore pressure of the heating phase (7.3kPa at 6.25m, 7.7kPa at 12.5m, 10.2kPa at 18.75m, 11.8kPa at 25m).

As concerns the cyclic solicitation, for both models, the volumetric behaviour is characterized by open loops with overall volumetric contraction at each depth (Figs. 5.52 and 5.53; after 5 cycles: 1.25% at 6.25m both H and HT; 0.7%, H, and 1.1%, HT, at 12.5m; 0.08%, H, and 1.3%, HT, at 18.75m; 1.75%, H, and 3.8%, HT, at 25m) and accumulation of excess pore water pressure with decreasing rate cycle after cycle (Figs. 5.54 and 5.55; after 5 cycles: 8.2kPa, H, and 17.2kPa, HT, at 6.25m; 6.6kPa, H, and 21.2kPa, HT, at 12.5m; 4kPa, H, and 22.2kPa, HT, at 18.75m; 5kPa, H, and 17.3kPa, HT, at 25m). In fact, regardless of the element location, the excess pressure doesn’t dissipate in the individual cycle. Since the behaviour is inelastic, the coupling between shear and volumetric strains affects the pore pressure system and can be responsible of the progressive accumulation. The behaviour stabilizes within 3 cycles.

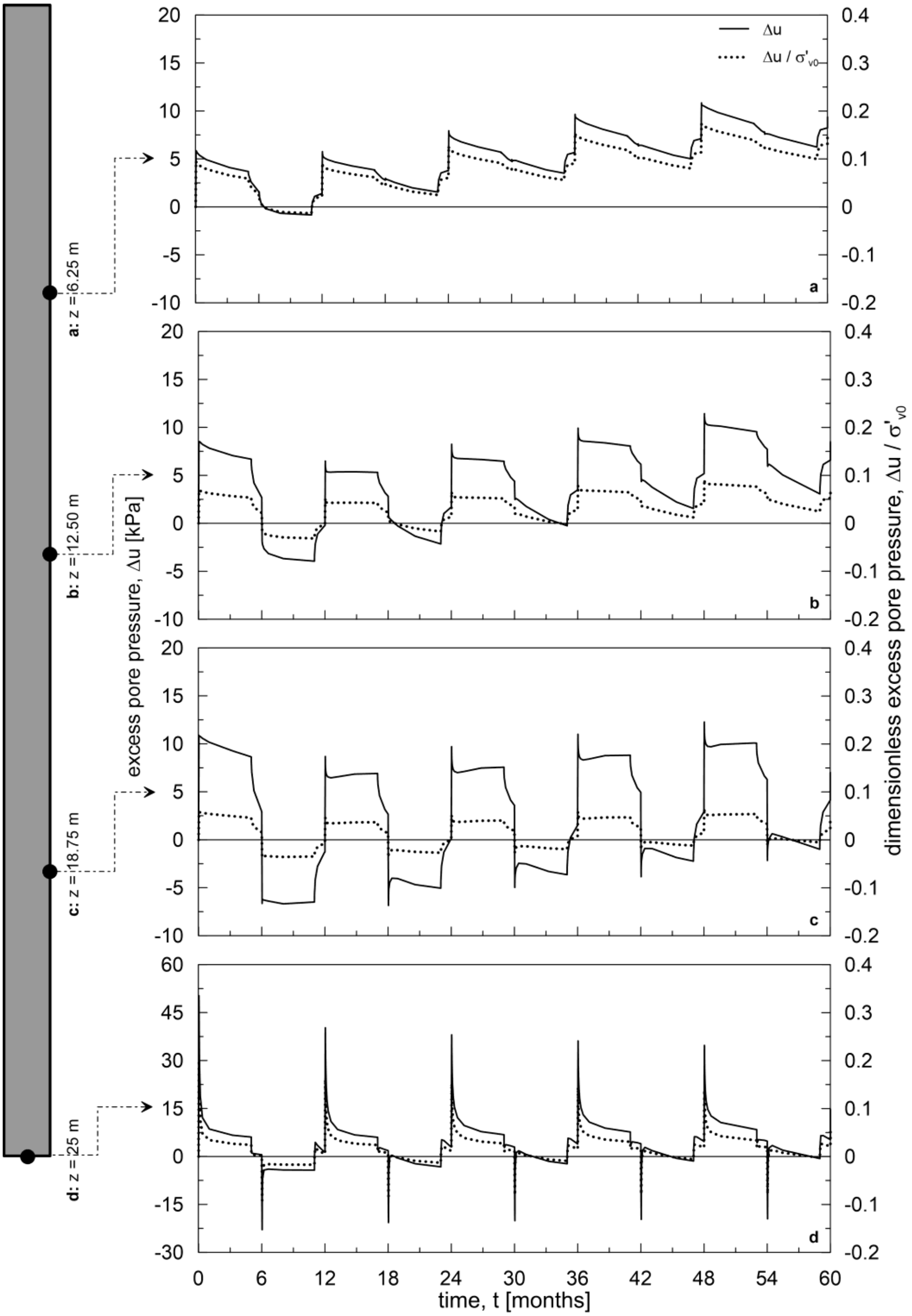

Figure 5.54. Excess pore pressure, free-head pile (H model, Q = 30% R_t).

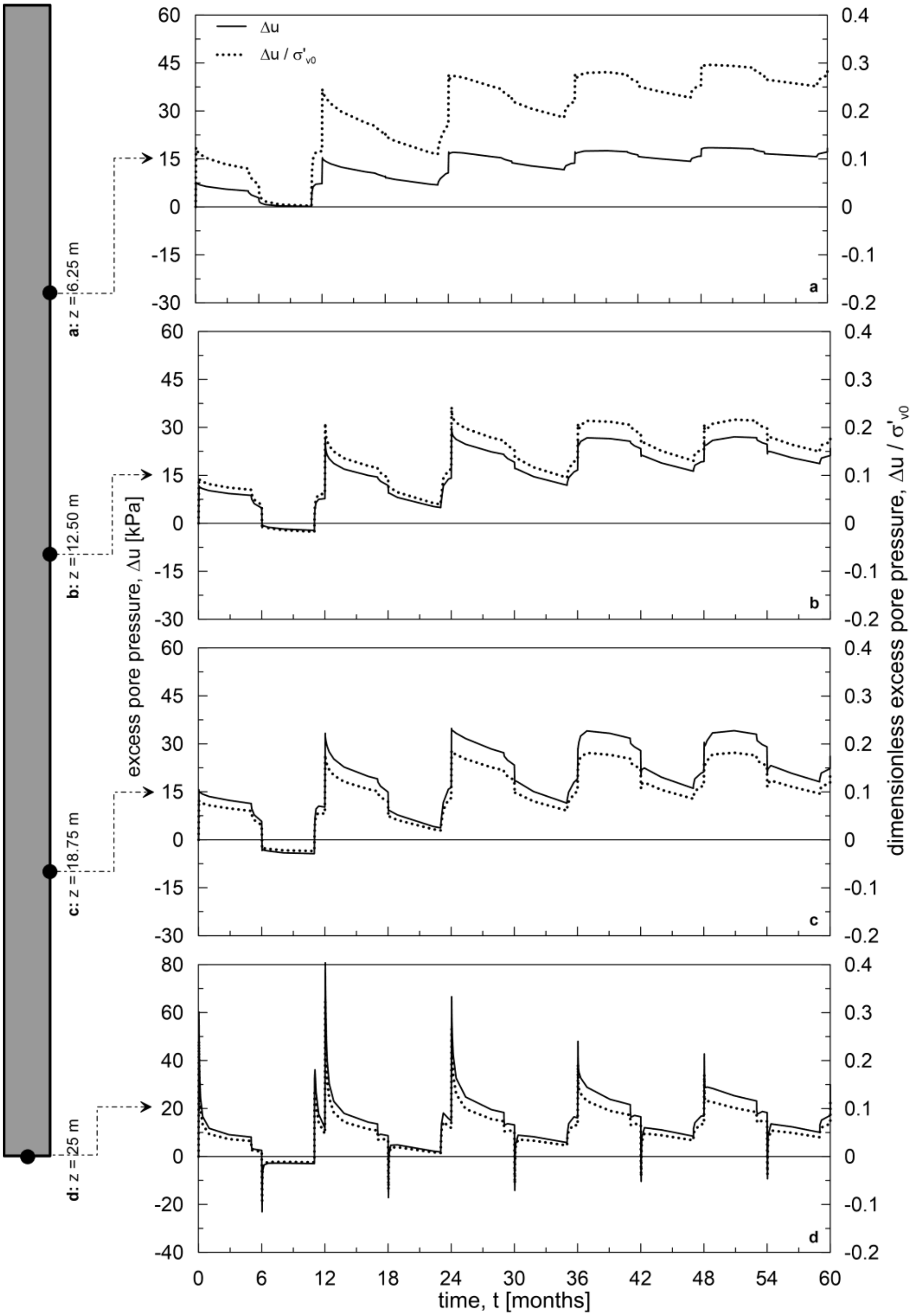

Figure 5.55. Excess pore pressure, free-head pile (HT model, Q = 30% R_t).

From the analyses of the pore pressure in the single cycle, it can be noted that: partial dissipation of positive pore pressures occurs during each step in which heating is kept constant for 5 months and during the rest phase after heating; when the temperature is reversed and during the continuous cooling, decrease of the excess pore pressure develops with no additional rate caused by the volumetric behaviour. Indeed, the actual accumulation is due to the response in the continuous cooling phase. During the first cycle, accumulation of negative pore pressure with no dissipation takes place for both models at any depth while in the following cycles, as a consequence of the accumulation, the excess pore pressure tends to be positive and the continuous cooling is dominated by the decrease of the pore pressure.

Contours of pore pressure distribution in the vicinity of the pile have been analysed at various time instants of the continuous cooling step (Fig. 5.56). It can be noted that the magnitude of the pore pressure at the pile soil interface is higher than that in the right-side zone. Because of the hydraulic gradient, a flux of water takes place from the interface. As a consequence, the pore pressure at the interface decreases until the equilibrium has been restored or until the temperature reversal starts. This behaviour involves the next cycles too, but at a decreasing rate. The comparison with the pore pressure distribution obtained with the MC and the MCC models, at the same depth and time, reveals that the pore pressure is lower at the interface than in the other zone of the soil and tends to increase due to hydraulic conduction (Fig. 5.57). The different response of the hypoplastic models is responsible of the accumulation of negative pore pressures during the continuous cooling of the first cycle.

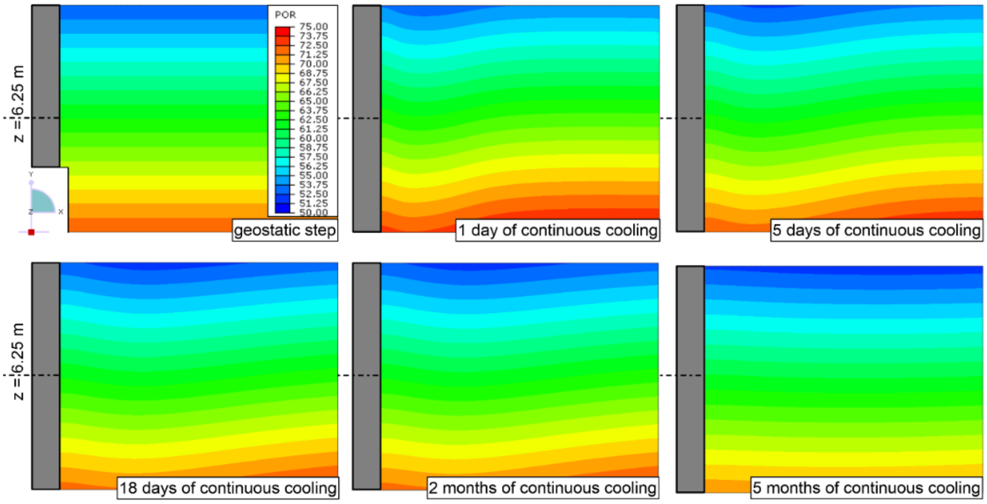

Figure 5.56. Pore pressure distribution [kPa] during the continuous cooling of the I cycle, free-head pile (H model, Q = 30% R_t).

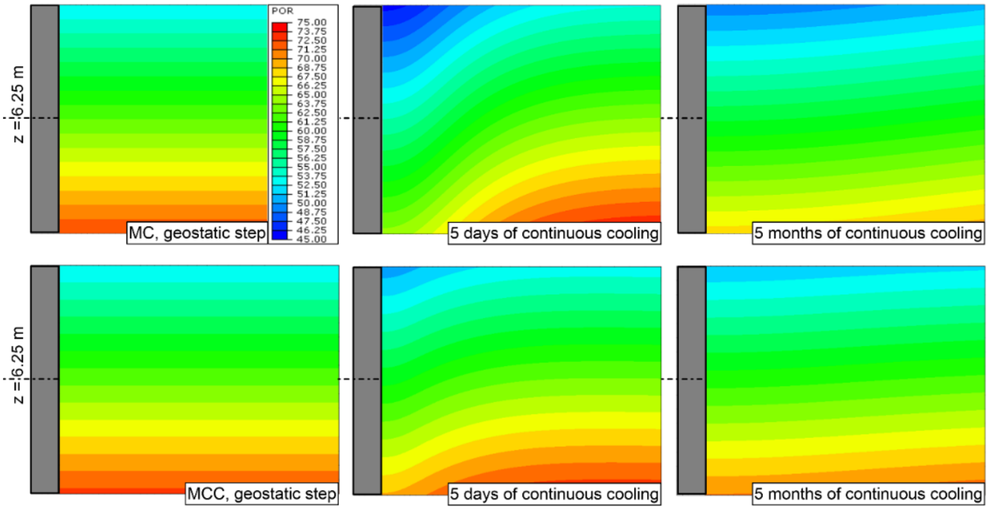

Figure 5.57. Pore pressure distribution [kPa] during the continuous cooling of the I cycle, free-head pile (MC and MCC models, Q = 30% R_t).

The behaviour in terms of local shear strain is reported in figures 5.58 and 5.59. Underneath pile base the shear strains are negligible if compared to the volumetric strains. Along the shaft, at the end of the mechanical loading phase, positive shear develops (0.5% at 6.25m, 0.28% at 12.5m, 0.2% at 18.75m for both models). After the first thermal cycle, the increase of γ is bigger in magnitude with increasing depth; the overall values are: 0.6%, H, 0.56%, HT, at 6.25m; 0.45%, H, 0.45%, HT, at 12.5m; 0.43%, H, 0.75%, HT, at 18.75m. In the following cycles, the shear strain increases with positive values, the only exception being the element at 6.25m. In fact, for the shallower elements the shear strain decreases showing overall negative values from the fourth cycle onward. If the thermo-hypoplastic model is used, the decrease of the shear strain is also encountered from the fourth cycle at the depth of 12.5m. After 5 cycles, the shear strains are: -0.8%, H and HT, at 6.25m; 1.2%, H, 1.25%, HT, at 12.5m; 0.89%, H, 1.65 %, HT, at 18.75m.

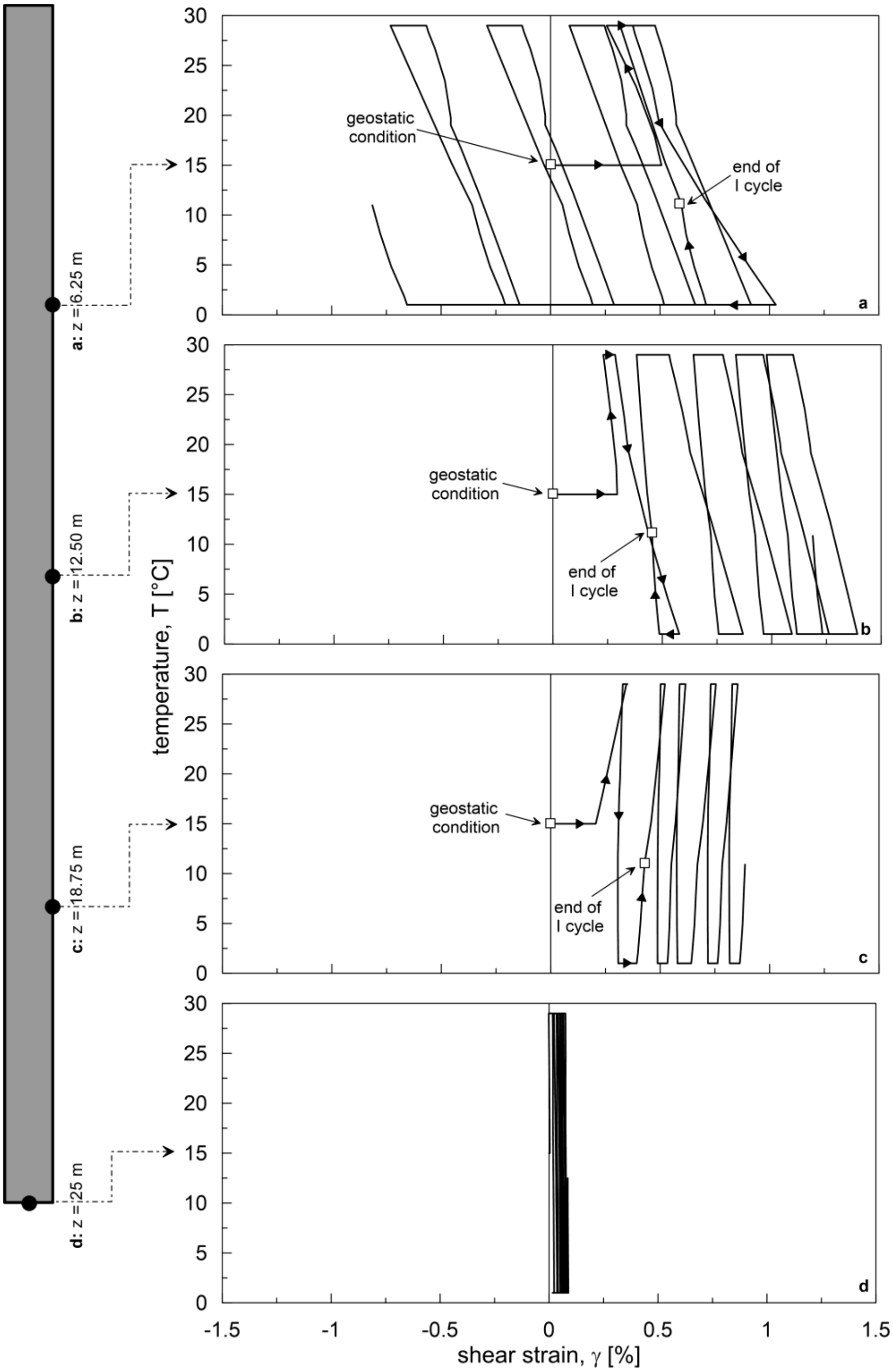

Figure 5.58. Shear strain versus temperature, free-head pile (H model, Q = 30% R_t).

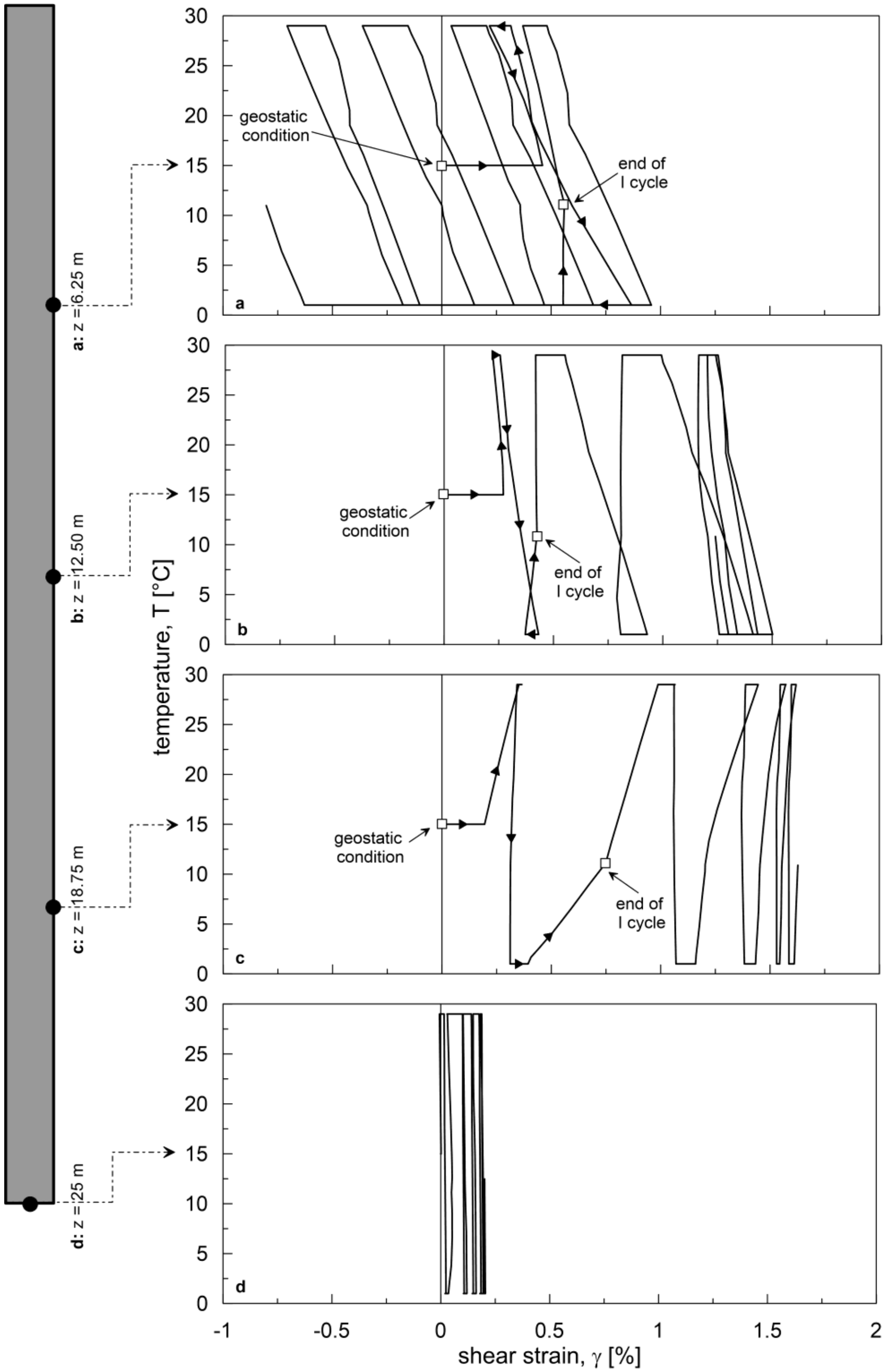

Figure 5.59. Shear strain, free-head pile (HT model, Q = 30% R_t).

Even though γ is progressively decreasing, at 6.25m the local settlements increases cycle after cycle (Figs. 5.60a and 5.61a). This behaviour seems not to be not consistent with the above results since, based on the shear strains trend, the settlements are expected to reduce. It can be explained considering that, in the uppermost part, the soil surrounding the pile is settling more than the pile itself, likely due to the consolidation phenomenon (Fig. 5.62); as a consequence, the shear strain decreases up to negative values. This effect plays a major role in the response of the shallower elements. For the other depths, shear strains are positive and cyclic downward movements develop (Figs. 5.60b, c, d and 5.61b, c, d). At the end of the mechanical loading phase, for both models, the local settlements are equal to 0.38% *d* at 6.25m, 0.3% *d* at 12.5m, 0.24% *d* at 18.75m, 0.2% *d* at 25m. During the cyclic variation of the pile temperature, accumulation of irreversible settlement takes place causing additional displacements cycle after cycle. After 5 thermal cycles, the settlements increase in magnitude up to 1.84% *d*, H, and 3.6% *d*, HT, at 6.25m, 1.7% *d*, H, and 3.45% *d*, HT, at 12.5m, 1.55% *d*, H, and 3.3% *d*, HT, at 18.75m, 1.5% *d*, H, and 3.2% *d*, HT, at 25m. It can be noted that, if the thermo-hypoplastic model is employed, the accumulated settlements get higher values due to the continuous heating phase. In fact, when the temperature is kept constant for 5 months, the heat flux leads to the increase of the temperature of farther portion of the soil and, consequently, the upward movements are partially or totally prevented by the thermal collapse of the clay. Therefore, differently from the other constitutive models, the continuous heating phase is mostly dominated by downward movements. This local behaviour is reflected at the global scale.

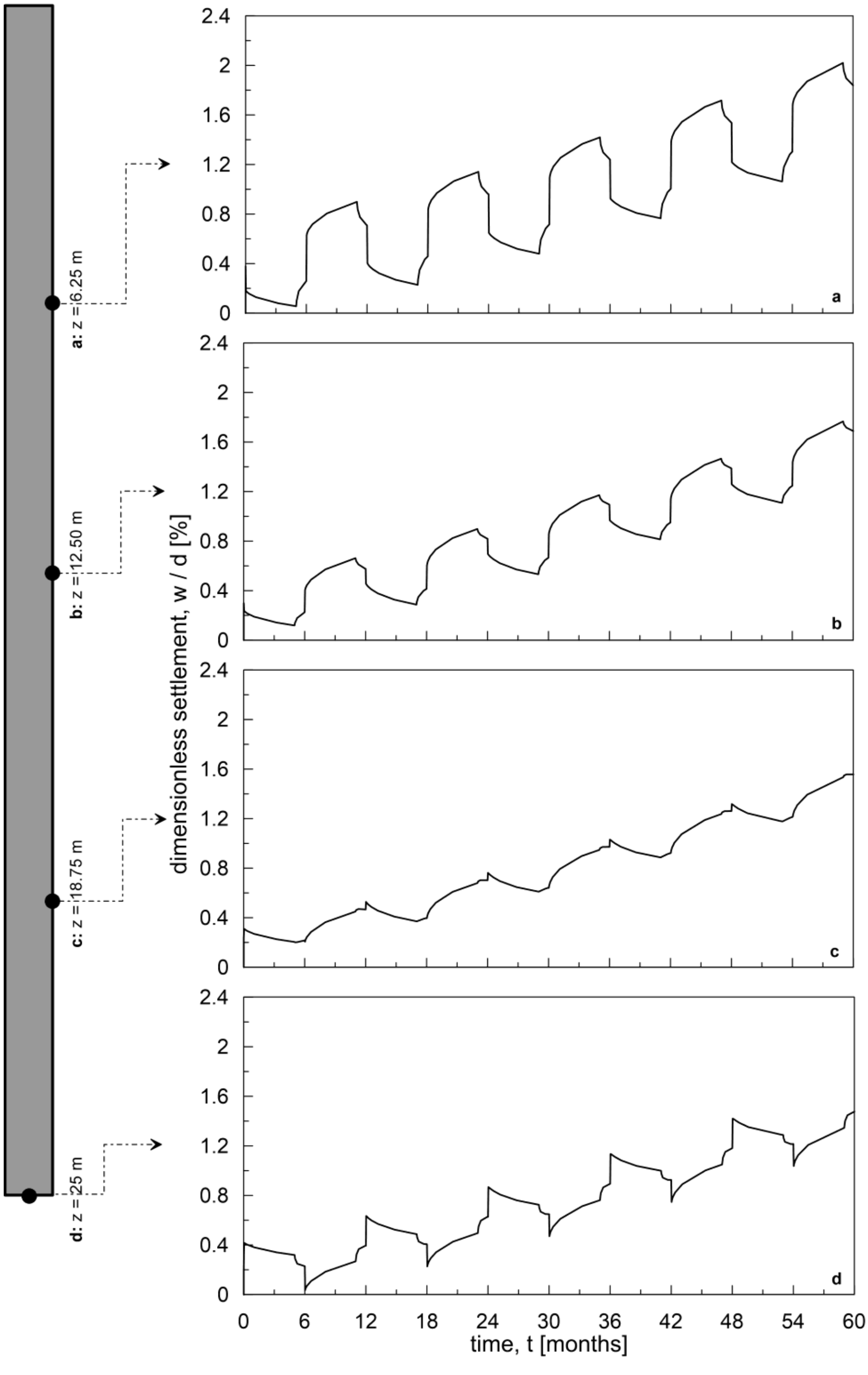

Figure 5.60. Local settlement versus time, free-head pile (H model, Q = 30% R_t).

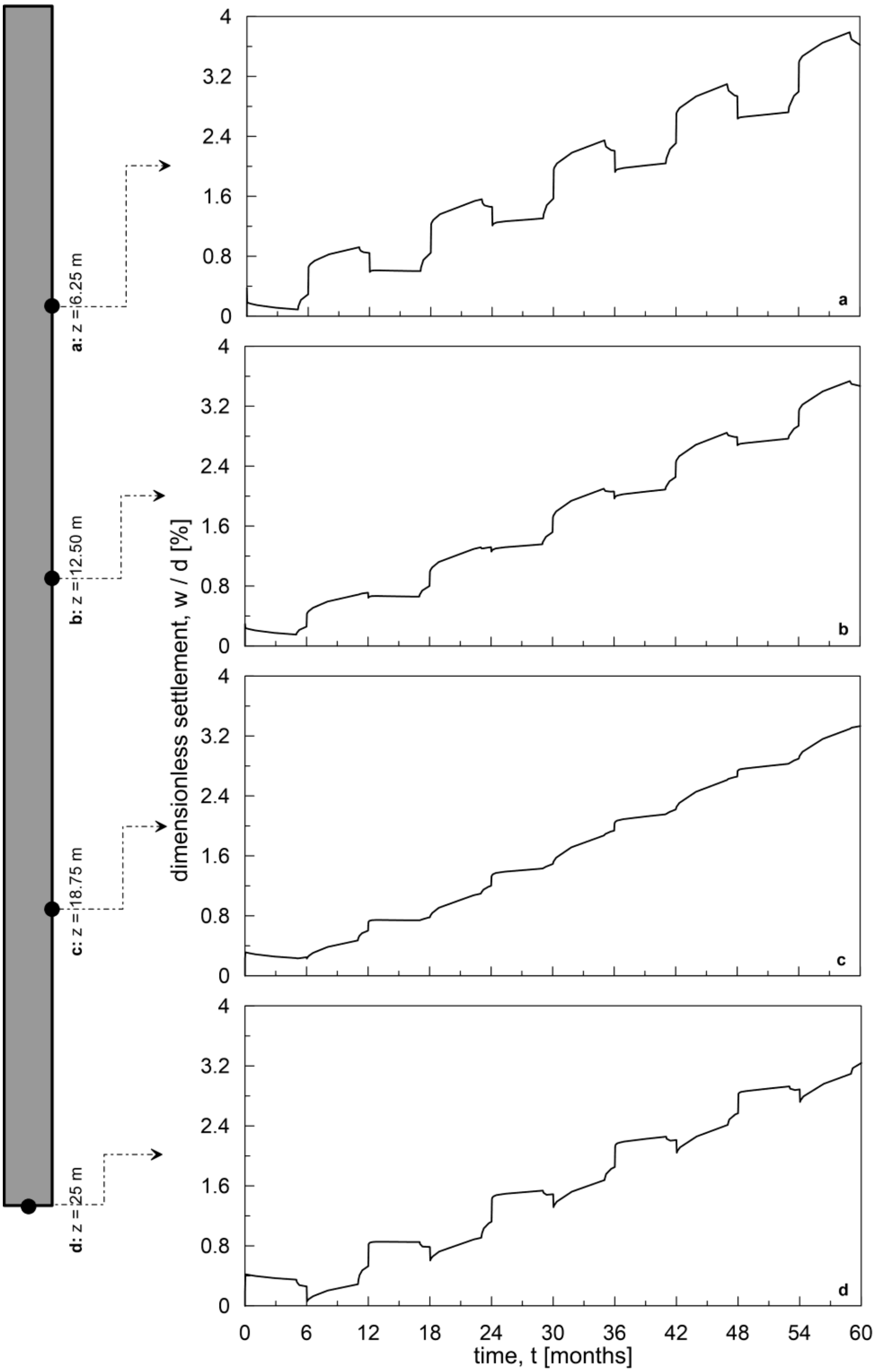

Figure 5.61. Local settlement, free-head pile (HT model, Q = 30% R_t).

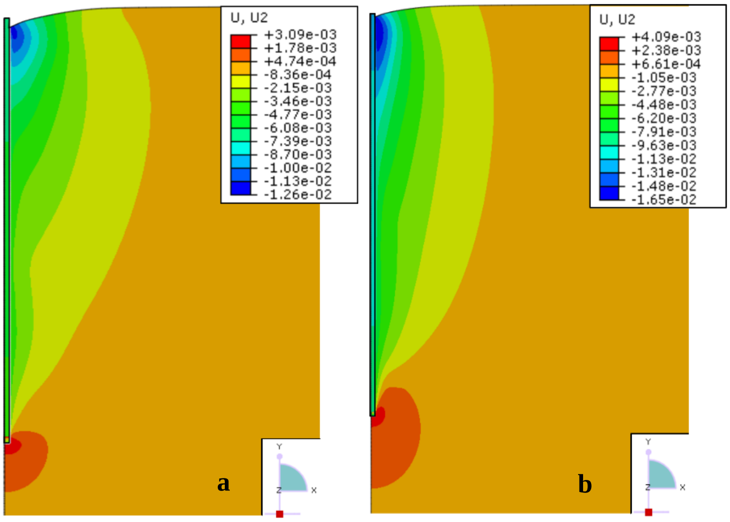

Figure 5.62. Vertical displacements [m] at the end of third cycle, free-head pile (a, H model, Q = 30% R_t; b, HT model, Q = 30% R_t).

The global settlements are reported in figure 5.63. When the applied load is equal to the 30% R_t, the overall displacement after 5 thermal cycles is equal to 1.97% *d* and to 3.75% *d* for the hypoplastic and the thermo-hypoplastic model, respectively. Therefore, with respect to the mechanical loading phase (0.47% *d*) the settlement is about 4.2 (H) and 7.9 (HT) times larger. The accumulation slightly decreases cycle after cycle; hence, the highest irreversible displacement occurs during the first cycle, the displacement being about 1.75 (H) and 2 (HT) times larger than that experienced at the end of the mechanical loading stage.

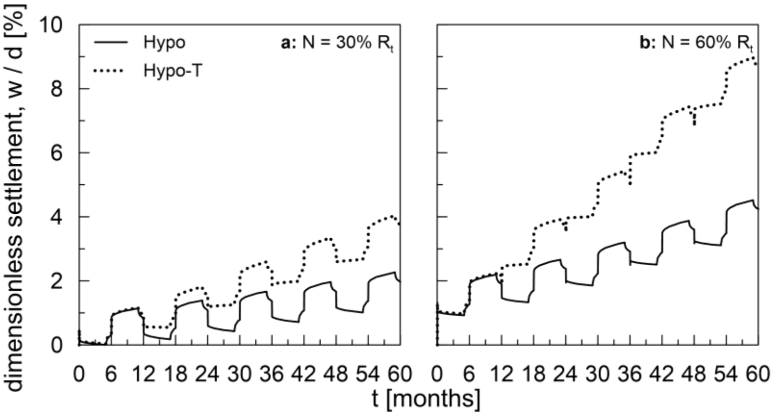

Figure 5.63. Dimensionless global settlement, free-head pile (Hypo and HT models).

If the applied mechanical load is equal to 60% R_t, although the overall magnitude of the global settlements is higher (4.2% *d*, H, and 8.7% *d*, HT), a lower accumulation of irreversible displacements is encountered compared to the mechanical loading phase (1.3% *d*). Indeed, the final settlement increases of about 3.2 (H) and 6.7 (HT) times while at the end of the first cycle the overall displacement is about 1.5 (H) and 1.7 (HT) times larger than the initial settlement. It is worth noting that the magnitude of the thermally-induced displacements increases with increasing the mechanical load level because the response is more dominated by non-linearity and irreversibility.

As regards the loading paths (Figs. 5.64 and 5.65), although the elements along the shaft are mainly characterized by the reduction of the mean effective stress and the deviatoric stress, the behaviour in terms of p' is quite different depending on the model used. In fact, when the hypoplastic model is employed, the decrease of p' is simlar from one cycle to the other; while, the activation of the thermal term leads to a stronger reduction of p' in the first and in the second cycle. In particular, in accordance with the excess pore pressure profiles (Fig. 5.54), the maximum reduction develops during the first rest phase after cooling. The values found at this step employing the HT model are equal to 33kPa at 6.25m, 75kPa at 12.5m and 101kPa at 18.75m and are approximately equal to that experienced in the same step using the hypoplastic model but after 5 thermal cycles: 26kPa, 66kPa, 118kPa, from the top to the bottom. As concerns the deviatoric stress, the reduction of q with respect to the geostatic step is maximum in the shallower elements and decreases with depth (68%, H, 74%, HT, at 6.25m; 63%, H, 65%, HT, at 12.5m; 38%, H, 26%, HT, at 18.75m). The element located underneath pile base experiences opposite behaviour in terms of p' depending on the choice of the constitutive model. If the H model is used, a progressive growth of p' and q is shown (Fig. 5.64d). In this case, after 5 thermal cycles, the mean effective stress and the deviatoric stress increase of about the 14% and 4%, respectively, with respect to the geostatic step. If the HT model is employed, while q increases of about the 14%, a decrease of -8% is found in terms of p'. This is likely due to the higher magnitude of the positive execess pore pressure caused by the volumetric collapse of the soil. In fact, even though for both models the pile is setteling and the soil is chracterized by volumetric contraction at any depth, the stronger development of positive excess pore pressure with the HT model may play a major role in the evolution of the mean effective stress.

The decrease of the mean effective stress is evident in the deviatoric plane (Figs. 5.66 and 5.67), where the surfaces related to the heating and cooling phases of the fifth cycle are smaller in size if compared with that of the first cycle. In the geostatic condition, the stress state is triaxial and the Lode angle is equal to 60°; during the loading process, the Lode angle varies according to the sign of the thermal solicitation imposed. At any depth, the stress state lies always inside the M-N surface.

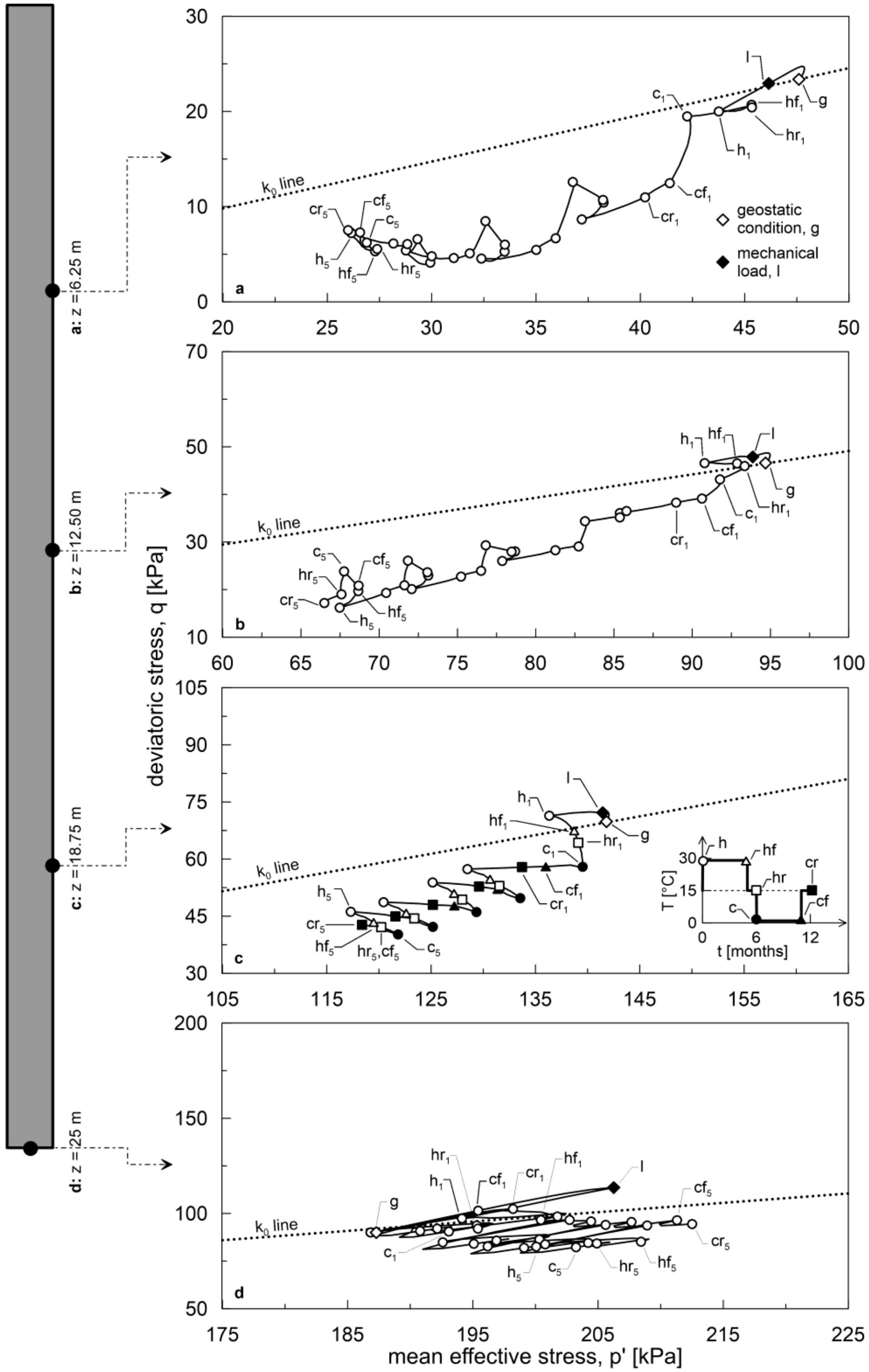

Figure 5.64. Load paths, free-head pile (H model, *Q* = 30% *R*$_t$).

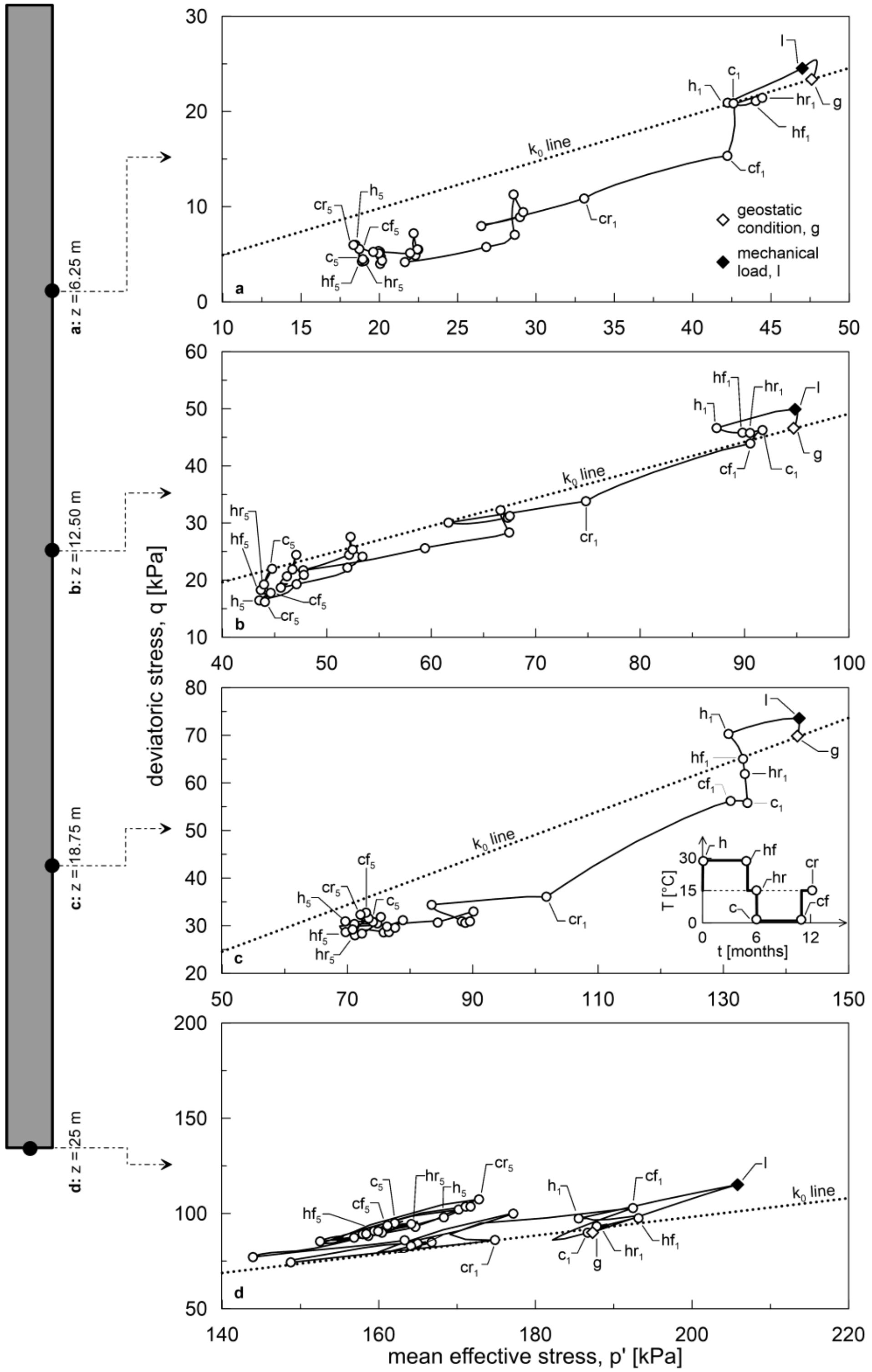

Figure 5.65. Load paths, free-head pile (HT model, $Q = 30\%\ R_t$).

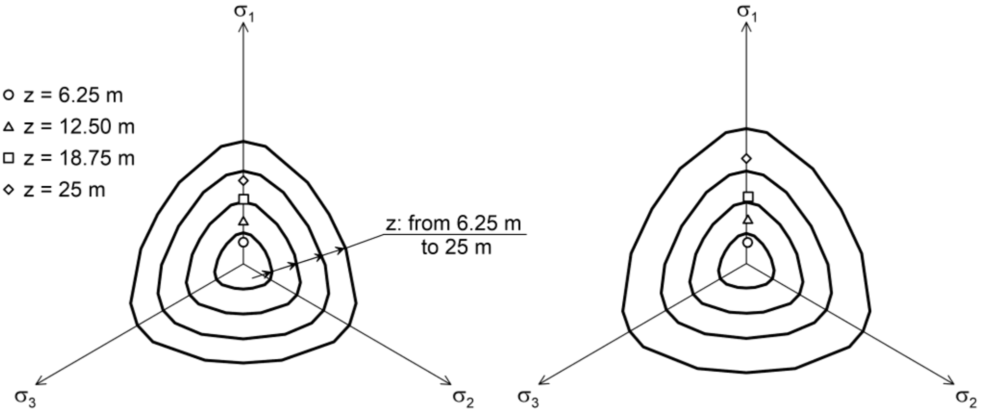

geostatic condition

mechanical loading

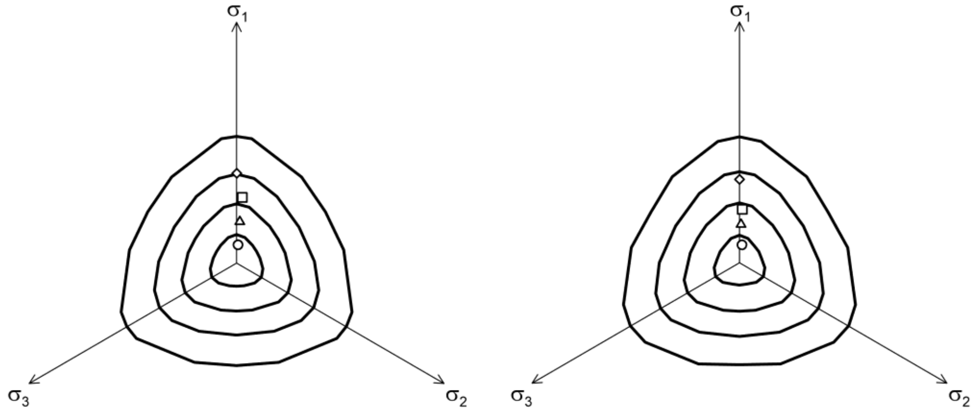

heating, I cycle

cooling, I cycle

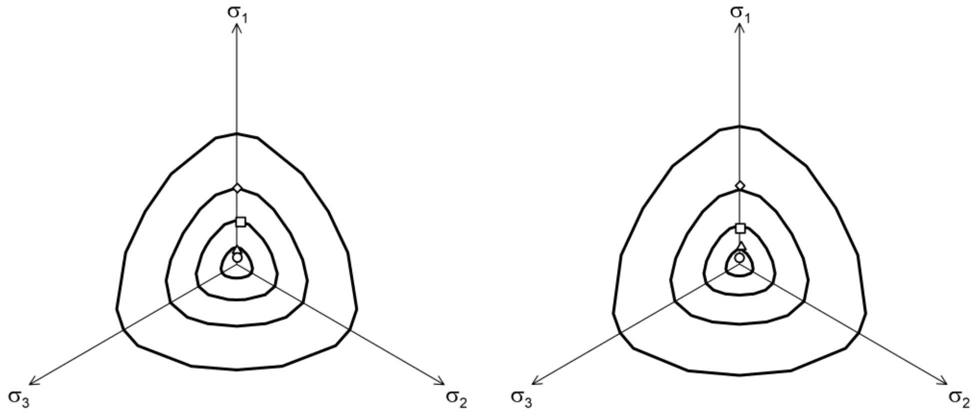

heating, V cycle

cooling, V cycle

Figure 5.66. Stress state in the deviatoric plane, free-head pile (H model, Q = 30% R_t).

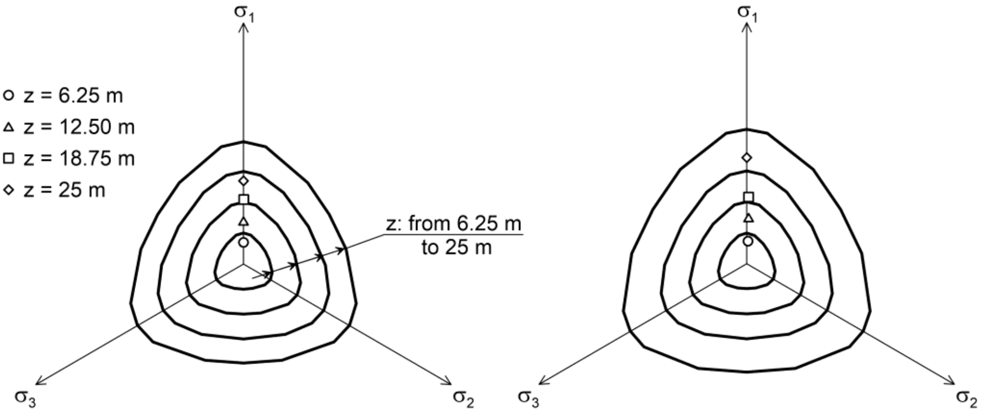

geostatic condition mechanical loading

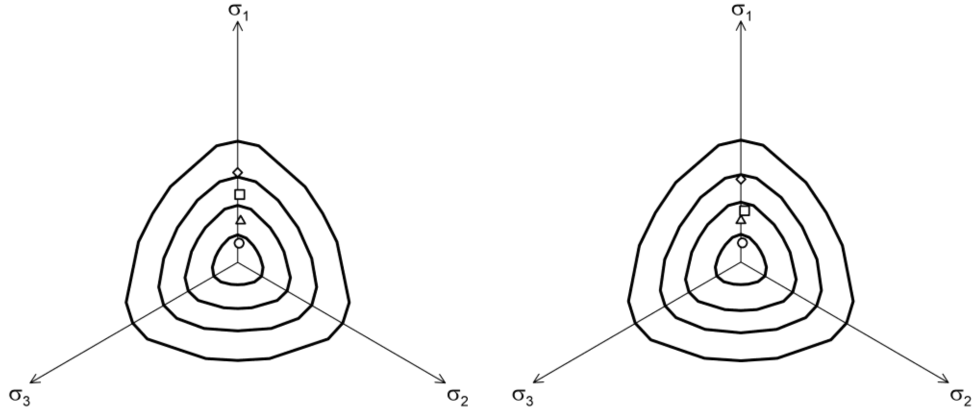

heating, I cycle cooling, I cycle

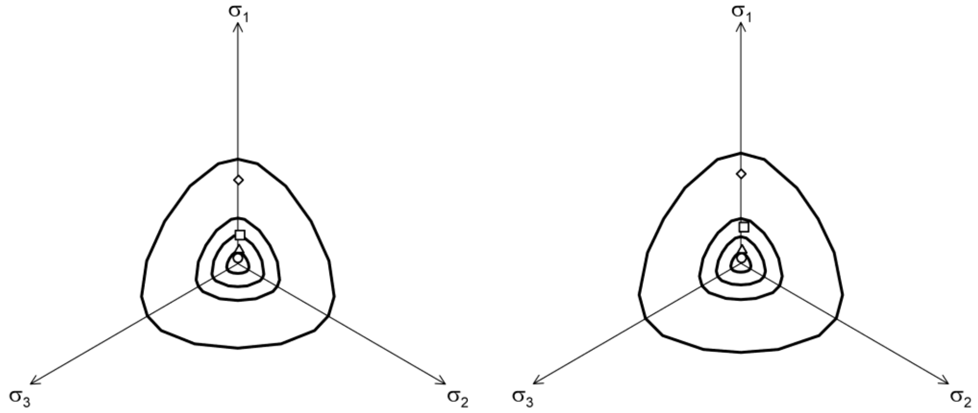

heating, V cycle cooling, V cycle

Figure 5.67. Stress state in the deviatoric plane, free-head pile (HT model, $Q = 30\%\ R_t$).

5.2.6.2. Fixed-head pile

The results in terms of axial load employing the hypoplastic and the thermo-hypoplastic models are shown in figures 5.68 and 5.69. In figure 5.68 the label h_f refers to the continuous heating, while in figure 5.69 the heating phase is labelled with h. It is worth noting that, when employing the thermo-hypoplastic model, the maximum axial force at head occurs in the heating phase rather in the continuous heating. In fact, during the continuous heating the thermal collapse opposes to pile expansion and the result is a reduction of the axial load at head. For the hypoplastic model, the higher value of the axial load at head is obtained, as for the other models, during the continuous heating phase. The maximum thermally-induced forces are in the first cycle and are equal to: 21% R_t, H (overall 51% R_t) and 17% R_t, HT (overall 47% R_t), for a load level of 30% R_t; 12% R_t, H (overall 72% R_t) and 6% R_t, HT (overall 66% R_t), for a load level of 60% R_t.

During the cooling phases the behaviour is exactly the same regardless the activation of the thermal term, the only difference lying in the magnitude of the axial force due to the different behaviour during the heating. The overall load decreases cycle after cycle. At the fifth cycle, a tensile load acts at head. The results obtained with the thermo-hypoplastic model show the lowest value for the tensile load for both the mechanical load levels: -39% R_t, H (overall -9% R_t) and -57% R_t, HT (overall -27% R_t), for a load level of 30% R_t; -62% R_t, H (overall -2% R_t) and -81% R_t, HT (overall 21% R_t), for a load level of 60% R_t. If more thermal cycles are applied, the reduction of the axial load would proceed until the soil shear strength has been fully mobilized.

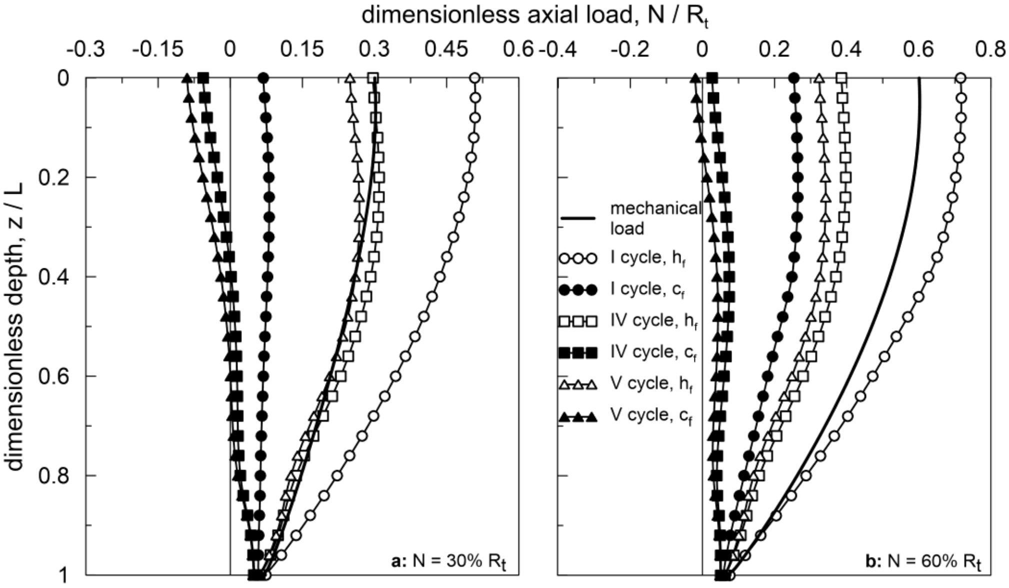

Figure 5.68. Axial load distribution in the I, IV and V cycles, fixed-head pile (Hypo model).

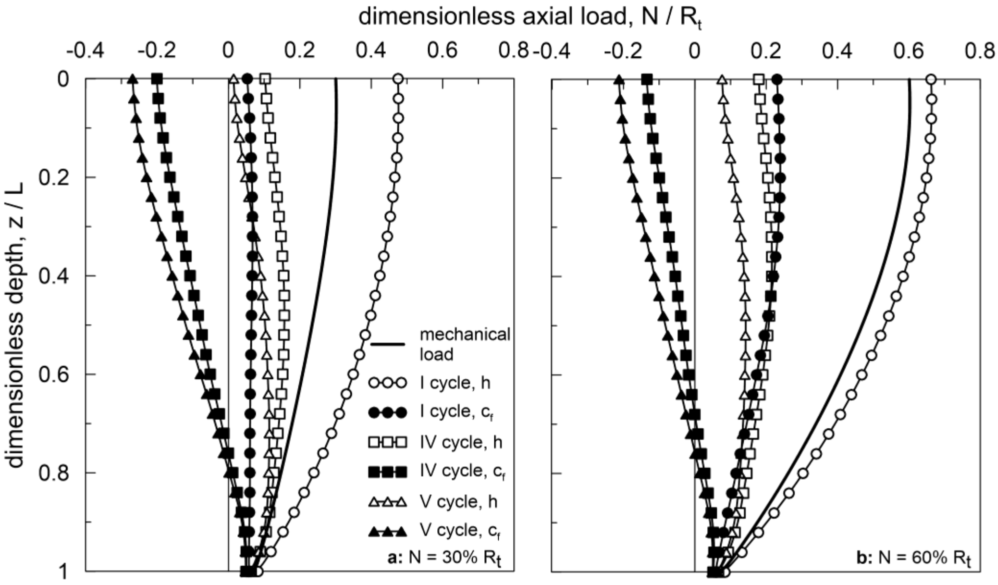

Figure 5.69. Axial load distribution in the I, IV and V cycles, fixed-head pile (HT model).

5.2.7. Further comments

Axial load profiles and boundary condition at pile head

As shown in figures 5.21, 5.34, 5.46, 5.68 and 5.69, the axial load distribution for the fixed-head pile tends to decrease cycle after cycle. While for the Elastic, the MC and the MCC models a stable behaviour is found from the second cycle, with the Hypo and Hypo-T models stability is not reached and tensile load develops along pile shaft and at its base. This tendency of the axial load to decrease cycle by cycle is not observed in the case of free-head pile (Figs. 5.12, 5.23, 5.35 and 5.49). For the free-head pile the last step of the cycle, i.e. the rest after cooling, give rise to an axial load that is higher compared to the initial mechanical load (Fig. 5.8b and 5.9b). Therefore, the axial load in the second cycle starts from this distribution and moves rightward toward higher compressive stress. On the contrary, at the end of the cooling rest for the fixed-head pile, the axial load distribution is lower than that coming from the mechanical load (Figs. 5.18b and 5.19b). This implies that the second cycle is characterized by an axial load distribution that moves leftward toward tensile values. These results are highlighted when irreversibility dominates the behaviour of the system. The same results are obtained by Suryatriyastuti et al. (2015) for piles embedded in sandy soil. Likewise, Nguyen et al. (2017) investigated the behaviour of a single free-head energy pile showing that if the applied mechanical load is ≥ 20% of the pile ultimate resistance, the axial load along the pile increases cycle after cycle.

Compared with the calculation of pile groups or piled rafts foundations, the analysis with reference to the single energy pile leads to the overestimation of the thermally-induced axial force and, neglecting the interaction (according to Rotta Loria et al. (2016a) the interaction factor is lower than 0.1 when the ratio $s/d > 3$) and considering that usually not all the piles of a foundation are energy piles, of the settlements too. Indeed, due the heat diffusion inside the soil, the long-term behaviour is characterized by the temperature variation of the non-energy piles leading to a reduction of the axial force in the active pile, while the settlements increases tending to the free-head condition. As a consequence, the maximum values of the axial force are found at the beginning of the thermal process and should be taken into account at the design stage.

In Salciarini et al. (2014) a group of 17 piles is surmounted by a stiff raft in contact with the ground and the geometrical configuration is such that the distance between the piles of the group is about $3d$. In one of the simulations, solely the central pile is heated (ΔT=20°C) in 1 day, then the temperature is kept constant until the steady state condition is reached. The maximum axial load at the head of the heated pile is registered after 1 month of continuous heating and is 3.5 times bigger than the load at the end of the mechanical loading phase; the effect on the other pile is basically negligible because the excess load (2.5) is shared between 16 piles. After one month, the other piles start to experience an increase in temperature that leads to a decrease in the axial load of the active pile. Thus, the highest difference of temperature is responsible of the highest axial load in the heated pile. If the applied temperature is of cooling (ΔT=-15°C) the energy pile is subjected to a decrease of the axial load whose maximum value is reached after 1 month and is equal to about 2 times the mechanical load; therefore, the overall load is tensile and of the same order of magnitude of the applied mechanical load. The Authors suggest that, since the considered time period of 1 month is well inside the normal operational conditions of the energy systems, the design of the foundation should properly consider this effect. In these analyses the soil is made of a stratification of sand and clay and the constitutive model employed is linear elastic. Therefore, the effects of plasticity are not taken into account and the axial load can increase or decrease without a limit. Nevertheless, it can be highlighted that, considering that the piled raft is analysed via a 3D FE analysis, if only one pile is activated, the foundation behaves qualitatively as the fixed-head pile studied in the present analyses. This behaviour is further confirmed in other works available in literature. Mimouni and Laloui (2015) report the results of a series of short tests carried out on a group of 4 energy piles. In particular: (i) a free-head pile test was performed on pile 1 before the construction of the tank; (ii) single pile tests were carried out after the construction of the tank activating one energy pile per each test; (iii) a final group test with all the piles thermally-activated was also performed. Defining the degree of freedom as the ratio between the mobilized thermal strain and the maximum thermal strain, it is shown that, during test (i) the degree of freedom at the head of pile 1 was about 0.82 and decreased to 0.1 when the pile 1 was activated after the tank construction (ii). Moreover, during the group test (iii) it gets a double value accompanied by lower thermal axial loads and higher pile head heave if compared to test (ii). They also showed that the restraint condition at head has an influence up to about 0.7 times the pile length. For the same test site, Rotta Loria and Laloui (2018a) report the data of two tests after the tank construction along with 3D thermo-mechanical analysis. Differently from the first tests, these tests are performed during a longer span of time: (iv) 5 months of heating followed by 10 months of passive cooling of the single pile; (v) 2 months of heating followed by 10 months of passive cooling with four operating energy piles. They showed that, compared to test (v), if only one pile is activated the vertical stresses in the energy pile increases while the upward movement along with the vertical strain decrease. Therefore, the thermally-induced load at head and along the shaft is always larger in magnitude when only one pile is activated. As concerns the activation of the whole group, it is worth noting that: for all the tests the raft is in contact with the ground and its stiffness has a finite value; the mechanical load at pile head varies according to the position of the pile in the group (Di Donna at al., 2016); the thermal field inside the piles is not uniform since the first four meters of the pile were thermally insulated to avoid the thermal interaction with the water stored inside the tank, leading to the compression of the top section of the pile and to a higher constraint when heating is imposed. As a consequence, the activation of the whole group of piles is characterized by the redistribution of the load with values at head that are different from that at the end of the mechanical loading phase. This is found also in Di Donna and Laloui (2014). The Authors report the results of a series of FE analyses on a single energy pile and on a piled raft composed by energy piles embedded in a normally consolidated clay. The raft is in contact with the ground and therefore, it is shown that, if the piles are thermally activated simultaneously, a redistribution of the axial loads among the piles is found; nevertheless, the thermally-induced head movement is the same of that experienced by the single energy pile. Moreover, the null point is always located below the pile mid length and its position is almost the same as that of the simulated free-head pile. This behaviour confirms that if all the piles are thermally-activated the variation of the axial load at head is caused by the presence of the raft while the overall behaviour is closer to the free-head pile. Similar results are obtained by Salciarini et al. (2017). They report the results of 3D FE analyses on a piled raft foundation and analysed both the configurations in which solely the central pile is activated and the whole group is thermo-active. Dupray et al. (2014) performed a series of numerical analyses on piled raft embedded in a clay; they compared the response of the activation of one pile and the whole pile group. The raft was in contact with the ground. It was shown that the highest thermal loads are inferred in the first configuration, while the use of the whole foundation allowed the reduction of the 60% of the load along with the global uplift of the foundation.

Null point

For all the models except the Linear Elastic in which there is no plastic component, the null point in heating shifts upward. With increasing the applied mechanical load, to cope with the mobilization of the shaft resistance with depth, the upward movement is more pronounced. The opposite behaviour is observed when the temperature is decreased. The results obtained are in accordance with Rotta Loria et al. (2015) and Di Donna and Laloui (2015a); the latter showed that the null point in always located below the pile mid length and that in heating its position is shallower than in cooling.

Cyclic settlements

The cyclic accumulation of irreversible settlements dominates the behaviour of the free-head pile with the Hypo and the Hypo-T models. As shown in figure 5.63, after 5 cycles, the accumulation of irreversible displacements is still relevant for both the hypoplastic and the thermo-hypoplastic models. To check if a stabilization can be reached after more cycles, 5 additional cycles have been performed. The results are shown in figure 5.70 for the thermo-hypoplastic model with applied mechanical load equal to the 30% of the pile bearing capacity. It can be noted that the trend is similar to the first 5 cycles. In fact, the final displacement is equal to about 6.8% *d*, i.e. 14.5 times bigger than the settlement at the end of the mechanical step and 1.8 times higher than that after 5 thermal cycles.

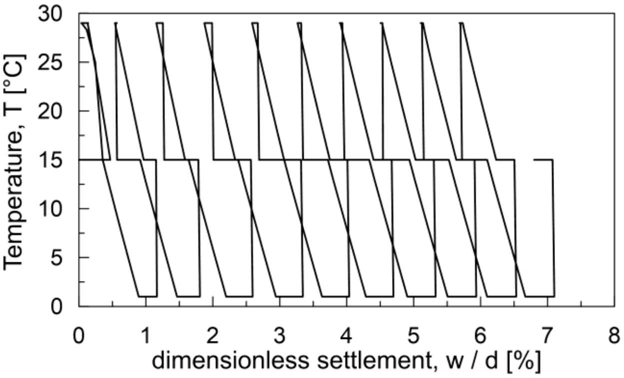

Figure 5.70. Dimensionless global settlement versus temperature after 10 cycles, free head pile (HT model, Q = 30% R_t).

Similar results are obtained by Wu et al. (2018). The data are reported in figures 5.71 and 5.72. They performed a series of tests on small scale floating energy piles subjected to mechanical load (around the 40% of the bearing capacity) and to 5 thermal cycles (14°C and -13°C). The piles were installed in normally consolidated saturated clays. They investigated the response of the energy pile with an adjacent non energy pile without a cap (EP-F); of the energy pile with an adjacent non energy pile connected by a cap (EP-R); of the single free energy pile (EP-S).

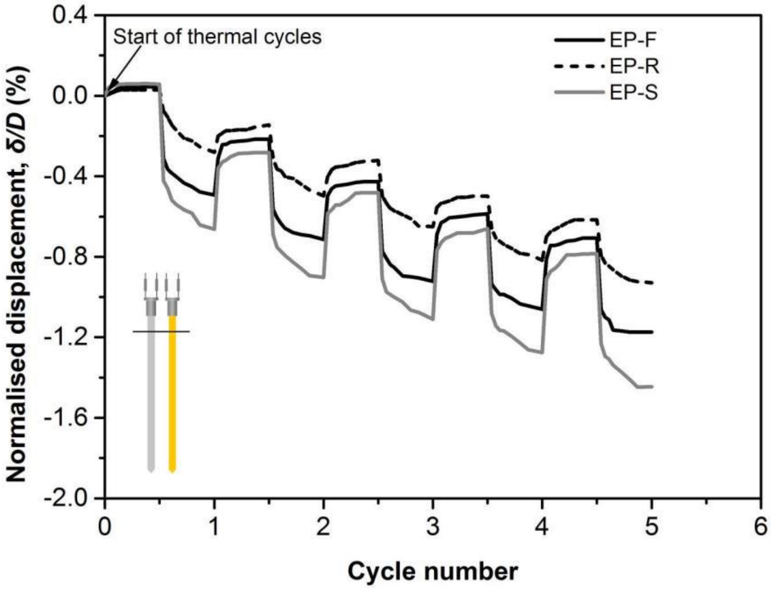

Figure 5.71. Dimensionless displacement after 5 cycles (adapted from Wu et al. 2018).

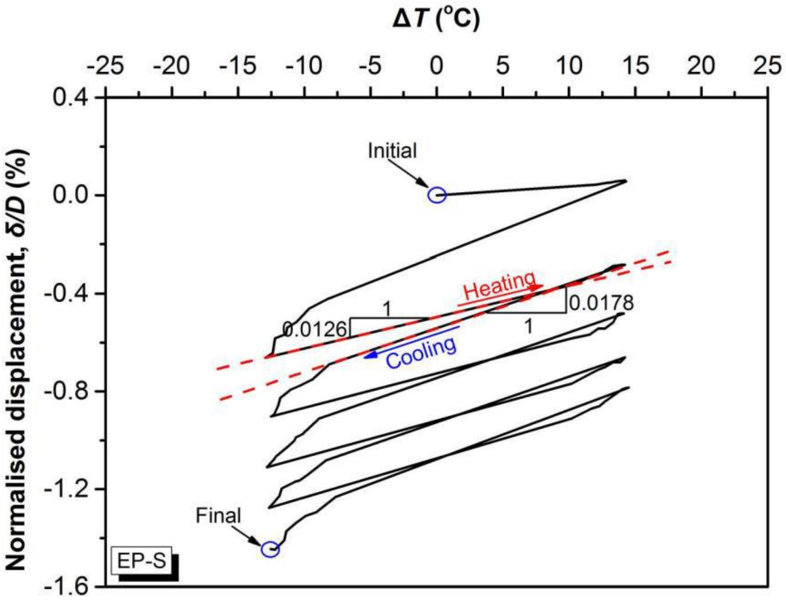

Figure 5.72. Dimensionless displacement versus applied temperature variation (adapted from Wu et al. 2018).

Reference is made to the EP-S. After the application of the mechanical load plus 5 thermal cycles, the pile continues to settle showing a similar trend as figures 5.63 and 5.70. The overall displacement due to the temperature variation is equal to about

1.5% *d*. It is important to consider that the effect of the cyclic settlements is mitigated by the presence of the other piles; the thermally inactive pile (EP-R) allow the reduction of about the 40% of the settlement. This behaviour is confirmed by Rotta Loria and Laloui (2018a) which show that in the group test (v) an average increase of about the 158% of the settlement of the single energy pile of test (iv) is obtained.

Many other studies showing the accumulation of irreversible settlements are available in literature. Among the others, the increase of irreversible settlement as a function of the load level is reported by Vieira and Maranha (2016). They analysed the response of the single pile in a normally consolidated soil and showed that at a load level equal to about the 80% of the pile ultimate capacity and after performing 5 thermal cycles (ΔT=±9°C) the thermal settlement is equal to about 3.8% *d*. Likewise, for a lightly overconsolidated clay (OCR=1.7), Ng et al (2014a) show that, after performing 5 cycles (ΔT=13°C and ΔT=-10°C), if the applied mechanical load is equal to the 40% of the pile bearing capacity, the thermally induced settlement is in the order of 3.8% *d*.

Di Donna and Laloui (2015a) report a different behaviour in terms of settlements. They show that the irreversible displacement mostly occurs in the first cycle, while the accumulation is negligible from the second cycle onward. The load level in the mechanical stage is about the 50% of the ultimate resistance, that has been evaluated with the available data. After the application of the mechanical load, the settlement is equal to about 0.62% *d* and slightly increase up to 0.75% *d* after the first thermal cycle.

To further explore the capabilities of the thermo-hypoplastic model, an additional analysis has been carried out using the parameters calibrated to reproduce the undrained triaxial test by Campanella and Mitchell (1968). In this case, considering that the model has been calibrated on thermal tests, the intent is to understand if a reduction of the thermally-induced settlement is reproduced. The results are reported in figure 5.73 after 10 cycles and after 25 cycles.

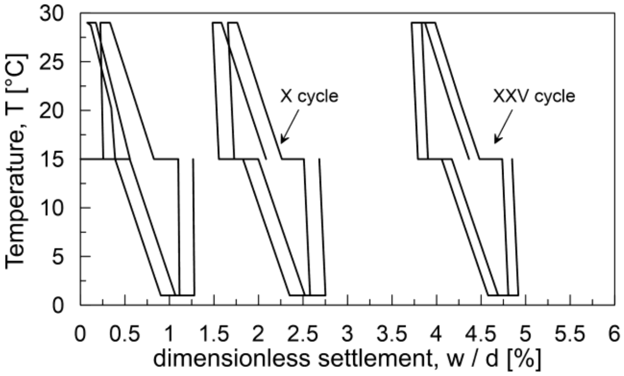

Figure 5.73. Dimensionless global settlement versus temperature, free-head pile (HT model, *Q* = 30% R_t; parameter calibrated from Campanella and Mitchell, 1968).

The accumulated plastic strains decrease but with a very slow rate. Up to the 10th cycle, the settlements (4.36 times bigger than the settlement after the mechanical load) seems not to reduce from one cycle to the other; at the 25th cycle a slightly lower increment is found (8 times higher with respect to the settlement after the mechanical load). Therefore, even though in the last analysis the model has been calibrated on the results of thermal tests, the behaviour is qualitatively similar to that obtained for the London clay.

Pore pressure distribution

To qualitatively compare the results with that of the present FE analyses, the pore pressure distribution relative to the small scale foundation EP-F by Wu et al. (2018) is reported in figures 5.74 and 5.75.

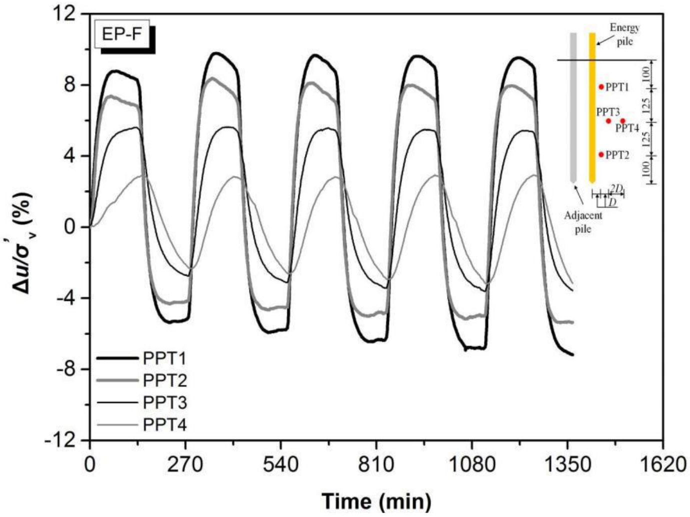

Figure 5.74. Dimensionless excess pore pressure distribution versus time (adapted from Wu et al. 2018).

It can be noted the response is close to the hysteretic behaviour with slight accumulation of pore pressures cycle after cycle. It is important to consider that for this test the drainage conditions are different from that imposed in the FE analyses (the small scale box has a membrane covering the upper part of the soil) and that the applied temperature cycles are characterized by a series of temperature reversals with no rest phases.

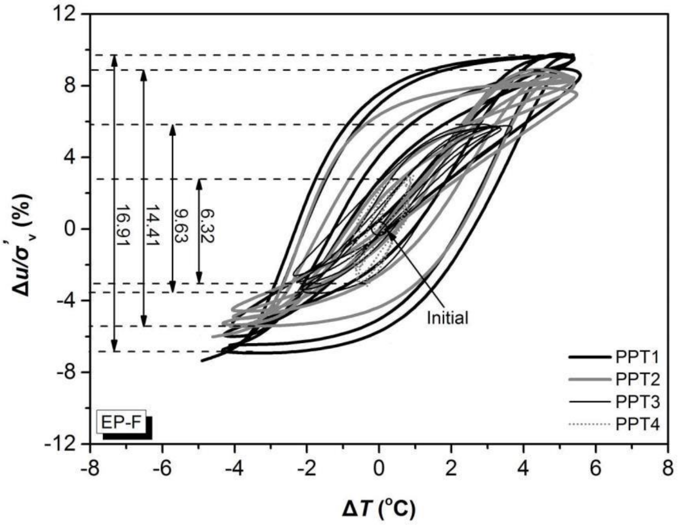

Figure 5.75. Dimensionless excess pore pressure distribution versus temperature (adapted from Wu et al. 2018).

The response of the FE analyses and the laboratory test shows, therefore, some dissimilarities. In figures 5.76 and 5.77 the excess pore pressure obtained with FE analyses is reported versus the temperature. For the elements along the shaft, the hysteretic behaviour can be obtained after few cycles following the accumulation of the excess pore pressures. On the contrary, the element underneath pile base shows a hysteretic behaviour since the early thermal process. The accumulation of shear strains can be responsible of this different response between shaft and base. At pile base, in fact, the behaviour is governed by accumulation of volumetric strains and, as expected, negligible shear strains develop. Moreover, it is worth noting that the thermal expansion coefficient of water has been considered constant with temperature. In figure 3.6 it is shown that this approximation determines hysteric loops from the third cycle onward, while considering a variable thermal expansion coefficient of water allows hysteresis from the beginning of the thermal process. This choice, made to reduce the computational efforts of the rather complex thermo-hydro-mechanical problem, can contribute to the differences between the results of the FE analyses and the laboratory tests.

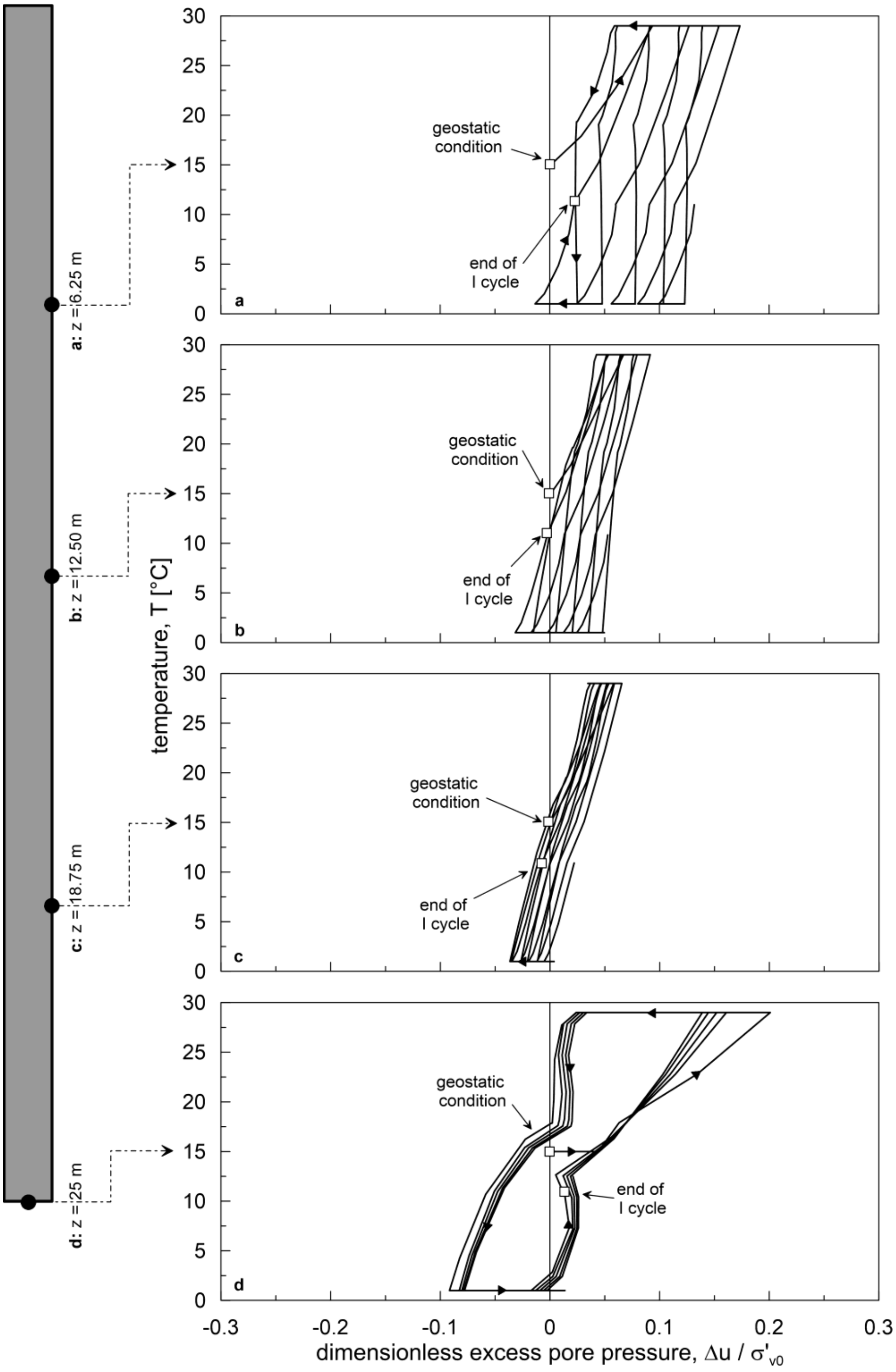

Figure 5.76. Excess pore pressure versus temperature, free-head pile (H model, Q = 30% R_t).

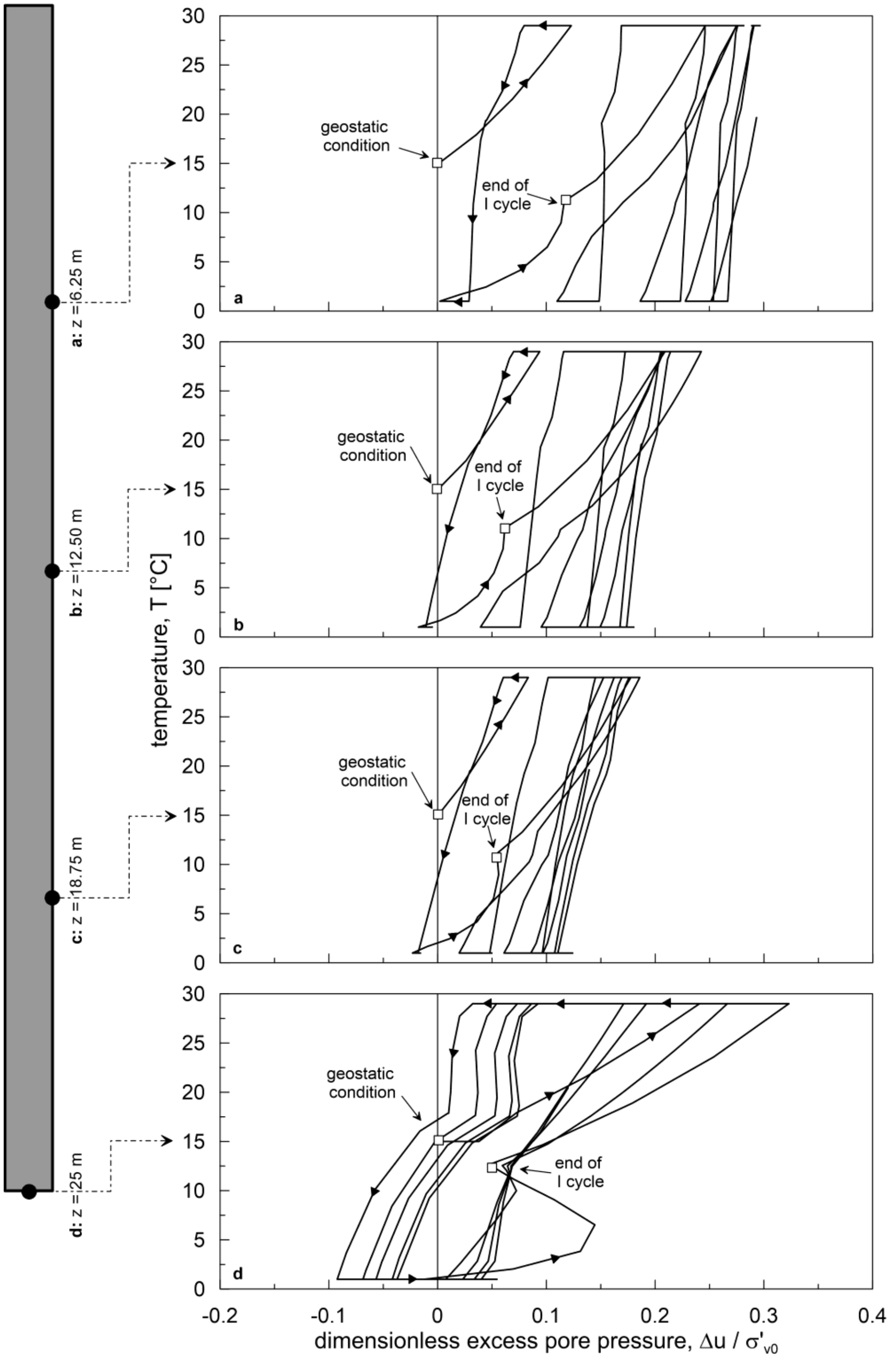

Figure 5.77. Excess pore pressure versus temperature (HT model, *Q* = 30% *R$_t$*).

The development of pore pressure is reported also by Salciarini et al. (2017). The soil has a permeability equal to 10^{-8}m/s while the applied temperature variation ranges between ΔT=±20°C (with a heating rate equal to about 0.2°C per day). They show that the excess pore pressure is about ±40kPa in the first cycle using the configuration in which all the piles are thermally activated. The obtained results are in contrast with Di Donna and Laloui (2014); in this work, although the soil permeability is equal to 10^{-7}m/s, the whole process occurs in drained conditions maybe due to the fact that the maximum temperature variation is reached after 4 months of heating with a very slow heating rate (about 0.12°C per day).

Average axial strain

In figure 5.78 the pile average axial strain is reported for all the models. The axial strain is evaluated with reference to each temperature reversal subtracting the value of the previous phase. In the graphs, the elongation is taken as negative while the shortening is positive.

When the temperature is increased, i.e. during the heating and the rest after cooling phases, the pile exhibits elongation. On the contrary, the decrease of temperature in the cooling and rest after heating phases is characterised by contraction. The continuous heating step causes further pile elongation due to the conduction of heat in the surrounding soil. The only exception is for the thermo-hypoplastic model for which the axial strain remains almost equal to that of the heating phase; this different behaviour can be ascribed to the thermal collapse of soil that turns out in an additional restraint to pile free movements. In the continuous cooling phase, further contraction is experienced regardless of the employed constitutive model.

Considering that the pile thermal expansion coefficient, α_c, is equal to 8.5 x 10^{-6}, a temperature variation of ΔT = 14°C would cause an axial strain of about 0.012% for a free column. This temperature variation is experienced during the heating phase of the first cycle, giving rise to an axial strain of about 0.01%. The value of the free column is almost reached in the continuous heating. If the ΔT = 28°C, the free axial strain is about 0.024%; this temperature variation is attained when reversing the temperature from the continuous cooling to the heating and from the continuous heating to the cooling. The axial strain found for the pile at these steps is of about ±0.021% and increases in the following continuous phases.

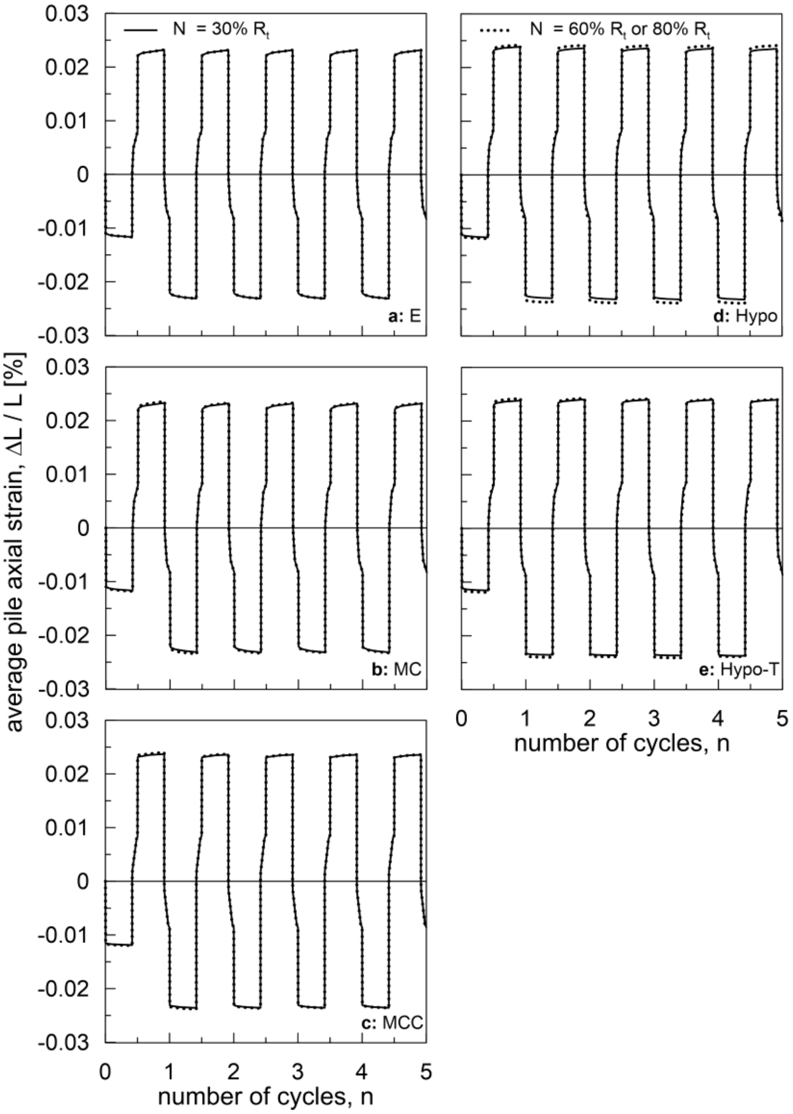

Figure 5.78 Free-head pile average axial strain.

Accordingly, for the fixed-head pile, elongation and shortening takes place respectively during heating and cooling steps for all the models at both mechanical load levels (Fig. 5.79). Since the pile is fixed at head, its movements are governed by the base movements. During the continuous cooling, the shortening of the pile reduces since elongation takes place. As stated before, this step in characterized by the thermal conduction in the surrounding soil; therefore, the pile movement is influenced by the soil contraction underneath its base. The opposite happens in the continuous heating. At this step, the thermo-hypoplastic model has a different response if compared with the other models. In fact, the elongation gets slightly higher in the continuous heating. This is due to the fact that the soil in the vicinity of pile tip contracts instead of expanding. This effect doesn't play a major role because the contraction is partially prevented by the low permeability of the soil. During the rest after heating, the temperature decreases and the pile shortens; during the rest after cooling, the temperature increases and the pile elongates.

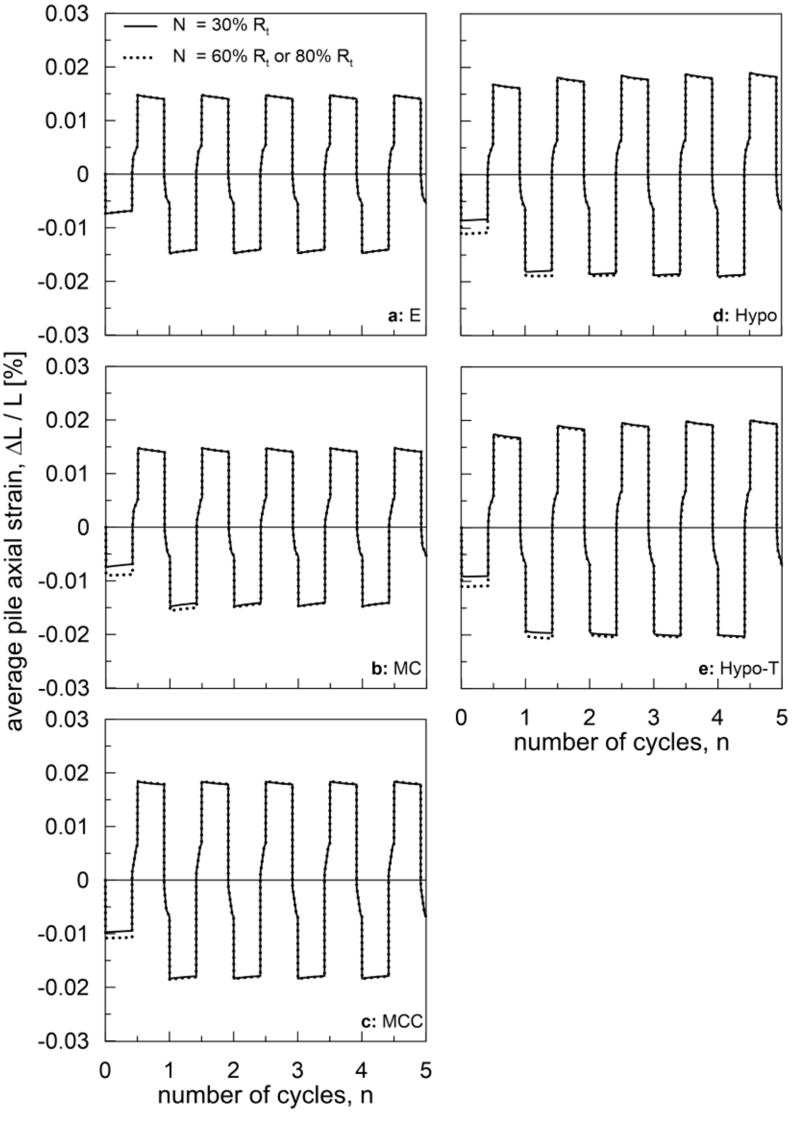

Figure 5.79. Fixed-head pile average axial strain.

6.Comparative analyses

In this chapter the simple analytical solution has been used to derive the thermally-induced axial load and the settlement experienced by the pile, comparing them with the results of the FE analysis related to the first heating phase taking place after the application of the mechanical load. This allows identifying some aspects related to the calibration of the stiffness in the approximate energy solutions.

6.1.Comparison between analytical solution and FE data

In the previous chapters, analytical solutions have been derived modelling the soil with elastic springs and FE analyses have been carried out employing more complex constitutive models. In this section a comparison between the approximate energy solution and the data obtained from the FE analyses is presented in terms of thermally-induced axial force after the application of the first heating phase. The first heating phase takes place at the end of the mechanical loading step and involves a temperature variation of 14°C.

With respect to the exact analytical solution, the approximate energy solution is suitable for any stiffness distribution with depth and can be employed also for any multilayer soil whose stiffness can vary in a continuous manner in each stratum. In order to obtain the stiffness of the springs from Eq. (2.32) it is necessary to choose a proper shear modulus distribution and afterwards to calculate δ using Eq. (2.33). In the following, the definition of the shear modulus profile to employ in the energy solution is detailed for each constitutive model.

As explained in chapter 4, in the analyses with the Elastic and the MC models the soil has been modelled with 2 meters' layers in which the stiffness is constant; this has been done to allow a stiffness increase with depth similar to that of the hypoplastic analyses. In the comparison with these two models, the shear modulus profile has been selected after exploring the results of two different configurations. In the first one, the soil has been considered as a multilayer soil with stiffness constant in each layer. In the second one, the soil is composed of one layer and a linear stiffness profile has been obtained via a linear regression:

$$G_{in}\left(z\right)=\overline{G}\,z \qquad (6.1)$$

Note that, in the two configurations the shear modulus at the ground level is zero for the one-layer case, and equal to that in the first layer for the multilayer case.

The results of the comparison with the Elastic analyses (Fig. 6.1) are independent of the applied mechanical load. No significant differences are observed between the FE data and the analytical solutions as the spring stiffness coefficient δ, although derived using the Eq. (2.33a), has been calibrated to match the maximum axial load in an elastic continuum analysis. However, the graph also highlights that the approximation of the 'actual' stiffness distribution through a linear profile leads to satisfactory results keeping the advantage of an easier calculation. For this reason, for the remaining comparisons the one-layer soil will be considered.

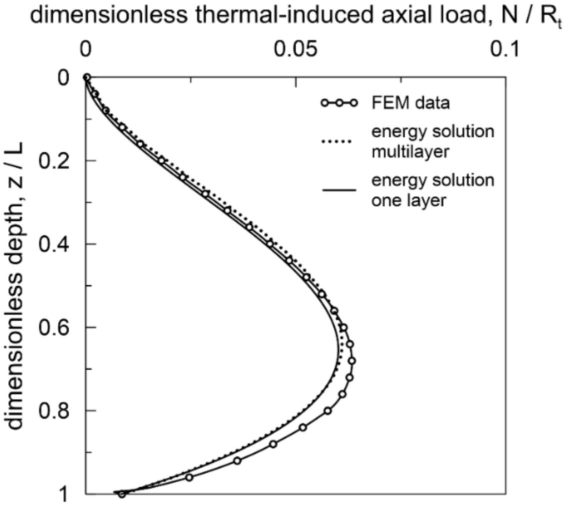

Figure 6.1. Comparison between FE data and energy solution employing two different configurations; E model, free-head pile.

In the FE analyses with the Hypo and the MCC models the soil initial shear modulus is a function of the mean effective stress and therefore of the depth; its variation can be expressed according to the following relation:

$$G_{in}\left(z\right)=\overline{G}\cdot z^{b} \tag{6.2}$$

For the hypoplastic model the initial stiffness coincides with the small-strain stiffness G_0 (Eq. (4.67)), while for the MCC model it can be derived from the following relation:

$$G_{in}=\frac{3\left(1-2\nu\right)\left(1+e_0\right)}{2\kappa\left(1+\nu\right)}p' \tag{6.3}$$

It is worth noting that the stiffness doesn't remain constant during the loading process as it decreases with increasing the load. Therefore, since the first variation of temperature is applied after the mechanical loading phase, the actual mobilized stiffness profile at the end of the mechanical step has been considered. For this scope, the mobilized shear modulus, G_{mech}, has been taken with reference to the shear stress and strain response of few elements at the interface; a linear variation with depth has been derived via a linear regression according to Eq. (6.1).

Moreover, in order to match the maximum thermally-induced axial force, an additional shear modulus distribution has been used. In particular, the shear modulus profile has been evaluated correcting the initial stiffness as follows:

$$G_{eff}\left(z\right)=R_G\,G_{in}\left(z\right) \tag{6.4}$$

where R_G is the correction factor of the initial stiffness.

In the following, the labels G_{in}, G_{mech} and G_{eff} are used to refer to the three cases in which (i) the initial stiffness, (ii) the stiffness mobilized after the application of the mechanical load and (iii) the corrected initial stiffness profiles are employed, respectively.

Tables 6.1 and 6.2 report the value of the shear modulus for each model.

		Q=30% R_t		Q=60% or 80% R_t	
	G_{in}	G_{mech}	G_{eff}	G_{mech}	G_{eff}
E, MC	$880 \cdot z^{0.76}$	-	-	-	-
MCC	$315 \cdot z^{0.87}$	$200 \cdot z$	$250 \cdot z^{0.87}$	$110 \cdot z$	$165 \cdot z^{0.87}$
Hypo	$1850 \cdot z^{0.76}$	$325 \cdot z$	$850 \cdot z^{0.76}$	$105 \cdot z$	$490 \cdot z^{0.76}$
Hypo-T	$1850 \cdot z^{0.76}$	$340 \cdot z$	$850 \cdot z^{0.76}$	$110 \cdot z$	$360 \cdot z^{0.76}$

Table 6.1. Shear modulus profiles employed in the energy solution, free-head pile.

		Q=30% R_t		Q=60% or 80% R_t	
	G_{in}	G_{mech}	G_{eff}	G_{mech}	G_{eff}
E, MC	$880 \cdot z^{0.76}$	-	-	-	-
MCC	$315 \cdot z^{0.87}$	$200 \cdot z$	$300 \cdot z^{0.87}$	$110 \cdot z$	$140 \cdot z^{0.87}$
Hypo	$1850 \cdot z^{0.76}$	$325 \cdot z$	$900 \cdot z^{0.76}$	$105 \cdot z$	$485 \cdot z^{0.76}$
Hypo-T	$1850 \cdot z^{0.76}$	$340 \cdot z$	$830 \cdot z^{0.76}$	$110 \cdot z$	$190 \cdot z^{0.76}$

Table 6.2. Shear modulus profiles employed in the energy solution, fixed-head pile.

The results obtained with the energy solution and the data of the FE analyses for both the free- and fixed-head configurations are shown in figures 6.2, 6.3 and 6.4.

While the energy solution applied for the Elastic model in the case of free-head pile provides a satisfactory match with the FE data, the results for fixed-head pile show a difference of about the 20% in predicting the maximum axial load (Fig. 6.2a). This may be due to the fact that the temperature variation in the FE analyses is applied during one day employing a transient analysis, while the spring stiffness coefficient δ has been calibrated via a static analysis. As a consequence of the transient calculation, a slight diffusion of heat in the surrounding soil occurs, the temperature of the soil in the vicinity of the pile increases and the soil moves upward while the pile head is fixed causing a slight increase in the axial load. A further reason for this difference is that the equations used for δ present some deviation from the calibration data.

In the response with the MC model the difference encountered for the fixed-head pile at applied mechanical load equal to the 30% of the bearing capacity are the same as for the Elastic model since the response is practically elastic. With increasing the applied mechanical load, the development of plasticity determines a decrease of the thermally-induced axial force. Although the results are satisfactory for both free- and fixed-head cases, the use of the effective shear modulus would improve the prevision.

For the MCC model using the shear modulus profile obtained after the application of the mechanical load is quite effective in reproducing the response of the FE analyses. Note that, when G_{eff} is employed, not only the maximum thermal-induced axial load but even the profile of the axial load with depth is quite accurate.

In the case of the hypoplastic models, only the use of the effective shear modulus profile gives a good fit of the results.

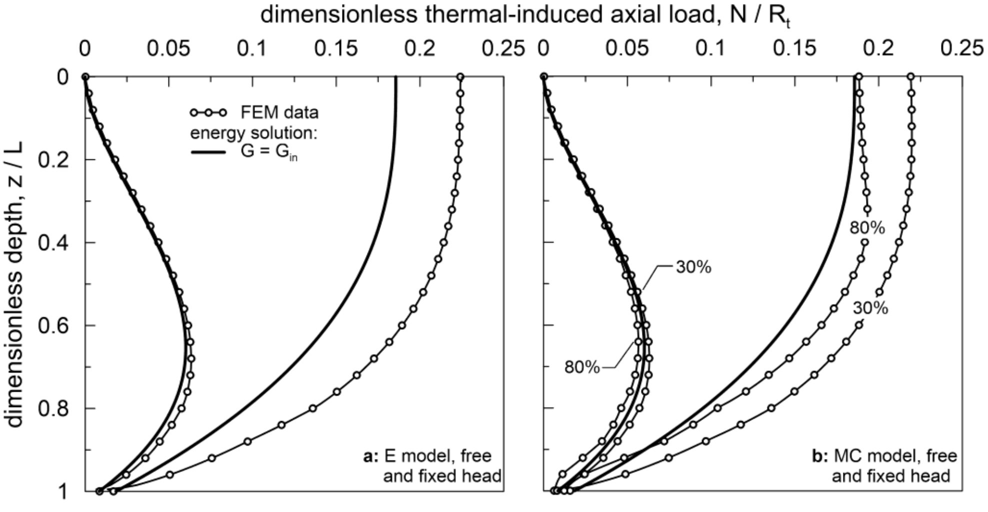

Figure 6.2. Comparison between FE data and energy solution: E and MC models.

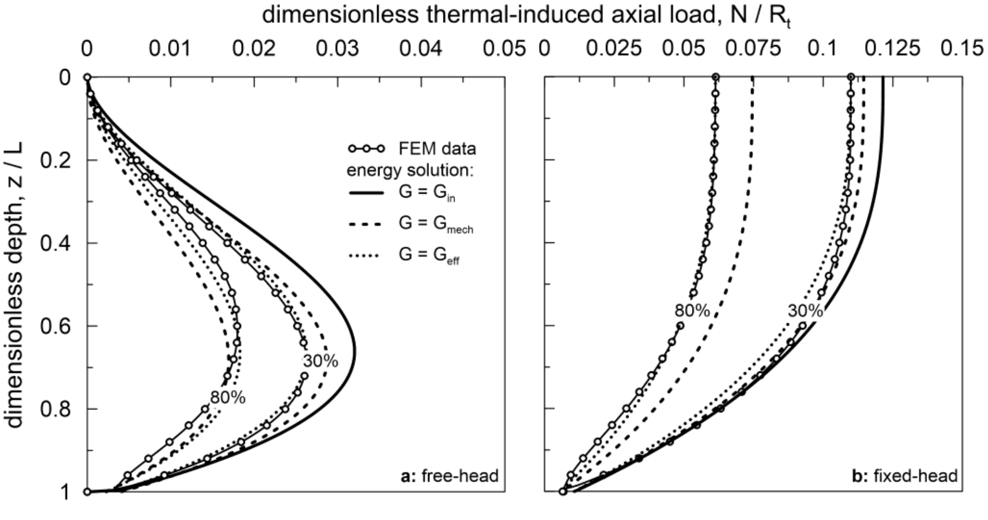

Figure 6.3. Comparison between FE data and energy solution: MCC model.

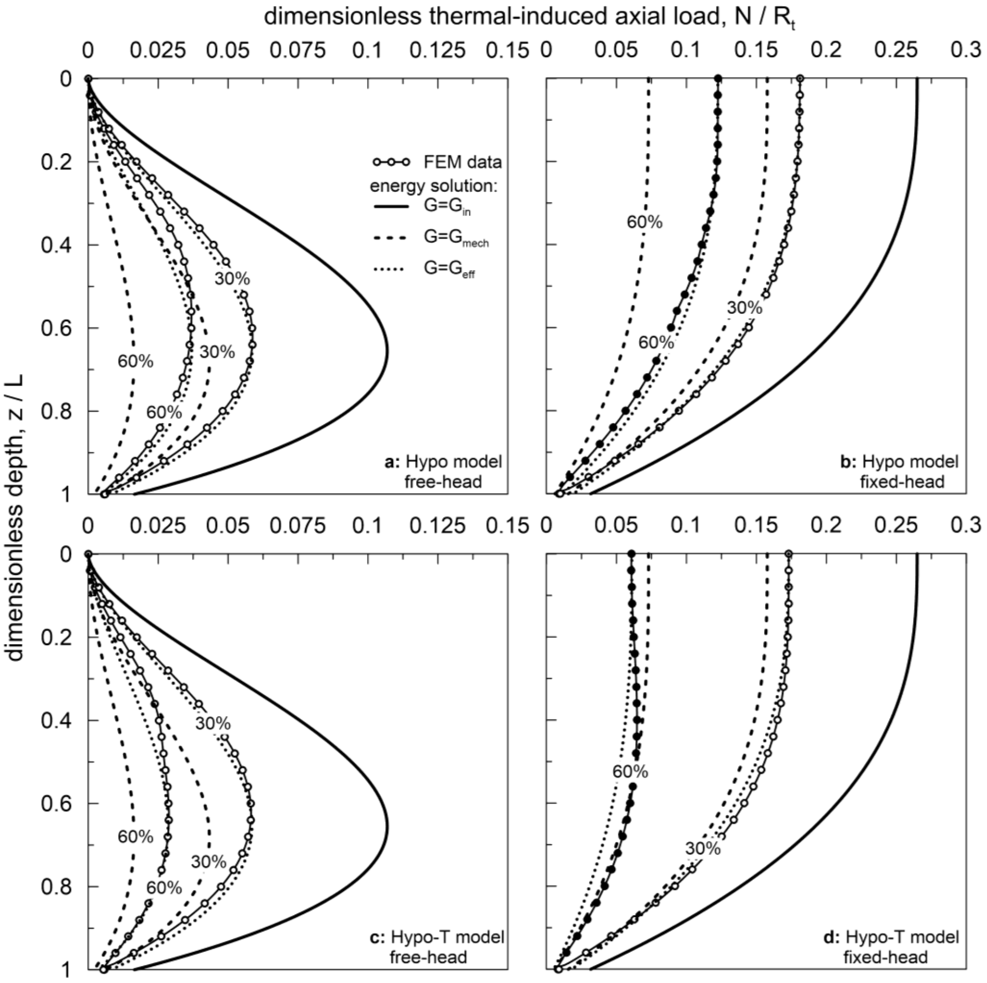

Figure 6.4. Comparison between FE data and energy solution: Hypo and Hypo-T models.

6.2.Estimation of the soil stiffness profile

In order to understand the trend of G_{eff} as a function of the load level, further FE analyses with different applied mechanical and thermal loads have been performed using the MC, the MCC and the Hypo models. These analyses consist of two phases, namely one mechanical and one thermal, in which the pile temperature is increased of 14, 5 and 1°C instantaneously. In figures 6.5, 6.6 and 6.7 the effective shear modulus over the initial shear modulus, i.e. the correction factor RG, is reported for each load level and for the free-head and the fixed-head conditions. Moreover, in these figures the load level has been referred to both the bearing capacity evaluated with the static formulae (R_t) and the bearing capacity derived from the load-settlement curves of the FE analyses (R_{FEM}).

For the MC model, up to about the 50% R_t the response is independent of the temperature variation and the load level; indeed, R_G has a constant value equal to 1.1 and 1.4 in the case of free-head and fixed-head, respectively. As stated before, the application of the energy solution with G_{eff} and the associated δ, allows to match the maximum thermally-induced axial force. Therefore, values of G_{eff} larger than G_{in}, i.e. $R_G > 1$, are justified considering that the spring model still produces some differences in the response as compared to a continuous model (i.e. the simplified expression of the spring stiffness coefficient δ, Eq. (2.33), presents some deviation from the calibration data). With increasing the load level and the applied temperature variation, G_{eff} decreases.

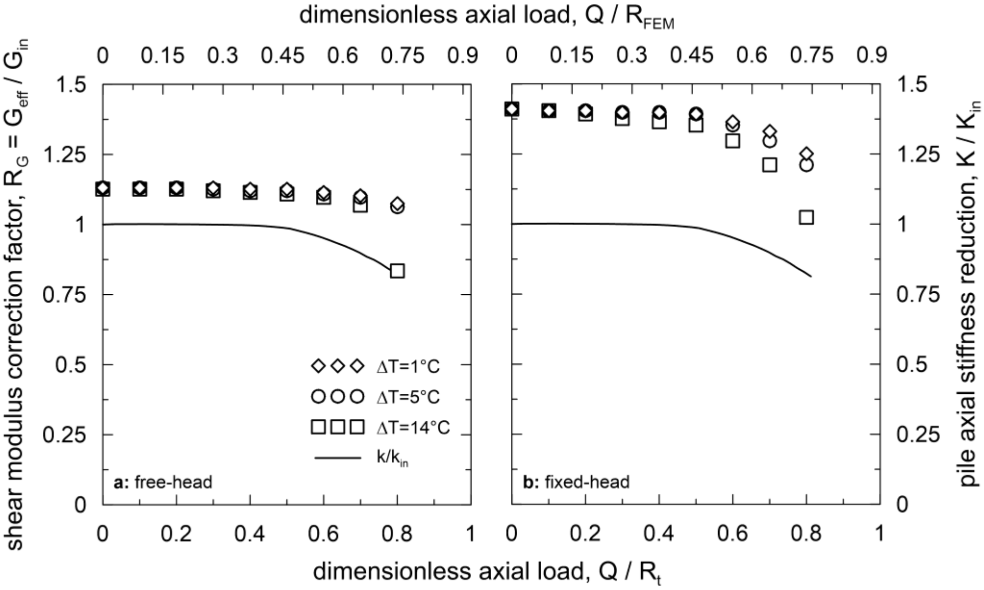

Figure 6.5. Effective shear modulus at each load level: MC model.

For the MCC model, since the stiffness of the soil is not constant during the loading process, the trend of G_{eff} is more affected by the load level and the temperature variation imposed. In the case of free-head pile and axial load lower than 50% R_t, the correction factor ranges between 0.94 (ΔT = 1°C and no axial load) and 0.81 (ΔT = 14°C and axial load equal to 50% R_t). With increasing the load level, lower values of G_{eff} are needed to match the results; more specifically, when the applied mechanical load is equal to 80% R_t, R_G is 0.63, 0.62 and 0.59 for ΔT = 1, 5 and 14°C, respectively. As concerns the fixed-head pile, R_G is about 1 for ΔT = 1, 5°C and no axial load applied, and it is lower than 1 for all the other cases, dropping to 0.4 when ΔT = 14°C and the load level is 80%.

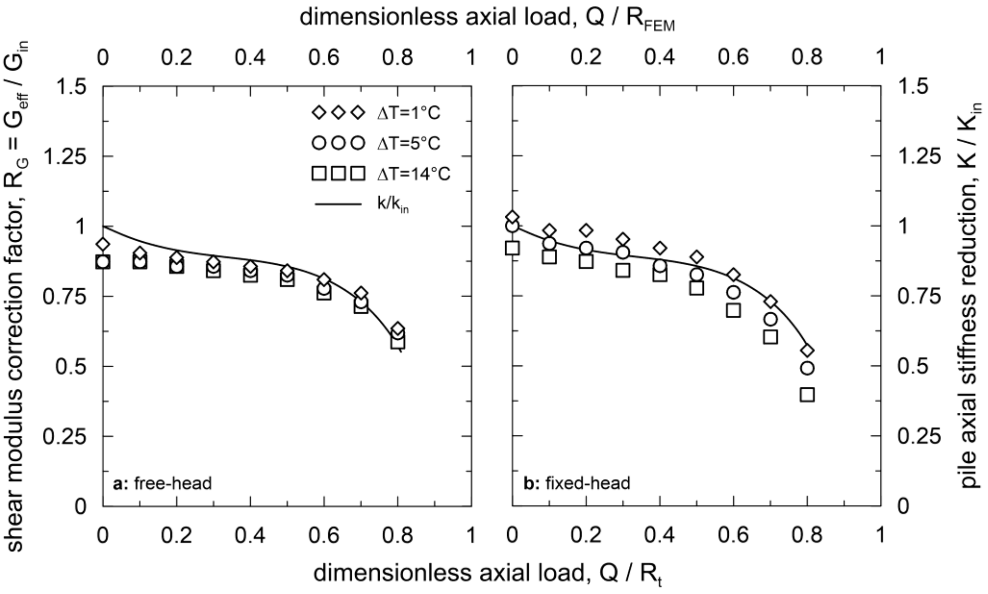

Figure 6.6. Effective shear modulus at each load level: MCC model.

Compared to the MC and MCC models, it is evident that for the hypoplastic model the reduction of the shear modulus with the load level and the applied temperature variation is more pronounced. For zero applied mechanical load and free-head pile, R_G is equal to 1.15, 0.99 and 0.78 for ΔT = 1, 5 and 14°C, respectively. As for the other models, the increase of the load level is characterized by a decrease of R_G that becomes 0.19 in the case of ΔT = 14°C and axial load equal to 70% R_t. A similar behaviour is found if the pile is fixed at head. In particular, when solely the temperature variation is applied, G_{eff} is 1.38, 1.2 and 0.92 G_{in} for ΔT = 1, 5 and 14°C, respectively; while with increasing the applied mechanical load the correction factor decreases up to 0.09 in the case of ΔT = 14°C and axial load equal to 70% R_t.

The differences found at zero applied mechanical load for both the Hypo and the MCC models can be explained considering that, (i) with increasing the applied temperature variation a further decrease in soil stiffness is experienced and that (ii) the spring stiffness coefficient δ is evaluated through simplified expressions. In general, with decreasing the applied temperature variation, the correction factor R_G increases and tends to 1 for zero mechanical load and if δ is exactly derived by matching the elastic FE analyses.

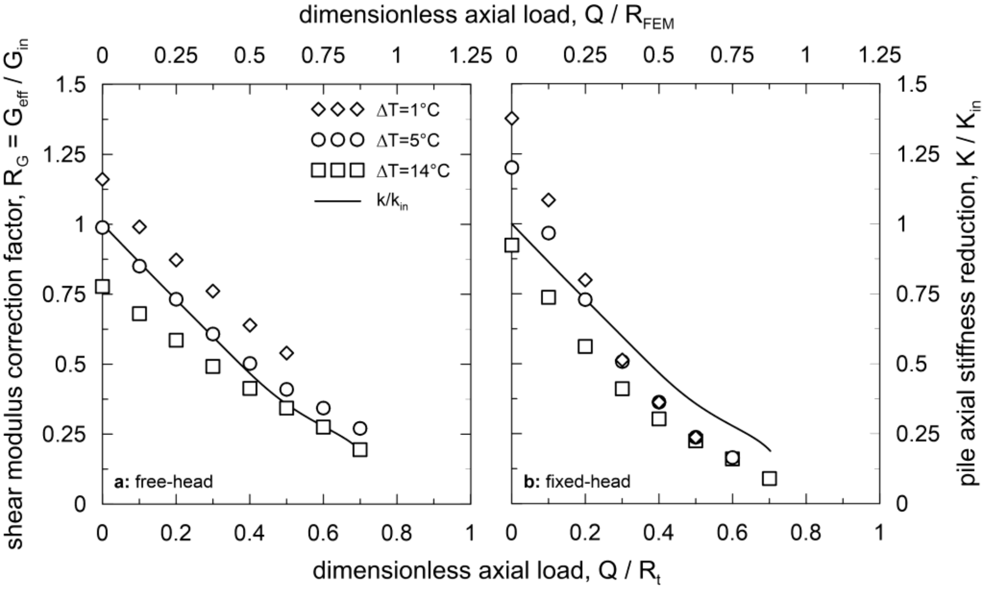

Figure 6.7. Effective shear modulus at each load level: Hypo model.

In practical applications, the difficulty in using the energy solutions lies in the estimation of the stiffness profile. As a first approximation G_{eff} can be set equal to G_{mech}. Nevertheless, this choice has some limitations: (i) the shear modulus G_{mech} is evaluated at the interface between pile and soil and, therefore, it represents a local response not capable to account for the stiffness variation in the adjacent portion of the soil; (ii) the evaluation of G_{mech} requires the response of the pile at the interface after the application of the mechanical load that is difficult to estimate without making use of a numerical analysis.

Another option is to establish an analogy between the variation of the shear modulus and the reduction in the pile axial stiffness with increasing the load level. In figures 6.5, 6.6 and 6.7 the curves K/K_{in} represent the pile axial stiffness at the considered applied mechanical load, K, over the pile axial initial stiffness, K_{in}, calculated from the load-settlement curve. The ratio K/K_{in} can be used as the correction factor of the stiffness profile. It can be noted that in the case of the MC model, the axial stiffness remains almost constant throughout the loading process and slightly decreases just at very high load level (e.g. 0.85 K_{in} at 80%R_t); as a consequence, the response during the thermal phase in not significantly affected by the variation of the applied mechanical load. For the MCC model, although non-linearity is evident since the beginning of the loading process, the reduction of the tangent stiffness proceeds at low rate showing a value of about 0.55 K_{in} at 80%R_t. On the contrary, the hypoplastic response is strongly affected by the non-linear component of the model; indeed, a reduction of the axial stiffness of about the 50% can be found already for Q = 25% R_t.

The use of K/K_{in} as correction factor allows to overcome the abovementioned limitations since the load-settlement curve is available from field load tests in most projects and, however, must be evaluated by the designers even if with simpler calculations (e.g. assuming a hyperbolic relationship between load and settlement).

To refine the choice of the effective stiffness and refer it to the load induced by the temperature variation, it is possible to develop a simple iterative procedure starting from the load-settlement curve of the pile. The step to follow are listed below:

1) Evaluation of the ratio between the tangent stiffness at the applied mechanical load and the initial stiffness $(K/K_{in})_1$ from the load-settlement curve;
2) Reduction of the initial shear modulus distribution of a factor equal to $(K/K_{in})_1$, to get $G_{eff,1}$;
3) Estimation of the maximum thermally-induced axial load N_{max1} with the energy solution employing the effective shear modulus distribution obtained at the step 2;
4) Evaluation of a new ratio $(K/K_{in})_2$ from the load settlement curve at a load equal to the applied mechanical load plus N_{max1};
5) Reduction of the shear modulus distribution of the soil according to $(K/K_{in})_2$, to get $G_{eff,2}$;
6) Estimation of N_{max2} with the energy solution employing the effective shear modulus distribution obtained at the step 5;
7) If $N_{max1} \sim N_{max2}$ the procedure has converged, otherwise steps 4-6 are carried out until convergence. However, generally 1-2 iterations are sufficient to get accurate results.

6.3. Calculation of the thermally-induced axial load from the load-settlement curve

In figures 6.8, 6.9 and 6.10 the axial load derived from the energy solution, $N_{analytical}$, over the axial load from the FE calculations, N_{FEM}, is reported for different load levels and applied temperature variation and for both free-head and fixed-head condition. Reference is made to the maximum values experienced by the pile during the thermal solicitation. The stiffness correction factor has been taken from the load-settlement curve without using the iterative procedure. For the MC and the MCC models the analytical value of the axial load ranges between 1.2 and 0.8 N_{FEM}, the only exception being the case of the MCC model at applied mechanical load equal to 80% R_t and ΔT = 14°C. As concerns the Hypo model, for the free-head pile, at increasing the load level and decreasing the applied temperature, the use of the energy solution leads to the underestimation of the axial load. On the contrary, for the case of the fixed-head pile, overestimation of the maximum axial load is produced at increasing the load level and the temperature.

It is worth noting that, when ΔT = 1°C, up to the applied mechanical load of 10% R_t the response of the hypoplastic model is reversible; in these cases, the underestimation of the axial load ($N_{analytical}$ = 0.9 N_{FEM}) is caused by the inaccuracy of the analytical model in reproducing the continuum with the δ estimated from the simplified expression. For all the other cases (i.e. ΔT > 1°C and Q > 10% R_t), the differences between the energy solution and the FE analyses are due to the approximation of a complex constitutive model with an equivalent linear elastic approach. Nevertheless, considering that in practical applications the applied working load is lower than the 30%÷40% R_t, the obtained results are satisfactory since the thermal load calculated via the energy solution is in the range of ±20% N_{FEM}.

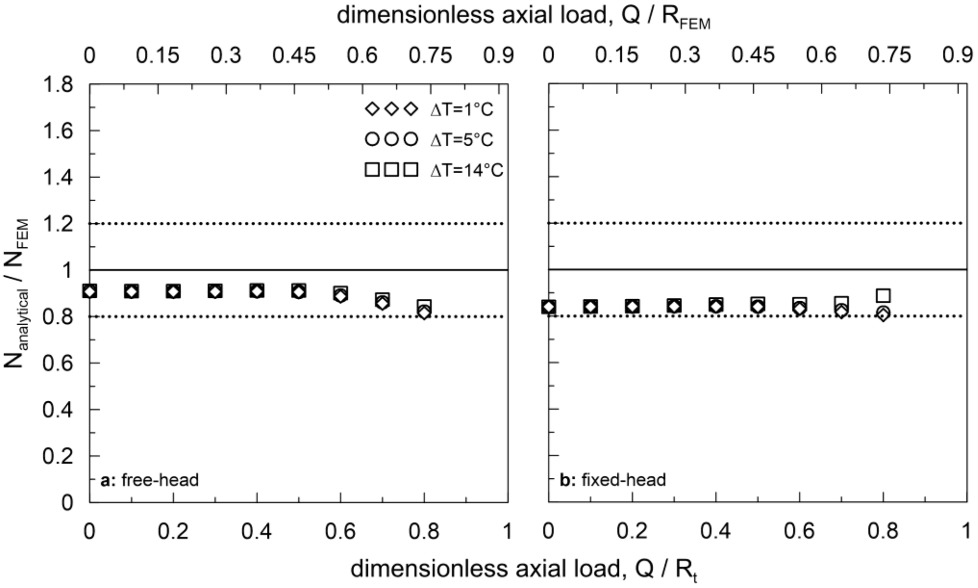

Figure 6.8. Ratio between the axial load from energy solution and FE calculations, MC model.

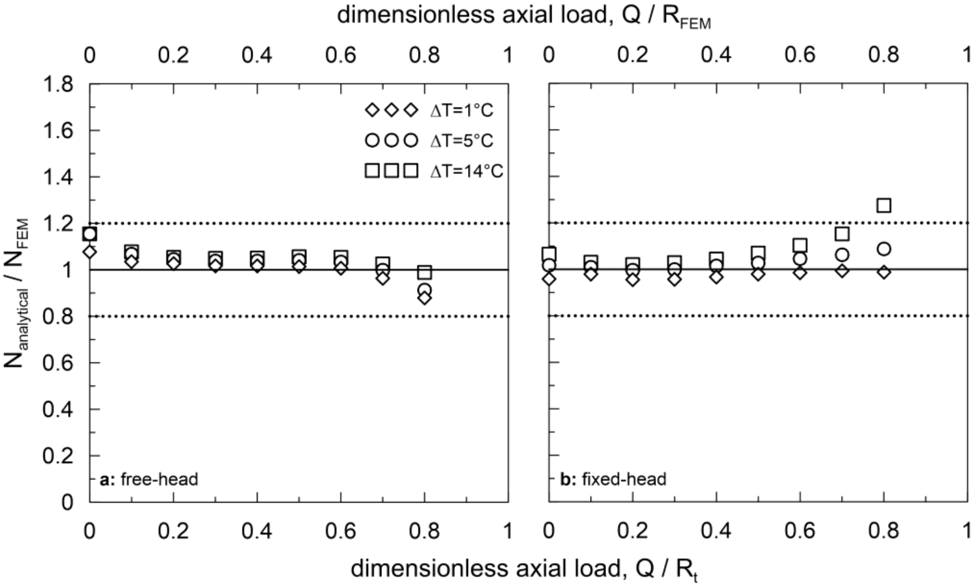

Figure 6.9. Ratio between the axial load from energy solution and FE calculations, MCC model.

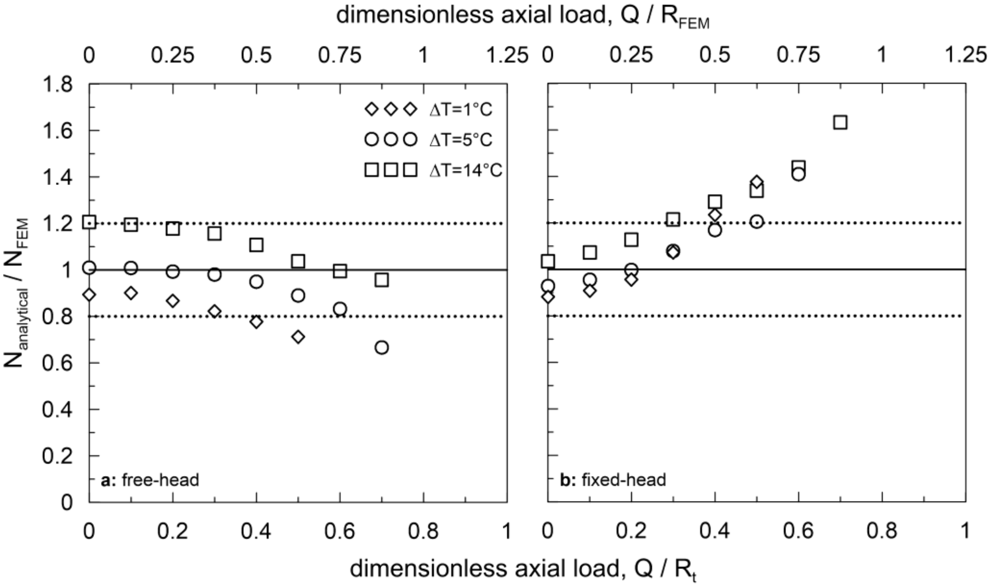

Figure 6.10. Ratio between the axial load from energy solution and FE calculations, Hypo model.

The main advantage of using the analytical procedure is that its application requires just the availability of the load-settlement curve of the pile and no constitutive choices are necessary. This way, the estimation of the thermally-induced axial force can be carried out by the designer without complex numerical calculations, taking into account in a simple manner all the peculiarities associated to the complex soil behaviour. Another strength of this approach is that, given the sensitivity of the constitutive models to the input parameters, and considering that very often in practice there are no sufficient laboratory data for a reliable estimation of these parameters, it appears as more robust if compared to more complex FE analyses. However, it is fair to mention that the validation of the proposed approach requires additional analyses to consider different pile geometry in different soil types. Moreover, further work is needed to extend it for the case of multiple cycles.

6.4. Calculation of the thermally-induced settlements from the load-settlement curve

Towards a deeper investigation of the behaviour in terms of cyclic settlements, further FE analyses have been performed employing the Hypo and the Hypo-T models considering two additional load levels. The cyclic settlements after 5 thermal cycles are reported in figure 6.11 for ΔT = 5 and 14°C. As already noted in Chapter 5, the choice of the constitutive model strongly affects the behaviour in terms of settlements, especially with increasing the axial load and the temperature.

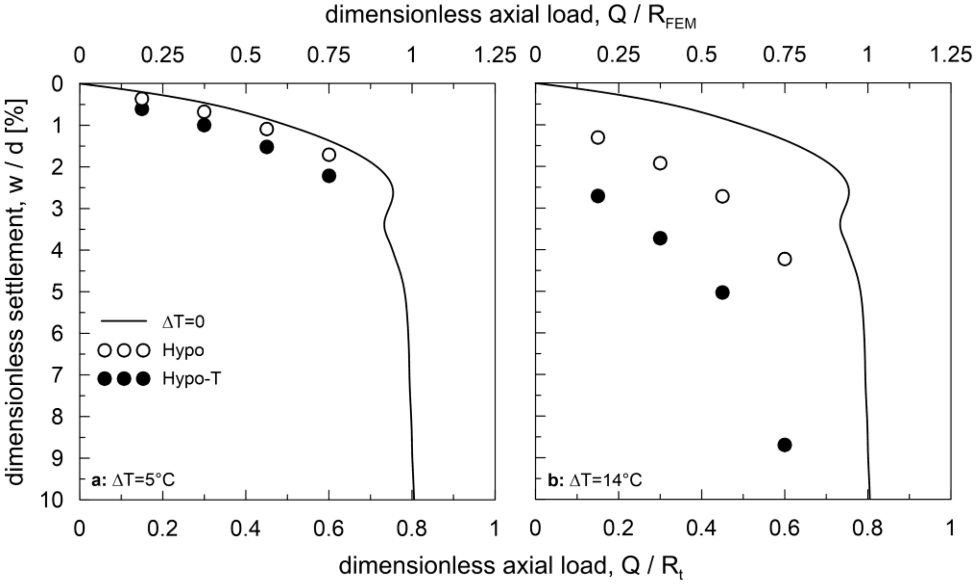

Figure 6.11. Dimensionless settlements after 5 thermal cycles, Hypo and Hypo-T models.

For the first heating phase it is possible to use the energy solution to calculate the thermally-induced pile shortening. As for the axial load, the stiffness profile is obtained correcting the initial stiffness of the soil in analogy with the load-settlement curve at the considered load level. The results are reported in figure 6.12 for the case of the Hypo model in terms of average pile axial strain. A good match is found between the analytical approach and the FE data. Furthermore, it can be noted that the heating-induced settlement during the first cycle doesn't change significantly with increasing the load level or the temperature.

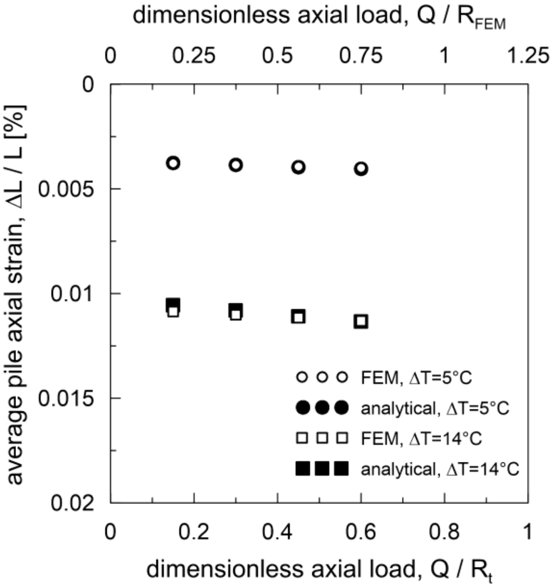

Figure 6.12. Comparison between the dimensionless settlement from the energy solution and the FE calculations, Hypo model.

Although the response in the first heating is slightly influenced by the magnitude of the mechanical and thermal solicitations, the thermally-induced settlements during each cycle strongly depend on the load level and the imposed temperature variation (Fig. 6.13). Moreover, it can be noted that 5 thermal cycles are not sufficient to induce a significant decrease of the accumulated cyclic settlements. As shown in figure 5.71, the same trend is visible in the case of the single energy pile tested in the small scale experiment by Wu et al. (2018).

It can be concluded that, for the evaluation of the cyclic settlement FE analyses are always required.

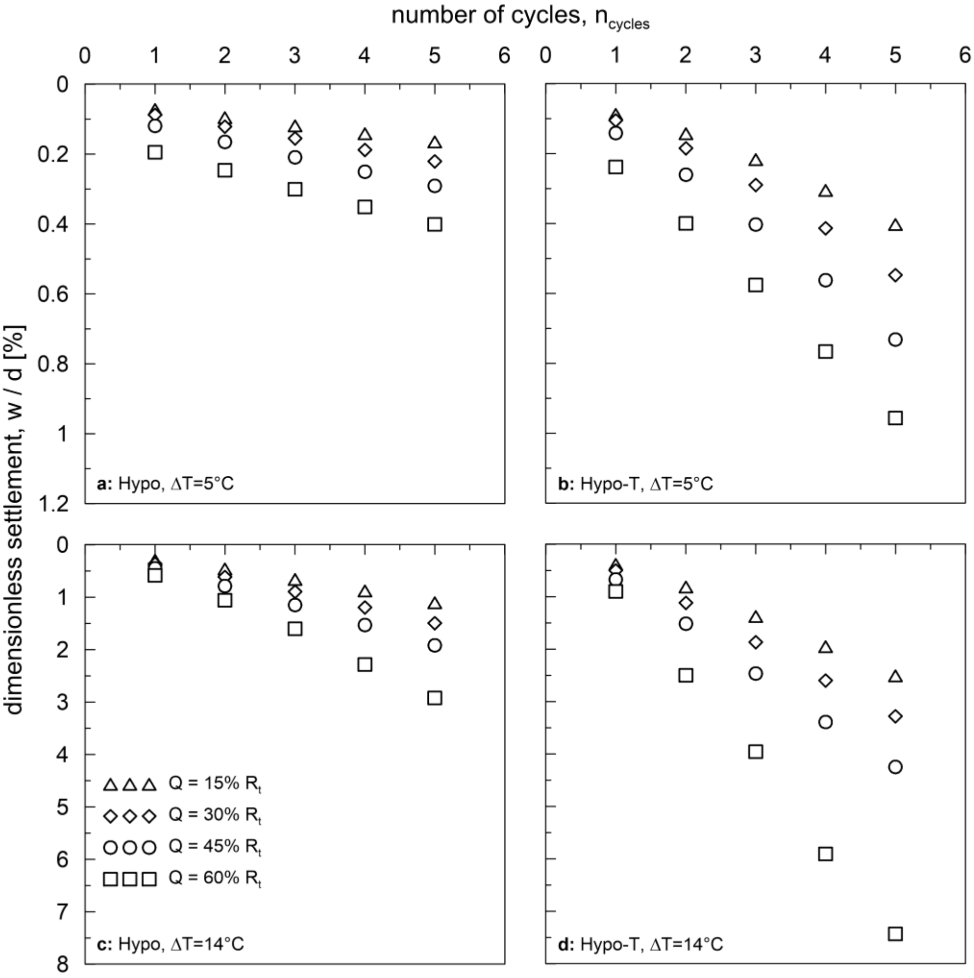

Figure 6.13. Cyclic dimensionless settlements, Hypo and Hypo-T models.

7.Conclusions

7.1.Summary of the main results

Traditional pile foundations are used with the purpose of transferring the structural loads to the soil through tangential stress along the shaft and normal pressures at the base. When these systems are coupled with closed loop pipes, they can be used to exchange heat with the surrounding soil thanks to the circulation of a heat carrier fluid. In this case, the energy piles can contribute to the welfare of a building transferring the heat between the soil, considered at a constant temperature, and the building itself, whose thermal demand varies seasonally. As a consequence, the mechanical solicitations are combined with the cyclic thermal loads. The use of these environmental friendly systems is facing an exponential growth all around the word. Although the benefits deriving from the exploitation of theses system in terms of implications on the environment, attention must be paid to the effects of the cyclic temperature variations on the performance of the energy piles. Indeed, two main aspects have to be considered: from one side, thermally-induced axial force develops along the piles with different magnitude depending on the degree of freedom of the energy pile; moreover, the additional cyclic movements caused by the temperature variation can be characterized by irreversible components that may accumulate cycle after cycle depending on the soil type.

The aim of the present thesis is to study the behaviour of the energy piles under both monotonic and cyclic thermal loading conditions. It is divided into three sections.

7.1.1. Analytical solutions

Based on the current state of knowledge, the analysis of energy piles must be carried out employing numerical techniques since there aren’t closed form solutions to employ for the study of the problem at hand. With the aim of filling this lack, a Winkler-type model has been proposed. The restraint provided by the soil and the structure connecting the pile heads is schematized using linear elastic distributed springs long the pile shaft and concentrated spring at base and head, respectively. Exact solutions have been derived for the case of homogenous, two-layer and Gibson soil for monotonic thermal load. It was found that the main dimensionless parameters governing the magnitude of the thermally-induced axial force are the mechanical slenderness, $\lambda_p L$ or μL, that incorporates both the pile geometry and the pile-soil stiffness ratio, and the ratio between the top and base stiffness, Θ; the parameter Ω, ratio between the shaft and base stiffness, can be derived from the two aforementioned parameters. In particular:

- the thermally-induced axial force increases with increasing the mechanical slenderness;
- the presence of a structure connecting the pile heads, i.e. $\Theta > 0$, always results in an increase of the axial force;
- for a given pair ($\lambda_p L$ or μL, Θ) the thermally-induced axial load is practically independent of the pile-soil stiffness ratio;
- in absence of restraints at pile ends, the mechanical slenderness would be the unique dimensionless parameter controlling the maximum axial force.

Considering a two-layer soil, for the majority of the cases encountered in practice, N_{max} occurs in the second (stiffer) layer; moreover, for end-bearing piles ($\rho > 2$, $\zeta \cong 1$) of ordinary length ($\lambda_1 L > 1$) the induced axial force is at least the 80% of the maximum value experienced if the energy pile is fully restrained at the ends.

In order to obtain closed-form expressions for a general subsoil condition, approximate solutions have been derived defining the pile thermally-induced displacement as a linear function of the depth. This assumption leads to accurate solutions since in the case of thermal loads, the description of the displacement profile as a linear function results in an error of minor concern. The extension to the multi-layer soil proved the versatility of the proposed solutions to any soil. It is worth noting that the approximation involved in the simplified assumption is cancelled out since spring stiffness has been calibrated for these solutions by comparison with FE analyses. Novel expressions for evaluating the springs properties as function of the pile-soil stiffness ratio and the pile geometry have been proposed for the specific problem of the thermally-loaded piles.

The successful match with two field tests available in literature as well as with rigorous fully coupled thermo-hydro-mechanical FE analyses proved that the proposed solutions provide reliable results by means of hand calculations. However, notwithstanding the practical appeal, it should be highlighted that the proposed formulae may assist the design of thermally loaded-piles only to get a first-order value of the thermally-induced axial force to be considered in the ULS checks. Anyhow, they can be employed by researchers to validate future more complex models.

7.1.2. Numerical techniques

Fully coupled thermo-hydro-mechanical finite element analyses have been carried out using the code ABAQUS. The scope of these analyses was to investigate the cyclic behaviour of a single pile in terms of both thermally-induced axial loads and displacements. To consider the restraining effect due to the structure connecting the pile heads, the fixed-head condition has been modelled along with the free-head pile. In addition to the thermal solicitation, two different levels of mechanical vertical load have been applied to account for working or close-to-failure conditions. Moreover, increasingly complex constitutive models have been used in order to compare the response of the classical models (Linear Elastic, Mohr-Coulomb and Modified Cam-Clay) with that of a more sophisticated model (Hypoplastic). In particular, since the pile was embedded in NC clay, a model capable of reproducing the thermal collapse of the clay has also been used (Hypoplastic with thermal formulation). The thermal path over one year included two phases of constant heating and cooling separated by a thermal rest.

For all the models, it was found that:

- for the free-head pile the maximum and minimum thermally-induced axial force occurs before the heat conduction in the surrounding soil;
- due to the restraining condition, for the fixed-head pile the maximum and minimum solicitations are found after the continuous heating and cooling phases; the only exception is the thermo-hypoplastic model for which, because of the thermal collapse, the maximum thermally-induced load occurs before the heat conduction.

For the elasto-plastic models, the main effects of the plasticity are:

- the redistribution of the axial load due to the progressive yielding of the elements along the shaft and, consequently the upward (during heating) or downward (during cooling) movement of the null point;
- the higher overall axial force during the cooling phase caused by the mobilisation of the ultimate shear resistance mainly for the points in the vicinity of pile head.

As concerns the advanced models, the main results are:

- as for the classical elasto-plastic models, a more evident upward shift of the null point is found during heating with increasing the applied mechanical load; the same statement holds for the downward movement occurring during cooling;
- the accumulation of irreversible settlements cycle after cycle governs the behaviour of the energy pile, especially with reference to the thermo-hypoplastic model due to the thermal collapse;
- the cycles performed are not sufficient to appreciate a significant reducing rate, therefore, stabilization is not obtained;
- the rate of accumulated settlements increases with increasing the mechanical load applied at pile head;

- along the shaft, the excess pore pressure accumulates during the cyclic solicitation stabilizing within few cycle, while the base is characterized by hysteric loops;
- for the fixed-head pile, the axial load distribution decreases cycle after cycle.

It is worth noting that, the calculation with reference to the single energy pile is conservative. The long-term behaviour is characterized by the thermal interaction between energy and traditional piles (i.e., by the temperature variation of the inactive piles) allowing the decrease of the axial force and the increase of the settlements. The latter, neglecting the interaction in terms of displacements, can be equal to that for the free-head pile at most.

It can be concluded that in the case of energy piles subjected to cyclic solicitation, the use of advanced constitutive models is the only way to properly predict the cyclic behaviour observed in the real applications. Nevertheless, the advantage of achieving detailed results is counterpoised to the effort paid for the calibration of a greater amount of parameters.

7.1.3. Comparisons between analytical and numerical approaches

In the last section of the thesis, the approximate solution has been used to derive both the thermally-induced axial load and the settlements as a consequence of the monotonic increase of pile temperature. The spring stiffness can be calculated using the expression proposed for the estimation of the coefficient δ and considering the stiffness of the soil employing various distributions. The results have been compared with that obtained from the FE analyses, showing the need to rely on the effective shear modulus profile for the stiffness of the soil. Therefore, a procedure has been proposed establishing an analogy between the effective shear modulus profile and the pile axial stiffness calculated from the load-settlement curve, finding out that modifying the soil initial stiffness by a factor equal to the ratio between the pile tangent axial stiffness at working load and the pile initial stiffness, provides accurate results.

It can be concluded that:

- as concerns the axial force, the obtained results are satisfactory since the thermal load calculated via the energy solution is in the range of ±20% of the axial force from the FE analyses; therefore, the method can be broadly employed for the preliminary design stage having the advantage of avoiding the complex FE analyses along with the required constitutive choices;
- with reference to the settlements, a good match is found for the first heating; nevertheless, the irreversible component that accumulates cycle after cycle

is such that, at the current stage, the use of numerical analyses is always needed.

7.2.Suggestions for future research

At the current stage, field and laboratory tests, numerical analyses and analytical approaches have been mainly devoted to the study of the energy foundations under monotonic loading conditions. The cyclic thermal loading would provide a better understanding of the thermally-induced axial force and settlements in the long-term condition, and it would help to exploit the interface behaviour. These studies should involve different energy pile configurations, i.e. piles connected by a raft in contact with the ground to simulate situations close to the real applications, along with different soil types. To this scope, field and laboratory test are the best suited, nevertheless, numerical analyses calibrated on the available experimental data are also a very useful tool. The main objective of these analyses should be the identification of the key aspects characterising the behaviour of these foundations to be used in the design, according to the soil type and the energy piles configurations (i.e. in clay soils the settlements may play a major role, while for sandy soils the degradation of the interface properties may not be neglected).

As concerns the analytical approaches, this thesis attempted to provide a simple analysis tool for the case of monotonic loading, based on the linear elasticity. As stated before, the energy piles are characterized by cyclic solicitation and, in some cases, by non-negligible irreversible components. Therefore, more efforts are required for the development of:

- a spring model with elasto-plastic springs;
- a simple procedure for the estimation of the thermally-induced cyclic axial force;
- a simple procedure for the estimation of the thermally-induced cyclic settlements.

APPENDIX I

Exact solutions

- Homogeneous soil

The general solution of Eq. (2.7) is:

$$u_p\left(z\right)=C_1e^{\lambda z}+C_2e^{-\lambda z} \tag{A.1}$$

with λ being expressed through Eq. (2.8). In order to get the two unknowns, *C*C_i, the two following boundary conditions are necessary:

$$\begin{aligned}\left.\frac{du_p\left(z\right)}{dz}\right|_{z=0}&=\alpha\,\Delta T+\frac{k_t\,u_p\left(z\right)\big|_{z=0}}{EA}\\ \left.\frac{du_p\left(z\right)}{dz}\right|_{z=L}&=\alpha\,\Delta T-\frac{k_b\,u_p\left(z\right)\big|_{z=L}}{EA}\end{aligned} \tag{A.2}$$

Once known the two constants C_i, the displacement $u_p(z)$ can be derived using Eq. (A.1):

$$\begin{aligned}u_p\left(z\right)=&\frac{\alpha\,\Delta T}{\lambda_p}\cdot\\ &\cdot\frac{\Omega\left(\cosh\left(\lambda_p z\right)-\cosh\left(\lambda_p\left(L-z\right)\right)\right)-\sinh\left(\lambda_p\left(L-z\right)\right)+\Theta\Omega\sinh\left(\lambda_p z\right)}{\left(1+\Theta\Omega\right)\cosh\left(\lambda_p L\right)+\left(\Omega-\Theta\right)\sinh\left(\lambda_p L\right)}\end{aligned} \tag{A.3}$$

Combining Eq. (A.3) with Eqs. (2.3) and (2.4), the axial load (Eq. 2.9) and the shear stress distributions are obtained; the latter has the following expression:

$$\begin{aligned}\tau\left(z\right)=&\frac{\alpha\,\Delta T\,EA\lambda_p}{2\pi r_0}\cdot\\ &\cdot\frac{\Omega\left(\cosh\left(\lambda_p\left(L-z\right)\right)-\cosh\left(\lambda_p z\right)\right)+\sinh\left(\lambda_p\left(L-z\right)\right)-\Theta\Omega\sinh\left(\lambda_p z\right)}{\left(1+\Theta\Omega\right)\cosh\left(\lambda_p L\right)+\left(\Omega-\Theta\right)\sinh\left(\lambda_p L\right)}\end{aligned} \tag{A.4}$$

- Two-layered soil

When the two-layer soil is considered, it is necessary to write two differential equations, one per each stratum. Those differential equations have the same expression as Eq. (2.7):

$$\begin{aligned} &\frac{d^2u_{p1}\left(z_1\right)}{dz_1^2}-\lambda_1{}^2u_p\left(z_1\right)=0 \\ &\frac{d^2u_{p2}\left(z_2\right)}{dz_2^2}-\lambda_1{}^2u_p\left(z_2\right)=0 \end{aligned} \qquad \text{(A.5)}$$

where λ_1 is the pile-soil wave number of the first layer. The general solutions of Eqs. (A.5) are:

$$\begin{aligned} &u_{p1}\left(z_1\right)=C_1e^{\lambda_1 z_1}+C_2e^{-\lambda_1 z_1} \\ &u_{p2}\left(z_2\right)=C_3e^{\rho\lambda_1 z_2}+C_4e^{-\rho\lambda_1 z_2} \end{aligned} \qquad \text{(A.6)}$$

In order to get the four unknowns, C_i, the following four boundary conditions are necessary:

$$\begin{aligned} &\left.\frac{du_{p1}\left(z\right)}{dz_1}\right|_{z_1=h_1}=\alpha\,\Delta T-\frac{k_t\,u_{p1}\left(z\right)\big|_{z_1=h_1}}{EA} \\ &\left.\frac{du_{p2}\left(z\right)}{dz_2}\right|_{z_2=h_2}=\alpha\,\Delta T-\frac{k_b\,u_{p2}\left(z\right)\big|_{z_2=h_2}}{EA} \\ &u_{p1}\left(z\right)\big|_{z_1=0}+u_{p2}\left(z\right)\big|_{z_2=0}=0 \\ &\left.\frac{du_{p1}\left(z\right)}{dz_1}\right|_{z_1=0}-\left.\frac{du_{p2}\left(z\right)}{dz_2}\right|_{z_2=0}=0 \end{aligned} \qquad \text{(A.7)}$$

Being the constants C_i known from the boundary conditions above and using Eqs. (A.6), the displacement expression can be obtained for both layer one and two:

$$\begin{aligned}
u_{p1}(z) &= \frac{\alpha \Delta T}{\lambda_1} \cdot \\
&\cdot \frac{\rho\left(a_3\left(a_6+\Omega_1 a_5\right)-\Omega_1\left(a_1+\Theta\, a_2\right)\right)+a_4\left(a_5+\Omega_1 \rho^2 a_6\right)}{\rho a_3\left(a_7\left(1+\Theta\Omega_1\right)+a_8\left(\Omega_1+\Theta\right)\right)+a_4\left(a_7\left(\Omega_1\rho^2+\Theta\right)+a_8\left(1+\Theta\Omega_1\rho^2\right)\right)} \\
u_{p2}(z) &= \frac{\alpha \Delta T}{\lambda_1} \cdot \\
&\cdot \frac{a_9\left(-a_4+\Omega_1 \rho\left(a_7-a_3+\Theta a_8\right)\right)+a_{10}\left(a_3+\Omega_1\left(a_8+\rho a_4+\Theta a_7\right)\right)}{\rho a_3\left(a_7\left(1+\Theta\Omega_1\right)+a_8\left(\Omega_1+\Theta\right)\right)+a_4\left(a_7\left(\Omega_1\rho^2+\Theta\right)+a_8\left(1+\Theta\Omega_1\rho^2\right)\right)}
\end{aligned} \tag{A.8}$$

Considering that the shear stress, $\tau(z)$, is proportional to the displacement through Eq. (2.4), it is possible to obtain the following expressions of $\tau(z)$:

$$\begin{aligned}
\tau_1(z) &= \frac{\alpha \Delta T\, EA \lambda_1}{2\pi r_0} \cdot \\
&\cdot \frac{\rho\left(a_3\left(a_6+\Omega_1 a_5\right)+\Omega_1\left(a_1+\Theta\, a_2\right)\right)-a_4\left(a_5+\Omega_1 \rho^2 a_6\right)}{\rho a_3\left(a_7\left(1+\Theta\Omega_1\right)+a_8\left(\Omega_1+\Theta\right)\right)+a_4\left(a_7\left(\Omega_1\rho^2+\Theta\right)+a_8\left(1+\Theta\Omega_1\rho^2\right)\right)} \\
\tau_2(z) &= \frac{\alpha \Delta T\, EA \lambda_1}{2\pi r_0} \cdot \\
&\cdot \frac{a_9\left(a_4-\Omega_1 \rho\left(a_7-a_3+\Theta a_8\right)\right)-a_{10}\left(a_3+\Omega_1\left(a_8+\rho a_4+\Theta a_7\right)\right)}{\rho a_3\left(a_7\left(1+\Theta\Omega_1\right)+a_8\left(\Omega_1+\Theta\right)\right)+a_4\left(a_7\left(\Omega_1\rho^2+\Theta\right)+a_8\left(1+\Theta\Omega_1\rho^2\right)\right)}
\end{aligned} \tag{A.9}$$

The expressions of the axial load, Eqs. (2.13), are found combining Eqs. (A.8) with Eq. (3).

The parameter ρ is expressed through Eq. (2.14), while the other parameters in Eqs. (A.8), (A.9) and (2.13) have the following expression:

$$\Omega_1 = \frac{k_1}{\lambda_1 k_b} = \frac{EA\lambda_1}{k_b} \tag{A.10}$$

$$\xi = \frac{h_2}{h_1} = \frac{1-\zeta}{\zeta} \tag{A.11}$$

$$\begin{aligned}
a_1 &= \cosh\left(\lambda_1 z\right) \\
a_2 &= \sinh\left(\lambda_1 z\right) \\
a_3 &= \cosh\left(\xi\, \rho h_1 \lambda_1\right) \\
a_4 &= \sinh\left(\xi\, \rho h_1 \lambda_1\right) \\
a_5 &= \cosh\left(\lambda_1 \left(h_1 - z\right)\right) \\
a_6 &= \sinh\left(\lambda_1 \left(h_1 - z\right)\right) \\
a_7 &= \cosh\left(\lambda_1 h_1\right) \\
a_8 &= \sinh\left(\lambda_1 h_1\right) \\
a_9 &= \cosh\left(\rho\lambda_1 \left(z - h_1\right)\right) \\
a_{10} &= \sinh\left(\rho\lambda_1 \left(z - h_1\right)\right)
\end{aligned} \tag{A.12}$$

with ζ being expressed through Eq. (2.15) and Θ having the same expression for the case of homogeneous soil except using Eq. (A.10) for Ω_1; h_1 and h_2 are the thickness of the first and the second layer respectively.

- Linear stiffness profile (Gibson soil)

When stiffness is varying proportionally to depth, the displacement is expressed through Eq. (2.16), whose general solution is:

$$u_p\left(z\right) = C_1 AiryAi\left(\mu z\right) + C_2 AiryBi\left(\mu z\right) \tag{A.13}$$

with μ being expressed through Eq. (3.17), *AiryAi* and *AiryBi* being Airy functions.

As in the case of constant stiffness, the boundary conditions are two:

$$\begin{aligned}
\left.\frac{du_p\left(z\right)}{dz}\right|_{z=0} &= \alpha\, \Delta T + \frac{k_t\, u_p\left(z\right)\big|_{z=0}}{EA} \\
\left.\frac{du_p\left(z\right)}{dz}\right|_{z=L} &= \alpha\, \Delta T - \frac{k_b\, u_p\left(z\right)\big|_{z=L}}{EA}
\end{aligned} \tag{A.14}$$

Once known the two constants C_i, the displacement $u_p(z)$ can be derived using Eq. (A.13); accordingly, the axial load distribution is obtained using Eq. (2.3). The expressions of the axial load at pile head and base are expressed by Eqs (2.18).

Approximate energy solutions

- Soil with continuous stiffness variation

The principal of virtual work and the equilibrium along the vertical direction, Eqs. (2.25) and (2.26) respectively, are written in terms of the two unknowns $\bar{u}_l$ and $\bar{z}_N$; their expressions are found to be:

$$\bar{u}_l = \alpha\,\Delta T\, 6\Omega_L\left(2+b\right)\left(3+b\right)\left(\lambda_L L\left(2+ab\left(3+b\right)\right)+2\Theta_L\left(1+b\right)\left(2+b\right)\right)\cdot$$
$$\cdot\begin{pmatrix} \Omega_L\lambda_L^3 L^3\left(12+ab\left(4+ab\right)\left(7+b\left(4+b\right)\right)\right)+ \\ +4\lambda_L^2 L^2\left(2+b\right)\cdot \\ \cdot\left(6+11ab+6ab^2+ab^3+\Theta_L\,\Omega_L\left(1+b\right)\left(2+b\right)\left(3+ab\right)\right)+ \\ +12\lambda_L L\left(2+b\right)^2\left(3+b\right)\left(\Omega_L+ab\Omega_L+\Theta_L+b\Theta_L\right)+ \\ +12\left(1+b\right)\left(2+b\right)^2\left(3+b\right)\left(1+\Theta_L\,\Omega_L\right) \end{pmatrix}^{-1} \tag{A.15}$$

$$\bar{z}_N = \frac{1}{2}\cdot\frac{\left(1+b\right)\left(2\left(2+b\right)+\Omega_L\lambda_L L\left(2+ab\right)\right)}{\left(2+b\right)\left(1+b+\Omega_L\lambda_L L\left(1+ab\right)+\Theta_L\,\Omega_L\left(1+b\right)\right)} \tag{A.16}$$

Expressions (A.15,16) allow to evaluate the axial load and the shear stress. The expression of the axial load is by Eq. (2.27), whereas the shear stress has the following expression:

$$\tau\left(z\right) = -\frac{EA\lambda_L}{2\pi r_0}\cdot\bar{u}_l\cdot\frac{\lambda_L L\left(a+\left(1-a\right)\left(\dfrac{z}{L}\right)^b\right)\left(\dfrac{z}{L}-\bar{z}_N\right)}{1-\bar{z}_N} \tag{A.17}$$

In the following, the general expressions of $\bar{u}_l$ and $\bar{z}_N$ along with the expressions of the axial load and the shear stress (Eqs. (A.15,16), (2.27) and (A.17) respectively), are written for four different profiles of shear stiffness.

- *Constant stiffness profile (*$a=1, b=0$*)*

$$\bar{u}_l = \alpha\,\Delta T\,\frac{6\Omega_L\left(\lambda_L L+2\Theta_L\right)}{12+\lambda_L L\left(12\Omega_L+\lambda_L L\left(4+\Omega_L\lambda_L L\right)\right)+4\Theta_L\left(3\Omega_L+\lambda_L L\left(3+\Omega_L\lambda_L L\right)\right)} \tag{A.18}$$

$$\bar{z}_N = \frac{1}{2}\cdot\frac{2+\Omega_L\lambda_L L}{1+\Omega_L\lambda_L L+\Theta_L\Omega_L} \qquad \text{(A.19)}$$

$$N(z) = EA\lambda_L L\bar{u}_l\cdot\frac{2\bar{z}_N\left(\Theta_L+\lambda_L L\frac{z}{L}\right)-\lambda_L L\left(\frac{z}{L}\right)^2}{2\left(1-\bar{z}_N\right)} \qquad \text{(A.20)}$$

$$\tau(z) = \frac{EA\lambda_L^2 L}{2\pi r_0}\cdot\bar{u}_l\cdot\frac{\frac{z}{L}-\bar{z}_N}{1-\bar{z}_N} \qquad \text{(A.21)}$$

- *Proportional stiffness profile ($a=0, b=1$)*

$$\bar{u}_l = \alpha\,\Delta T\,\frac{12\Omega_L\left(\lambda_L L+6\Theta_L\right)}{72+\lambda_L L\left(36\Omega_L+\lambda_L L\left(6+\Omega_L\lambda_L L\right)\right)+18\Theta_L\left(4\Omega_L+\lambda_L L\left(4+\Omega_L\lambda_L L\right)\right)} \qquad \text{(A.22)}$$

$$\bar{z}_N = \frac{2\left(3+\Omega_L\lambda_L L\right)}{3\left(2+\Omega_L\lambda_L L+2\Theta_L\Omega_L\right)} \qquad \text{(A.23)}$$

$$N(z) = EA\lambda_L L\bar{u}_l\cdot\frac{3\bar{z}_N\left(\lambda_L L\left(\frac{z}{L}\right)^2+2\Theta_L\right)-2\lambda_L L\left(\frac{z}{L}\right)^3}{6\left(1-\bar{z}_N\right)} \qquad \text{(A.24)}$$

$$\tau(z) = \frac{EA\lambda_L^2 L}{2\pi r_0}\cdot\bar{u}_l\cdot\frac{\frac{z}{L}\left(\frac{z}{L}-\bar{z}_N\right)}{1-\bar{z}_N} \qquad \text{(A.25)}$$

- *Linear stiffness profile ($b=1$)*

$$\begin{aligned}\bar{u} &= 12\Omega_L\left(\lambda_L L\left(1+2a\right)+6\Theta_L\right)\cdot\\ &\cdot\begin{bmatrix}\Omega_L\lambda_L^3 L^3\left(1+a\left(4+a\right)\right)+6\lambda_L^2 L^2\left(1+3a+\Theta_L\Omega_L\left(3+a\right)\right)+\\ +36\lambda_L L\left(\Omega_L+a\Omega_L+2\Theta_L\right)+72\left(1+\Theta_L\Omega_L\right)\end{bmatrix}^{-1}\end{aligned} \qquad \text{(A.26)}$$

$$\bar{z}_N = \frac{6+\Omega_L\lambda_L L\left(2+a\right)}{3\left(\Omega_L\lambda_L L\left(1+a\right)+2\left(1+\Theta_L\Omega_L\right)\right)} \qquad \text{(A.27)}$$

$$N(z)=EA\lambda_L L\bar{u}_l\cdot$$
$$\cdot\frac{3\bar{z}_N\left(\lambda_L L\left(\frac{z}{L}\right)^2(1-a)+2\left(\Theta_L+a\lambda_L L\frac{z}{L}\right)\right)-\lambda_L L\left(\frac{z}{L}\right)^2\left(3a+2\frac{z}{L}(1-a)\right)}{6\left(1-\bar{z}_N\right)} \quad \text{(A.28)}$$

$$\tau(z)=\frac{EA\lambda_L^2 L}{2\pi r_0}\cdot\bar{u}_l\cdot\frac{\left(a\left(1-\frac{z}{L}\right)+\frac{z}{L}\right)\left(\frac{z}{L}-\bar{z}_N\right)}{1-\bar{z}_N} \quad \text{(A.29)}$$

- *Power law stiffness profile (* $a=0$ *)*

$$\bar{u}_l=\alpha\,\Delta T\,\Omega_L\left(2+b\right)\left(3+b\right)\left(2\lambda_L L+2\Theta_L\left(1+b\right)\left(2+b\right)\right)\cdot$$
$$\cdot\left(2\begin{pmatrix}\Omega_L\lambda_L^3L^3+\lambda_L^2L^2\left(2+b\right)\left(2+\Theta_L\,\Omega_L\left(1+b\right)\left(2+b\right)\right)+\\+\lambda_L L\left(2+b\right)^2\left(3+b\right)\left(\Omega_L+\Theta_L+b\Theta_L\right)+\\+\left(1+b\right)\left(2+b\right)^2\left(3+b\right)\left(1+\Theta_L\,\Omega_L\right)\end{pmatrix}\right)^{-1} \quad \text{(A.30)}$$

$$\bar{z}_N=\frac{\left(1+b\right)\left(2+b+\Omega_L\lambda_L L\right)}{\left(2+b\right)\left(1+b+\Omega_L\lambda_L L+\Theta_L\,\Omega_L\left(1+b\right)\right)} \quad \text{(A.31)}$$

$$N(z)=EA\lambda_L L\,\bar{u}_l\cdot\left(\Theta_L\frac{\bar{z}_N}{1-\bar{z}_N}+\lambda_L L\frac{1}{1-\bar{z}_N}\left(\frac{z}{L}\right)^{b+1}\left(\frac{\bar{z}_N}{1+b}-\frac{z}{L\left(2+b\right)}\right)\right) \quad \text{(A.32)}$$

$$\tau(z)=\frac{EA\lambda_L^2 L}{2\pi r_0}\cdot\bar{u}_l\cdot\frac{\left(\frac{z}{L}\right)^b\left(\frac{z}{L}-\bar{z}_N\right)}{1-\bar{z}_N} \quad \text{(A.33)}$$

APPENDIX II

The ABAQUS code allows to add to its library any user-defined mechanical material behaviour by means of an interface. To this scope, the constitutive model is required to be programmed in a user subroutine, UMAT, using the Fortran language. Since the analyses carried out in the present work involved the use of the thermo-hypoplastic model, an advanced model not available in ABQUS, the constitutive behaviour has been provided by a subroutine.

The isothermal version of the hypoplastic model has been implemented by professor David Mašín and is accessible form the Soil Models website. The constitutive equation is integrated employing a stress-point algorithm. In particular, the explicit adaptive Runge-Kutta-Fehlberg embedded algorithm of the third order (RFK-23) is used (Sloan, 1987; Tamagnini et al., 2000). The Runge-Kutta-Fehlberg algorithms are explicit schemes with adaptive substepping, in which the idea is to estimate the substep size which would provide a solution of the desires accuracy, comparing two solutions obtained with two Runge-Kutta algorithms of different order. Based on these available solutions, to check if the substep size is sufficiently small, the relative error is measured and compared with a prescribed tolerance. If the control is true, the dimension of the next substep is updated using an extrapolation; on the contrary, both the solutions are rejected and the substep dimension is reduced employing a different extrapolation. In the latter case, the integration procedure stops when the tolerance check is satisfied or when the maximum required number of substeps is attained.

The isothermal hypoplastic model requires the input of 22 material constants and 16 solution-dependent state variables. The variables passed in the UMAT for information are:

- STRAN (NTENS) and DSTRAN (NTENS) that are the array of the total strain at the beginning of the increment and the strain increments, respectively;
- TIME and DTIME that are the value of step time at the beginning of the current increment and the time increment, respectively;
- NDI, NSHR, NTENS, NSTATEV, PROPS (NPROPS), NPROPS, COORDS, NOEL, NPT, KSTEP, KINC that are the number of direct stress components at the point, the number of engineering shear stress components at the point, the size of the stress or strain component array, the number of the solution-dependent state variables (i.e. 16 in the case of isothermal hypoplastic model), the user-specified array of material constants, the user defined number of material constants (i.e. 22 in the case of isothermal

hypoplastic model), the array of the coordinates of the point, the element number, the integration point number, the section point number within the layer, the increment number, respectively.

The variables that have been defined in the UMAT subroutine are:

- DDSDDE (NTENS, NTENS) that is the Jacobian matrix of the constitutive model;
- STRESS (NTENS) that is the array containing the stress tensor at the beginning of the increment to be update in the routine in order to give the stress tensor at the end of the increment;
- STATEV (NSTATEV) that is the array of the solution-dependent state variables at the beginning of the increment; as for the stress tensor, the values must be updated to get that at the end of the increment.

The thermal version of the hypoplastic model requires also:

- the definition of one additional temperature related state variable, pr_n, obtaining a total number of 17 solution-dependent state variables;
- the definition of the 6 additional material parameters for a total of 28 constants;
- TEMP and DTEMP, that are the temperature at the start of the increment and the increment of temperature, respectively, must be passed in the UMAT for information;
- the definition of the variable DDSDDT (NTENS) that accounts for the variation of the stress increments with respect to the temperature.

The available UMAT consists of an initial section in which all the variables are defined and initialized and of a time integration section in which the time integration is carried out with reference to other subroutines included in the final part of the UMAT. The thermal term has been implemented as follows.

1. In the initial part, the temperature related state variable and the temperature increment are initialized:

```
pr_n = statev(17)
pr_np1 = 0.0d0
tmp_n = temp
tmp_np1 = temp + dtemp
dtmp = dtemp
```

2. The modifications to the time integration section are:

- The numerical solution of the equation y' = f(y) is addressed in the *rkf23_update_hcea* subroutine in which the RK functions are built through the *rhs_hcea* subroutine. In the *rhs_hcea* subroutine the F_sig(ntens) and

F_q(nasv) vectors are found in f(y) through the *get_F_sig_q_hcea* subroutine, in which the thermal contribution is accounted as follows:

```
c ... initialize Ht and compute positive part of dtmp

         do ii=1,6
           Ht(ii) = 0.0d0
         end do

         if (dtmp.le.0.0d0) then
           pos_dtmp = 0.0d0
         else
           pos_dtmp = dtmp
         end if

         call get_tan_hcea(deps,sig,q,nasv,parms,nparms,MM,
        &                HH,LL,NN,istrain,error,
        &                tmp_n,dtmp,T_k,pr_n,pr_np1,Ht)

      c ... add termal contribution to stress rate

         do ii=1,6
              F_sig(ii) = F_sig(ii)+Ht(ii)*pos_dtmp
         end do
```

- The *get_tan_hcea* subroutine computes the matrix M.
  First, the thermal material parameters are defined as follows:

```
         n_t=parms(23)
         l_t=parms(24)
         tr_t=parms(25)
         k_t=parms(26)
         c_t=parms(27)
         gamma_t=parms(28)

         tmp_k = tmp_n + dtmp*T_k

         lam_star = parms(3) + l_t*dlog(tmp_k/tr_t)
         N_par = parms(5) + n_t*dlog(tmp_k/tr_t)
```

  Then, the thermal contribution is added by implementing the equations (3.72)÷(3.78):

```
         pr_np1 = pmean/(1.0-sin2phim)**(1/npow)
```

```
if (pr_np1.lt.pmean) then
  pr_np1 = pmean
end if

if (pr_n.lt.pr_np1) then
  pr_n = pr_np1
end if

psbs_t = pr_n*(1.0-sin2phim)**(1.0/npow)
N_par_t = N_par-(lam_star-kap_par)*dlog(pr_n/psbs_t)
void_t_psbs = dexp(N_par_t-lam_star*dlog(psbs_t))-1.0
void_t = dexp(N_par_t-lam_star*dlog(pmean))-1.0

x1_t = dlog(psbs_t)

if (tmp_k.ge.tr_t) then
  y1_t = dlog(1.0+void_t_psbs)+c_t*n_t*dlog(tmp_k/tr_t)
else
  y1_t = dlog(1.0+void_t_psbs)
end if

x_t = log(pmean)
y_t = -k_t*(x_t-x1_t)+y1_t
void_t_star = dexp(y_t)-1.0

tempdata_t = 0.0

if (void.gt.void_t_star) then
  if (void_t.ne.void_t_star) then
    tempdata_t = (void-void_t_star)/(void_t-void_t_star)
  end if
end if

if(tempdata_t.lt.0.0) then
    tempdata_t = 0.0
else if(tempdata_t.gt.1.0) then
    tempdata_t = 1.0
end if

fu_t = tempdata_t**gamma_t

fddivfdsbs_t=(pmean/psbs_t)**alpha_power
```

```
cv_t=(1.0+nuhh)/(1.0-2.0*nuhh)
ci_t=cv_t-(fddivfdsbs_t)*(cv_t-3.0*pmean/fs/lam_star)

ci_t=(fs*lam_star/3.0/pmean)*ci_t

h_t=n_t-l_t*dlog(peast/p_ref)

h_t=fu_t*(ci_t/tmp_k/lam_star)*h_t

do i=1,6
  HHt(i) = h_t*sig(i)
end do
```

- The consistent tangent stiffness is numerically computed in the *perturbate_hcea* subroutine adding the following part:

```
if (dtmp.gt.zero) then
        do jj=1,6
          DSDT(jj) = Ht(jj)
        end do
      end if
```

- The UMAT output is modified adding the following lines to the *solout_hcea* subroutine:

```
do i=1,ntens
     ddsddt(i) = DSDT(i)
ddsddt(i)=0.0d0
end do
```

The thermal version of the UMAT will be shared on the www.soilmodels.com website.

REFERENCES

Abaqus 6.14 Online Documentation

Abuel-Naga, H. M., Bergado, D. T., Ramana, G. V., Grino, L., Rujivipat, P. and Thet, Y. (2006a). Experimental evaluation of engineering behavior of soft Bangkok clay under elevated temperature. *Journal of Geotechnical and Geoenvironmental Engineering*, 132(7), 902-910.

Abuel-Naga, H. M., Bergado, D. T. and Chaiprakaikeow, S. (2006b). Innovative thermal technique for enhancing the performance of prefabricated vertical drain system. *Geotextiles and Geomembranes* 24(6): 359–370.

Abuel-Naga, H., Bergado, D. T., Bouazza, A. and Ramana, G. (2007). Volume change behaviour of saturated clays under drained heating conditions: experimental and constitutive modelling. *Canadian Geotechnical Journal*, 44, 942-956.

Adam, D., and Markiewicz, R. (2009). Energy from earth-coupled structures, foundations, tunnels and sewers. *Géotechnique*, 59(3), 229-236.

Akrouch, G. A., Sánchez, M., and Briaud, J. L. (2014). Thermo-mechanical behavior of energy piles in high plasticity clays. *Acta Geotechnica*, 9(3), 399-412.

Adinolfi, M., Maiorano, R. M. S., Mauro, A., Massarotti, N. and Aversa, S. (2018). On the influence of thermal cycles on the yearly performance of an energy pile. *Geomechanics for Energy and the Environment*, 16, 32–44.

Allani, M., Van Lysebetten, G., and Huybrechts, N. (2017). Experimental and numerical study of the thermo-mechanical behaviour of energy piles for Belgian practice. In *Advances in laboratory Testing and modelling of soils and Shales* (pp. 405-412). Springer, Cham.

Amatya, B. L., Soga, K., Bourne-Webb, P. J., Amis, T. and Laloui, L. (2012). Thermo-mechanical behaviour of energy piles. *Géotechnique*, 62(6), 503–519.

Aversa, S., and Evangelista, A. (1993). Thermal expansion of Neapolitan yellow tuff. *Rock Mechanics and Rock Engineering*, 26(4), 281-306.

Baldi, G., Hueckel, T., and Pellegrini, R. (1988). Thermal volume changes of the mineral–water system in low-porosity clay soils. *Canadian geotechnical journal*, 25(4), 807-825.

Baldi, G., Hueckel, T., Peano, A., and Pellegrini, R. (1991). Developments in modelling of thermohydro-geomechanical behaviour of Boom clay and clay-based buffer materials. Volume 1. *Commission of the European Communities*.

Batini, N., Loria, A. F. R., Conti, P., Testi, D., Grassi, W., and Laloui, L. (2015). Energy and geotechnical behaviour of energy piles for different design solutions. *Applied Thermal Engineering*, 86, 199-213.

Berezantzev, V. G. (1961). Load bearing capacity and deformation of piled foundations. *In Proceedings of the 5th international conference on soil mechanics and foundation engineering* (Vol. 2, pp. 11-15).

Bourne-Webb, P. J., Amatya, B., Soga, K., Amis, T., Davidson, C. and Payne, P. (2009). Energy pile test at Lambeth College, London: geotechnical and thermodynamic aspects of pile response to heat cycles. *Géotechnique*, 59(3), 237–248.

Bourne-Webb, P. J., Amatya, B., and Soga, K. (2013). A framework for understanding energy pile behaviour. *Proceedings of the Institution of Civil Engineers-Geotechnical Engineering*, 166(2), 170-177.

Bourne-Webb, P., Burlon, S., Javed, S., Kürten, S., and Loveridge, F. (2016). Analysis and design methods for energy geostructures. *Renewable and Sustainable Energy Reviews*, 65, 402-419.

Brandl, H. (2006). Energy foundation and other thermo-active ground structures. *Géotechnique*, 56(2), 81–122.

Brandl, H. (2008). Energy piles concepts. *In Deep Foundations on Bored and Auger Piles-BAP V* (pp. 89-108). CRC Press.

Burghignoli, A., Desideri, A., and Miliziano, S. (2000). A laboratory study on the thermomechanical behaviour of clayey soils. *Canadian Geotechnical Journal*, 37(4), 764-780.

Butterfield, R. and Douglas, R. A. (1981). “Flexibility coefficients for the design of piles and pile groups”, *Construction Industry Research and Information Association, Technical Note*, 108.

Campanella, R. G., and Mitchell, J. K. (1968). Influence of temperature variations on soil behaviour. *Journal of Soil Mechanics and Foundations Div*. Vol. 94(3), pp. 709–734, 1968.

Caulk, R., Ghazanfari, E., and McCartney, J. S. (2016). Parameterization of a calibrated geothermal energy pile model. *Geomechanics for Energy and the Environment*, 5, 1-15.

Cecinato, F., and Loveridge, F. A. (2015). Influences on the thermal efficiency of energy piles. *Energy*, 82, 1021-1033.

Cekerevac, C., and Laloui, L. (2004). Experimental study of thermal effects on the mechanical behaviour of a clay. *International journal for numerical and analytical methods in geomechanics*, 28(3), 209-228.

Chen, D. and McCartney, J.S. (2016). Parameters for load transfer analysis of energy piles in uniform soils. *International Journal of Geomechanics*, ASCE, 1-17. 10.1061/(ASCE) GM.1943-5622.0000873. 04016159.

Chen, Y., Xu, J., Li, H., Chen, L., Ng, C. W., and Liu, H. (2017). Performance of a prestressed concrete pipe energy pile during heating and cooling. *Journal of Performance of Constructed Facilities*, 31(3), 06017001.

Clancy, P., and Randolph, M. F. (1993). An approximate analysis procedure for piled raft foundations. *International Journal for Numerical and Analytical Methods Geomechanics*, 17(12), 849-869

Coyle, H. M. and Reese, L. C. (1966). Load transfer for axially loaded piles in clay. *Journal of the Soil Mechanics and Foundations Division*, 92(2), 1–26.

Crispin, J., Su, H., Round, K. and Mylonakis, G. (2019). Energy Formulation for Axial Pile Head Stiffness in Inhomogeneous Soil. *El-Naggar H., Abdel-Rahman K., Fellenius B., Shehata H. (eds) Sustainability Issues for the Deep Foundations. GeoMEast 2018. Sustainable Civil Infrastructures.* Cairo, 181–190.

Di Donna, A. and Laloui, L. (2014). Numerical analysis of the geotechnical behaviour of energy piles. *International journal for numerical and analytical methods in geomechanics*, 39(8), 861–888.

Di Donna, A. and Laloui, L. (2015a). Response of soil subjected to thermal cyclic loading: experimental and constitutive study. *Engineering Geology*, 190, 65–76.

Di Donna, A., Ferrari, A., and Laloui, L. (2015b). Experimental investigations of the soil–concrete interface: physical mechanisms, cyclic mobilization, and behaviour at different temperatures. *Canadian Geotechnical Journal*, 53(4), 659-672.

Di Donna, A., Loria, A. F. R. and Laloui, L. (2016). Numerical study of the response of a group of energy piles under different combinations of thermo-mechanical loads. *Computers and Geotechnics*, 72, 126–142.

Dupray, F., Laloui, L., and Kazangba, A. (2014). Numerical analysis of seasonal heat storage in an energy pile foundation. *Computers and Geotechnics*, 55, 67-77.

Ennigkeit, A., and Katzenbach, R. (2001). The double use of piles as foundation and heat exchanging elements. *In Proceedings of the international conference on soil mechanics and geothecnical engineering*. Vol. 2, pp. 893-896.

Fadejev, J., Simson, R., Kurnitski, J., and Haghighat, F. (2017). A review on energy piles design, sizing and modelling. *Energy*, 122, 390-407.

Frank, R., and Zhao, S. R. (1982). “Estimation par les paramètres pressiométriques de l’enfoncement sous charge axiale de pieux forés dans des sols fins.” *Bull. Liaison Lab. Ponts Chaussees*, 119, 17–24.

Fuentes, R., Pinyol, N., and Alonso, E. (2016). Effect of temperature induced excess porewater pressures on the shaft bearing capacity of geothermal piles. *Geomechanics for Energy and the Environment*, 8, 30-37.

Goode III, J. C. and McCartney, J. S. (2015). Centrifuge modeling of end-restraint effects in energy foundations. *Journal of Geotechnical and Geoenvironmental Engineering*, ASCE, 141(8), 04015034-1–04015034-13.

Gudehus, G. (1996). A comprehensive constitutive equation for granular materials. *Soils and foundations*, 36(1), 1-12.

Haenel, R., Rybach, L., and Stegena, L. (Eds.). (1988). *Handbook of terrestrial heat-flow density determination.* Kluwer Academic, Dordrecht, Netherlands, 9-57.

Hirschberg, S., Wiemer, S., and Burgherr, P. (Eds.). (2014). *Energy from the Earth: Deep Geothermal as a Resource for the Future?* (Vol. 62). vdf Hochschulverlag AG.

Hueckel, T. and Pellegrini, R. (1989). *Modelling of thermal failure of saturated clays*. International symposium on numerical models in geomechanics - NUMOG, 81-90.

Hueckel, T. and Baldi, M. (1990). Thermoplastic of saturated clays: an experimental constitutive study. *Journal of Geotechnical Engineering*, ASCE 116: 1778–1796.

Hueckel, T., Pellegrini, R. and Del Olmo, C. (1998). A constitutive study of thermo-elasto-plasticity of deep carbonatic clays. *International Journal for Numerical and Analytical Methods in Geomechanics*, 22(7), 549-574.

Iodice, C., Di Laora, R. and Mandolini A. (2020). Analytical solutions for Ultimate Limit State design of thermal piles. *Journal of Geotechnical and Geoenvironmental Engineering*, ASCE. 146(5), 04020016.

Karatzia, X. and Mylonakis, G. (2016). Horizontal stiffness and damping of piles in inhomogeneous soil. *Journal of Geotechnical and Geoenvironmental Engineering*, ASCE, 143(4), 04016113-1–04016113-19.

Katzenbach, R., Ramm, H., and Waberseck, T. (2008). Economic and eniviroment-friendly ways of designing and-using deep foundations. *In Proceedings of the Eighth International Conference on the Application of Stress Wave Theory to Piles 2008* (pp. 77-84).

Khalili, N., Uchaipichat, A., and Javadi, A. A. (2010). Skeletal thermal expansion coefficient and thermo-hydro-mechanical constitutive relations for saturated homogeneous porous media. *Mechanics of materials*, 42(6), 593-598.

Knellwolf, C., Peron, H. and Laloui, L. (2011). Geotechnical analysis of heat exchanger piles. *Journal of Geotechnical and Geoenvironmental Engineering*, ASCE, 137(10), 890–902.

Kolymbas, D. (1991). An outline of hypoplasticity. *Archive of applied mechanics*, 61(3), 143-151.

Laloui, L., Moreni, M., Fromentin, A., Pahud, D. and Steinmann, G. (1999). Heat exchanger pile: effect of the thermal solicitations on its mechanical properties. *Bulletin d'Hydrogéologie*, 17(1), 331–340.

Laloui, L., Moreni, M. and Vulliet, L. (2003). Comportement d'un pieu bi-fonction, fondation et échangeur de chaleur. *Canadian Geotechnical Journal*, 40(2), 388–402.

Laloui, L., Nuth, M. and Vulliet, L. (2006). Experimental and numerical investigations of the behaviour of a heat exchanger pile. *International Journal for Numerical and Analytical Methods in Geomechanics,* 30(8), 763–781.

Luo, J., Zhao, H., Gui, S., Xiang, W., and Rohn, J. (2017). Study of thermal migration and induced mechanical effects in double U-tube energy piles. *Computers and Geotechnics*, 91, 1-11.

Ma, Q. J., Ng, C. W. W., Mašín, D. and Zhou, C. (2017). An approach for modelling volume change of fine-grained soil subjected to thermal cycles. *Canadian Geotechnical Journal*, 54(6), 896–901.

Mašín, D. (2005). A hypoplastic constitutive model for clays. *International Journal for Numerical and Analytical Methods in Geomechanics*, 29(4), 311-336. Mašín, D.: Hypoplastic Cam-clay model. Géotechnique 62(6), 549–553 (2012)

Mašín, D., and Khalili, N. (2012). A thermo-mechanical model for variably saturated soils based on hypoplasticity. *International journal for numerical and analytical methods in geomechanics*, 36(12), 1461-1485.

Mašín, D. (2013). Clay hypoplasticity with explicitly defined asymptotic states. *Acta Geotechnica*, 8(5), 481-496

Mašín, D. (2014). Clay hypoplasticity model including stiffness anisotropy. *Géotechnique*, 64(3), 232-238.

Mašín, D. (2019). Modelling of Soil Behaviour with Hypoplasticity: Another Approach to Soil Constitutive Modelling. Springer.

McCartney, J. S. and Murphy, K. D. (2012). Strain distributions in full-scale energy foundations (DFI Young Professor Paper Competition 2012). *DFI Journal-The Journal of the Deep Foundations Institute*, 6(2), 26–38.

Mimouni, T., and Laloui, L. (2015). Behaviour of a group of energy piles. Canadian Geotechnical Journal, 52(12), 1913-1929.

Murphy, K. D. and McCartney, J. S. (2015). Seasonal response of energy foundations during building operation. *Geotechnical and Geological Engineering*, 33(2), 343–356.

Mylonakis, G. (2001). Winkler modulus for axially loaded piles. *Geotechnique*, 51(5), 455–462.

Niemunis, A., and Herle, I. (1997). Hypoplastic model for cohesionless soils with elastic strain range. *Mechanics of Cohesive-frictional Materials: An International Journal on Experiments, Modelling and Computation of Materials and Structures*, 2(4), 279-299.

Ng, C. W. W., Shi, C., Gunawan, A. and Laloui, L. (2014a). Centrifuge modelling of energy piles subjected to heating and cooling cycles in clay. *Geotechnique letters*, 4(4), 310–316.

Ng, C. W. W., Shi, C., Gunawan, A. and Laloui, L., and Liu, H. L. (2014b). Centrifuge modelling of heating effects on energy pile performance in saturated sand. *Canadian Geotechnical Journal*, 52(8), 1045–1057.

Ng, C. W. W., Wang, S. H., and Zhou, C. (2016a). Volume change behaviour of saturated sand under thermal cycles. *Géotechnique Letters*, 6(2), 124-131.

Ng, C. W. W., Ma, Q. J., and Gunawan, A. (2016b). Horizontal stress change of energy piles subjected to thermal cycles in sand. *Computers and Geotechnics*, 78, 54-61.

Ng, C. W. W., Gunawan, A., Shi, C., Ma, Q. J. and Liu, H. L. (2016c). Centrifuge modelling of displacement and replacement energy piles constructed in saturated sand: a comparative study. *Géotechnique Letters*, 6(1), 34–38.

Ng, C. W. W., and Ma, Q. J. (2019). Energy pile group subjected to non-symmetrical cyclic thermal loading in centrifuge. *Géotechnique Letters*, 1-5.

Nguyen, V. T., Tang, A. M., and Pereira, J. M. (2017). Long-term thermo-mechanical behavior of energy pile in dry sand. *Acta Geotechnica*, 12(4), 729-737.

Nguyen, V. T., Wu, N., Gan, Y., Pereira, J. M., and Tang, A. M. (2019). Long-term thermo-mechanical behaviour of energy piles in clay. *Environmental Geotechnics*, 1-12.

Pasten, C., and Santamarina, J. (2014). Thermally induced long-term displacement of thermoactive piles. *Journal of Geotechnical and Geoenvironmental Engineering*, ASCE, 140(5), 06014003.

Pahud, D., and Hubbuch, M. (2007). Measured thermal performances of the energy pile system of the dock midfield at Zürich Airport.

Plum R. L. and Esrig M.I. (1969) Some temperature effects on soil compressibility and pore water pressure. In *Effects of Temperature and Heat on Engineering Behavior of Soils*. Highway Research Board, Washington, DC, USA, Special Report No. 103, 231–242.

Rammal, D., Mroueh, H. and Burlon, S. (2018). Impact of thermal solicitations on the design of energy piles. *Renewable and Sustainable Energy Reviews*, 92, 111–120.

Randolph, M.F. and Wroth, C.P. (1978). Analysis of vertical deformation of vertically loaded piles. *Journal of Geotechnical and Geoenvironmental Engineering*, ASCE, 104(12), 1465–1488.

Roscoe, K. H., Schofield, A., and Wroth, A. P. (1958). On the yielding of soils. *Geotechnique*, 8(1), 22-53.

Roscoe K.H. and Burland J.B. (1968). On the generalised stress-strain behaviour of ‘wet’ clay. *Eng. plasticity*, Cambridge Univ. Press, 535-609

Rotta Loria, A. F. R., Gunawan, A., Shi, C., Laloui, L., and Ng, C. W. (2015). Numerical modelling of energy piles in saturated sand subjected to thermo-mechanical loads. *Geomechanics for Energy and the Environment*, 1, 1-15.

Rotta Loria, A. F. and Laloui, L. (2016a). Thermally induced group effects among energy piles. *Géotechnique*, 67(5), 374–393.

Rotta Loria, A. F., and Laloui, L. (2016b). The interaction factor method for energy pile groups. *Computers and Geotechnics*, 80, 121-137.

Rotta Loria, A. F., and Laloui, L. (2017a). Thermally induced group effects among energy piles. *Géotechnique*, 67(5), 374-393.

Rotta Loria, A. F., and Laloui, L. (2017b). The equivalent pier method for energy pile groups. *Géotechnique*, 67(8), 691-702.

Rotta Loria, A. F., and Laloui, L. (2017c). Displacement interaction among energy piles bearing on stiff soil strata. *Computers and Geotechnics*, 90, 144-154.

Rotta Loria, A. F., and Laloui, L. (2018a). Group action effects caused by various operating energy piles. *Géotechnique*, 68(9), 834-841.

Rotta Loria, A. F. R., Vadrot, A. and Laloui, L. (2018b). Analysis of the vertical displacement of energy pile groups. *Geomechanics for Energy and the Environment*, 16, 1–14.

Rui, Y., and Yin, M. (2017). Investigations of pile–soil interaction under thermo-mechanical loading. *Canadian Geotechnical Journal,* 55(7), 1016-1028.

Rui, Y., and Soga, K. (2019). Thermo-hydro-mechanical coupling analysis of a thermal pile. *Proceedings of the Institution of Civil Engineers-Geotechnical Engineering*, 172(2), 155-173.

Salciarini, D., Ronchi, F., Cattoni, E., and Tamagnini, C. (2014). Thermomechanical effects induced by energy piles operation in a small piled raft. *International journal of Geomechanics*, 15(2), 04014042.

Salciarini, D., Ronchi, F., and Tamagnini, C. (2017). Thermo-hydro-mechanical response of a large piled raft equipped with energy piles: a parametric study. *Acta Geotechnica*, 12(4), 703-728.

Sani, A. K., Singh, R. M., Amis, T., and Cavarretta, I. (2019). A review on the performance of geothermal energy pile foundation, its design process and applications. *Renewable and Sustainable Energy Reviews*, 106, 54-78.

Schofield, A., and Wroth, P. (1968). Critical state soil mechanics (Vol. 310). *London: McGraw-Hill.*

Seed, H. B., and Reese, L. C. (1957). The action of soft clay along friction piles. *Transactions of the American Society of Civil Engineers* 122: 731–754

Skempton, A. W. (1951). The bearing capacity of clays. *Selected Papers on Soil Mechanics*, 50-59.

Sloan, S. W., 1987. Substepping schemes for the numerical integration of elastoplastic stress-strain relations. *International Journal of Numerical Methods in Engineering*, 24, 893-911.

Stewart, M. A. and McCartney, J. S. (2013). Centrifuge modeling of soil-structure interaction in energy foundations. *Journal of Geotechnical and Geoenvironmental Engineering*, ASCE, 140(4), 04013044-1–04013044-11.

Sultan, N., Delage, P., and Cui, Y. J. (2002). Temperature effects on the volume change behaviour of Boom clay. *Engineering Geology*, 64(2-3), 135-145.

Suryatriyastuti, M. E., Mroueh, H. and Burlon, S. (2012). Understanding the temperature-induced mechanical behaviour of energy pile foundations. Renewable and sustainable energy reviews, 16(5), 3344–3354.

Suryatriyastuti, M. E., Mroueh, H. and Burlon, S. (2014). A load transfer approach for studying the cyclic behavior of thermo-active piles. *Computers and Geotechnics*, 55, 378–391.

Suryatriyastuti, M. E., Burlon, S., and Mroueh, H. (2015). On the understanding of cyclic interaction mechanisms in an energy pile group. *International journal for numerical and analytical methods in geomechanics*, 40(1), 3-24.

Sutman, M., Olgun, C. G., and Brettmann, T. (2015). Full-scale field testing of energy piles. In IFCEE 2015 (pp. 1638-1647).

Sutman, M., Olgun, C. G., and Laloui, L. (2019). Cyclic load–transfer approach for the analysis of energy piles. *Journal of Geotechnical and Geoenvironmental Engineering*, 145(1), 04018101.

Tamagnini, C., Viggiani, G., Chambon, R., and Desrues, J. (2000). Evaluation of different strategies for the integration of hypoplastic constitutive equations: Application to the CLoE model. *Mechanics of Cohesive-frictional Materials: An International Journal on Experiments, Modelling and Computation of Materials and Structures*, *5*(4), 263-289.

Tamagnini, C., and Viggiani, G. (2002). Constitutive modelling for rate-independent soils: a review. *Revue française de génie civil*, 6(6), 933-974.

Terzaghi, K. V. (1923). Die berechnung der durchlassigkeitsziffer des tones aus dem verlauf der hydrodynamischen spannungserscheinungen. *Sitzungsberichte der Akademie der Wissenschaften in Wien, Mathematisch-Naturwissenschaftliche Klasse, Abteilung IIa*, 132(3–4), 125-138.

Thomas, H. R. and King, S. D. (1994). A nonlinear, 2-dimensional, potential-based analysis of coupled heat and mass-transfer in a porous-medium. *International Journal for Numerical Methods in Engineering*, 37(21), 3707-3722, doi: 10.1002/nme.1620372108.

Towhata, I., Kuntiwattanakul, P., Seko, I., and Ohishi, K. (1993). Volume change of clays induced by heating as observed in consolidation tests. *Soils Foundations* 334: 170–183

Truesdell, C. (1956). Hypo-elastic shear. *Journal of Applied Physics*, 27(5), 441-447.

Vardanega, P. J. and Bolton M. D. (2011). Predicting shear strength mobilization of London clay. *Proc. 15th Eur. Conf. on Soil Mech. and Geoth. Eng.*, Athens, 1, 487–492.

Vega, A., and McCartney, J. S. (2014). Cyclic heating effects on thermal volume change of silt. Environmental Geotechnics, 2(5), 257-268.

Viggiani, G., and Atkinson, J. H. (1995). Stiffness of fine-grained soil at very small strains. *Géotechnique*, 45(2), 249-265.

Vieira, A., and Maranha, J. R. (2016). Thermoplastic analysis of a thermoactive pile in a normally consolidated clay. *International journal of Geomechanics*, 17(1), 04016030.

Wegener, D., and Herle, I. (2014). Prediction of permanent soil deformations due to cyclic shearing with a hypoplastic constitutive model. *Geotechnik*, 37(2), 113-122.

Wu, D., Liu, H. L., Kong, G. Q., Ng, C. W. W., and Cheng, X. H. (2018). Displacement response of an energy pile in saturated clay. *Proceedings of the Institution of Civil Engineers-Geotechnical Engineering*, 171(4), 285-294.

Yavari, N., Tang, A. M. and Pereira, J. M. (2014). A simple method for numerical modelling of mechanical behaviour of an energy pile. *Geotechnique letters*, 4(2), 119–124.

You, S., Cheng, X., Guo, H., and Yao, Z. (2016). Experimental study on structural response of CFG energy piles. *Applied Thermal Engineering*, 96, 640-651.

Zienkiewicz, O. C., Chan, A. H. C., Pastor, M., Schrefler, B. A., and Shiomi, T. (1999). *Computational geomechanics* (pp. 105-110). Chichester: Wiley.